

**Please cite the Published Version**

Rowley-Neale, Samuel James (2017) Development of novel catalytic solutions applied for the hydrogen evolution and oxygen reduction reactions. Doctoral thesis (PhD), Manchester Metropolitan University.

**Downloaded from:** <https://e-space.mmu.ac.uk/622449/>

**Usage rights:**  [Creative Commons: Attribution-Noncommercial-No Derivative Works 4.0](https://creativecommons.org/licenses/by-nc-nd/4.0/)

**Enquiries:**

If you have questions about this document, contact [openresearch@mmu.ac.uk](mailto:openresearch@mmu.ac.uk). Please include the URL of the record in e-space. If you believe that your, or a third party's rights have been compromised through this document please see our Take Down policy (available from <https://www.mmu.ac.uk/library/using-the-library/policies-and-guidelines>)

# **Development of Novel Catalytic Solutions Applied for the Hydrogen Evolution and Oxygen Reduction Reactions**

---

Samuel James Rowley-Neale

Submitted in partial fulfilment of the  
requirements of Manchester Metropolitan  
University for the degree of Doctor of  
Philosophy

October 2017

Faculty of Science and Engineering  
School of Science and the Environment

# Contents.

---

<b>Contents</b> .....	2
<b>Abstract</b> .....	6
<b>Aims and Objectives</b> .....	9
<b>Acknowledgments</b> .....	11
<b>List of Tables</b> .....	12
<b>List of Figures</b> .....	14
<b>Abbreviations</b> .....	27
<b>Chapter 1</b> .....	30
1.1. The Hydrogen Economy.....	30
1.1.1. The Hydrogen Evolution Reaction.....	32
1.1.2. The Oxygen Reduction Reaction.....	35
1.1.3. Triple Phase Boundary.....	37
1.1.4. 2D-MoS <sub>2</sub> Nanosheets.....	39
1.2. Fundamental Electrochemistry.....	41
1.2.1. The Electrochemical Cell.....	41
1.2.2. Potential Sweep Experiments.....	43
1.2.3. Chronoamperometry.....	49
1.2.4. Electrochemical Impedance Spectroscopy Experiments.....	50
1.3. Assessing a Materials HER and ORR Performance.....	52
1.3.1. Exchange Current Density.....	53
1.3.2. Overpotential.....	55
1.3.3. Tafel Equation and Slopes.....	56
1.4. Summation.....	59
<b>Chapter 2</b> .....	60
2.1. Chemicals.....	60
2.2. Physicochemical Characterisation of the 2D nanomaterials Utilised.....	61
2.2.1. Characterisation Equipment Specification.....	61

2.2.2.1. Physicochemical Characterisation of the 2D-MoS <sub>2</sub> and 2D-MoS <sub>2</sub> -SC.....	62
2.2.2.2. Lateral Width and Number of Layers of MoS <sub>2</sub> Utilised Determined <i>via</i> Optical Extinction Spectroscopy.....	67
2.2.3. Physicochemical Characterisation of the 2D-MoS <sub>2</sub> Nanosheets Explored towards the HER and ORR.....	69
2.2.4. Physicochemical Characterisation of 2D-MoS <sub>2</sub> Flakes Utilised in the Production of 2D-MoS <sub>2</sub> -SPEs.....	73
2.2.5. Physicochemical Characterisation of the 2D-MoSe <sub>2</sub> Flakes Utilised in the Production of 2D-MoSe <sub>2</sub> SPEs.....	81
2.3. Electrochemical Measurements.....	84
2.4. Drop-casting Modification of the Electrodes.....	85
2.5.1. Screen-Printed Electrode Fabrication .....	86
2.5.2. Fabrication of the MoS <sub>2</sub> and MoSe <sub>2</sub> Incorporated SPEs.....	88
2.6. Summation.....	93
<b>Chapter 3</b> .....	94
3.1. Introduction.....	94
3.2. Results and Discussion.....	98
3.2.1. Characterisation.....	98
3.2.2. Electrocatalytic Activity of 2D-MoS <sub>2</sub> and 2D-MoS <sub>2</sub> -SC.....	98
3.2.3. Tafel Analysis in Order to Determine the Rate Limiting HER Step.....	101
3.2.4. Electrochemical HER: Critical Coverage of 2D-MoS <sub>2</sub> Modification.....	104
3.3. Summation.....	107
<b>Chapter 4</b> .....	108
4.1. Introduction.....	108
4.2. Results and Discussion.....	113
4.2.1. Electrochemical Activity of the 2D-MoS <sub>2</sub> .....	113
4.2.2. Benchmarking the HER Activity of the Electrodes Utilised.....	115
4.2.3. Electrochemical Activity of the 2D-MoS <sub>2</sub> Towards the HER at an Assigned Mass of Electrode Coverage.....	116

4.2.5. Coverage of the Electrodes at Varying Masses of 2D-MoS <sub>2</sub> .....	119
4.2.6. Electrochemical Activity of the 2D-MoS <sub>2</sub> towards the HER at Varying Masses of Electrode Coverage.....	123
4.2.7.1. Assessment of the Intrinsic Electrochemical Activity of the 2D-MoS <sub>2</sub> nanosheets.....	125
4.2.7.2. Roughness Factor Calculation.....	125
4.2.7.3. Turn over Frequency Calculation.....	130
4.2.7.4. Number of Electrocatalytic Active Sites.....	133
4.2.7.5. Critical Coverage of 2D-MoS <sub>2</sub> Modification.....	136
4.3. Summation.....	141
<b>Chapter 5</b> .....	143
5.1. Introduction.....	143
5.2. Results and Discussion.....	147
5.2.1. Benchmarking the ORR Activity of the Electrodes Utilised.....	147
5.2.2. Electrochemical Activity of the 2D-MoS <sub>2</sub> towards the ORR at an Assigned Mass of Electrode Coverage.....	148
5.2.3. Electrochemical Activity of 2D-MoS <sub>2</sub> towards the ORR at Varying Masses of Electrode Coverage.....	149
5.2.4. Tafel Analysis and Assessment of the ORR Mechanism.....	155
5.3. Summation.....	164
<b>Chapter 6</b> .....	166
6.1. Introduction.....	166
6.2. Results and Discussion.....	168
6.2.1. Fabrication and Characterisation of the 2D-MoS <sub>2</sub> -SPEs.....	168
6.2.2. Electrocatalytic Activity of the 2D-MoS <sub>2</sub> -SPEs towards the HER.....	168
6.2.2.1. Tafel Analysis in order to Determine the Rate Limiting HER Step Exhibited by the 2D-MoS <sub>2</sub> -SPEs <sub>400nm</sub> .....	170
6.2.2.2. HER Turn over Frequency of the 2D-MoS <sub>2</sub> -SPEs <sub>400nm</sub> .....	171
6.2.3.1. Electrocatalytic Activity of the 2D-MoS <sub>2</sub> -SPEs <sub>400nm</sub> towards the ORR.....	171

6.2.3.2. Tafel Analysis and the Assessment of the ORR Mechanism for 2D-MoS <sub>2</sub> -SPEs <sub>400nm</sub> .....	174
6.2.4. Exploring the Effect of Altering the MoS <sub>2</sub> Flake Size upon the HER Activity of the 2D-MoS <sub>2</sub> -SPEs.....	175
6.2.5. Exploring the Effect of Altering the MoS <sub>2</sub> flake Size upon the ORR Activity of the 2D-MoS <sub>2</sub> -SPEs.....	177
6.2.6. The Cycling Stability and MoS <sub>2</sub> Coverage of the MoS <sub>2</sub> -SPEs.....	182
6.3. Summation.....	189
<b>Chapter 7</b> .....	191
7.1. Introduction.....	191
7.2. Results and Discussion.....	195
7.2.1. Fabrication and Characterisation of the MoSe <sub>2</sub> -SPEs.....	195
7.2.2.1. Electrocatalytic Activity of the MoSe <sub>2</sub> -SPEs towards the HER.....	195
7.2.2.2. Tafel Analysis in order to Determine the Rate Limiting HER Step Exhibited by the 2D-MoSe <sub>2</sub> -SPEs.....	197
7.2.2.3. HER Turn over Frequency of the 2D-MoSe <sub>2</sub> -SPEs.....	199
7.2.3. The Cycling Stability and 2D-MoSe <sub>2</sub> coverage of the 2D-MoSe <sub>2</sub> -SPEs.....	201
7.3. Summation.....	211
<b>Conclusion</b> .....	213
<b>Future Work</b> .....	215
<b>Appendix</b> .....	216
<b>References</b> .....	225
<b>Publication's Arising from this Thesis</b> .....	234

# Abstract.

---

This thesis reports the utilisation of 2D nanomaterials, namely molybdenum disulphide (2D-MoS<sub>2</sub>) and molybdenum diselenide (2D-MoSe<sub>2</sub>), as cheap, earth abundant and effective catalytic alternatives to platinum (Pt) for hydrogen production (*via* the hydrogen evolution reaction (HER)) within electrolyzers and energy generation (*via* the oxygen reduction reaction (ORR)) within proton exchange membrane fuel cells (PEMFC). Chapter 1 introduces the chemical reactions associated with electrolyzers and PEMFCs, then gives an overview of the relevant fundamental electrochemical concepts utilised throughout this thesis. Subsequent to this, Chapter 2 specifically describes the equipment and fabrication techniques implemented herein, in addition to providing the full physicochemical characterisation of the 2D-MoS<sub>2</sub> and 2D-MoSe<sub>2</sub> utilised in later chapters.

Chapter 3 demonstrates that a commonly employed surfactant (sodium cholate) used in the liquid exfoliation of 2D-MoS<sub>2</sub> has a profound effect upon its electrocatalytic activity. It is shown that the surfactant has a negative effect upon the observed HER signal output (decreasing the current density and increasing the electronegativity of the HER onset potential) of the 2D-MoS<sub>2</sub> compared to “pristine” 2D-MoS<sub>2</sub> (produced without a surfactant present). This suggests that future studies utilising 2D nanomaterials should carefully consider their use of a surfactant as well as perform the necessary control experiments.

Chapters 4 and 5 reveal that, in specific conditions, 2D-MoS<sub>2</sub> nanosheets are effective at reducing the electronegativity of the HER and ORR onset potentials, increasing their achievable current density and allowing the ORR reaction mechanism to occur *via* the desirable 4 electron process (product: H<sub>2</sub>O). This electrocatalytic

effect is reported herein for the first time. Research was undertaken by electrically wiring the 2D-MoS<sub>2</sub> to four commonly employed commercially available carbon based electrode support materials, namely edge plane pyrolytic graphite (EPPG), glassy carbon (GC), boron-doped diamond (BDD) and screen-printed graphite electrodes (SPE). The reduction in the electronegativity of the HER and ORR onset potential is shown to be associated with each supporting electrode's individual electron transfer kinetics/properties and is thus distinct from the literature, which predominately uses just GC as a supporting electrode material. It is revealed that the ability to catalyse the HER and ORR is dependent on the mass deposited until a critical coverage of 2D-MoS<sub>2</sub> nanosheets is achieved, after which its electrocatalytic benefits and/or surface stability curtail.

In Chapter 6, 2D-MoS<sub>2</sub> screen-printed electrodes (2D-MoS<sub>2</sub>-SPEs) are designed, fabricated and their performance is evaluated towards the electrochemical HER and ORR within acidic aqueous media. A screen-printable ink is developed, which allows for the tailoring of the 2D-MoS<sub>2</sub> content/mass used in the fabrication of the 2D-MoS<sub>2</sub>-SPEs. The 2D-MoS<sub>2</sub>-SPEs are shown to exhibit an electrocatalytic behaviour towards the ORR, which is found, critically, to be reliant upon the percentage mass incorporation of 2D-MoS<sub>2</sub> in the 2D-MoS<sub>2</sub>-SPEs. Chapter 7 utilises the exact methodology for electrocatalytic ink production as Chapter 6, however it incorporates 2D-MoSe<sub>2</sub> and explores the fabricated 2D-MoSe<sub>2</sub>-SPEs towards the HER where beneficial electrochemistry is observed. Both the 2D-MoS<sub>2</sub>-SPEs and 2D-MoSe<sub>2</sub>-SPEs display remarkable stability with no degradation in their respective performances over the course of 1000 repeat scans. The electrocatalytic inks produced in these chapters and the resultant mass producible electrodes mitigate the need to *post hoc* modify an electrode *via* the drop-casting technique that has been shown to result in poor stability.

This thesis reports that novel 2D nanomaterials can be implemented as beneficial electrode materials towards enhancing “green” energy generation technologies. Specifically, 2D-MoS<sub>2</sub> is shown to be effective at lowering the onset potential and increasing the achievable current density for the HER and ORR, giving rise to further benefits when 2D-MoS<sub>2</sub> (and 2D-MoSe<sub>2</sub> towards the HER) are incorporated into SPEs. These novel electrodes exhibit the inherent unique electrochemical behaviour of the 2D nanomaterials incorporated and benefit from the remarkable stability attributed to the intrinsic properties of a SPE. Consequently, the findings of this thesis are highly applicable to industrial electrolyser/fuel cell applications.

## Academic Aims of the Investigation.

---

**Academic Aim:** To conduct a detailed investigation of the production and characterisation of 2D nanomaterials for the HER (the reaction by which hydrogen is produced within an electrolyser) and ORR (a reaction essential to the production of an electrical current within a PEM fuel cell) and to develop potential electrocatalyst platforms.

### Objective

1. To study the effect that utilising a surfactant in the fabrication process of 2D-MoS<sub>2</sub> has upon its electrocatalytic behaviour.
2. Undertake a detailed study of how 2D-MoS<sub>2</sub> operate as HER and ORR electrode materials.
3. Translate the knowledge gained about the utilisation of 2D nanomaterials into production of electrocatalytic platforms, which incorporate 2D-MoS<sub>2</sub> and 2D-MoSe<sub>2</sub>, *via* the use of screen-printing technology, with appropriate literature benchmarking.

“If I can go the distance, you see, and that bell rings and I’m still standing, I’m gonna know for the first time in my life, see, that I weren’t just another bum from the neighbourhood”

Michael Sylvester Gardenzio Stallone – Rocky  
1976

## **Acknowledgements.**

---

Firstly, I would like to thank Professor Craig E. Banks for taking a chance on me. Offering a candidate (myself) who was unexperienced and unqualified an opportunity to prove his worth to the world. Thank you.

I can take little credit for the achievements of the past three years of study as without the support and love of my mother Gillian Rowley; it, simply, would have been impossible. Any accolade's I ever gain, are yours, a meagre gift of repayment but the best I can give. Your loving son, Sam.

To Julie Stott, little can be said as "thank you" is insufficient. You followed me down a bleak and difficult trail for two years when you could have took so many well-lit paths of your own. Maybe I could have done this alone but without you the final destination would not have been worth the effort.

I would also like to extend my gratitude to everyone in the Banks Research Group as well as the staff of MMU. In particular Amer Gaffar who for me has been equal parts; friend, mentor and bad influence. They all contributed in some part to the adventure of this PhD.

## List of Tables.

---

1. **Table 2.2.** Compositional analysis of XPS presented in Figure 2.09(C) and 2.09(D), shown in atom percentage concentration, excluding H which is not detected by this technique.
2. **Table 3.1.** Comparison of literature reporting surfactant fabricated MoS<sub>2</sub> based catalysts that have been explored towards the HER.
3. **Table 4.1.** Comparison of current literature reporting the use of MoS<sub>2</sub> as a catalyst explored towards the HER.
4. **Table 4.2.** The determined roughness factor ( $R_F$ ) values and the number of active sites (per cm<sup>2</sup>) for BDD, EPPG, GC and SPE all of which had been modified with 0, 252, 1009, 2019 ng cm<sup>-2</sup> 2D-MoS<sub>2</sub> nanosheets. Values determined using double layer capacitance obtained *via* cyclic voltammetry between the potential range of 0.01V and 0.1V.
5. **Table 5.1.** Comparison of current literature reporting the use of 2D-MoS<sub>2</sub> and related catalytic materials explored towards the ORR.
6. **Table 6.1.** Determined values for the Tafel Slope Gradient and  $\log I / \log v$  for a (bare) SPE, 5, 10, 20 and 40% 2D-MoS<sub>2</sub>-SPE<sub>400nm</sub>.
7. **Table 6.2.** Compositional analysis of XPS spectra for a SPE, 20% 2D-MoS<sub>2</sub>-SPE<sub>400nm</sub> *pre-* and *post-* 1000 repeat scan in 0.5 M H<sub>2</sub>SO<sub>4</sub>. Scan rate: 100 mVs<sup>-1</sup> (*vs.* SCE). Results shown in atom percentage concentration, excluding H which is not detected by this technique.
8. **Table 7.1.** Comparison of current literature reporting the use of MoSe<sub>2</sub> and related catalytic materials explored towards the HER.
9. **Table 7.2.** Compositional analysis of XPS spectra for a 10% 2D-MoSe<sub>2</sub>-SPE *pre* and *post* 1000 repeat scan in 0.5 M H<sub>2</sub>SO<sub>4</sub>. Scan rate utilised 100 mVs<sup>-1</sup>

(vs. SCE). Results shown in atom percentage concentration, excluding H which is not detected by this technique.

10. **Table A.1.** Determined values for the Tafel slopes,  $\log V/\log I$  and the size of the diffusional zone for BDD, EPPG, GC and SPE which had been modified with 0, 252, 504, 762, 1009, 1267, 1524, 1771, 2018, 2261 and 2533  $\text{ng cm}^{-2}$  of 2D-MoS<sub>2</sub>.

11. **Table A.2.** The determined roughness factor  $R_F$  values for BDD, EPPG, GC and SPE which had been modified with 0, 252, 1009, 2019  $\text{ng cm}^{-2}$  2D-MoS<sub>2</sub>. Values determined using double layer capacitance obtained *via* cyclic voltammetry between the potential range of 0.01V and 0.1 V.

## List of Figures.

---

It is important to note that all the figures presented within this thesis are original and represent novel data, apart from, a few examples that are reproduced from previous works and clearly stated as such, with the appropriate reference given.

1. **Figure 1.01.** Schematic of a proton exchange membrane electrolyser
2. **Figure 1.02.** Schematic of a proton exchange membrane fuel cell
3. **Figure 1.03.** Cross section of a PEMFC membrane electrode assembly and the three phase boundary as well as the reactions occurring.
4. **Figure. 1.04.** The Hexagonal lattice structure of 2D-MoS<sub>2</sub> nanosheets (molybdenum atoms in green and sulphur atoms in yellow).
5. **Figure 1.05.** (A) A typical three electrode system used to perform the electrochemical testing during this work. An SPE is visible as the working electrode to act as a representative example for the other working electrodes along with a SCE and Pt wire as a reference and counter electrodes respectively. (B) A simplified potentiostatic circuit that is representative of the one utilised within this study, the image is modified from Gamry.<sup>1</sup>
6. **Figure 1.06.** The typical electron pathway occurring at a working electrode, modified from a figure by Zoski.<sup>2</sup>
7. **Figure 1.07.** A reproduction of the triangular waveform of linear sweep voltammetry and cyclic voltammetry from Compton *et al.*<sup>3</sup>
8. **Figure 1.08.** Linear sweep voltammetry (LSV) of Pt electrode MoSe<sub>2</sub>-SPEs showing the onset of the HER (Solution composition: 0.5 M H<sub>2</sub>SO<sub>4</sub>) and ORR (Solution composition: oxygenated 0.1 M H<sub>2</sub>SO<sub>4</sub>). Scan rate: 25 mVs<sup>-1</sup> (vs. SCE).
9. **Figure 1.09.** Concentration profiles for a potential step based experiments at different times from, Compton *et al.*<sup>3</sup>

10. **Figure 1.09.** Typical cyclic voltammogram for a reversible redox process (1 mM  $[\text{Ru}(\text{NH}_3)_6]^{3+/2+}$  in 0.1 M KCl) using a glassy carbon electrode, where  $E_{p_a}$  and  $E_{p_c}$  correspond to the potential values at which the maximum anodic and cathodic peak currents ( $I_{p_c}$  and  $I_{p_a}$ , respectively) are recorded.
11. **Figure 1.10.** Ideal Randles equivalent circuit and corresponding Nyquist plot.
12. **Figure 1.11.** Typical polarization curves for a cathodic (blue) and anodic (red) electrode.  $j_0$  is the exchange current when  $j_a = -j_c$ . The overpotential ( $\eta$ ) is determined by a current density (current/area of the working electrode) of  $25 \mu\text{A cm}^{-2}$  deviation from the background current.
13. **Figure 1.12.** Slope B represents the Tafel slope and is assumed to be the steepest part (maximal Log current ( $i$ ) change to minimal  $\eta$  change) of the curve. The exchange current density ( $i_0$ ) is found *via* exfoliating the Tafel curve to  $\eta = 0$ . Modified from a figure by Bard *et al.*<sup>4</sup>
14. **Figure 2.01.** TEM images of the commercially sourced 2D-MoS<sub>2</sub> (A1) Scale bar: 50 nm; (A2) Scale bar: 1 nm; and the exfoliated 2D-MoS<sub>2</sub>-SC (B1); Scale bar: 100 nm, (B2); Scale bar: 2 nm.
15. **Figure 2.02.** Characterisation of the 2D-MoS<sub>2</sub> and 2D-MoS<sub>2</sub>-SC; (A) XRD (deposited on a glass slide), (B) Raman spectra (deposited onto a silicon wafer between 300 and 500  $\text{cm}^{-1}$ ). High resolution XPS spectra for the Mo 3d and S 2d regions of 2D-MoS<sub>2</sub> and 2D-MoS<sub>2</sub>-SC. (D) Extinction spectra (nanosheets dispersed in ethanol ( $1.22 \text{ mg L}^{-1}$ )).
16. **Figure 2.03.** TEM images of the commercially sourced 2D-MoS<sub>2</sub> nanosheets deposited onto a holey carbon grid. (A) TEM image at 5,800 times magnification (scale bar: 2  $\mu\text{m}$ ), (B) TEM image at 13,500 times magnification (scale bar: 1  $\mu\text{m}$ ).

17. **Figure 2.04.** (A) SEM image of a multi-layered 2D-MoS<sub>2</sub> nanosheet flake on top of few layer 2D-MoS<sub>2</sub> nanosheets immobilised on a silicon wafer along with EDS analysis highlighting the underlying silicon support (B, in red), molybdenum (C, in green) and sulphur (D, in blue) coverage of image A respectively.
18. **Figure 2.05.** XPS survey spectrum for a sample of the 2D-MoS<sub>2</sub> nanosheets once deposited onto a Si (111) wafer showing a 1:2.2 concentration percentage for Mo and S respectively.
19. **Figure. 2.06.** Curve fitted XPS Mo 3d spectrum
20. **Figure 2.07.** TEM images of the commercially sourced 400 nm 2D-MoS<sub>2</sub>. (A) Scale bar: 20 nm, (B) scale bar: 500 nm.
21. **Figure 2.08.** Characterisation of the commercially sourced 400 nm 2D-MoS<sub>2</sub> which is the basis of the fabricated 2D-MoS<sub>2</sub>-SPES<sub>400nm</sub>; (A) XRD spectra of the 2D-MoS<sub>2</sub> and (B) Raman spectra 2D-MoS<sub>2</sub>. High-resolution XPS spectra of Mo 3d and S 2d regions of MoS<sub>2</sub> (C and D respectively).
22. **Figure 2.09.** TEM images of the commercially sourced *ca.* 2 μm 2D-MoS<sub>2</sub> used in the fabrication of 2D-MoS<sub>2</sub>-SPES<sub>2μm</sub>. Scale bar: 2 μm.
23. **Figure 2.10.** TEM images of the commercially sourced *ca.* 6 μm 2D-MoS<sub>2</sub> used in the fabrication of 2D-MoS<sub>2</sub>-SPES<sub>2μm</sub>. Scale bar: 2 μm.
24. **Figure 2.11.** Characterisation of the commercially sourced *ca.* 2 μm 2D-MoS<sub>2</sub>; (A) XRD spectra of the 2 μm 2D-MoS<sub>2</sub> (B) Raman spectra *ca.* 2 μm 2D-MoS<sub>2</sub> deposited onto a silicon wafer between 300 and 500 cm<sup>-1</sup>. High-resolution XPS spectra of Mo 3d and S 2p regions of 2D-MoS<sub>2</sub> (C and D respectively).

25. **Figure 2.12.** Characterisation of the commercially sourced *ca.* 6  $\mu\text{m}$  2D-MoS<sub>2</sub>; (A) XRD spectra of the *ca.* 6  $\mu\text{m}$  2D-MoS<sub>2</sub> (B) Raman spectra *ca.* 6  $\mu\text{m}$  2D-MoS<sub>2</sub> deposited onto a silicon wafer between 300 and 500  $\text{cm}^{-1}$ . High-resolution XPS spectra of Mo 3d and S 2p regions of 2D-MoS<sub>2</sub> (C and D respectively).
26. **Figure 2.13.** TEM images of the commercially sourced 2D-MoSe<sub>2</sub>. (A) Scale bar: 100 nm, (B) scale bar: 500 nm.
27. **Figure 2.14.** Characterisation of the commercially sourced 2D-MoSe<sub>2</sub>; (A) XRD spectra of the 2D-MoSe<sub>2</sub> (B) Raman spectra 2D-MoSe<sub>2</sub> deposited onto a silicon wafer between 220 and 320  $\text{cm}^{-1}$ . High-resolution XPS spectra of Mo 3d and Se 3d regions of 2D-MoSe<sub>2</sub> (C and D respectively).
28. **Figure 2.15.** Graphical representation of the drop-casting procedure.
29. **Figure 2.16.** Photographs of SPEs: possible variants of SPE designs. Each of which has a varied working electrode of; (A) 0.01  $\text{cm}^2$  (B) 0.0196  $\text{cm}^2$  (x6), (C) the design utilised herein with a working area of 0.0707  $\text{cm}^2$  and (D) a dual electrode (4.5  $\text{cm}^2$ ).
30. **Figure 2.17.** Illustration of the screen-printing process (A) employed in this paper and (B) the individual stages necessary in order to fabricate the mass producible 2D-MoS<sub>2</sub>-SPEs.
31. **Figure 2.18.** Characterisation of a 20% 2D-MoS<sub>2</sub>-SPE<sub>400nm</sub> *via* XPS analysis; High-resolution XPS spectra of Mo 3d and S 2p regions of 2D-MoS<sub>2</sub> (A and B respectively).
32. **Figure 2.19.** High-resolution XPS spectra of Mo 3d and Se 3d regions of a 10% 2D-MoSe<sub>2</sub>-SPE (A and B respectively).

33. **Figure 3.01.** A) Typical LSV of bare/unmodified SPE, SPE modified with *ca.* 2.8 mg cm<sup>-2</sup> of SC, SPE modified with *ca.* 1725 ng cm<sup>-2</sup> of 2D-MoS<sub>2</sub>, SPE modified with *ca.* 1725 ng cm<sup>-2</sup> of 2D-MoS<sub>2</sub>-SC and a Pt electrode showing the onset of the HER. Scan rate; 0.25mVs<sup>-1</sup> (*vs.* SCE). Solution composition: 0.5 M H<sub>2</sub>SO<sub>4</sub>. (B) Tafel analysis; potential *vs.* ln of current density for Faradaic section of the LSV presented in (A). (C) The current densities observed at – 1.5 V for SPEs modified with 172, 345, 518, 690, 863, 1035, 1207, 1380, 1553 and 1726 ng cm<sup>-2</sup> of 2D-MoS<sub>2</sub> (green circles) and 2D-MoS<sub>2</sub>-SC (yellow triangles) as well as SPEs modified with *ca.* 282, 565, 848, 1131, 1414, 1697, 1980, 2263, 2545, 2828 mg cm<sup>-2</sup> of SC (red squares) (average standard deviation of 3 replicates). Scan rate; 0.25mVs<sup>-1</sup> (*vs.* SCE). Solution composition: 0.5 M H<sub>2</sub>SO<sub>4</sub>.
34. **Figure. 4.01.** Typical CV response of 2D-MoS<sub>2</sub> nanosheets immobilised upon a SPE in pH 7 phosphate buffer solution (PBS). First scan: solid black line. Second scan (representative of subsequent scans): red dotted line. Scan rate: 5 mVs<sup>-1</sup> (*vs.* SCE).
35. **Figure. 4.02.** (A) LSV of unmodified EPPG, GC, SPE, BDD and Pt electrodes showing the onset of the HER. In all cases, scan rate: 25 mVs<sup>-1</sup> (*vs.* SCE). Solution composition: 0.5 M H<sub>2</sub>SO<sub>4</sub>. (B) Tafel analysis; potential *vs.* natural log (ln) of current density for faradaic section of the LSV presented in (A).
36. **Figure. 4.03.** (A) LSV of 1267 ng cm<sup>-2</sup> modified EPPG, GC, SPE, BDD electrodes and an unmodified Pt electrode showing the onset of the HER. In all cases, scan rate: 25 mVs<sup>-1</sup> (*vs.* SCE). Solution composition: 0.5 M H<sub>2</sub>SO<sub>4</sub>. (B) Tafel analysis; potential *vs.* natural log (ln) of current density for Faradaic section of the LSV presented in (A).

37. **Figure. 4.04.** (A) Raman Spectra peak intensity and position for 504 (black), 1009 (red), 2019 (blue) and 2533 (green)  $\text{ng cm}^{-2}$  2D-MoS<sub>2</sub> nanosheet modifications on SPEs. (B) Depicts 2D-MoS<sub>2</sub> nanosheet coverage plotted against Raman peak intensity for  $E_{2g}^1$  (black) and  $A_{1g}$  (red) vibrational bands, showing a constant peak distance of  $24.7 \text{ cm}^{-1}$  at all coverages.
38. **Figure. 4.05.** Raman maps of SPE surface, each point showing the intensity ratio between the sum of the characteristic MoS<sub>2</sub> peak areas ( $380$  and  $405 \text{ cm}^{-1}$ ) against the area of the underlying graphite peak ( $1550 \text{ cm}^{-1}$ ). Using varying surface coverages of the 2D-MoS<sub>2</sub> nanosheets; 504 (A), 1009 (B), 2019 (C) and 2533 (D)  $\text{ng cm}^{-2}$ . The grey maps are the modified electrodes and the black map in each represents an unmodified electrode surface.
39. **Figure. 4.06.** Current density values taken at  $-0.75 \text{ V}$  from LSV from 0, 128.6, 252, 504, 762, 1009, 1267, 1524 and 1771  $\text{ng cm}^{-2}$  2D-MoS<sub>2</sub> nanosheets immobilised upon: (A) EPPG, (B) GC, (C) SPE (D) BDD. Each graph showing the plateauing effect of current density when a critical coverage of the 2D-MoS<sub>2</sub> nanosheets is deposited onto the electrodes surface. Error bars are the average and standard deviation of 3 replicates.
40. **Figure 4.07.** White light profilometry surface topography maps of SPE's modified with (A) 252, (B) 1009 and (C) 2019  $\text{ng cm}^{-2}$  of 2D-MoS<sub>2</sub> nanosheets. It is evident that the surface roughness remains relatively constant with the increasing 2D-MoS<sub>2</sub> nanosheet modification.
41. **Figure. 4.08.** CVs recorded in  $0.5 \text{ M H}_2\text{SO}_4$  solution for SPE's with varying amounts of 2D-MoS<sub>2</sub> nanosheet modification; (A) 0, (B) 252, (C) 1009, (D) 2019  $\text{ng cm}^{-2}$ . Scan rate:  $100 \text{ mVs}^{-1}$  (vs. SCE).

42. **Figure. 4.09.** The difference in anodic and cathodic current density taken at +0.06 V *versus* scan rate ( $\text{mVs}^{-1}$  vs. SCE). The slope of the linear regression indicates the value of double layer capacitance ( $C_{dl}$ ).
43. **Figure 4.10.** An EIS study showing charge transfer resistance (ohm) values for EPPG, GC, SPE and BDD against 2D-MoS<sub>2</sub> nanosheet coverages of 0, 252, 1009 and 2019  $\text{ng cm}^{-2}$ . Increasing coverage leading to a decrease in EIS followed by a plateau. The EIS study was carried out in 0.5 M H<sub>2</sub>SO<sub>4</sub>, the frequency was from 0.1–100,000 Hz, and an amplitude of 10 mV (vs. SCE). Inset: circuit utilised within experiments.
44. **Figure. 4.11.** Stability studies using SPEs modified with (A) 252, (B) 1009 and (C) 2019  $\text{ng cm}^{-2}$  2D-MoS<sub>2</sub> nanosheets. Cyclic Voltammetry was performed between the potential range of 0 to –0.8 V, repeated for 1000 cycles, these figures show the initial (black line) and 1000<sup>th</sup> (red line) scans.
45. **Figure. 5.01.** (A) LSVs of bare/unmodified EPPG, GC, SPE, BDD and Pt electrodes showing signals corresponding to the ORR. (B) LSVs recorded using 1524  $\text{ng cm}^{-2}$  2D-MoS<sub>2</sub> modified EPPG, GC, SPE, BDD and Pt electrodes showing the position of ORR peaks. In all cases; scan rate: 25  $\text{mVs}^{-1}$  (vs. SCE) and a solution composition of 0.1 M H<sub>2</sub>SO<sub>4</sub> which is oxygen saturated.
46. **Figure. 5.02.** ORR peak positions (black circles, left Y axis) taken from LSV, the ORR onset potential (blue triangles, left Y axis) and the number of electrons involved in the reaction mechanism (red squares, right Y axis) for 0, 252, 504, 762, 1009, 1267, 1524, 1771, 2018, 2261 and 2533  $\text{ng cm}^{-2}$  of 2D-MoS<sub>2</sub> deposited onto the following electrodes: (A) BDD, (B) EPPG, (C) GC and (D) SPE. Error bars are the standard deviation of 3 replicates. In all cases;

scan rate:  $25 \text{ mVs}^{-1}$  (vs. SCE) and a solution composition of  $0.1 \text{ M H}_2\text{SO}_4$  which is oxygen saturated.

47. **Figure 5.03.** Tafel slopes corresponding to the faradaic region of the LSVs for (A) BDD, (B) EPPG, (C) GC and (D) SPE all of which have been modified with 0, 252, 504, 762, 1009, 1267, 1524, 1771, 2018, 2261 and  $2533 \text{ ng cm}^{-2}$  of 2D-MoS<sub>2</sub>.
48. **Figure 5.04.** White light profilometry surface topography maps of bare/unmodified (A) BDD, (B) EPPG, (C) GC and (D) SPE. It is evident that the surface roughness of an SPE is far greater than that of the other carbon based electrodes. SQ being the Root mean squared value of the heights over the whole surface, SA being is the arithmetic average values of absolute height values over the whole surface.
49. **Figure 5.05.** SEM images of a typical SPE (A) and of a SPE which has been polished (B). Scale bar:  $10 \mu\text{m}$ .
50. **Figure 5.06.** White light profilometry surface topography maps of (A) a bare/unmodified and unpolished SPE, (B) a unpolished SPE modified with  $1009 \text{ ng cm}^{-2}$  of 2D-MoS<sub>2</sub>, (C) a bare/unmodified and polished SPE and (D) a polished SPE modified with  $1009 \text{ ng cm}^{-2}$  of 2D-MoS<sub>2</sub>. It is evident that the surface roughness of a unpolished SPE is far greater than that of a polished SPE. SQ being the Root mean squared value of the heights over the whole surface, SA being is the arithmetic average values of absolute height values over the whole surface.
51. **Figure 6.01.** LSVs of (bare) SPEs, 5%, 10%, 20% and 40% 2D-MoS<sub>2</sub>-SPE<sub>400nm</sub> showing the onset of the HER. Scan rate:  $25 \text{ mVs}^{-1}$  (vs. SCE). Solution composition:  $0.5 \text{ M H}_2\text{SO}_4$

52. **Figure 6.02.** (A) LSVs of SPE and 5%, 10%, 20% and 40% 2D-MoS<sub>2</sub>-SPE<sub>S400nm</sub> showing the onset and peak potential for the ORR. Scan rate: 25 mVs<sup>-1</sup> (vs. SCE). Solution composition: 0.1 M H<sub>2</sub>SO<sub>4</sub>. (B) Tafel analysis; ln of current density vs potential for faradaic section of the LSV presented in (A). (C) The number of electrons involved in the ORR mechanism for a (bare) SPE and 5%, 10%, 20% and 40% 2D-MoS<sub>2</sub>-SPE<sub>S400nm</sub> (average standard deviation of 3 replicates). The green and red dotted lines show the number of electrons required for the ORR process to proceed *via* the desirable mechanism to produce H<sub>2</sub>O ( $n = 4$ ) or the undesirable mechanism to H<sub>2</sub>O<sub>2</sub> ( $n = 2$ ) respectively.
53. **Figure 6.03.** LSVs of (bare) SPEs, 5%, 10%, 20% and 40% 2D-MoS<sub>2</sub>-SPE<sub>2μm</sub> showing the onset of the HER. Scan rate: 25 mVs<sup>-1</sup> (vs. SCE). Solution composition: 0.5 M H<sub>2</sub>SO<sub>4</sub>.
54. **Figure 6.04.** LSVs of (bare) SPEs, 5%, 10%, 20% and 40% 2D-MoS<sub>2</sub>-SPE<sub>6μm</sub> showing the onset of the HER. Scan rate: 25 mVs<sup>-1</sup> (vs. SCE). Solution composition: 0.5 M H<sub>2</sub>SO<sub>4</sub>.
55. **Figure 6.05.** (A) LSVs of (bare) SPE, 5%, 10%, 20% and 40% 2D-MoS<sub>2</sub>-SPE<sub>S2μm</sub> showing the onset and peak potential for the ORR. Scan rate: 25 mVs<sup>-1</sup> (vs. SCE). Solution composition: 0.1 M H<sub>2</sub>SO<sub>4</sub>. (B) Tafel analysis; ln of current density vs potential for Faradaic section of the LSV presented in (A). (C) The number of electrons involved in the ORR mechanism for a (bare) SPE, 5%, 10%, 20% and 40% 2D-MoS<sub>2</sub>-SPE<sub>S2μm</sub> (average of 3 results plus standard deviation). The green and red dotted lines show the number of electrons required for the ORR process to proceed *via* the desirable mechanism to

produce  $\text{H}_2\text{O}$  ( $n = 4$ ) or the undesirable mechanism to  $\text{H}_2\text{O}_2$  ( $n = 2$ ) respectively.

56. **Figure 6.06.** (A) LSVs of (bare) SPE, 5%, 10%, 20% and 40% 2D-MoS<sub>2</sub>-SPE<sub>S6 $\mu$ m</sub> showing the onset and peak potential for the ORR. Scan rate: 25 mVs<sup>-1</sup> (vs. SCE). Solution composition: 0.1 M H<sub>2</sub>SO<sub>4</sub>. (B) Tafel analysis; ln of current density vs potential for Faradaic section of the LSV presented in (A). (C) The number of electrons involved in the ORR mechanism as a function of electrode composition: (bare) SPE, 5%, 10%, 20% and 40% 2D-MoS<sub>2</sub>-SPE<sub>S6 $\mu$ m</sub> (average of 3 results plus standard deviation). The green and red dotted lines show the number of electrons required for the ORR process to proceed *via* the desirable mechanism to produce  $\text{H}_2\text{O}$  ( $n = 4$ ) or the undesirable mechanism to  $\text{H}_2\text{O}_2$  ( $n = 2$ ) respectively.

57. **Figure 6.07.** An EIS study showing charge transfer resistance (ohm) values for the (bare) SPE, 5, 10, 20 and 40% 400 nm 2D-MoS<sub>2</sub>-SPE<sub>S400nm</sub> (average of 3 results plus standard deviation). The EIS study was carried out in a solution of 1 mM potassium ferrocyanide (II) / 1 M KCl, the frequency was from 0.1–100,000 Hz using an amplitude of 10 mV (vs. SCE). Inset: circuit utilised within experiments. Error values stated within the manuscript.

58. **Figure 6.08.** Raman maps of (A) 5% 2D-MoS<sub>2</sub>-SPE<sub>S400nm</sub>, (B) 10% 2D-MoS<sub>2</sub>-SPE<sub>S400nm</sub>, (C) 20% 2D-MoS<sub>2</sub>-SPE<sub>S400nm</sub> and (D) 40% 2D-MoS<sub>2</sub>-SPE<sub>S400nm</sub>. Each point shows the intensity ratio between the sum of the characteristic MoS<sub>2</sub> peak areas (380 cm<sup>-1</sup>) against the area of the underlying graphite peak (1580 cm<sup>-1</sup>). The green map is the 2D-MoS<sub>2</sub>-SPE and the underlying red in each map represents an unmodified electrode surface.

59. **Figure 6.09.** SEM images of a (bare) SPE surface (A and B) and a 40% 2D-MoS<sub>2</sub>-SPE<sub>400 nm</sub> (C and D). SEM magnifications were  $\times 1000$  with a scale bar of 10  $\mu\text{m}$  and  $\times 10,000$  with a scale bar of 1  $\mu\text{m}$  respectively for the progressive images (A to B and C to D).
60. **Figure 6.10.** Cyclic stability examination of (A) 20% 2D-MoS<sub>2</sub>-SPE<sub>400 nm</sub> and (B) a SPE with 250  $\text{ng cm}^{-2}$  of 2D-MoS<sub>2</sub> drop-cast onto its surface. Performed *via* cycling voltammetry (scan rate: 100  $\text{mVs}^{-1}$  (*vs.* SCE), using a carbon counter electrode) between the potential range of 0 to  $-1.4$  V, repeated for 1000 cycles. These figures show the initial (yellow line), 10<sup>th</sup> (green line) scans, 100<sup>th</sup> (dark green) and 1000<sup>th</sup> scan (black line). (C) The current observed using chronoamperometry with the potential held at  $-0.75$  V (*vs.* SCE) for 36,000 seconds using a 20% 2D-MoS<sub>2</sub>-SPE<sub>400 nm</sub> recorded in 0.5 M H<sub>2</sub>SO<sub>4</sub>.
61. **Figure 7.01.** (A) LSV of bare/unmodified SPE, 5%, 10%, 20% and 40% 2D-MoSe<sub>2</sub>-SPEs showing the onset of the HER. Scan rate: 25  $\text{mVs}^{-1}$  (*vs.* SCE). Solution composition: 0.5 M H<sub>2</sub>SO<sub>4</sub>. (B) Tafel analysis; potential *vs.*  $\ln$  of current density for Faradaic section of the LSV presented in (A). (C) Cyclic stability examination of a 10% 2D-MoSe<sub>2</sub>-SPE *via* linear sweep voltammetry (scan rate: 100  $\text{mVs}^{-1}$  (*vs.* SCE)) was performed between the potential range of 0 to  $-1.4$  V, repeated for 1000 cycles, these figures show the initial (black), 10<sup>th</sup> (yellow) scans, 100<sup>th</sup> (light green) and 1000<sup>th</sup> scan (dark green).
62. **Figure 7.02.** Raman maps showing the surface of (A) 5% 2D-MoSe<sub>2</sub>-SPE, (B) 10% 2D-MoSe<sub>2</sub>-SPE, (C) 20% 2D-MoSe<sub>2</sub>-SPE and (D) 40% 2D-MoSe<sub>2</sub>-SPE. Each point shows the intensity ratio between the sum of the characteristic MoSe<sub>2</sub> peak areas ( $240\text{ cm}^{-1}$ ) against the area of the underlying graphite peak

( $1580\text{ cm}^{-1}$ ). The green maps are the 2D-MoSe<sub>2</sub>-SPE and the underlying red in each map represents an unmodified electrode surface.

63. **Figure 7.03.** SEM images of a bare/unmodified SPE surface (A and B) and a 10% 2D-MoSe<sub>2</sub>-SPE (C and D). SEM magnifications were  $\times 1\text{k}$  (scale bare,  $10\text{ }\mu\text{m}$ ) and  $\times 10\text{k}$  (scale bare,  $1\text{ }\mu\text{m}$ ) respectively for the progressive images (A to B and C to D).
64. **Figure 7.04.** An EIS study showing charge transfer resistance (ohm) values for the bare/unmodified, 5, 10, 20 and 40% 2D-MoSe<sub>2</sub>-SPEs. The EIS study was carried out in 1 mM potassium ferrocyanide (II) in 1 M KCl, the frequency was from 0.1–100,000 Hz using an amplitude of 10 mV (vs. SCE). Inset: circuit utilised within experiments.
65. **Figure 7.05.** Cyclic stability examination of a 10% 2D-MoSe<sub>2</sub>-SPE LSV performed between the potential range of 0 to  $-1.4\text{ V}$  using a carbon counter electrode, repeated for 1000 cycles. The figures shows the initial (yellow line), 10<sup>th</sup> (green line) scans, 100<sup>th</sup> (dark green) and 1000<sup>th</sup> scan (black line). Scan rate:  $100\text{ mVs}^{-1}$  (vs. SCE).
66. **Figure 7.06.** The current observed using chronoamperometry with the potential held at  $-0.75\text{ V}$  (vs. SCE) for 36,000 seconds using a 10% 2D-MoSe<sub>2</sub>-SPE recorded in  $0.5\text{ M H}_2\text{SO}_4$ .
67. **Figure 7.07.** Cyclic stability examination of a  $400\text{ mg cm}^{-2}$  2D-MoSe<sub>2</sub> SPE modified, *via* the drop-casting technique using LSVs. The potential range of 0 to  $-1.4\text{ V}$  was utilised and repeated for 1000 cycles. The figures show the initial (yellow line), 10<sup>th</sup> (green line) scans, 100<sup>th</sup> (dark green) and 1000<sup>th</sup> scan (black line). Scan rate:  $100\text{ mVs}^{-1}$  (vs. SCE).

68. **Figure A.1.** The difference in anodic and cathodic current density (potential range 0.01 to 0.11 V) taken at +0.06 V *versus* scan rate ( $\text{mV s}^{-1}$  *vs.* SCE) for a bare/unmodified SPE, SPE modified with *ca.*  $2.8 \text{ mg cm}^{-2}$  of SC, SPE modified with *ca.*  $1725 \text{ ng cm}^{-2}$  of 2D-MoS<sub>2</sub> and a SPE modified with *ca.*  $1725 \text{ ng cm}^{-2}$  of 2D-MoS<sub>2</sub>-SC. The slope of the linear regression indicates the value of double layer capacitance ( $C_{\text{dl}}$ :  $\mu\text{F cm}^{-2}$ ).
69. **Figure A.2.** Typical CVs recorded for (A) 5, (B) 10, (C) 20 and (D) 40 % 2D-MoS<sub>2</sub>-SPE<sub>S400nm</sub> between 0.01 to 0.11 V, which is assumed to be non-Faradaic, at various scan rates (*vs.* SCE) of 20, 40, 60, 80 and 100  $\text{mVs}^{-1}$ . Solution composition: 0.5 M H<sub>2</sub>SO<sub>4</sub>.
70. **Figure A.3.** The difference in the anodic and cathodic current density of a (bare) SPE, 5, 10, 20 and 40 % 2D-MoS<sub>2</sub>-SPE<sub>S400nm</sub> taken at +0.06 V from Figure A.2. *versus* scan rate ( $100 \text{ mVs}^{-1}$  *vs.* SCE). The slope of the linear regression is the value of double layer capacitance,  $C_{\text{dl}}$ : ( $\mu\text{F cm}^{-2}$ ). Solution composition: 0.5 M H<sub>2</sub>SO<sub>4</sub>.
71. **Figure A.4.** Typical cyclic voltammograms recorded in a solution of 0.5 M H<sub>2</sub>SO<sub>4</sub> using 5, 10, 20 and 40% 2D-MoSe<sub>2</sub>-SPEs. Scan rate:  $100 \text{ mVs}^{-1}$  (*vs.* SCE).
72. **Figure A.5.** The difference in the anodic and cathodic current density of a (bare) SPE, 5, 10, 20 and 40 % 2D-MoS<sub>2</sub>-SPE<sub>S400nm</sub> taken at +0.06 V from Figure A.4. *versus* scan rate ( $100 \text{ mVs}^{-1}$  *vs.* SCE). The slope of the linear regression is the value of double layer capacitance,  $C_{\text{dl}}$ : ( $\mu\text{F cm}^{-2}$ ). Solution composition: 0.5 M H<sub>2</sub>SO<sub>4</sub>.

# Abbreviations.

---

2D-MoS<sub>2</sub>: 2 Dimensional Molybdenum Disulphide

2D-MoSe<sub>2</sub>: 2 Dimensional Molybdenum Diselenide

2D-MoS<sub>2</sub>-SC: 2 Dimensional Molybdenum Disulphide Fabricated *via* a liquid exfoliation technique using the surfactant Sodium Cholate

2D-MoS<sub>2</sub>-SPES: 2 Dimensional Molybdenum Disulphide bulk mediated Screen-Printed Electrodes

2D-MoS<sub>2</sub>-SPES<sub>2μm</sub>: 2 Micrometre Molybdenum Disulphide bulk mediated Screen-Printed Electrodes

2D-MoS<sub>2</sub>-SPES<sub>400nm</sub>: 400 Nanometre Molybdenum Disulphide bulk mediated Screen-Printed Electrodes

2D-MoS<sub>2</sub>-SPES<sub>6μm</sub>: 6 Micrometre Molybdenum Disulphide bulk mediated Screen-Printed Electrodes

2D-MoSe<sub>2</sub>-SPES: Molybdenum Diselenide bulk mediated Screen-Printed Electrodes

Ads: adsorbed

Aq: aqueous

BDD: Boron Doped Diamond

C<sub>dl</sub>: Double Layer Capacitance

CP: Carbon Paper

CTAB: Cetyltrimethyl ammonium bromide

CV: Cyclic Voltammetry

EDS: Energy Dispersive Spectroscopy

EIS: Electrochemical Impedance Spectroscopy

E<sub>pa</sub>: Anodic Peak Potential

E<sub>pc</sub>: Cathodic Peak Potential

EPPG: Edge Plane Pyrolytic Graphite

GC: Glassy Carbon

GN: Graphene Nanosheets

HER: Hydrogen Evolution Reaction

HET: Heterogeneous Electron Transfer

HOR: Hydrogen Oxidation Reaction

$i$ : Current Density

$i_0$ : Exchange Current Density

$I_{p_a}$ : Anodic Peak Current

$I_{p_c}$ : Cathodic Peak Potential

$j$ : Overall Current

$j_a$ : Anodic Currents

$j_c$ : Cathodic Currents

$L_a$ : Lateral Length

LSV: Linear Sweep Voltammetry

MCN: Mesoporous Carbon Nanospheres

$M_I$ : Mass of Ink

MNT: Molybdenum disulphide Nanotubes

$M_P$ : Mass of Additive

NAS: Nano-assembled Structures

NF: Nanofibres

NG: Nitrogen Doped Graphene

NP: Nanoparticle

NW: Nanowires

OER: Oxygen Evolution Reaction

ORR: Oxygen Reduction Reaction

PECVD: Plasma-enhanced Chemical Vapor Deposition

PEM: Proton Exchange Membrane

PEMFC: Proton Exchange Membrane

PET: Polyethylene Terephthalate

RDE: Rotating Disk Electrode

$R_F$ : Roughness Factor

rGO: reduced graphene oxide

RHE: Reversible Hydrogen Electrode

RSD: Relative Standard Deviation

SC: Sodium Cholate

SCE: Saturated Calomel Electrode

SDS: Single Walled Nanotubes

SEM: Scanning Electron Microscope

SPE: Screen-Printed Electrode

TEM: Transmission Electron Microscope

TMD: Transition Metal Dichalcogenide

ToF: Turn Over Frequency

VB: Vibrational Bands

WLP: White Light Profilometry

XPS: X-ray photoelectron spectroscopy

XRD: X-ray Diffraction

# Chapter 1.

## The Hydrogen Economy and Electrochemistry

This chapter will describe the importance of finding an alternative electrode material to platinum for the hydrogen evolution reaction (within an electrolyser) and oxygen reduction reaction (within a hydrogen fuel cell). It will also give an outline as to the fundamental electrochemistry and electrochemical techniques utilised within this thesis.

### 1.1. The Hydrogen Economy

---

The increasing scarcity of fossil fuels, coupled with the consequences of anthropogenic climate change, has produced a global need to find feasible alternatives for energy generation.<sup>5-7</sup> One scenario of change is creating a global hydrogen economy, in which energy generation demands are met partially, or entirely by hydrogen fuel cells.<sup>8-10</sup> Utilising hydrogen fuels in this manner would cause a dramatic decrease in the anthropogenic greenhouse emissions and ozone precursors released by fossil fuel combustion, given that the major waste product of a hydrogen fuelled fuel cell is H<sub>2</sub>O.<sup>8, 11</sup>

The most widely used fuel cell is the proton exchange membrane (PEM) fuel cell, which can be utilised for a plethora of applications from vehicles to combined heat and power units.<sup>12</sup> They have advantages over typical fossil fuel engines, due to their zero carbon emissions and ability to undergo long periods of inactivity without detrimental energy output loss.<sup>13, 14</sup> The reason why they are not currently a viable alternative to fossil fuel engines in the majority of applications is the substantial cost per unit energy.<sup>15</sup> Therefore there is a demand to lower the cost of energy production associated with fuel cells. This can be done *via* lowering the cost of a PEM fuel cells fuel, typically H<sub>2</sub>, as well as increasing the energy output per unit fuel by increasing

the efficiency of the PEM fuel cell itself. It is therefore essential that the scientific field focuses research on trying to produce electrocatalysts in order to solve these problems.

### 1.1.1. The Hydrogen Evolution Reaction

As mentioned above the typical fuel for a PEM fuel cell is hydrogen. A common method of hydrogen production is the hydrogen evolution reaction (HER),<sup>16</sup> which is the focus of industrial electrolyzers, such as the proton exchange membrane (PEM) electrolyser depicted in Figure 1.01.

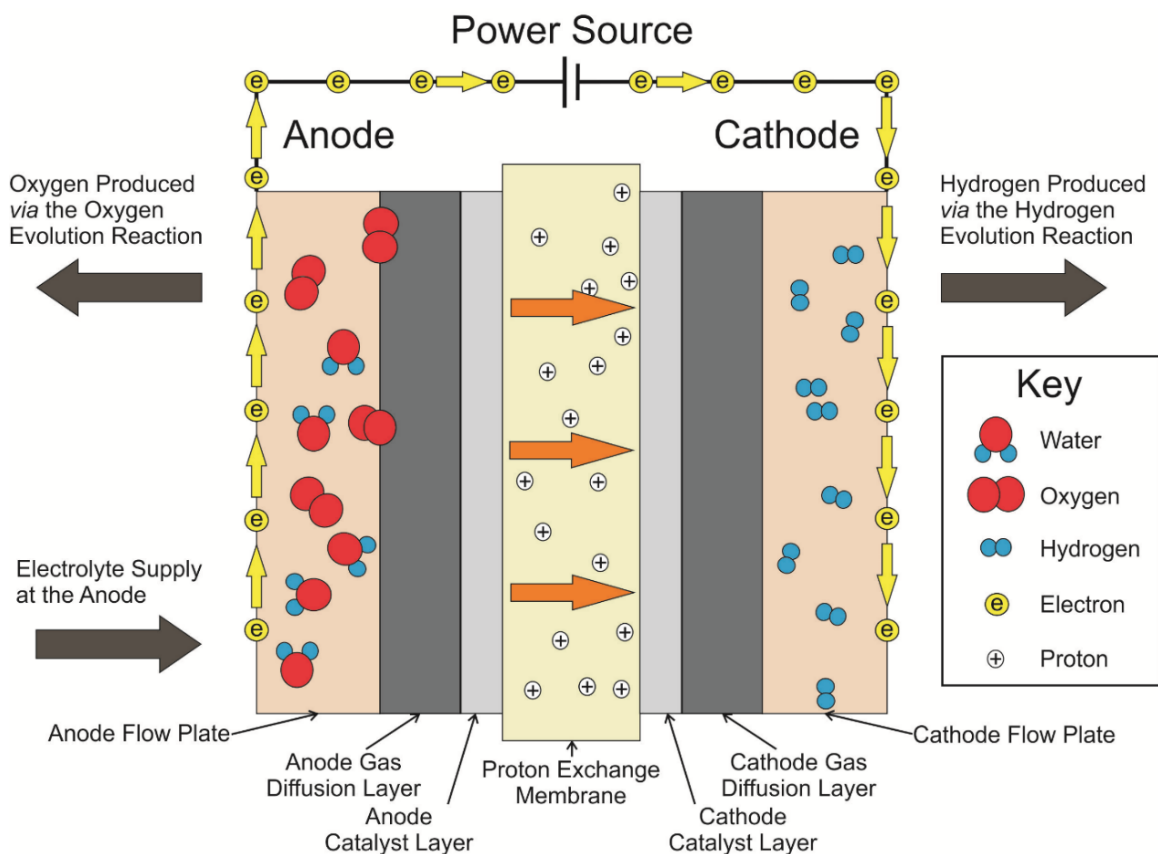
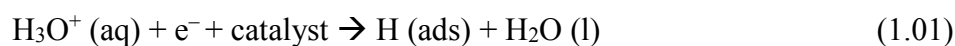


**Figure 1.01.** Schematic of a proton exchange membrane electrolyser

A PEM electrolyser comprises of separate anode and cathode compartments, each consists of an electrode block, gas diffusion layer, electrocatalyst, with a PEM membrane in the centre.<sup>17</sup> The functional properties of each of these components result in the overall functionality and performance of an electrolyser. The two major reactions that occur within an electrolyser are the oxygen evolution reaction (OER) and the HER, which occur at the anode and cathode respectively. The following

study will focus on the HER ( $2\text{H}^+ + 2\text{e}^- \rightarrow \text{H}_2$ ). The HER involves the electrocatalytic splitting of water, known to occur *via* one of two routes; these being either the Volmer-Tafel or the Volmer-Heyrovsky reactions, as seen below.<sup>18,19,20</sup>



The Volmer step (above) can then be followed by one of two possible steps; either the Heyrovsky step:<sup>18</sup>



or the Tafel step:<sup>18</sup>



The efficiency of the HER is dependent on the choice of electrocatalyst, with an optimal catalyst having a binding energy for adsorbed  $\text{H}^+$  close to that of the reactant or product.<sup>11</sup> Currently, the most proficient catalyst for the HER is platinum (Pt) which has a small binding energy for the reaction to occur, resulting in the reaction proceeding at a near zero over-potential.<sup>11, 18, 21, 22</sup> Pt is a precious metal with a low natural abundance of  $0.001\text{--}0.005 \text{ mg kg}^{-1}$  within the Earth's crust. This, coupled with its high demand, results in Pt having a very high cost.<sup>23</sup> Consequently, current research is focused on finding a cheaper, more sustainable catalyst for the HER, whilst maintaining performance and offering a binding energy towards  $\text{H}^+$  close to that of Pt,<sup>11</sup> thus contributing to making a hydrogen based energy economy substantially more feasible.

Carbon based materials have long been utilised as electrodes in a plethora of analytical and industrial electrochemical applications.<sup>24-30</sup> They have the distinct advantage of being comparatively cheap and easily obtainable, compared to the

traditional noble metal based materials. Carbon based electrodes benefit from structural polymorphism, chemical stability, wide operable potential windows and relatively inert electrochemistry.<sup>24, 25</sup> Carbon based electrodes are often used as the supporting material for a plethora of electrocatalytic materials, which lower HER onset potentials and, thus greatly improve the HER kinetics in comparison to the bare/unmodified carbon based electrode.<sup>5, 11, 31-35</sup>

The current challenge within HER research is finding a low-cost, abundantly available, non-polluting catalyst, which is capable of matching the HER onset potential observed when Pt is used as a catalyst.<sup>31, 34, 36, 37</sup> Towards this goal, Mo based catalysts have been explored as electrocatalysts for the HER. Table 4.1 (see Chapter 4 page 104) presents a thorough literature overview of Mo based electrocatalysts explored towards the HER, which is a combination and adaptation of work presented in papers by Joesen, Li and Ji,<sup>38-40</sup> in addition to recent literature reports. It is evident that 2D-MoS<sub>2</sub> and 2D-MoSe<sub>2</sub> have shown promising results as HER catalysts. MoS<sub>2</sub> is a semiconductor with a direct band gap of *ca.* 1.9 eV and excellent charge carrier mobility (reported to be no less than 200 cm<sup>2</sup> V<sup>-1</sup> s<sup>-1</sup>).<sup>41</sup> It has been beneficially implemented in numerous electrochemical applications, such as in transistors, sensors, solar cells, and lithium ion batteries.<sup>5, 42, 43</sup> Later Chapters (3, 4, 6 and 7) will explore the effectiveness of 2D-MoS<sub>2</sub> nanosheets and 2D-MoSe<sub>2</sub> at lowering the HER onset potential and increasing the achievable current density.

### 1.1.2. The Oxygen Reduction Reaction

The essential reactions which allow a fuel cell to produce a current are the hydrogen oxidation reaction (HOR) and the oxygen reduction reaction (ORR).<sup>44-46</sup> A PEM Fuel Cell is depicted in Figure 1.02. The HOR occurs on the anode and typically has a negligible overpotential, whilst the ORR occurs at the cathode and has a large kinetic inhibition, given the strong (di)oxygen double bond, resulting in a large energy input to initiate the reaction.<sup>44, 47</sup>

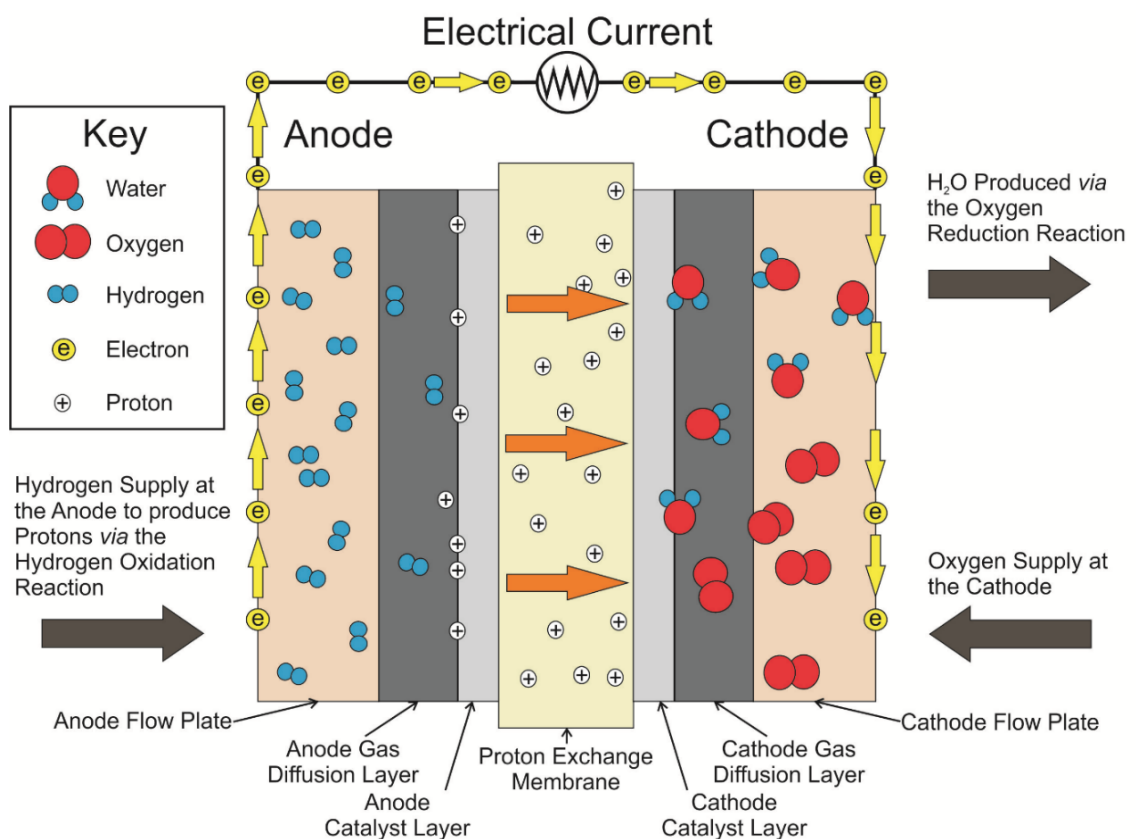
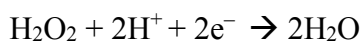


**Figure 1.02.** Schematic of a proton exchange membrane fuel cell

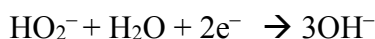
This results in the ORR being the rate determining step in the production of output energy from the initial H<sub>2</sub> fuel source. Taking this into account, by reducing the overpotential at which ORR occurs at the cathode, the process will be “more energetically favourable” and it is possible to make a significant increase within fuel

cell efficiency.<sup>48, 49</sup> Ideally this reaction combines O<sub>2</sub> (typically atmospheric, in the case of PEM fuel cells) with hydrogen in order to produce H<sub>2</sub>O; however, the reaction mechanism is dependent upon the pH of the electrode material and/or electrolyte used.<sup>50</sup> The ORR has proven to be problematic in fuel cells due to membrane degradation and electrode fouling, which occurs when the electrode utilised reduces O<sub>2</sub> *via* a 2 electron pathway (see below) resulting in the unfavourable production of H<sub>2</sub>O<sub>2</sub>.<sup>16-18, 21</sup> PEM fuel cell degradation *via* H<sub>2</sub>O<sub>2</sub> induced electrode fouling is the predominate factor in limiting the lifespan of this PEM fuel cell, potentially limiting the voltage output by up to 50% as a result of cathode corrosion (causing slow ORR kinetics).<sup>51</sup> The exact mechanism for H<sub>2</sub>O<sub>2</sub> poisoning of the cathode is unclear, with direct<sup>52</sup> and indirect<sup>53</sup> attack mechanisms proposed in the literature. The ORR processes in alkaline and acidic media are as follows: <sup>54, 55</sup>

**Acidic media:**



**Alkaline media:**



In order to avoid the production of H<sub>2</sub>O<sub>2</sub>, it is essential that an effective electrocatalyst is used so that a direct and more efficient 4-electron pathway is

favourable, producing only water as the product. Platinum (Pt) is typically implemented as an electrocatalyst for the ORR as this reaction mechanism occurs *via* the desirable 4 electron pathway, which produces the favourable product, H<sub>2</sub>O.<sup>45</sup> However, the use of Pt on a global industrial scale as an electrode material within PEM fuel cells has numerous real world limitations, such as its high cost and the relative global scarcity.<sup>56</sup> Clearly, finding a cheap, non-polluting and widely/consistently available alternative to Pt to be used as a catalyst for the ORR,<sup>52, 57</sup> but yet, is capable of matching the ORR onset potential observed when using Pt is a clear research goal.

In order to try and achieve this goal, researchers have investigated the electrocatalytic activity/ performance of various 2D materials towards the ORR.<sup>55, 58, 59</sup> Recent interest has been directed towards 2D-MoS<sub>2</sub>, Table 5.1. (see Chapter 5 and page 141), presents a thorough overview of the literature where 2D-MoS<sub>2</sub> is utilised towards the ORR. Taking this into account, later chapters (5 and 6) will explore the effectiveness of 2D-MoS<sub>2</sub> at lowering the ORR onset potential, increasing the peak current density and whether it allows the ORR to occur *via* the desirable 4 electron pathway.

### 1.1.3. Triple phase boundary

---

In both electrolyzers and fuel cells there is a region upon the electrodes surface where there is contact between three different phases; the electrode, electrolyte and gaseous inputs (be that hydrogen or oxygen). This region is commonly known as the triple phase boundary (TPB). A representation of this can be observed in Figure 1.03.

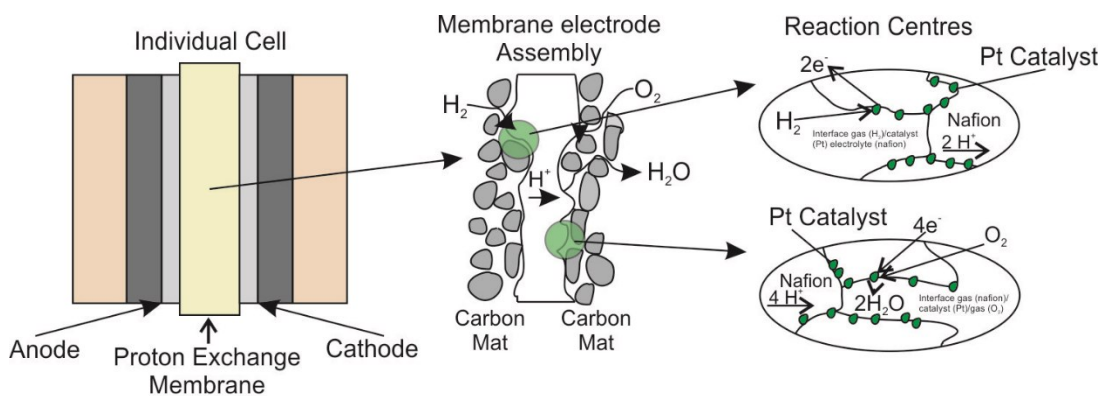


Figure 1.03. Cross section of a PEMFC membrane electrode assembly and the three phase boundary as well as the reactions occurring.

The electrochemical reactions, which occur with electrolyser and fuel cells happen at the TPB, so the TPB can be considered the active components of an electrode. It is therefore important to increase the area/density of the TPB in order to increase the efficiency of an electrode. Using a typical PEMFC with a platinum catalyst as a representative example Figure 1.03 shows how the carbon electrodes are porous and coated with finely divided Pt. The small particle size of Pt and its fine distribution helps to lower the amount utilised and therefore the cost. The typical modern cell works uses a coverage of  $0.1 \text{ mg cm}^{-2}$ . The electrolyte is a typical made from a proton porous membrane (typically nafion). In order to give full conductivity the membrane needs to be fully hydrated, in the case of PEMFC's this limits the temperate ranges to less than  $100 \text{ }^\circ\text{C}$ . The electrocatalyst is imbedded within the membrane in order to extend the membrane into the porous electrodes. Thereby creating the TPB where the catalyst can be in contact simultaneously with the gas, the proton conductor (membrane) and the electron conductor (carbon electrode). In the majority of cases this membrane/electrode assembly is less than a 1mm thick. Within this thesis the 2D nanomaterials studied herein shall take the place of Pt as the catalyst component of the TPB.

#### 1.1.4. 2D-MoS<sub>2</sub> Nanosheets

In the search for an effective electrocatalyst for the HER and ORR, research has focused on 2D-MoS<sub>2</sub>.<sup>33,34,40,60-62</sup> 2D-MoS<sub>2</sub> is a typical dichalcogenide, where a single layer comprises of two monoatomic planes of hexagonally arranged sulphur atoms linked to molybdenum atoms<sup>11, 60</sup> (see Figure 1.04). Such catalytic activity was however, shown to be anisotropic, with the basal plane of the 2D-MoS<sub>2</sub> nanosheet being relatively inert and the exposed sulphur edges being the active sites of electron transfer,<sup>11, 20, 33, 39, 63, 64</sup> each having distinct electrocatalytic properties in certain scenarios.<sup>65</sup> In the case of the HER, it is the dangling bonds of the electronegatively charged S atoms, located at the edge sites, which have an affinity for binding electropositive H<sup>+</sup> atoms within the electrolyte. Whilst for the ORR, it is the electropositive charge on the Mo atoms (induced by a polarization effect of the electronegative S atoms present), found at the edge planes, that are the binding sites for the electronegative O atoms within the electrolyte, thus making them the sites responsible for the electrocatalytic reactions observed when using 2D-MoS<sub>2</sub> as an electrochemical material towards the ORR.<sup>66</sup> The di-pole between the Mo and S increases the electron density near the Fermi level of the S atoms, which induces an increase in the electropositive charge on the adjacent Mo atom, *via* a polarization effect, thus facilitating the binding of the electronegative O atoms within the electrolyte and making the electropositive Mo atoms the sites responsible for the ORR and S atoms responsible for electrocatalytic activity. However, the activity of the semiconducting 2H MoS<sub>2</sub> phase nanosheets is primarily limited by its high electrical resistance which hinders charge transfer kinetics. Numerous studies have tried to mitigate this effect using dopants and various fabrication techniques in order to allow MoS<sub>2</sub> nanosheets to exhibit conductivity in a 1T metallic phase. Such as Voiry et al.<sup>67</sup> whom utilised

highly oxidised MoS<sub>2</sub> fabricated using an intercalation technique that involved SWCNTs in order to produce an abundance of 1T phase sites.

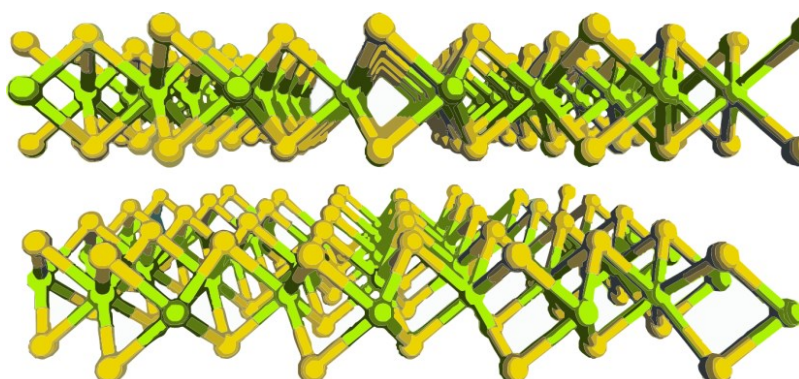


**Figure. 1.04.** *The Hexagonal lattice structure of 2D-MoS<sub>2</sub> nanosheets (molybdenum atoms in green and sulphur atoms in yellow).*

As a result of this, highly defected sheets of 2D-MoS<sub>2</sub> have a greater catalytic activity due to the larger number of exposed edges.<sup>21</sup> The 2D-MoS<sub>2</sub> edge-terminated sites have high energy kinetics,<sup>33</sup> thus making their production difficult, as thermodynamic instability results in the active edges forming fullerene-like structures, which have few exposed edge sites.<sup>33</sup> In its ‘bulk’ form, 2D-MoS<sub>2</sub> is an inefficient HER catalyst, due to it possessing a low ratio of exposed electroactive edges to inert basal-like planes and a high resistance resulting in slow ion transfer.<sup>5, 40, 68</sup> Interestingly, 2D-MoS<sub>2</sub> nanosheets have been reported to possess 13× more active sites compared to the alternative bulk MoS<sub>2</sub>.<sup>69,50</sup> Throughout this study 2D-MoS<sub>2</sub> will be the main “potential” electrocatalyst investigated towards lowering the onset potentials and increasing the achievable current of the HER and ORR.

## 1.2. Fundamental Electrochemistry

In order to explore how 2D nanosheets, such as 2D-MoS<sub>2</sub>, can be utilised as an alternative to Pt for the HER and ORR's it is necessary to implement electrochemical techniques.<sup>3, 70</sup> This section will outline the electrochemical theory and techniques used throughout the rest of this thesis.

### 1.2.1. The Electrochemical Cell

The typical electrochemical experimental involves a three electrode cell (See Figure 1.05), however the minimum required for an operational electrochemical cell is two. These two essential electrodes are referred to as “working” and “reference”. The working electrode is the electrode that interacts with the electrolyte, whilst the reference electrode sustains a persistent potential that is autonomous of the electrolyte and allows for an accurate measurement/comparison for the other electrodes.

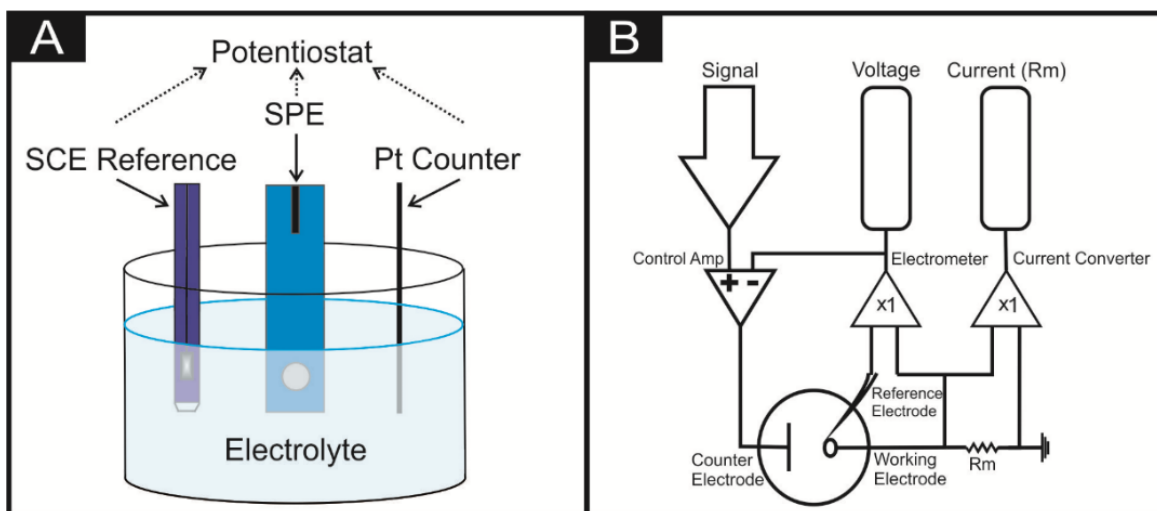


**Figure 1.05.** (A) A typical three electrode system used to perform the electrochemical testing during this work. An SPE is visible as the working electrode to act as a representative example for the other working electrodes along with a SCE and Pt wire as a reference and counter electrodes respectively. (B) A simplified potentiostatic circuit that is representative of the one utilised within this study, the image is modified from Gamry.<sup>1</sup>

A potentiostat (see Figure 1.05(B)), coupled with a two electrode cell, allows for controlled potential (potentiostatic) techniques, with minimal interference from ohmic drop, that involve the charge transfer processes between the electrode/electrolyte interfaces. The electrode of most concern is the working, since it is where the investigated reactions will occur. Figure 1.06 graphically represents a basic overview of the processes that occur at the working electrode. The observed current at the working electrode is dependent upon several factors, such as; mass transport, heterogeneous rate constants, chemical reactions and adsorption/desorption.

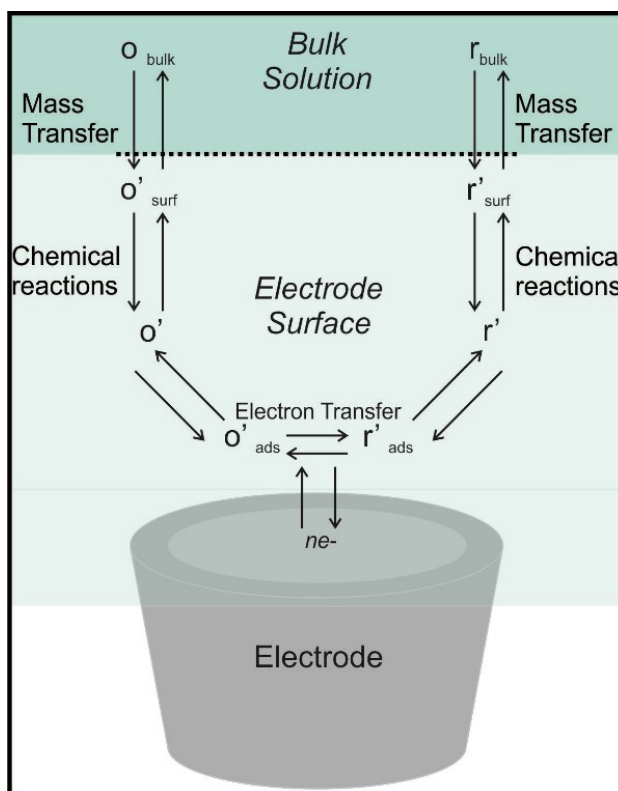


**Figure 1.06.** The typical electron pathway occurring at a working electrode, modified from a figure by Zoski.<sup>2</sup>

The reference electrode utilised within this study is a saturated calomel electrode (SCE), there is, however, a plethora of different options within the literature.<sup>2-4, 71</sup> In the case of potentiostatic measurements, such as the electrochemical measurements carried out within this study, it is typically the case that a third

“counter” electrode will be employed in order to operate in conjunction with the working electrode to form a circuit, *via* the electrolyte. The current that flows through this circuit can then be measured. The counter electrode is typically a non-reactive pure metal, such as a polycrystalline platinum electrode, with a high surface area. The three electrode system described above enables an accurate measurement of the working electrodes potential, in relation to the reference electrode, without having to pass a current over it.<sup>70</sup> An electrochemical cell can be divided into two categories based upon whether they; require an external energy input to operate (electrolytic) or produce an electrical energy (galvanic) by the constant input of a fuel source. This is an important distinction to know for this thesis as an electrolyser is an electrolytic cell whereas a PEM fuel cell is a galvanic cell.<sup>72, 73</sup> In other words, after an initial energy input (that could be drawn from renewable sources) to produce hydrogen, in an electrolyser, it is possible to yield an electrical current *via* the input of the hydrogen fuel source into a PEM fuel cell.

### 1.2.2. Potential Sweep Experiments

---

Many of the experiments performed herein involve a linear sweeping of an electrode’s potential from an initial potential  $V_1$  to an end potential  $V_2$ , this is known as linear sweep voltammetry (LSV). The potential sweep can sub-sequentially be reversed, resulting in the electrode going back to its initial  $V_1$  potential. This process is referred to as cyclic voltammetry (CV). It is possible to alter the rate of this potential sweep, which is measured in  $\text{Vs}^{-1}$ , *via* the use of a potentiostat. This is depicted graphically in Figure 1.07.

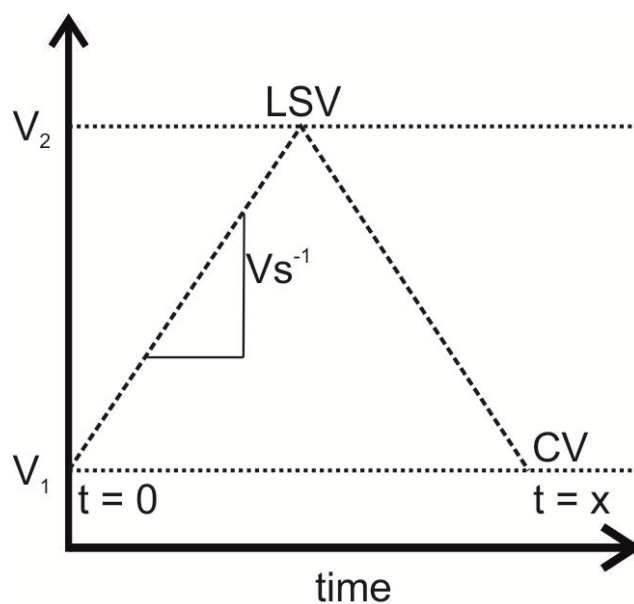


**Figure 1.07.** A reproduction of the triangular waveform of linear sweep voltammetry and cyclic voltammetry from Compton et al.<sup>3</sup>

This technique provides qualitative data about the Faradaic processes occurring at the electrode/electrolyte interface. There are numerous methodologies for interpreting the data that a LSV or CV provides. This study will focus on using LSV's as a technique to interpret the properties of various electrocatalytic materials explored towards the HER and ORR. For example the typical HER and ORR LSV responses for a polycrystalline platinum micro-electrode (Pt) are displayed in Figure 1.08 (A) and (B), respectively. The observed onset potentials of *ca.*  $-0.25$  V (v. SCE) and  $+0.5$  V (v. SCE) are consistent with the literature standards.<sup>74,75</sup> This thesis will attempt to use 2D nanomaterials (namely 2D-MoS<sub>2</sub>) in order to achieve comparable onset potentials. Thus, producing a cheaper, more earth abundant cathodic electrode material for electrolysers and fuel cells. The fundamental interpretation of a LSV can be described *via* concentration-time plots as seen in Figure 1.08.

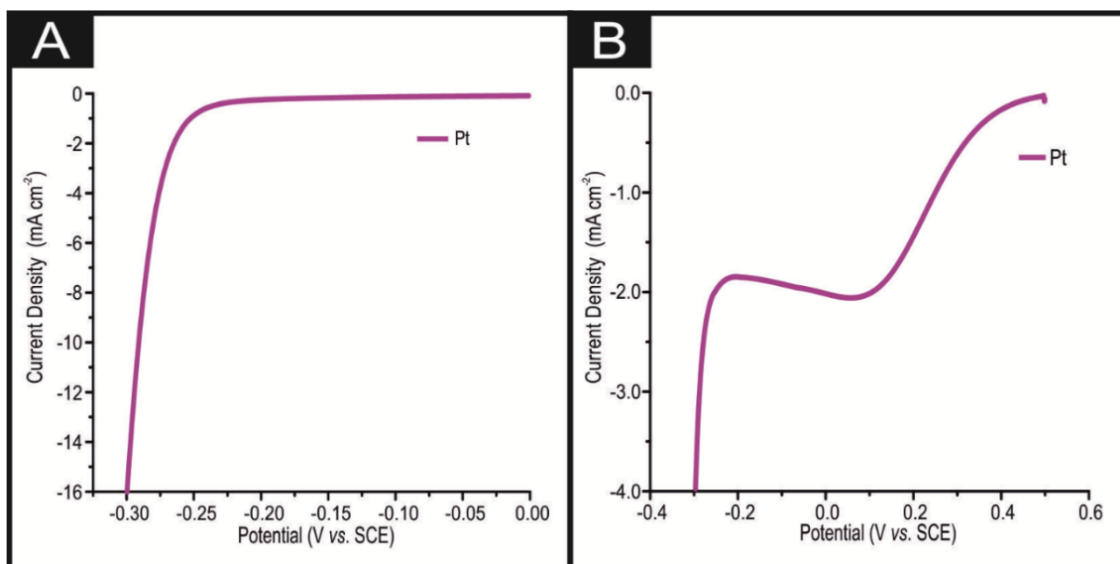


**Figure 1.08.** Linear sweep voltammetry (LSV) of Pt electrode 2D-MoSe<sub>2</sub>-SPEs showing (A) the onset of the HER (Solution composition: 0.5 M H<sub>2</sub>SO<sub>4</sub>) and (B) ORR (Solution composition: oxygenated 0.1 M H<sub>2</sub>SO<sub>4</sub>). Scan rate: 25 mVs<sup>-1</sup> (vs. SCE).

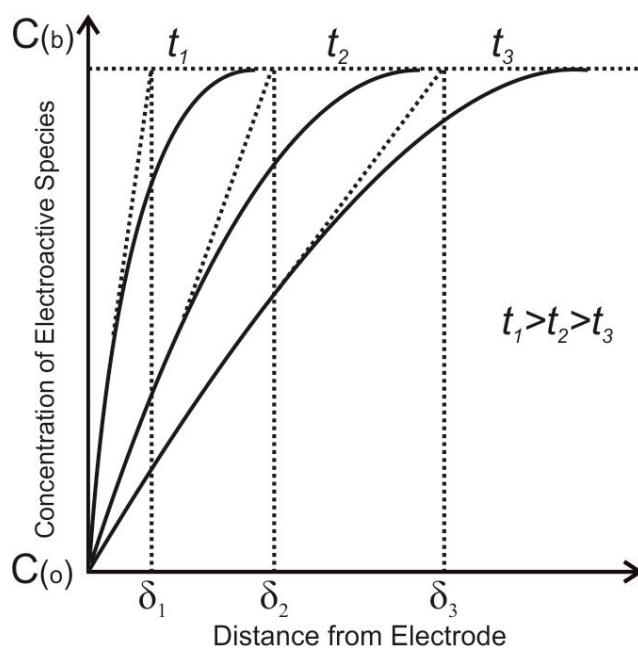


**Figure 1.09.** Concentration profiles for a potential step based experiments at different times, from Compton et al.<sup>3</sup>

The zone within the electrode/electrolyte which is depleted of all reactants is termed the *diffusional zone* (D). The thickness of this zone will vary and will be herein referred to as  $\delta$ . Initially upon inducing a potential to an electrode, the diffusional zone thickness will be narrow and there will be a large concentration gradient between products and reactants. As the amount of the time that the voltage has been applied increases, the diffusional layer will expand, and cause a subsequent decrease in the concentration gradient (see Figure 1.09). The concentration gradient slope is termed  $(C_o(b,t)/C_r(0,t)/\delta)$ , where  $C_o(b,t)$  and  $C_r(0,t)$  refer to the bulk concentration and surface concentration of  $O$ , respectively. The current, therefore, is related to the change in this slope and is dependent upon  $C_o(0,t)$  as well as  $\delta^2$ . When the applied potential ( $E$ ) reaches the standard cell potential ( $E^\circ$ ) of the particular redox couple, there is an acceleration in the concentration change of the surface concentrations. This is in accordance with Nernstian dynamics (See Equation 1.18). Once  $E = E^\circ$  the oxidised and reduced species can be assumed to be at equilibrium,  $(C_o(0,t)/C_r(0,t)=1)$ . At greater electronegative potentials ( $E > E^\circ$ ) the  $C_r(0,t)$  can be considered to be in an 10 x excess  $(C_o(0,t)/C_r(0,t) = 1/10, n = 1)$ . There is a parallel increase in the diffusional layer's thickness and a decrease in  $C_o(0,t)$ . This controls the slope value after  $C_o(0,t)$  approaches 0, giving a peak shaped voltammogram. The decrease in achievable current observed in Figure 1.08 is inversely proportional to the  $\sqrt{time}$  ( $t^{-0.5}$ ) and can be modelled by the Cottrell equation:<sup>3, 4</sup>

$$i(t) = -\frac{nFAD_oC_o(b)}{(\pi D_o t)^{\frac{1}{2}}} + \frac{nFAD_oC_o(O)}{r} \quad (1.08)$$

where  $(\pi D_o t)^{\frac{1}{2}}$  relates to the thickness of the diffusion layer.

A typical CV for a reversible reaction can be observed in Figure 1.09. Whilst there is a plethora of information that can be drawn from such a CV (electrochemical working area of the working electrode and the heterogeneous electron transfer kinetics ( $K^\circ$ ), to name just two), this study predominately is interested in determining the onset potential, which we will explore later, and the magnitude (current) of the Faradaic redox peaks.<sup>76</sup> In later chapters, it will be important to determine the magnitude of the ORR peak potential/current.

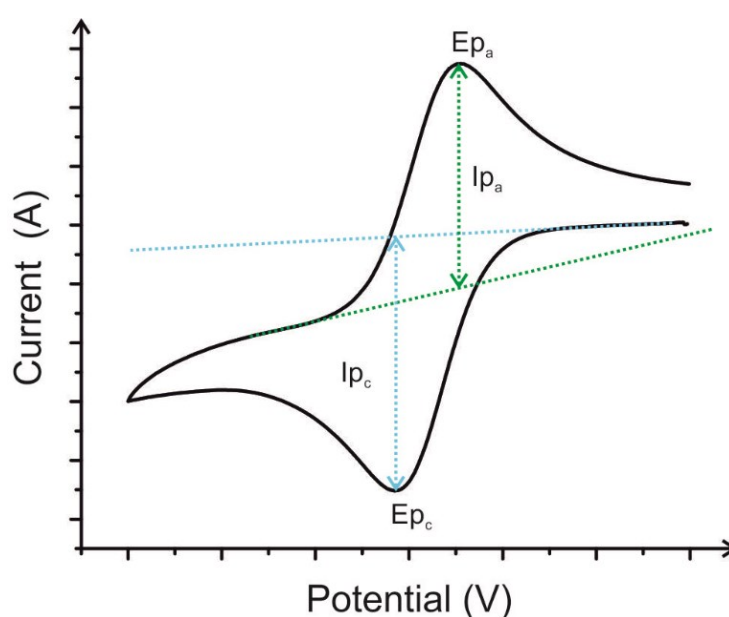


**Figure 1.09.** Typical cyclic voltammogram for a reversible redox process (1 mM  $[Ru(NH_3)_6]^{3+/2+}$  in 0.1 M KCl) using a glassy carbon electrode, where  $E_{p_a}$  and  $E_{p_c}$  correspond to the potential values at which the maximum anodic and cathodic peak currents ( $I_{p_a}$  and  $I_{p_c}$ , respectively) are recorded.

The magnitude of a current ( $i$ ) produced from a electroactive species being reduced or oxidised is determined by the flux value given that:<sup>4</sup>

$$i = -nFAJ \quad (1.09)$$

where  $n$  is the number of electrons involved in the reaction mechanism,  $F$  is the Faraday's constant and  $A$  is the area of the working electrode. Therefore, with  $J$  being

the only variable value, the current must depend upon it.  $J$  can be described as the number of molecules penetrating past an imaginary line to reach the electrode's surface and has the units:  $\text{mol s}^{-1} \text{cm}^{-2}$ . There are three typical scenarios that can determine the movement of molecules (mass transport) within an electrolyte,<sup>3</sup> those being; 1) Convection that involves the forced movement of the electrolyte, *via* an influence of such things as stirring, induced electrolyte flow and temperature variations within the electrolyte. 2) Migration, which typically involves the inducement of an electric field, *via* two electrodes having different potentials, repelling or attracting charged ions. 3) Diffusion, the movement of charged/uncharged ions through the electrolyte due to concentration gradients. In electrochemical systems that are controlled solely by diffusional electron transfer,  $J$  can be quantified by Fick's 1<sup>st</sup> law of mass transport.<sup>4</sup>

$$J(x, t) = -D \frac{\partial C(x, t)}{\partial x} \quad (1.10)$$

When  $\frac{\partial c}{\partial x}$  is the concentration gradient at distance  $x$ ,  $t$  is time and  $D$  is the diffusional coefficient. Fick's 2<sup>nd</sup> law introduces time and distance to the concentration relationship, giving:

$$\frac{\partial c}{\partial t} = D \frac{\partial^2 c}{\partial x^2} \quad (1.11)$$

In a scenario where convection, migration and diffusion are all occurring, a more complicated modelling of mass transport must be implemented. The relationship between the three transport modes can be described, in a one dimensional process, *via* the Nernst-Planck equations:<sup>3</sup>

$$J(x, t) = -D \frac{\partial C(x, t)}{\partial x} - \frac{zFD C(x, t)}{RT} \frac{\partial \varphi(x, t)}{\partial x} \varphi + CV(x, t) \quad (1.12)$$

where  $\frac{\partial\phi(x,t)}{\partial x}$  is the potential gradient,  $z$  is the charge of the electroactive species and  $V(x, t)$  is the hydrodynamic velocity in aqueous media.

Taking flux into account, it is possible to produce a general expression for current response, *via* the combination of Equations 1.09 and 1.10, that being:<sup>3</sup>

$$i = -nFAD \frac{\partial C(x,t)}{\partial x} \quad (1.13)$$

### 1.2.3. Chronoamperometry Experiments

---

The electrochemical technique of chronoamperometry entails the maintenance of a set potential for a prolonged period of time outside of, or, within a Faradaic potential window.<sup>4</sup> Typically researchers utilising chronoamperometry will apply a set-potential, below that where Faradaic processes are induced, for a set amount of time. The potential will then be raised to one where the Faradaic processes are initiated. The current throughout this process is measured and plotted as a function of time. When this potential step is initiated, there is a spike in the current due to the occurrence of Faradaic processes. After this spike the current degrades in a manner described by the Cottrell equation (see Equation 1.08). This allows a researcher to investigate the current/time relationship occurring at the electrode/electrolyte interface as the mass transport is solely governed by diffusion. As is common within the literature, this study utilises chronoamperometry in a simplified manner in order to investigate the stability of the electrodes studied herein. This is done by holding a Faradaic potential ( $-0.75$  V) for a set time (36,000 seconds) and observing if there is a degradation and maintenance in the achievable current.

### 1.2.4. Electrochemical Impedance Spectroscopy Experiments

Electrochemical impedance spectroscopy (EIS) allows for the frequency dependent properties of an electrode to be studied. It involves the application of a small amplitude sinusoidal voltage to a cell across range of frequencies, as well as a set direct current potential.<sup>3,4</sup> EIS can be utilised to investigate numerous phenomena from corrosion, the adsorption properties of certain molecules and importantly battery/fuel cell performance. The resulting excitation caused at the electrode/electrolyte interface results in a change of output current. The level and phase angle of this current (relative to the AC voltage) are measured by a potentiostat. This data is manipulated (by Ohm's law, seen below) to deduce a value for impedance.<sup>4</sup>

$$V = IR \quad (1.14)$$

The interpretation of this received data is done typically *via* one of two methods. The first being a Nyquist plot (See Figure 1.10), which involves the real and imaginary impedances plotted against each other, or a Bode plot, which is the impedance and phase angle difference plotted as a function of frequency.

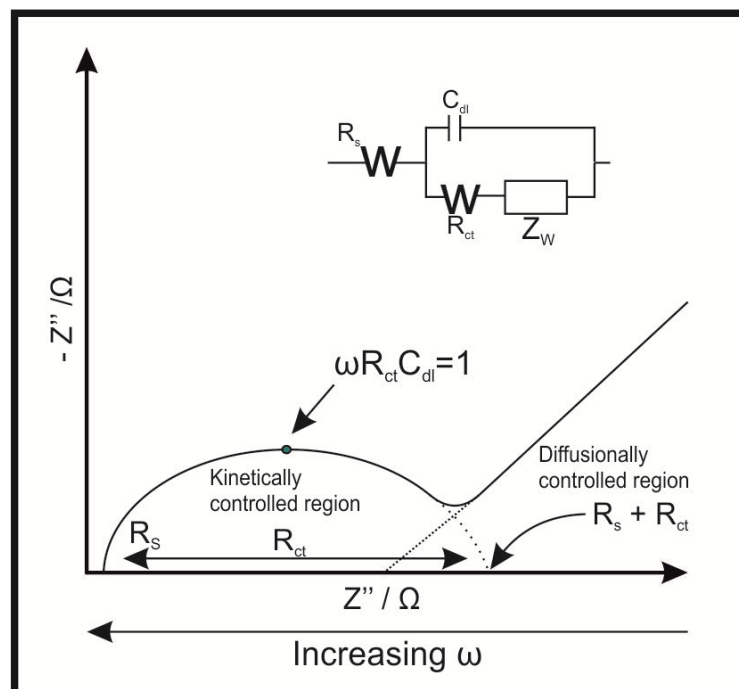


Figure 1.10. Ideal Randles equivalent circuit and corresponding Nyquist plot.

In order to help with the complex interpretation of the gathered impedance values it is necessary to produce an equivalent circuit model that allows for specific electronic processes to be understood, such as charge transfer, capacitance, diffusion, inductance and solution resistance. Charge transfer resistance values for the electrode/electrolyte interface are studied herein by Nyquist plots, due to them allowing for an insight into the effect of concentration upon impedance within the cell. In essence impedance can be thought of as the retarding force of an electrical current within a circuit and is measured in Ohm's ( $\Omega$ ), the same units as resistance. There is however, a fundamental difference between resistance and impedance due to resistance obeying Ohm's Law (see above) and uses is particular to DC circuits in which resistance is equal to impedance with a zero phase angle resulting from the none alternating current. In the majority of AC circuits where the phase angle is not equal to zero, due to the interference of capacitive/inductive forces, which are observed across a wide range of frequencies. The theory of impedance allows a quantitative modelling of the retarding force in AC circuits to current. In general EIS can grouped into potentiostatic and galvanic. The EIS experiments carried out within this thesis are potentiostatic in which a set sinusoidal voltage and a DC voltage are applied to the circuit (involving a typical three electrode cell) *via* a potentiostat. The electrochemical reaction that occurs at the working electrode induces a AC current that is subsequently measured by the potentiostat. Using the applied potentials, the measured potentials and the formula below it is possible to calculate the total impedance of a system.

$$Z = \frac{V_t}{I_t} = \frac{E_0 \sin(\omega t)}{I_0 \sin(\omega t + \phi)} = Z_0 \frac{\sin(\omega t)}{\sin(\omega t + \phi)} \quad (1.15)$$

Equation .. determines impedance in relation to potential, current, time ( $t$ ) and the phase angle ( $\emptyset$ ). It is necessary to determine the features of an EIS output graph in order to differentiate specific processes occurring. In order to help with the determination of important features of the EIS signal output the potentiostat and its corresponding software convert the recorded current output of the cell actual and imaginary components. This process is repeated across a wide frequency window and a value for overall impedance is deduced. The actual component and imagined components of a Nyquist plot are described by Equations 1.16 and 1.17, seen below.

$$Z' = R_S + \frac{R_{CT}}{1 + \omega^2 R_{CT}^2 C_{DL}^2} \quad (1.16)$$

$$Z'' = R_S + \frac{R_{CT}^2 C_{DL} \omega}{1 + \omega^2 R_{CT}^2 C_{DL}^2} \quad (1.16)$$

Where  $Z'$  and  $Z''$  are the obtained impedances occurring as a result of real and imaginary components respectively.  $R_S$  is the solution resistance,  $R_{CT}$  is the charge transfer resistance,  $\omega$  is the angular frequency and  $C_{DL}$  is the double layer capacitance.

Note that in this thesis the EIS experiments are carried out in solutions of  $H_2SO_4$  in order to mimic the system set up found within an acidic electrolyser or PEMFC.

### 1.3. Assessing a Materials HER and ORR Performance

---

It is important to set out a criteria by which the HER and ORR can be assessed herein. This begins with defining what we deem to be an electrocatalyst. An electrocatalyst is an entity that facilitates a chemical reaction that involves the transfer of charge, an example of such a reaction is given in equation:<sup>4</sup>



Typically an electrocatalyst lowers the overpotential or increases the achievable current of a specific reaction. A given catalyst is usually deposited upon the surface of an electrode with known heterogeneous electron transfer kinetics, or it can act as the electrode itself.<sup>77</sup> As an intermediate between the electrode and the electrolyte, the electrocatalyst adsorbs the reactant *via* its unique binding sites, thereby creating an intermediate reaction step, which serves to facilitate charge transfer. When choosing an effective electrocatalyst, the main kinetic parameters to evaluate are the exchange current density, the Tafel slope analysis and the overpotential. These parameters will be explored more thoroughly in the sections below.

### 1.3.1 Exchange Current Density

---

The exchange current density ( $i_o$ ) of an electrochemical reaction is an important indicator as to the reactions kinetics. The overall achievable ( $j$ ) current for a given electrochemical reaction is the sum of the anodic ( $j_a$ ) and cathodic currents ( $j_c$ ) as seen in Equation 1.16:<sup>2</sup>

77

$$j = j_a + j_c \quad (1.16)$$

the individual contributions of the anode and cathode are shown in Equations 1.17 and 1.18 respectively.<sup>2,77</sup>

$$j_a = nFk_a[C_R] \exp\left(\frac{\alpha_a nFE}{RT}\right) \quad (1.17)$$

$$j_c = nFk_c[C_o] \exp\left(-\frac{\alpha_c nFE}{RT}\right) \quad (1.18)$$

Where  $k$  and  $\alpha$  represent the rate constant and the transfer coefficient of the half-cell reactions, respectively, with  $a$  and  $c$  denoting whether it is the anodic or cathodic reaction,

$n$  is the number of electrons involved in the reaction,  $F$  is the Faraday constant,  $E$  is the applied cell potential,  $R$  is the universal gas constant and  $T$  denotes the temperature (Kelvin). When a reaction is in a state of equilibrium, the anodic and cathodic current are equal, resulting in there being a net current equal to zero (See Figure 1.11).

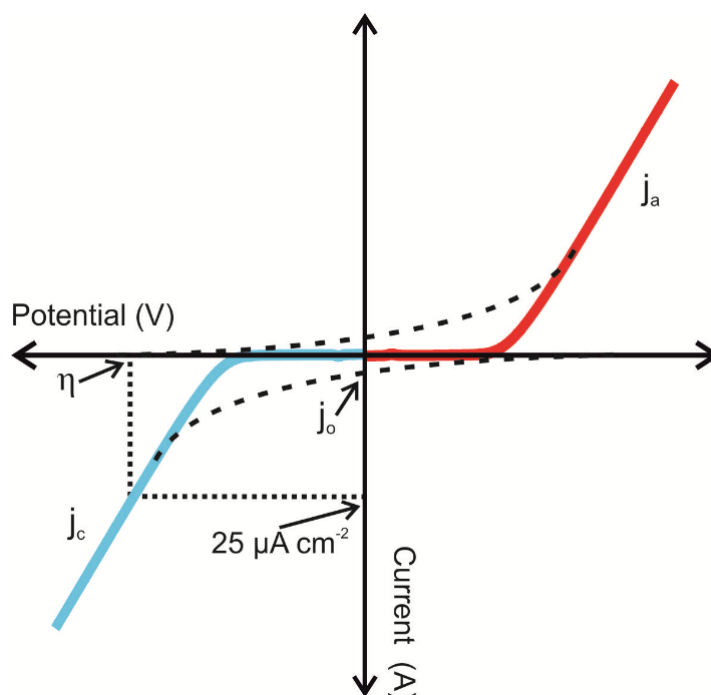


**Figure 1.11.** Typical polarization (LSV) curves for a cathodic (blue) and anodic (red) electrode.  $j_o$  is the exchange current when  $j_a = -j_c$ . The overpotential ( $\eta$ ) is determined by a current density (current/area of the working electrode) of  $25 \mu\text{A cm}^{-2}$  deviation from the background current.

It is possible to determine the exchange current ( $j_o$ ) by the magnitude of the intercepts at  $\eta = 0$  ( $\eta$  being the overpotential), then in order to calculate the exchange current density,  $j_o$  should be divided by the area (A) of the working electrode, as seen in Equation 1.19.<sup>77</sup>

$$j_o/A = i_o \quad (1.19)$$

The exchange current density can be used as a tool for exploring the intrinsic electrocatalytic properties of a catalyst, as a large exchange current density is typically the result of an effective catalyst allowing for efficient bonding/charge transferring interactions between the electrode and electrolyte.<sup>4</sup> It is often difficult to determine the exchange current density since experimental data will only yield overall current density. A common method within the literature to determine the exchange current density is Tafel analysis.<sup>77</sup> Tafel analysis will therefore be more thoroughly explore later within this study.

### 1.3.2. Overpotential

---

Along with exchange current density, the overpotential is a essential descriptor as to the efficiency of an electrocatalyst. For any redox reaction, it is possible to determine a standard cell potential (also known as the formal potential) at equilibrium using the Nernst equation, depicted below:<sup>78</sup>

$$E = E^o + \frac{RT}{nF} \ln \frac{C_O(0,t)}{C_R(0,t)} \quad (1.20)$$

where  $E$  is the applied potential,  $E^o$  is the standard cell potential,  $C_O$  is the concentration of the oxidised reagents and  $C_R$  is the concentration of the reduced reagent. In an optimal scenario the potential applied to induce a reaction would be equal to the standard cell potential, however very often due to the kinetic barrier imposed by the electrode, the applied potential is greater than the standard cell potential. The additional potential applied over the standard cell potential is known as the overpotential ( $\eta$ ), see Equation 1.21.<sup>78</sup>

$$\eta = E - E^o \quad (1.21)$$

Often within the literature, overpotential is defined as the potential required to achieve a current density that deviates from the background current by a set value. Whilst there are

several current densities within the literature that different studies utilise in order to signify the overpotential, this study uses the current density value of  $25 \mu\text{A cm}^{-2}$ . Whilst the value of  $25 \mu\text{A cm}^{-2}$  may seem arbitrary, using it allows for a clear and consistent measure as to when the current density has derivated from the background current enough to signify the definite occurrence of Faradaic processes. Given the above, an effective electrocatalyst is one that has a  $\eta$  as close to 0 V as possible.

### 1.3.3. Tafel Equation and Slopes

---

In order to increase the magnitude of current density ( $i$ ) observed at an electrode a larger overpotential ( $\eta$ ) can be applied. Ideally an effective electrocatalyst will allow for a rapid increase in current density at a minimal overpotential with the potential applied to overcome the reactions kinetic barrier being close to the standard cell potential. The  $i$  and the applied  $\eta$  can be modelled using the Butler-Volmer equation below:<sup>3,4,77</sup>

$$i = i_o \left[ \exp\left(\frac{\alpha_a n F E}{RT}\right) - \exp\left(-\frac{\alpha_c n F E}{RT}\right) \right] \quad (1.22)$$

Where  $\alpha_a$  and  $\alpha_c$  are the anodic and cathodic charge transfer coefficients, respectively. The Butler-Volmer equation shows that under high cathodic conditions, the overall potential can be attributed to the cathodic side and the anodic side can be considered to be negligible. It is, therefore, possible to simplify the Butler-Volmer equation into the so-called Tafel equation, as seen below:<sup>3,4,77</sup>

$$i = i_o \exp\left(\frac{\alpha_c n F E}{RT}\right) \quad (1.23)$$

The Tafel equation (1.23) can be translated into its logarithm form of:

$$\log(i) = \log(i_o) + \frac{\eta}{B} \quad (1.24)$$

which can be further translated to: <sup>3,4,77</sup>

$$B = \frac{\partial \eta}{\partial \log(i)} = \frac{2.303 RT}{\alpha F} \quad (1.25)$$

where B is the so-called Tafel slope and can be calculated accordingly, with an example being given in Figure 1.12. The most modern interpretation, and the one utilised herein, of the Tafel equation is given in Equation 1.26.

$$\ln(i) = \ln(i_o) - \frac{\alpha n F \eta}{RT} \quad (1.26)$$

The Tafel equation can be expected to be accurate as long as the back reaction (the anodic reaction in regards to the HER and ORR, which are both cathodic reactions) contributes less than 1% of the current. Using Equation 1.25 or 1.26 it is possible to discern the rate of current increase against  $\eta$ , with the value being heavily dependent upon the transfer coefficient ( $\alpha$ ). A smaller B value indicates that  $i$  can increase at a faster rate with a smaller  $\eta$ , thus implying that the electrode in question has faster heterogeneous electron transfer kinetics. The B value is also a useful tool in determining the HER reaction mechanism.

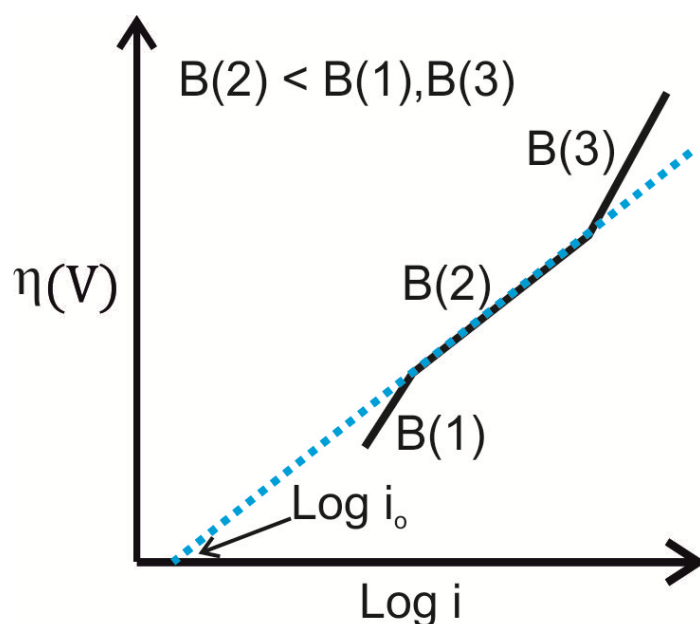


**Figure 1.12.** Slope  $B$  represents the Tafel slope and is assumed to be the steepest part (maximal Log current ( $i$ ) change to minimal  $\eta$  change) of the curve. The exchange current density ( $i_0$ ) is found via extrapolating the Tafel curve to  $\eta = 0$ . Modified from a figure by Bard et al. <sup>4</sup>

Using the Tafel slope it is possible to discern the average number of electrons involved in the reaction mechanism, which can be utilised to suggest a rate determining step. This subsequently offers fundamental insights into the effectiveness of the electrocatalyst being employed.

Tafel analysis is a useful tool in the determination for the reaction mechanism, however it is typical to use an alternative rotating disk electrode (RDE) technique in order to calculate this. An RDE more closely mimics the actual conditions within an electrolyser/fuel cell due to the rotation of the working electrode causing a constant flow of electrolyte to the electrodes surface prevents the development the diffusion layer typical within a static cell set up. Analysis of the RDE study (in which CV's are performed at differing rates of rotation) via the Koutecky-Levich approach,<sup>79</sup> allows for a determination of the HER and ORR reaction mechanism, however there is not a known rotating RDE methodology that utilises SPEs, therefore this thesis shall use the Tafel method.

## 1.4. Summation

---

Inspired by the above insights and attempts in the literature to utilise 2D nanomaterials as an alternative catalyst to Pt for the HER and ORR, this thesis aims to explore the use of 2D-MoS<sub>2</sub> nanosheet modified carbon-based electrodes towards the possible electrocatalysis of the HER and the ORR, *via* the use of electrochemical techniques. The 2D-MoS<sub>2</sub> nanosheets are thoroughly characterised with scanning electron microscopy (SEM), transmission electron microscopy (TEM), Raman spectroscopy, energy dispersive spectroscopy (EDS), X-ray diffraction (XRD), UV-visual spectroscopy and X-ray photoelectron spectroscopy (XPS). Linear sweep voltammetry is utilised to measure the onset, current density and reaction mechanism of the HER and ORR with four carbon based electrodes as the underlying support materials; namely edge plane pyrolytic graphite (EPPG), glassy carbon (GC), boron-doped diamond (BDD) and screen-printed graphite electrodes (SPE). After which, this report will endeavour to demonstrate a facile methodology for the fabrication of intrinsically electrocatalytic (2D-material incorporated) SPE's that can extend the research outcomes to potentially viable industrial applications.

This work is distinct from the literature, given that it also explores a range of electrode substrates, correlates our electrochemical responses with supplementary Raman mapping of the electrode surfaces (and other complementary physicochemical characterisation) and explores the effect of 2D-MoS<sub>2</sub> coverage; each noted component is routinely overlooked in the literature. This work also benchmarks the electrochemical performance of the 2D-MoS<sub>2</sub> nanosheets towards the HER and ORR (utilising turn-over frequency (ToF) calculations) and compares our results to Pt and literature reports.

## Chapter 2.

# Experimental

Chapter 2 will give a description of the chemicals, as well as a full independent physicochemical characterisation, of the two dimensional nanomaterials utilised in the later chapters of this thesis. It will also describe the techniques by which carbon-based electrodes are modified.

### 2.1. Chemicals

---

All chemicals utilised within this thesis were of analytical grade and were used as received from Sigma-Aldrich without any further purification, including the 2D-MoS<sub>2</sub> 2D-MoSe<sub>2</sub> flakes utilised in the 2D-material incorporated SPEs. The three variants of MoS<sub>2</sub> powders utilised in the fabrication of the 2D-MoS<sub>2</sub>-SPEs each had a distinct flake lateral width, reported independently by Sigma-Aldrich: 90 nm,<sup>80</sup> < 2 μm,<sup>81</sup> and *ca.* 6 μm.<sup>82</sup> Sigma-Aldrich report the average lateral width of the MoS<sub>2</sub> particles in powder but details are lacking about the characterisation performed to justify these numbers. It was observed that the 90 nm 2D-MoS<sub>2</sub>, when suspended into a solvent and subsequently re-dispersed to allow characterisation to be performed, agglomerates to form larger particles with an average lateral width of *ca.* 400 nm (see Figure 2.07, page 78). This increase in lateral width as a result of agglomeration was not observed for the MoS<sub>2</sub> particles with lateral widths of < 2 μm,<sup>81</sup> and *ca.* 6 μm.<sup>82</sup> Therefore this study uses the notations 400 nm, 2 μm and 6 μm when differentiating between the 2D-MoS<sub>2</sub> particles utilised within this study. The 2D-MoS<sub>2</sub> nanosheets were commercially procured from ‘Graphene Supermarket’ (Reading, MA, USA).<sup>83</sup> The 2D-MoS<sub>2</sub> nanosheets have a reported purity of >99 % and are dispersed in ethanol at a concentration of 18 mg L<sup>-1</sup>.<sup>83</sup> The suspended flakes are reported to have an average lateral flake size of 100–400 nm and a thickness of between 1 and 8 monolayers.<sup>83</sup>

## 2.2. Physicochemical Characterisation of the 2D nanomaterials utilised

---

It was important to perform independent physicochemical characterisation on all the 2D nano-materials utilised within this thesis. Specifications of the equipment utilised in this study are found below.

### 2.2.1. Characterisation Equipment Specification

---

Transmission electron microscopy (TEM) images were obtained on a JEOL 2010 analytical TEM using a 200 kV primary beam under conventional bright-field conditions. The TEM images presented within this thesis were performed by Dr Kerstin Jurkschat (*University of Oxford, OMCS, Begbroke Science Park, Yarnton, OX5 1PF*). The 2D-nanomaterials sample was dispersed onto a holey-carbon film supported on a 300 mesh Cu TEM grid. Raman spectroscopy was performed using a ‘Renishaw InVia’ spectrometer equipped with a confocal microscope ( $\times 50$  objective) and an argon laser (514.3 nm excitation). Measurements were performed at a very low laser power level (0.8 mW) to avoid any heating effects. X-ray diffraction (XRD) was performed using an “X’pert powder PANalytical” model with a copper source of  $K_{\alpha}$  radiation (of 1.54 nm) and  $K_{\beta}$  radiation (of 1.39 nm), using a thin sheet of nickel with an absorption edge of 1.49 Å to absorb  $K_{\beta}$  radiation. A reflection transmission spinner stage (15 rpm) was implemented to hold the commercially sourced MoSe<sub>2</sub> nano-powder. The range was set between 10 and 100  $2\theta$ , to correspond with literature ranges.<sup>84</sup> Additionally, to ensure well defined peaks an exposure of 50 seconds per  $2\theta$  step was implemented with a step size of 0.013°. The X-ray photoelectron spectroscopy (XPS) data was acquired using a bespoke ultra-high vacuum system fitted with a Specs GmbH Focus 500 monochromated Al  $K_{\alpha}$  X-ray source, Specs

GmbH Phoibos 150 mm mean radius hemispherical analyser with 9-channeltron detection, and a Specs GmbH FG20 charge neutralising electron gun.<sup>85</sup> Survey spectra were acquired over the binding energy range 1100 – 0 eV using a pass energy of 50 eV and high resolution scans were made over the C 1s and O 1s lines using a pass energy of 20 eV. Under these conditions the full width at half maximum of the Ag 3d<sub>5/2</sub> reference line is *ca.* 0.7 eV. In each case, the analysis was an area-average over a region approximately 1.4 mm in diameter on the sample surface, using the 7 mm diameter aperture and lens magnification of ×5. The energy scale of the instrument is calibrated according to ISO 15472, and the intensity scale is calibrated using an in-house method traceable to the UK National Physical Laboratory.<sup>86</sup> Data were quantified using Scofield cross sections corrected for the energy dependencies of the electron attenuation lengths and the instrument transmission.<sup>87</sup> Data interpretation was carried out using CasaXPS software v2.3.16.<sup>88</sup> It is important to note that the XPS characterisation presented within this study was performed and analysed by Professor Graham C. Smith (*Faculty of Science and Engineering, Department of Natural Sciences, University of Chester, Thornton Science Park, Pool Lane, Ince, Chester CH2 4NU, UK*).

#### 2.2.2.1. Fabrication and Physicochemical Characterisation of the 2D-MoS<sub>2</sub> and 2D-MoS<sub>2</sub>-SC

---

The 2D-MoS<sub>2</sub>-SC utilised in Chapter 3 was synthesised *via* a surfactant based liquid exfoliation, ultrasonication and centrifugation methodology. Liquid exfoliation was performed by placing bulk *ca.* 90 nm flake size MoS<sub>2</sub> powder (Sigma-Aldrich: see Experimental Section) into an aqueous solution of sodium cholate hydrate (SC: concentration, 6 g/L) within a 100 mL beaker, the resulting dispersion of bulk MoS<sub>2</sub>

comprised a concentration of 30 g L<sup>-1</sup>. This dispersion was then sonicated in a ultrasonic bath (Ultrawave, UK; 60 Hz) for 1 hour and then centrifuged at 5000 rpm for 90 minutes. Following centrifugation, the corresponding supernatant was discarded and the resulting sediment was re-agitated/dispersed into aqueous SC (2 g L<sup>-1</sup>, 100 mL). Next, the said re-agitated sediment underwent further ultrasonication for a further 5 hours. Upon completion of the sonication, the solution was separated into 20 mL aliquots before each sample was centrifuged at 2000 rpm for 90 mins (separately). The sediment from this process contained un-exfoliated MoS<sub>2</sub> and was consequently discarded, with the remaining supernatant being subjected to a further centrifugation period at 5000 rpm for 90 minutes. Finally, the supernatant was removed and found to contain the 2D-MoS<sub>2</sub>-SC nanosheets that are utilised herein. The 2D-MoS<sub>2</sub> was commercially procured from Graphene Supermarket and is fully characterised in the following sections.<sup>83</sup>

TEM was performed on the 2D-MoS<sub>2</sub> and 2D-MoS<sub>2</sub>-SC nanosheets with the obtained images reported in Figure 2.01. The 2D-MoS<sub>2</sub> and 2D-MoS<sub>2</sub>-SC have a lateral widths of *ca.* 60 and 100 nm, respectively, with an inter nanosheet spacing of 0.33 nm and likely is a visual image of the 100 (basal) MoS<sub>2</sub> plane. This corresponds strongly with the average values determined *via* analysis of the extinction spectra (Figure 2.02.(D)).

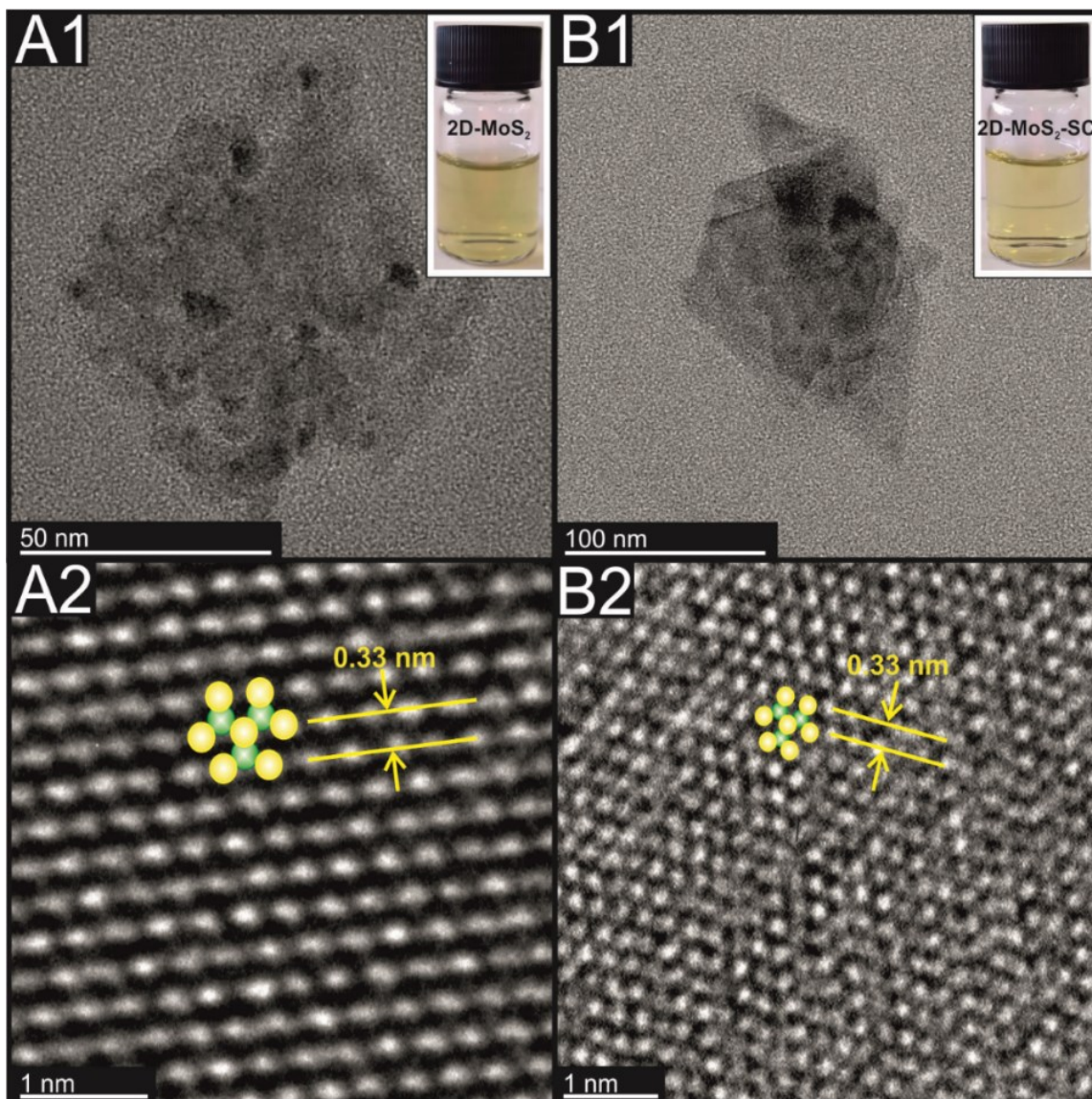


**Figure 2.01.** TEM images of the commercially sourced 2D-MoS<sub>2</sub> (A1) Scale bar: 50 nm; (A2) Scale bar: 1 nm; and the exfoliated 2D-MoS<sub>2</sub>-SC (B1); Scale bar: 100 nm, (B2); Scale bar: 2 nm.

XRD analysis exhibited characteristic (002) diffraction peaks for the 2D-MoS<sub>2</sub> and 2D-MoS<sub>2</sub>-SC, nanosheets with  $2\theta$  corresponding to  $14.2^\circ$ , indicating the presence of MoS<sub>2</sub> via the reflection of separated MoS<sub>2</sub> layers, see Figure. 2.02(A), which is in agreement with literature reports.<sup>38, 68</sup> The broad peak between 20 and 30 ( $2\theta$ ) is attributed to the supporting amorphous glass slide.

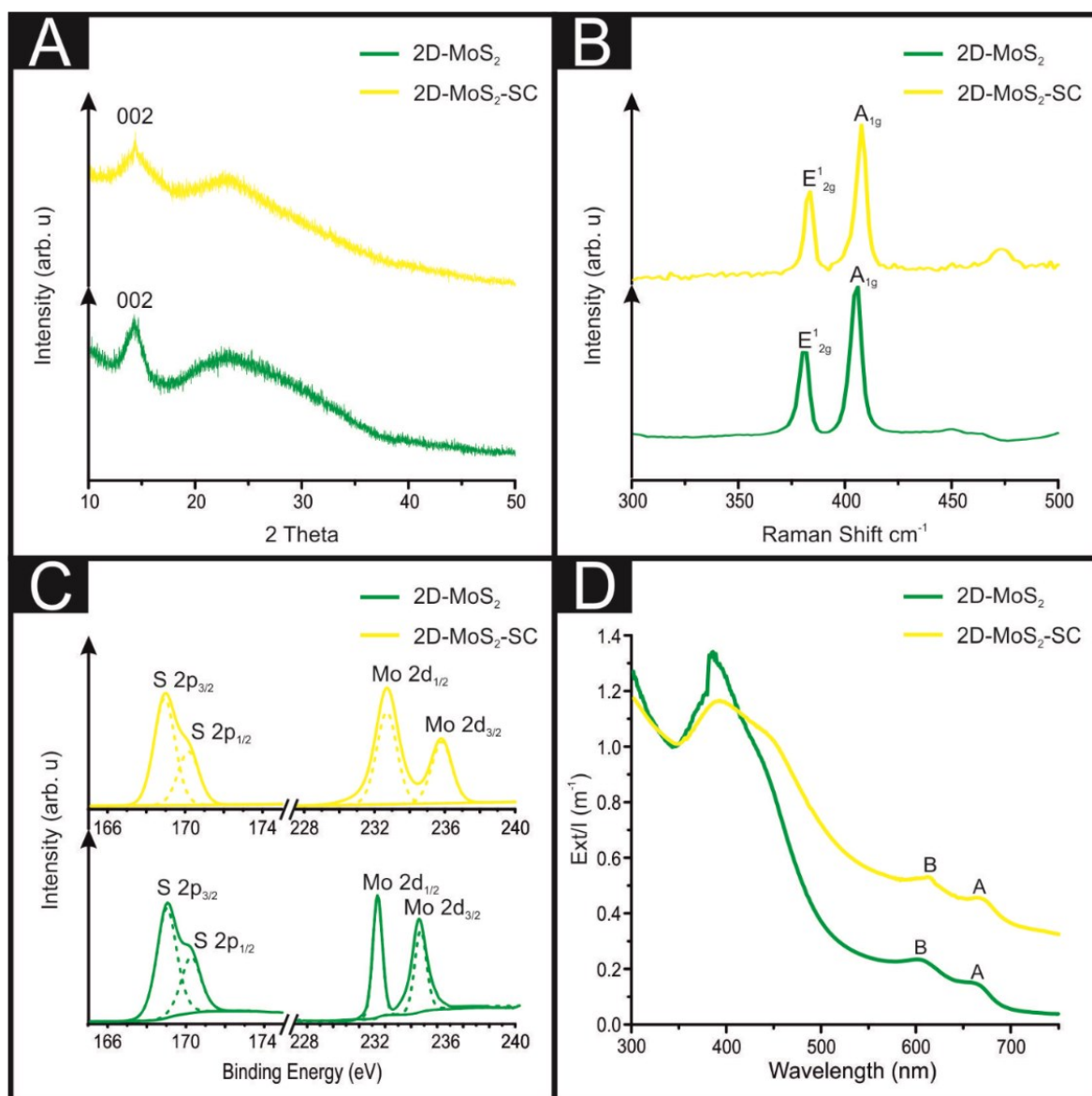


**Figure 2.02.** Characterisation of the 2D-MoS<sub>2</sub> and 2D-MoS<sub>2</sub>-SC; (A) XRD (deposited on a glass slide), (B) Raman spectra (deposited onto a silicon wafer between 300 and 500 cm<sup>-1</sup>). High resolution XPS spectra for the Mo 3d and S 2p regions of 2D-MoS<sub>2</sub> and 2D-MoS<sub>2</sub>-SC. (D) Extinction spectra (nanosheets dispersed in ethanol (1.22 mg L<sup>-1</sup>)).

Next Raman analysis was undertaken (Figure 2.02.(B)) where the E<sub>2g</sub><sup>1</sup> and A<sub>1g</sub> vibrational bands vibrational peaks are clearly visible at 376.8 and 402.5 cm<sup>-1</sup> for the 2D-MoS<sub>2</sub> and 383.3 and 409.4 cm<sup>-1</sup> for the 2D-MoS<sub>2</sub>-SC. It is possible to determine the stacking number by comparison of E<sub>2g</sub><sup>1</sup> and A<sub>1g</sub> vibrational bands (VB) as the

observed Raman spectrum evolves with the number of layers present. The  $E_{2g}^1$  VB results due to the opposite vibration of two S atoms in respect to a Mo atom, whereas the  $A_{1g}$  peak represents the S atoms vibrating in opposite directions and out of plane.<sup>89</sup> As  $MoS_2$  moves from single layer to bulk, the  $E_{2g}^1$  VB downshifts from 384 to 382  $cm^{-2}$ , whilst  $A_{1g}$  VB shifts upwards from 403 to 408  $cm^{-1}$ , where a separation of *ca.* 19  $cm^{-1}$  between the VBs is indicative of single layer  $MoS_2$  and a value of *ca.* 25  $cm^{-1}$  represents the bulk material.<sup>90 33, 64</sup> In both cases giving a peak ( $E_{2g}^1 - A_{1g}$ ) distance of 25.7  $cm^{-1}$ . This ( $E_{2g}^1 - A_{1g}$ ) distance corresponds to the literature value expected for bulk  $MoS_2$  (< 6  $MoS_2$  nanosheet layers).<sup>74, 89, 90</sup> XPS analysis was performed to determine the elemental composition of the 2D- $MoS_2$  and 2D- $MoS_2$ -SC utilised herein, with Figure 2.02(C) showing high resolution XPS spectra for the Mo 3d and S 2d regions. The Mo and S were present at the expected ratios (1.0 : 2.2 and 1.0 : 1:7 for the 2D- $MoS_2$  and 2D- $MoS_2$ -SC, respectively). The XPS analysis also showed that C and O present are a result of residuals from the sodium cholate surfactant used in the fabrication of the 2D- $MoS_2$ . The presence of a C-O component in the C 1s spectrum confirmed this, with the Na attributed to the sodium of the cholate structure. Overall, the 2D- $MoS_2$  and 2D- $MoS_2$ -SC utilised in this work has been fully characterised and revealed to comprise of high quality 2D- $MoS_2$  nanosheets for implementation as an electrocatalyst towards the HER.

### 2.2.2.2. Lateral Width and Number of Layers of 2D-MoS<sub>2</sub> Utilised Determined *via* Optical Extinction Spectroscopy

---

The lateral length ( $L_a$ ) and number of the commercially procured 2D-MoS<sub>2</sub> nanosheets and the fabricated 2D-MoS<sub>2</sub>-SC nanosheets can be readily deduced from absorption spectroscopy. It has been observed that actually the terminology is more correctly optical extinction spectroscopy; since the optical beam interacts with the dispersed nanosheets by both absorption and scattering.<sup>91-93</sup> The extinction coefficient of dispersed 2D-MoS<sub>2</sub> nanosheets is 6,820 L g<sup>-1</sup> m<sup>-1</sup> at the local minimum of 345 nm. Using this information along with an absorption spectrum it is possible to determine the concentration of dispersed 2D-MoS<sub>2</sub> nanosheets.<sup>92</sup> Varrla, *et al.*<sup>91</sup> uses this information to calculate the concentration as a function of mixing parameters whilst also showing that the extinction spectra can be used to determine information regarding the 2D-MoS<sub>2</sub> nanosheet length and thickness. Figure 2.02(D) shows the optical extinction spectra of the 2D-MoS<sub>2</sub> and the 2D-MoS<sub>2</sub>-SC.

It is readily evident that the spectrum display A- and B- excitonic transitions as well as other pertinent features consistent with the 2H polytype of MoS<sub>2</sub>.<sup>91, 92, 94</sup> The extinction spectrum of a nanosheet allows one to readily determine the mean nanosheet lateral length, due to the effect that 2D-MoS<sub>2</sub> nanosheet edges have upon the spectral profile. The extinction spectrum also allows the number of layers (thickness) to be determined as a result of quantum confinement effects causing a well-defined shift in A-exciton position, corresponding to nanosheet thickness. The lateral length,  $L(\mu\text{m})$  of the MoS<sub>2</sub> can be deduced from the following equation:<sup>92</sup>

$$L(\mu\text{m}) = \frac{3.5(\text{Ext}_B / \text{Ext}_{345}) - 0.14}{11.5 - (\text{Ext}_B / \text{Ext}_{345})} \quad (2.1)$$

where  $(Ext_B / Ext_{345})$  is the ratio of extinction at the B-excitation to that at 345 nm since the spectral profile is dependent upon the lateral length of the 2D-MoS<sub>2</sub>. Further information can be obtained in terms of the number of nanosheets,  $N_{MoS_2}$ , expressed as the number of monolayers per nanosheet. This can be determined from the wavelength associated with the A-excitation, since the quantum confinement effects result in well-defined shifts in the A-excitation position with the thickness of the nanosheet; this is summarized by the following equation:<sup>91, 92</sup>

$$N_{MoS_2} = 2.3 \times 10^{36} e^{-54888 \lambda_A} \quad (2.2)$$

$N$  being the average number of monolayers per nanosheet of the 2D-MoS<sub>2</sub> and can be determined from the wavelength associated with the A-exciton,  $\lambda_A$ .<sup>92</sup> From the spectrum presented in Figure 2.02., the lateral length and number of 2D-MoS<sub>2</sub> nanosheets are determined to correspond to 61.5 nm and 3 (2.89), respectively. This work notes that the lateral size is smaller than the value given by the commercial supplier. The average of 3 monosheets per nanosheet agrees strongly with the commercial supplier, who notes the number of monolayers per nanosheet to be between 1-8 in solution.<sup>83</sup> The 2D-MoS<sub>2</sub>-SC comprises of nanosheets with average lateral widths and number of layers of *ca.* 120 nm and 2, respectively. It is important to point out that the lateral size and the number of 2D-MoS<sub>2</sub> sheets are for when these are in solution; when immobilised upon a surface, these values will deviate from these measured values, as this work will show later, but is a common issue in the whole of the literature.

### 2.2.3. Physicochemical Characterisation of the 2D-MoS<sub>2</sub> Nanosheets Explored towards the HER and ORR

---

As fully described later in Chapter 3; 2D-MoS<sub>2</sub> displays a greater electrocatalytic proficiency (less electronegative onset potential and higher achievable current density) than the 2D-MoS<sub>2</sub>-SC. Therefore additional physicochemical characterisation is provided for the 2D-MoS<sub>2</sub> below. TEM and SEM images of the commercially sourced 2D-MoS<sub>2</sub> nanosheets are shown in Figures 2.03. and 2.04.

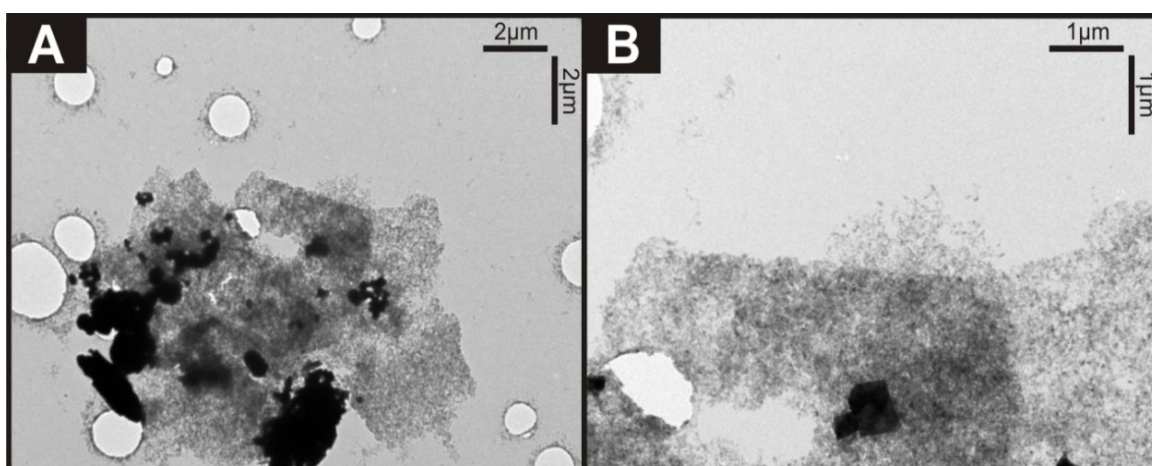


**Figure 2.03.** TEM images of the commercially sourced 2D-MoS<sub>2</sub> nanosheets deposited onto a holey carbon grid. (A) TEM image at 5,800 times magnification (scale bar: 2  $\mu\text{m}$ ), (B) TEM image at 13,500 times magnification (scale bar: 1  $\mu\text{m}$ ).

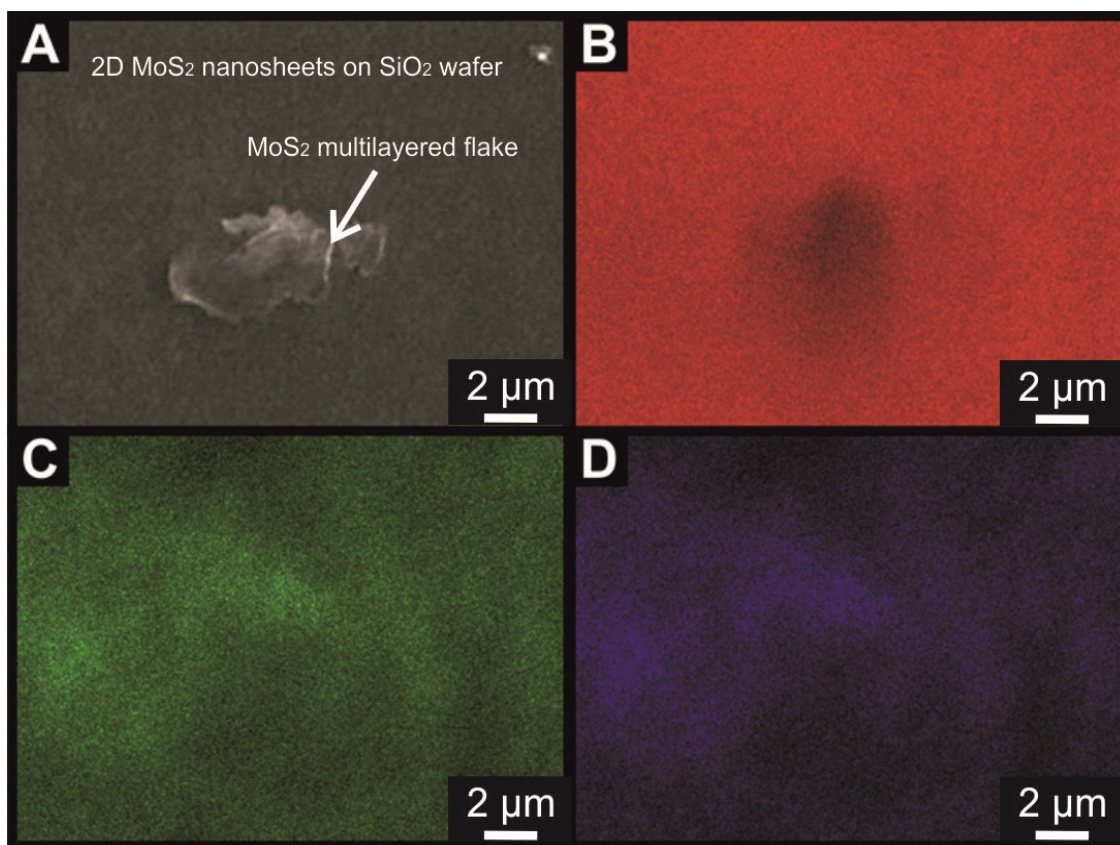


**Figure 2.04.** (A) SEM image of a multi-layered 2D-MoS<sub>2</sub> nanosheet flake on top of few layer 2D-MoS<sub>2</sub> nanosheets immobilised on a silicon wafer along with EDS analysis highlighting the underlying silicon support (B, in red), molybdenum (C, in green) and sulphur (D, in blue) coverage of image A respectively.

Despite some aggregation, which is the case for all nanosheet materials, upon close inspection, their appearance is within the acceptable widths with a lateral size of *ca.* 100-400 nm evident as quoted by the supplier and measurements undertaken above. The 2D-MoS<sub>2</sub> nanosheets immobilised upon the silicon wafer generally exhibit a uniform coverage. Complimentarily EDS mapping analysis was performed to offer insight into the elemental composition of the area shown in Figure 2.04. Analysis of the EDS map shows uniform distribution of Mo and S atoms with a ratio of 0.55% At. and 1.35% At. and this composition correlates with expected values for the structure of 2D-MoS<sub>2</sub> nanosheets (*ca.* 1:2 ratio of Mo and S respectively) agreeing with

independent literature.<sup>41</sup> Further analysis is described later where Raman mapping is utilised to explore MoS<sub>2</sub> mass modifications deposited onto electrode surface.

2D-MoS<sub>2</sub> nanosheets suspended in ethanol were prepared for X-ray photoelectron spectroscopy (XPS) analysis by pipetting a few drops of the suspension onto a fragment of a clean Si (111) wafer and allowing the ethanol to evaporate. The XPS spectrum is shown in Figure 2.05 and the results of the surface composition analysis (excluding hydrogen) are shown in Table 2.1.

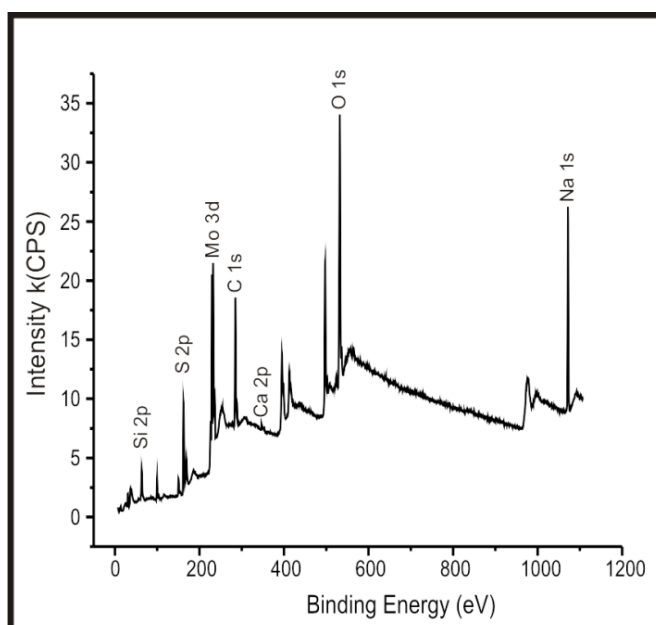


**Figure 2.05.** XPS survey spectrum for a sample of the 2D-MoS<sub>2</sub> nanosheets once deposited onto a Si (111) wafer showing a 1:2.2 concentration percentage for Mo and S respectively.

**Table 2.1.** Compositional analysis for the XPS spectrum of the 2D-MoS<sub>2</sub> nanosheets presented in Figure 2.06., shown in atomic percentage concentration, excluding H which is not detected by this technique.

Element	Atom % Concentration
Na 1s	8.36
Mo 3d	7.44
C 1s	34.41
Ca 2p	0.61
S 2p	16.3
Si 2p	5.47
O 1s	27.4

The C and O present is likely a result of residuals from the ethanol used to disperse the 2D-MoS<sub>2</sub>. This is supported by the presence of a component peak at *ca.* 286.6 eV, showing that alcohol groups were present on the sample surface. The Si present can be accounted for by the use of a Si (111) wafer as an underlying support material for the drop coating. Na is liable to be present from an organic Na contaminant or *via* contributions from the supporting wafer. The Mo to S % atomic concentrations are observed at a 1:2.2 ratio, respectively, agreeing well with the Raman and EDS analysis performed above (further indicating the presence of the target material). Shin, *et al.*<sup>95</sup> theorises that the deviation from an expected stoichiometry ratio of 1:2 for Mo and S, respectively, in 2D-MoS<sub>2</sub> nanosheets is due to the presence of MoS<sub>3</sub>.<sup>63</sup> It is of note that Mo is present in three valence states, with each of the valence states consisting of a Mo 3d<sub>5/2</sub> and Mo 3d<sub>3/2</sub> doublet. The curve-fitted high resolution Mo 3d spectral region is shown in Figure 2.06.

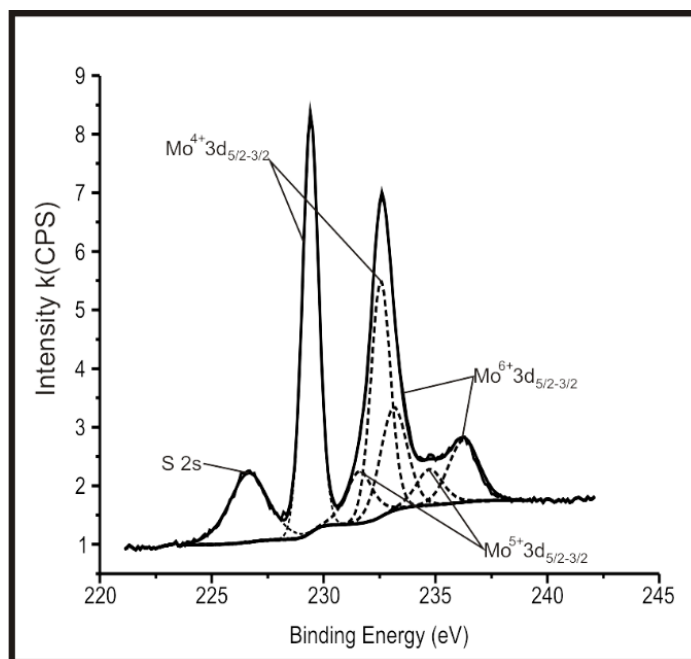


**Figure. 2.06.** Curve fitted XPS Mo 3d spectrum

The area ratios of the doublets are constrained to the ratios of the Scofield cross sections (*i.e.*  $\text{Mo } 3d_{3/2} = 0.6904 \times \text{Mo } 3d_{5/2}$ ), the two components of each doublet are constrained to the same line shape and ‘full width at half maximum’, and their separations are fixed at the known reference value of 3.13 eV. The  $3d_{5/2}$  components were found at 229.4 eV ( $\text{Mo}^{4+}$ ), 231.6 eV ( $\text{Mo}^{5+}$ ) and 233.1 eV ( $\text{Mo}^{6+}$ ). The spectral region also includes the S 2s peak at 226.6 eV.

#### 2.2.4. Physicochemical Characterisation of 2D-MoS<sub>2</sub> Flakes Utilised in the Production of 2D-MoS<sub>2</sub>-SPEs

Independent physicochemical characterisation was performed on the commercially sourced 2D-MoS<sub>2</sub> powders utilised to produce the 2D-MoS<sub>2</sub>-SPEs described in Chapter 6.<sup>80-82</sup> Figure 2.07 depicts typical TEM images of the 2D-MoS<sub>2</sub> that was reported to have a 90 nm lateral width in its powder form by Sigma-Aldrich.<sup>80</sup> Based upon a visual assessment of several 2D-MoS<sub>2</sub> nanosheets it was possible to estimate

that the lateral width of the 2D-MoS<sub>2</sub> nanosheets is *ca.* 400 nm with an inter-nanosheet spacing of *ca.* 0.7 nm, which agrees with the literature.<sup>96</sup> Figure 2.07(B) indicates that there is some aggregation of the nanosheets, which is the case for all nanosheet materials after dispersion from their supporting solvents onto a platform where it possible to image them *via* TEM. This agglomeration explains the increase in the lateral width of the observed flakes from the sizes reported by Sigma-Aldrich.

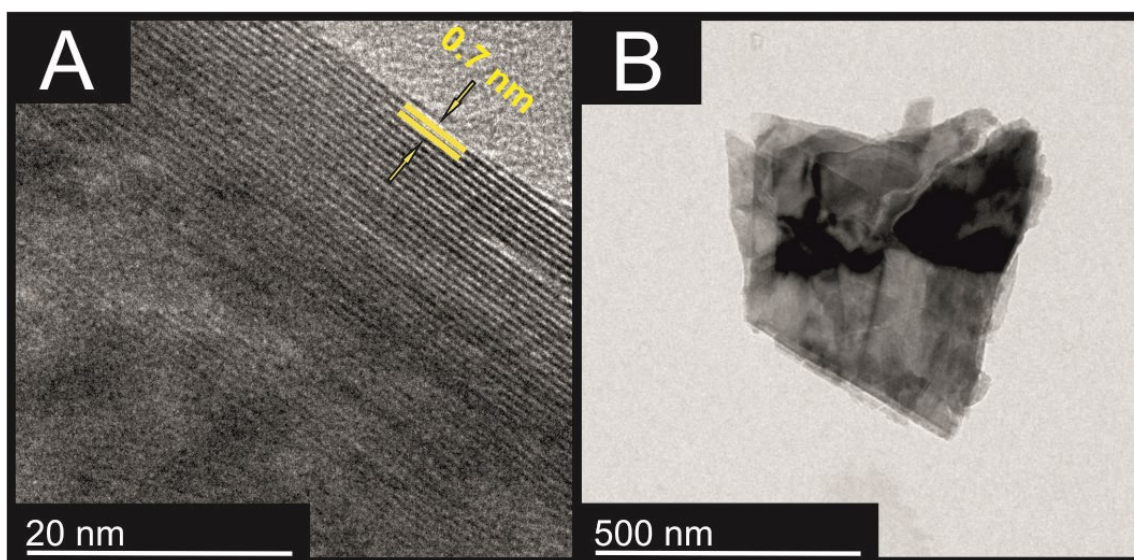


**Figure 2.07.** TEM images of the commercially sourced 400 nm 2D-MoS<sub>2</sub>. (A) Scale bar: 20 nm, (B) scale bar: 500 nm.

XRD analysis performed of the 2D-MoS<sub>2</sub> is presented in Figure 2.08(A). Major diffraction peaks that are characteristic of hexagonal MoS<sub>2</sub>, observed within the literature are visible at  $2\theta = 14.7^\circ, 29.4^\circ, 33.1^\circ, 33.9^\circ, 36.3^\circ, 40.0^\circ, 44.6^\circ, 50.2^\circ$  and  $58.8^\circ$ , corresponding to the planes of (002), (004), (100), (101), (102), (103), (006), (105), and (110), respectively.<sup>97, 98</sup> Next, Raman analysis was undertaken (Figure 2.08(B)) where the E<sub>1</sub>2g and A<sub>1</sub>g vibrational bands vibrational peaks are clearly visible at 376.8 and 402.5 cm<sup>-1</sup>, respectively, giving a peak (E<sub>1</sub>2g - A<sub>1</sub>g) distance of 25.7 cm<sup>-1</sup>, which is more sensitive to MoS<sub>2</sub> thickness than individual Raman vibrational band frequencies. The E<sub>1</sub>2g - A<sub>1</sub>g distance corresponds to the literature value expected for

bulk MoS<sub>2</sub> (< 6 MoS<sub>2</sub> nanosheet layers).<sup>74, 89, 90</sup> Last, XPS analysis was performed to determine the elemental composition of the 2D-MoS<sub>2</sub> powder utilised herein, with Figure 2.08(C) and (D) and Table 2.2. showing high resolution spectra of the Mo 3d and S 2p regions of 2D-MoS<sub>2</sub>.

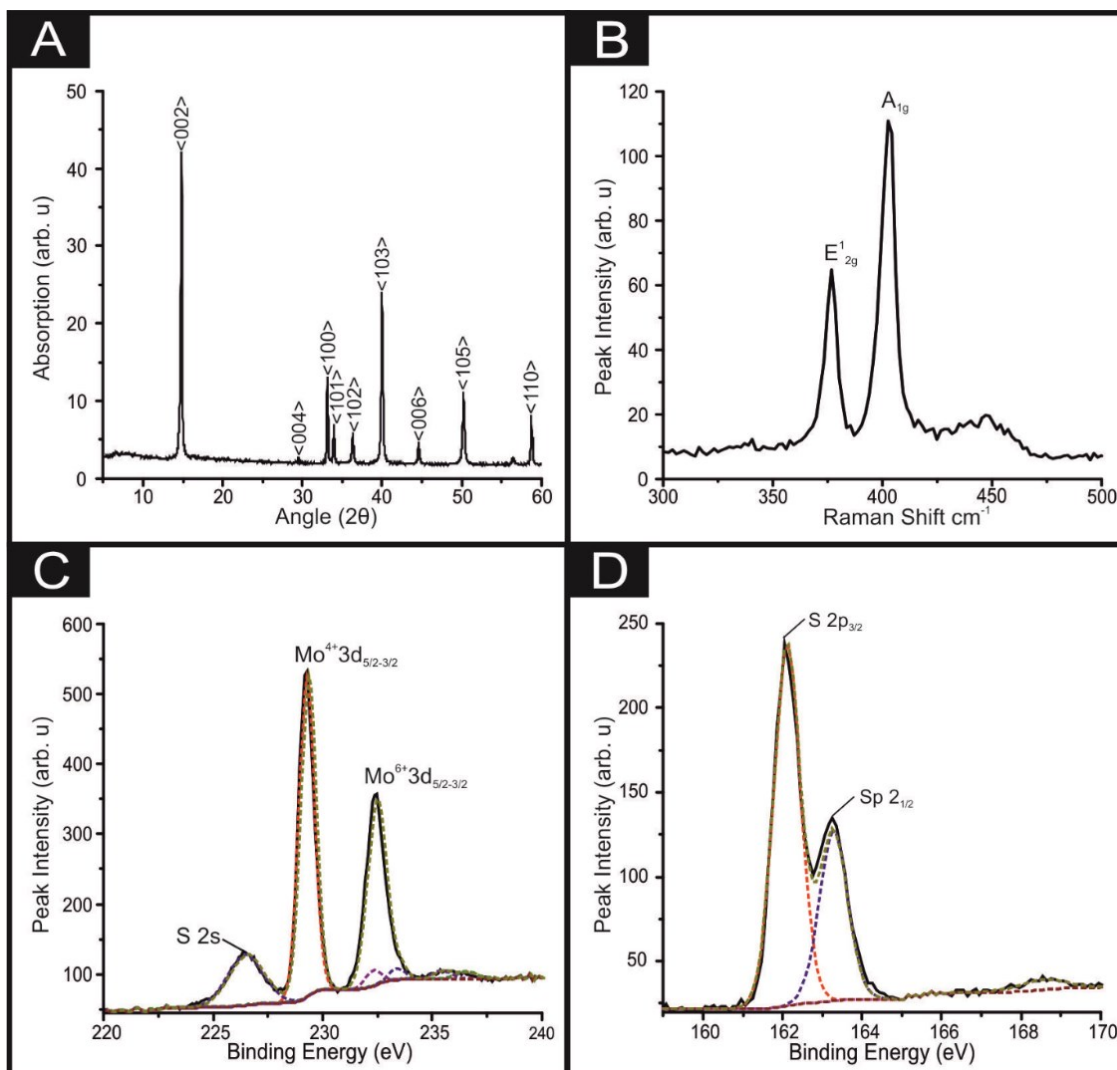


**Figure 2.08.** Characterisation of the commercially sourced 400 nm 2D-MoS<sub>2</sub> which is the basis of the fabricated 2D-MoS<sub>2</sub>-SPEs<sub>400nm</sub>; (A) XRD spectra of the 2D-MoS<sub>2</sub> and (B) Raman spectra 2D-MoS<sub>2</sub>. High-resolution XPS spectra of Mo 3d and S 2d regions of MoS<sub>2</sub> (C and D respectively).

Table 2.2. indicates that the Mo and S were present at the expected ratios (8.43% Mo atomic concentration to 20.11% S atomic concentration, which gives a 1:2.4 ratio respectively).

**Table 2.2.** Compositional analysis for the XPS spectra of the commercially sourced 400 nm 2D-MoS<sub>2</sub> presented in Figure 2.09(C) and 2.09(D), shown in atomic percentage concentration, excluding H which is not detected by this technique.

Element	Atom % Concentration
O 1s	13.46
Mo 3d	8.43
C 1s	56.86
S 2p	20.11
Si 2p	1.13

Note, 2D-MoS<sub>2</sub> flakes with lateral widths of *ca.* 2 and 6  $\mu\text{m}$  were also used in the fabrication of 2D-MoS<sub>2</sub>-SPEs, with their physicochemical characterisation being presented in Figures 2.11 and 2.12, respectively. Utilising 2D-MoS<sub>2</sub> flakes with different lateral widths (*ca.* 400 nm, 2  $\mu\text{m}$  and 6  $\mu\text{m}$ ) allowed us to investigate the effect of altering the active-edge to relatively inert-basal site ratio upon the 2D-MoS<sub>2</sub>-SPEs ability to catalyse the ORR. As flakes with small lateral widths will have a larger edge to basal site ratio than flakes with larger lateral widths.

Given the results of the physicochemical analysis performed on the commercially sourced MoS<sub>2</sub> powder, which was utilised in this work to produce the electrocatalytic inks, it is evident that it is comprised of high quality 2D-MoS<sub>2</sub> nanosheets.

Independent physicochemical characterisation was performed on the commercially sourced 2  $\mu\text{m}$  and 6  $\mu\text{m}$  flake size 2D-MoS<sub>2</sub> and is reported below.<sup>81, 82</sup> Figures 2.9 and 2.10 depict typical TEM images of the 2D-MoS<sub>2</sub> nanosheets that have

an average lateral width of *ca.* 2 and 6  $\mu\text{m}$ , respectively. Figures 2.9 and 2.10 indicate that there is some aggregation of the nanosheets.<sup>74</sup>

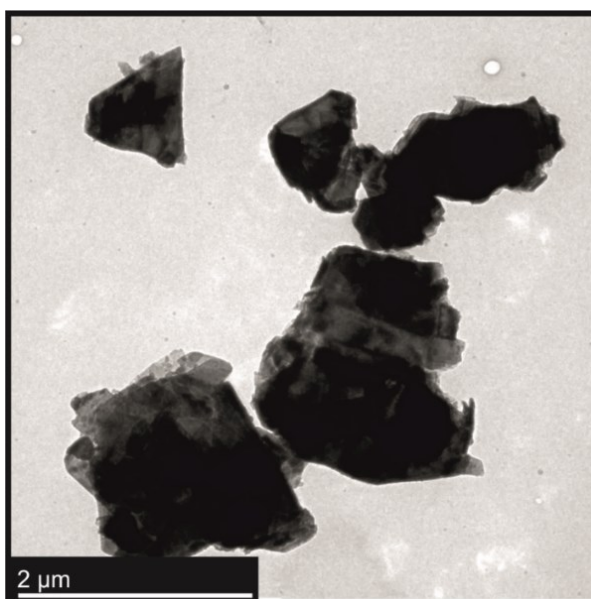


**Figure 2.09.** TEM images of the commercially sourced *ca.* 2  $\mu\text{m}$  2D-MoS<sub>2</sub> used in the fabrication of 2D-MoS<sub>2</sub>-SPES<sub>2 $\mu\text{m}$</sub> . Scale bar: 2  $\mu\text{m}$ .

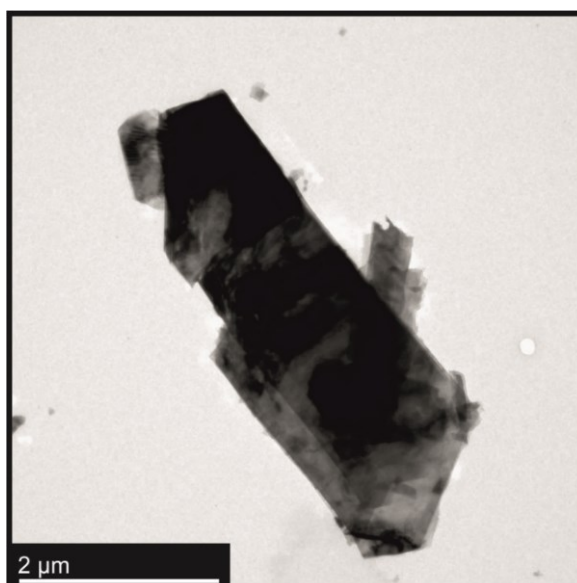


**Figure 2.10.** TEM images of the commercially sourced *ca.* 6  $\mu\text{m}$  2D-MoS<sub>2</sub> used in the fabrication of 2D-MoS<sub>2</sub>-SPES<sub>6 $\mu\text{m}$</sub> . Scale bar: 2  $\mu\text{m}$ .

XRD analysis performed on the 2  $\mu\text{m}$  and 6  $\mu\text{m}$  2D-MoS<sub>2</sub> powders is presented in Figure 2.12 and 2.13, respectively. As with the 400nm 2D-MoS<sub>2</sub> the major

diffraction peaks that are characteristic of hexagonal MoS<sub>2</sub> are visible at  $2\theta = 14.7^\circ$ ,  $29.4^\circ$ ,  $33.1^\circ$ ,  $33.9^\circ$ ,  $36.3^\circ$ ,  $40.0^\circ$ ,  $44.6^\circ$ ,  $50.2^\circ$  and  $58.8^\circ$  corresponding to the planes of (002), (004), (100), (101), (102), (103), (006), (105), and (110), respectively.<sup>97, 98</sup> After this raman analysis was undertaken on the 2  $\mu\text{m}$  and 6  $\mu\text{m}$  2D-MoS<sub>2</sub> powders with Figures 2.11 (B) and 2.12(B) displaying the observed spectra. As with the 400nm 2D-MoS<sub>2</sub> the E<sub>1</sub>2g and A<sub>1</sub>g vibrational bands vibrational peaks can be observed at 376.8 and 402.5 cm<sup>-1</sup>, respectively, with a peak (E<sub>1</sub>2g - A<sub>1</sub>g) distance of 25.7 cm<sup>-1</sup>. The distance between the E<sub>1</sub>2g - A<sub>1</sub>g bands agrees to the expected for bulk MoS<sub>2</sub> (< 6 MoS<sub>2</sub> nanosheet layers).<sup>74, 89, 90</sup> The elemental composition of the 2  $\mu\text{m}$  and 6  $\mu\text{m}$  MoS<sub>2</sub> flakes was determined *via*, with Figure 2.11(C), 2.12(D) and Figure 2.11(C), 2.12(D) showing high resolution spectra of the Mo 3d and S 2p regions of the 2  $\mu\text{m}$  and 6  $\mu\text{m}$  2D-MoS<sub>2</sub>.

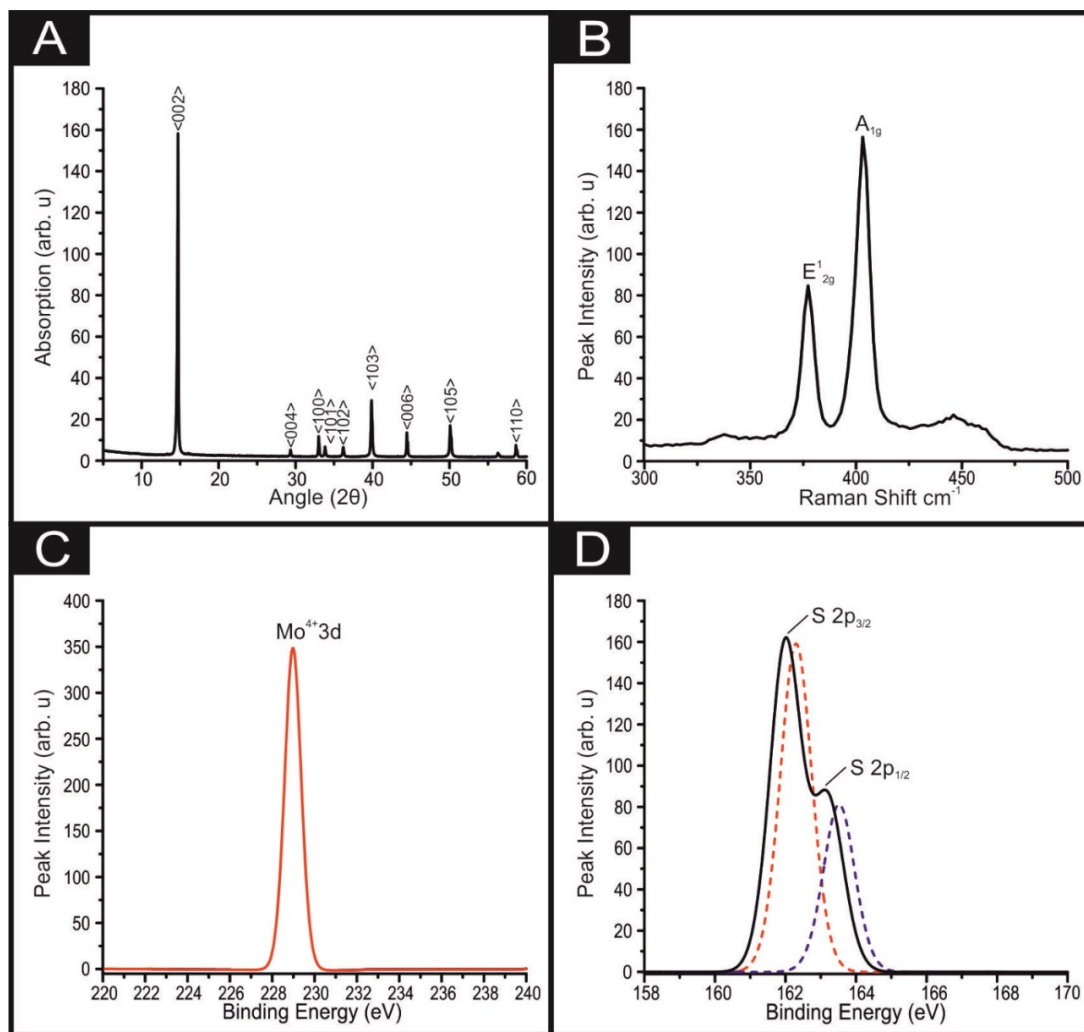


**Figure 2.11.** Characterisation of the commercially sourced *ca.* 2  $\mu\text{m}$  2D-MoS<sub>2</sub>; (A) XRD spectra of the 2  $\mu\text{m}$  2D-MoS<sub>2</sub> (B) Raman spectra *ca.* 2  $\mu\text{m}$  2D-MoS<sub>2</sub> deposited onto a silicon wafer between 300 and 500  $\text{cm}^{-1}$ . High-resolution XPS spectra of Mo 3d and S 2p regions of 2D-MoS<sub>2</sub> (C and D respectively).

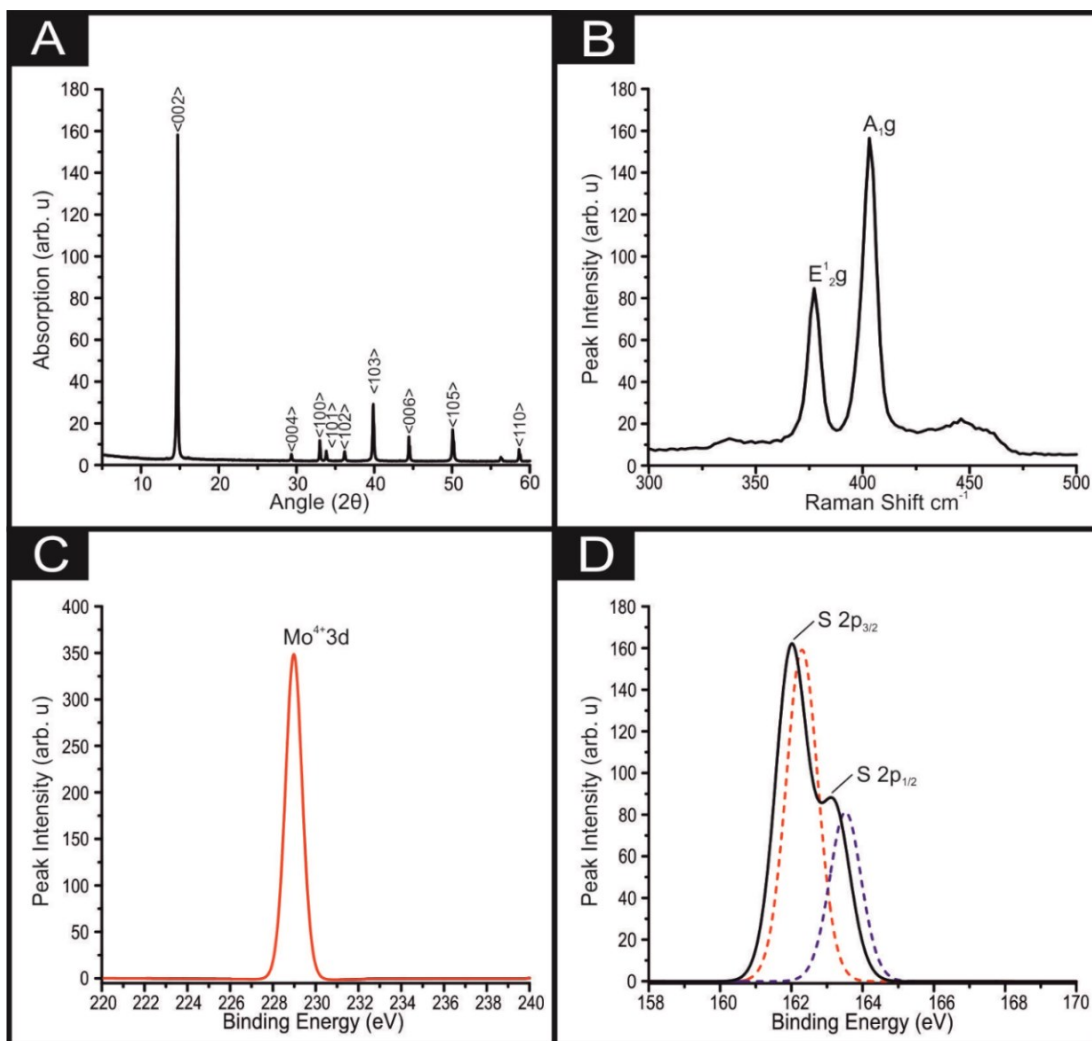


**Figure 2.12.** Characterisation of the commercially sourced ca. 6  $\mu\text{m}$  2D-MoS<sub>2</sub>; (A) XRD spectra of the ca. 6  $\mu\text{m}$  2D-MoS<sub>2</sub> (B) Raman spectra ca. 6  $\mu\text{m}$  2D-MoS<sub>2</sub> deposited onto a silicon wafer between 300 and 500  $\text{cm}^{-1}$ . High-resolution XPS spectra of Mo 3d and S 2p regions of 2D-MoS<sub>2</sub> (C and D respectively).

### 2.2.5. Physicochemical Characterisation of 2D-MoSe<sub>2</sub> Flakes Utilised in the Production of 2D-MoSe<sub>2</sub>-SPEs

---

Independent physicochemical characterisation was performed on the commercially sourced 2D-MoSe<sub>2</sub> used in Chapter 7 and reported below.<sup>99</sup> Figure 2.13 depicts typical TEM images of the 2D-MoSe<sub>2</sub>, it is clear upon a visual inspection of several 2D-MoSe<sub>2</sub> nanosheets that they have a average lateral size of *ca.* 500 nm, with an inter-nanosheet distance of *ca.* 3 nm, which strongly corresponds with literature.<sup>84</sup> Again there is evidence of nanosheet aggregation<sup>74</sup>

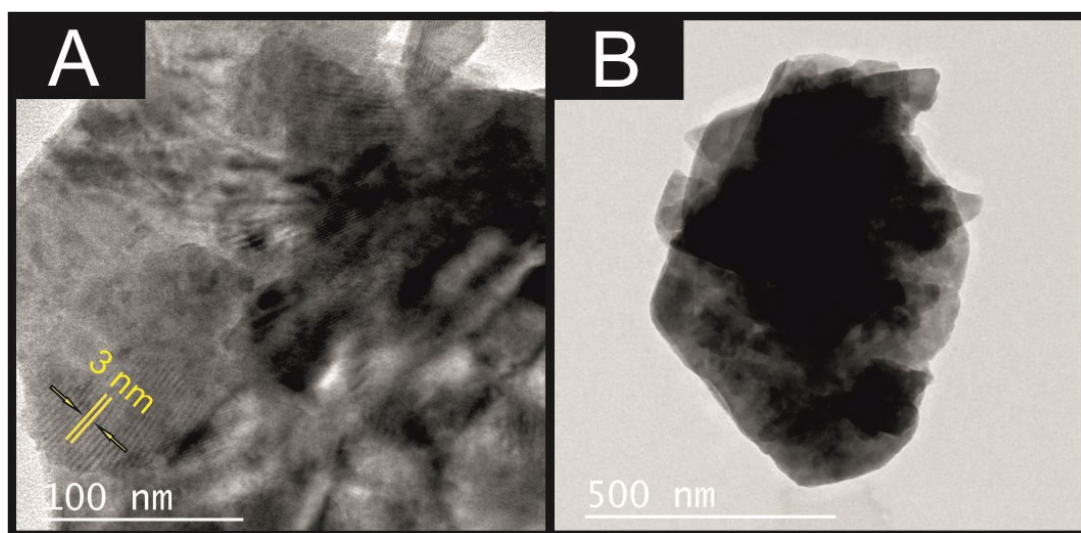


**Figure 2.13.** TEM images of the commercially sourced 2D-MoSe<sub>2</sub>. (A) Scale bar: 100 nm, (B) scale bar: 500 nm.

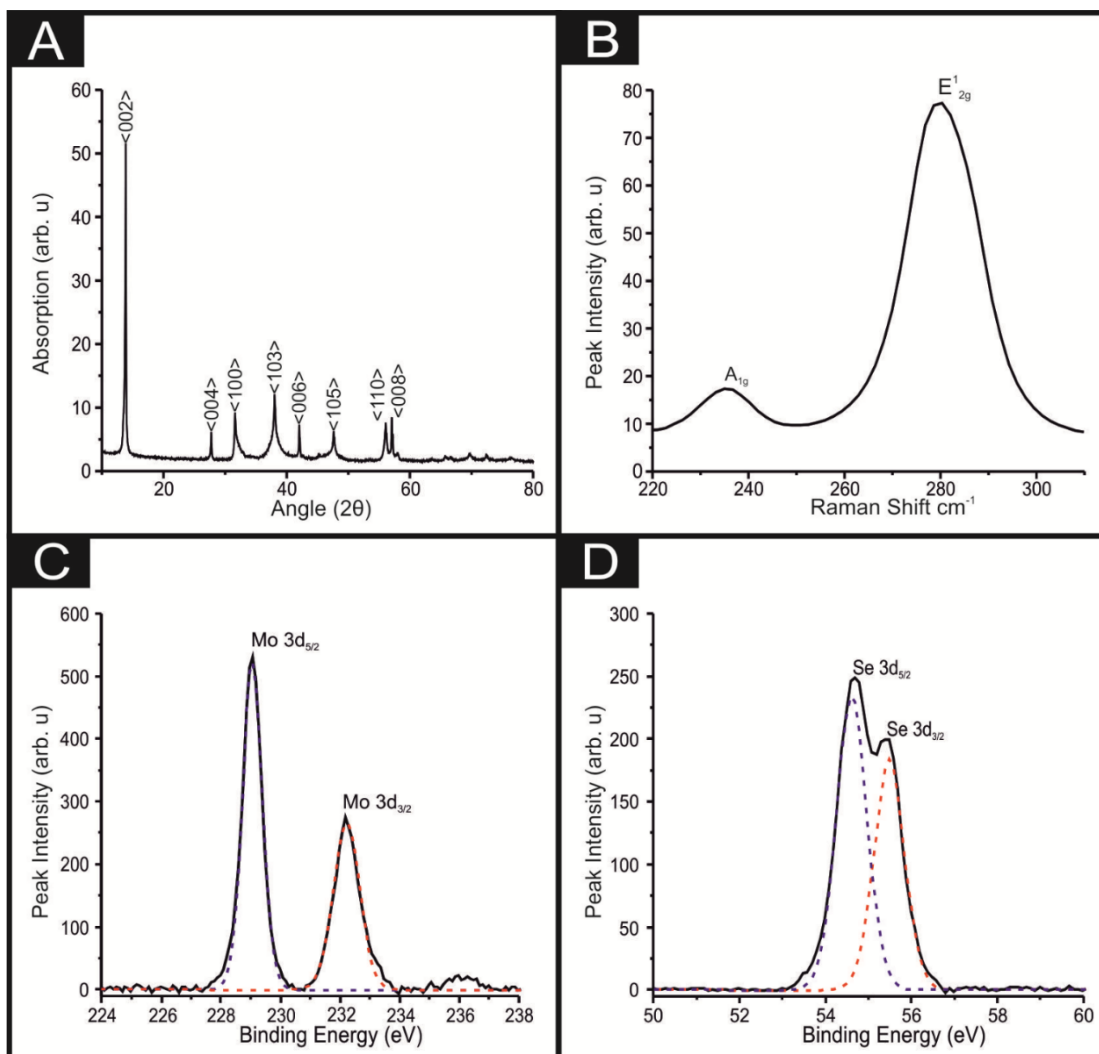


**Figure 2.14.** Characterisation of the commercially sourced 2D-MoSe<sub>2</sub>; (A) XRD spectra of the 2D-MoSe<sub>2</sub> (B) Raman spectra 2D-MoSe<sub>2</sub> deposited onto a silicon wafer between 220 and 320 cm. High-resolution XPS spectra of Mo 3d and Se 3d regions of MoSe<sub>2</sub> (C and D respectively).

XRD analysis obtained for the 2D-MoSe<sub>2</sub> utilised herein is presented in Figure 2.14(A). The characteristic diffraction peaks at  $2\theta = 13.7^\circ, 37.8^\circ, 47.5^\circ, 55.8^\circ$  and  $56.7^\circ$  are assigned to the (002), (103), (105), (110) and (008) faces of the hexagonal face of MoSe<sub>2</sub> (2H crystallinity), respectively.<sup>84</sup> Raman analysis was also implemented (see Figure 2.14.(B)), with a Raman spectrum showing the  $A_{1g}$  and  $E'_{2g}$  vibrational bands at *ca.* 238 and 283  $\text{cm}^{-1}$ , respectively, which are two of the most prominent peaks associated with 2D-MoSe<sub>2</sub>, agreeing well with literature.<sup>100-102</sup> The  $A_{1g}$  peak corresponds to the out-of-plane Mo-Se phonon mode whilst the  $E'_{2g}$  vibrational band is the in-plane mode.<sup>100-102</sup>

The 2D-MoSe<sub>2</sub> nanosheets utilised to fabricate the 2D-MoSe<sub>2</sub>-SPEs were next investigated by XPS. Upon inspection of Figure 2.14.(C) binding energies are evident for both Mo3d <sup>5/2</sup> and Mo3d <sup>3/2</sup> at 229.0 and 232.3 eV, respectively; such analysis reveals a Mo<sup>4+</sup> oxidation state. Also shown within Figure 2.14.(D) are binding energies for Se3d <sub>5/2</sub> and Se3d <sub>3/2</sub> positioned at 54.6 and 55.4 eV, indicating a Se<sup>2-</sup> oxidation state.<sup>103</sup> De-convolution of the XPS spectra reveals a Mo/Se stoichiometric ratio of 1:1.8, which could be attributed to a slightly defected 2D-MoSe<sub>2</sub> structure but agrees well with the expected ratio of 1:2.

Overall, the 2D-MoSe<sub>2</sub> utilised in this work to produce the novel electrocatalytic inks has been fully characterised and revealed to comprise of high quality 2D-MoSe<sub>2</sub> nanosheets for implementation as an electrocatalyst towards the HER.

### 2.3. Electrochemical Measurements

---

All solutions were prepared with deionised water of resistivity not less than 18.2 M $\Omega$  cm. HER measurements were performed in 0.5 M H<sub>2</sub>SO<sub>4</sub> and the sulfuric acid solution utilised was of the highest possible grade available from Sigma-Aldrich (99.999%, double distilled for trace metal analysis). This solution was vigorously degassed prior to electrochemical measurements with high purity, oxygen-free nitrogen. The above ensures the removal of any trace of oxygen from test solutions, which if present would convolute the observed results for HER with the competing oxygen evolution reaction; this is common practice in the literature.<sup>104, 105</sup> All ORR measurements were performed in 0.1 M H<sub>2</sub>SO<sub>4</sub>. The 0.1 M sulfuric acid solution utilised for the ORR tests was oxygenated and subjected to rigorous bubbling of 100% medical grade oxygen for one hour, resulting in a 0.9 mM concentration of oxygen, assuming this to be a completely saturated solution at room temperature, which is common practice in the literature.<sup>54, 55</sup> Where the HER and ORR onset potentials are denoted within the manuscript, note that this is defined as the potential at which the current initially deviates from the background current by a value of 25  $\mu\text{A cm}^{-2}$ , thus signifying the commencement of the Faradaic current associated with the HER and ORR redox reactions.

Electrochemical measurements were performed using an Ivium Compactstat<sup>TM</sup> (Netherlands) potentiostat. Measurements were carried out using a typical three electrode system, as represented in Figure 1.04. (Chapter 1, page 40) with a Pt wire counter electrode and a saturated calomel electrode (SCE) as the reference. The working electrodes used were as follows: an edge plane pyrolytic graphite (EPPG) (Le Carbone, Ltd. Sussex, UK) electrode, which was machined into a 4.9 mm diameter disc, with the disc face parallel to the edge plane, as required from a slab of highly ordered pyrolytic graphite (HOPG, highest grade available with a lateral grain

size,  $L_a$  of 1–10  $\mu\text{m}$  and  $0.4 \pm 0.1^\circ$  mosaic spread); a glassy carbon (GC) electrode (3 mm diameter, BAS, USA); a boron-doped diamond (BDD) electrode (3 mm diameter, BAS, USA); a Pt electrode (3 mm diameter, BAS, USA); and screen-printed graphite electrodes (SPE), which have a 3 mm diameter working electrode. The SPEs were fabricated in-house with appropriate stencil designs using a DEK 248 screen-printing machine (DEK, Weymouth, U.K.).

#### 2.4. Drop-casting Modification of the Electrodes

---

The modification of each electrode was carried out using a drop casting approach, where an aliquot of the 2D-MoS<sub>2</sub> nanosheet suspension was deposited onto the desired supporting electrode surface using a micropipette (See Figure 2.15).<sup>106</sup> This deposition was then allowed 5 minutes to dry (at 35 °C) to ensure complete ethanol evaporation. Finally, the electrode was allowed to cool to ambient temperature, after which the process was repeated until the desired mass was deposited onto the surface. The electrode was then ready to use.

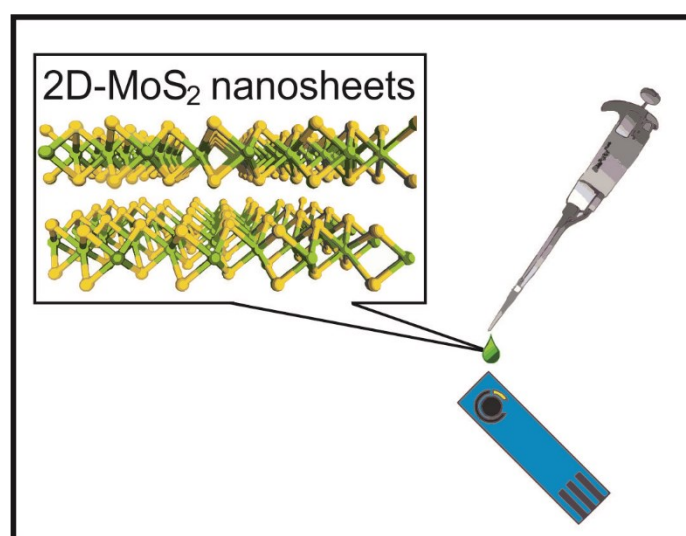


**Figure 2.15.** Graphical representation of the drop-casting procedure.

### 2.5.1. Screen-Printed Electrode Fabrication

---

Screen-printed electrodes (SPE) were fabricated in-house. A carbon-graphite ink formulation (product code C2000802P2; Gwent Electronic Materials Ltd., U.K.) was screen-printed onto a polyester (Autostat, 250  $\mu\text{m}$  thickness) flexible film (denoted throughout as standard-SPE); these electrodes have been used extensively in other work.<sup>107-110</sup> This layer was cured in a fan oven at 60  $^{\circ}\text{C}$  for 30 minutes. Next, a silver/silver chloride reference electrode was included by screen-printing Ag/AgCl paste (product code C2040308D2; Gwent Electronic Materials Ltd., U.K.) onto the polyester substrates. Finally, a dielectric paste (product code D2070423D5; Gwent Electronic Materials Ltd., U.K.) was then printed onto the polyester substrate to cover the connections. After curing at 60  $^{\circ}\text{C}$  for 30 minutes the SPEs are ready to be used. SPEs have been reported previously and shown to exhibit a heterogeneous electron transfer rate constant,  $k^{\circ}$ , of *ca.*  $10^{-3} \text{ cm s}^{-1}$ , as measured using the  $[\text{Ru}(\text{NH}_3)_6]^{3+/2+}$  redox probe.<sup>106, 109, 111-113</sup> Note that for the purpose of this work, electrochemical experiments were performed using the working electrode of the SPEs only and that external reference and counter electrodes were utilised as detailed earlier to allow a direct comparison between all the utilised electrodes.

Figure 2.16. shows the range of designs and geometries that can be achieved *via* screen-printing, ranging from microbands (50 micron width by 2 cm length), as seen in Figure 2.16. (A) through to macroelectrodes, such as the SPE shown within Figure 2.16. (D), which has a working area of 4.5  $\text{cm}^2$ . Finally, the design that was utilised in this work is shown in Figure 2.16. (C), which has a diameter and working area of 3 mm and 0.0707  $\text{cm}^2$ , respectively. This figure demonstrates a range of screen-printed electrode designs in order to highlight the versatility of electrode design inherent with the screen-printing technology.<sup>114</sup>

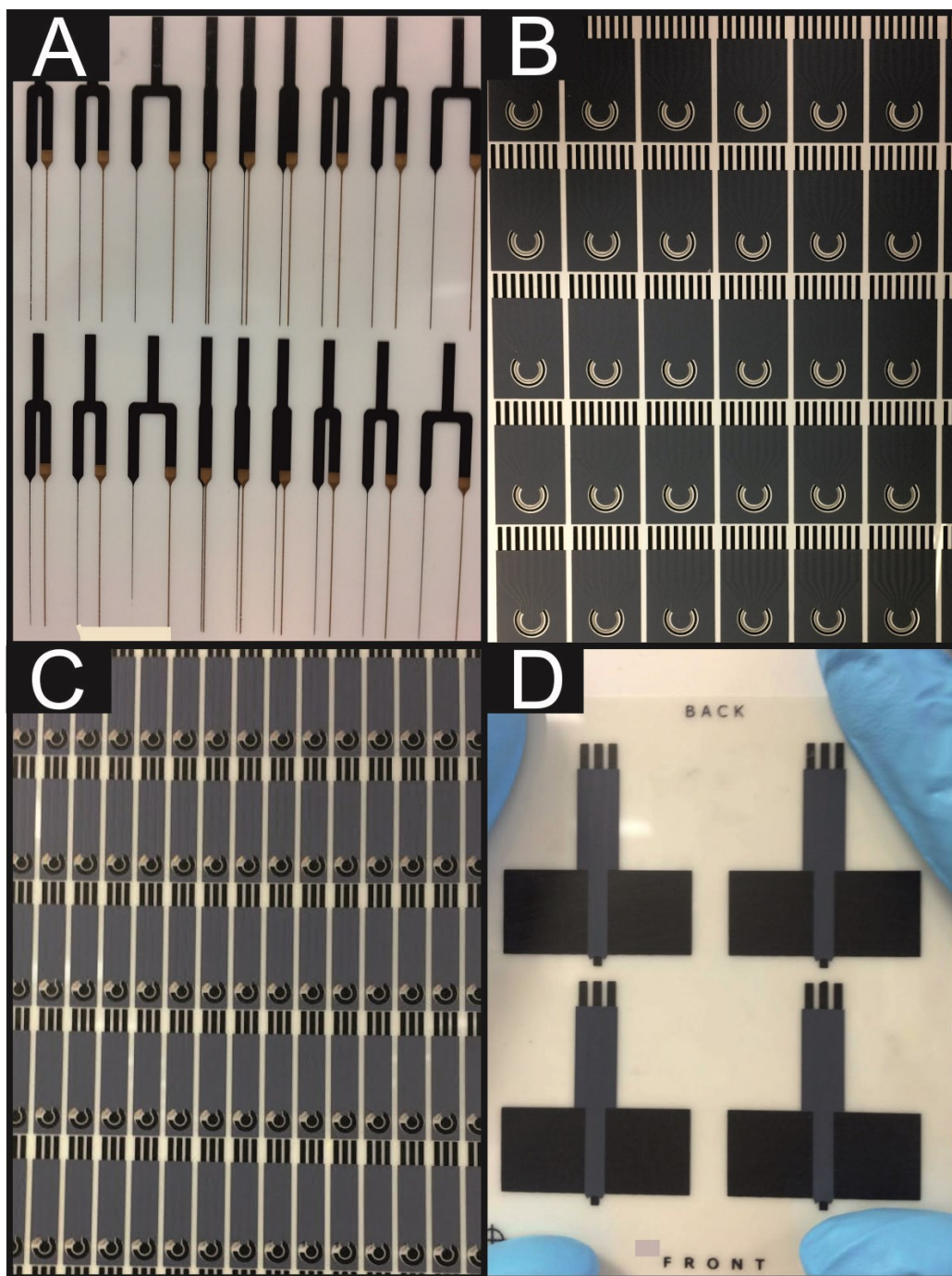


**Figure 2.16.** Photographs of SPEs: possible variants of SPE designs. Each of which has a varied working electrode of; (A)  $0.01 \text{ cm}^2$  (B)  $0.0196 \text{ cm}^2$  (x6), (C) the design utilised herein with a working area of  $0.0707 \text{ cm}^2$  and (D) a dual electrode ( $4.5 \text{ cm}^2$ ).

### 2.5.2. Fabrication of the 2D-MoS<sub>2</sub> and 2D-MoSe<sub>2</sub> Incorporated SPE's

---

The following section will refer to Chapter 6 and 7, which aim to produce electrocatalytic inks, *via* incorporation of 2D-MoS<sub>2</sub> or 2D-MoSe<sub>2</sub> into a bulk ink solution. In the following section it will only refer to the 2D-MoS<sub>2</sub> but it should be noted that the same technique was implemented using 2D-MoSe<sub>2</sub> as well. Initially a 2D-MoS<sub>2</sub> ink, made from first principles, was considered using a range of solvents, binders and graphitic materials. A range of inks were formulated using a combination of fast and slow drying solvents, along with just solely 2D-MoS<sub>2</sub> (the variants reported earlier) and a range of polymeric binders. Other ink formulations, which have additional supporting carbon black/graphite materials as well as the 2D-MoS<sub>2</sub>, variants were also explored. In all endeavours, it was found that inks were produced and were able to be screen-printed, but had poor/non-existent electrochemical responses in terms of the ORR overpotential ( $> 0.89$  V *vs.* SCE). Tailoring/optimising the components of the ink formulation did not result in better performances and additionally the screen-printing process resulted in only a few print cycles being possible prior to the screen drying and becoming unusable. Consequently, this avenue of research was discontinued. To overcome the problems identified above, it was therefore decided to utilise a pre-existing commercial graphitic ink. This has the advantage that the commercial ink allows the mass production of 2D-MoS<sub>2</sub> electrodes that can be printed for many print cycles without the screen blocking, but yet provide advantageous electrochemical performance. Thus, it was decided to incorporate the 2D-MoS<sub>2</sub> variants into an existing carbon-graphite ink formulation (product code C2000802P2; Gwent Electronic Materials Ltd., U.K.). The 2D-MoS<sub>2</sub> was incorporated into the bulk of the graphite ink on the basis of the weight percent of  $M_P$  and  $M_I$ , where  $M_P$  is the mass of particulate, in this case the 2D-MoS<sub>2</sub> and  $M_I$  is the mass of

the ink formulation used in the printing process, *i.e.*  $\% = (M_P / M_I) \times 100$ . The weight percent of  $M_P$  and  $M_I$  varied over the range 0 – 40%. The maximum amount of 2D-MoS<sub>2</sub> that can be incorporated into the carbon-graphite ink was found to correspond to 40%, as any further percentage incorporation increases the viscosity of the resultant ink to such an extent where it is not screen-printable *via* the technique utilised herein. It is possible to make an estimate as to the mass loading of each 2D-MoS<sub>2</sub>-SPE in regards to weight. By making a weight measurement *pre* and *post* Stage 4 of the screen-printing process, it is possible to ascertain the weight of 2D-MoS<sub>2</sub> modified ink on the surface of each electrode. We then prescribe a percentage of this weight to the 2D-MoS<sub>2</sub>. Utilising this method we deduced a value of 101.4, 202.7, 405.5 and 810.9  $\mu\text{g}$  for the mass loading of 2D-MoS<sub>2</sub> in a 5, 10, 20 and 40% 2D-MoS<sub>2</sub>-SPEs. Due to the nature of the screen-printing process, it is only possible to ascertain roughly accurate mass of 2D-MoS<sub>2</sub> within the ink of each working electrode; we therefore use a percentage denotation throughout.

In order to reduce the amount of 2D-MoS<sub>2</sub> material utilised in the fabrication of the 2D-MoS<sub>2</sub>-SPEs, this resulting mixture was screen-printed on top of an initial screen-printed carbon-graphite surface which, was screen-printed using only the carbon-graphite ink formulation (see earlier). A visual description of the screen-printed process is presented in Figure 2.17. Following screen-printing of the 2D-MoS<sub>2</sub> modified ink, a curing step is required. A variety of temperatures and curing times were considered before an optimised time period and temperature of 30 minutes at 60 °C were implemented; prior curing times and temperatures resulted in poor electrochemical performances. The 2D-MoS<sub>2</sub> was screen-printed on top of the carbon-graphite surface, but with only the working electrode area being printed upon and then

cured as described earlier (60 °C for 30 minutes). This is to save the amount of 2D-MoS<sub>2</sub> required and reduce the overall cost of the electrodes.

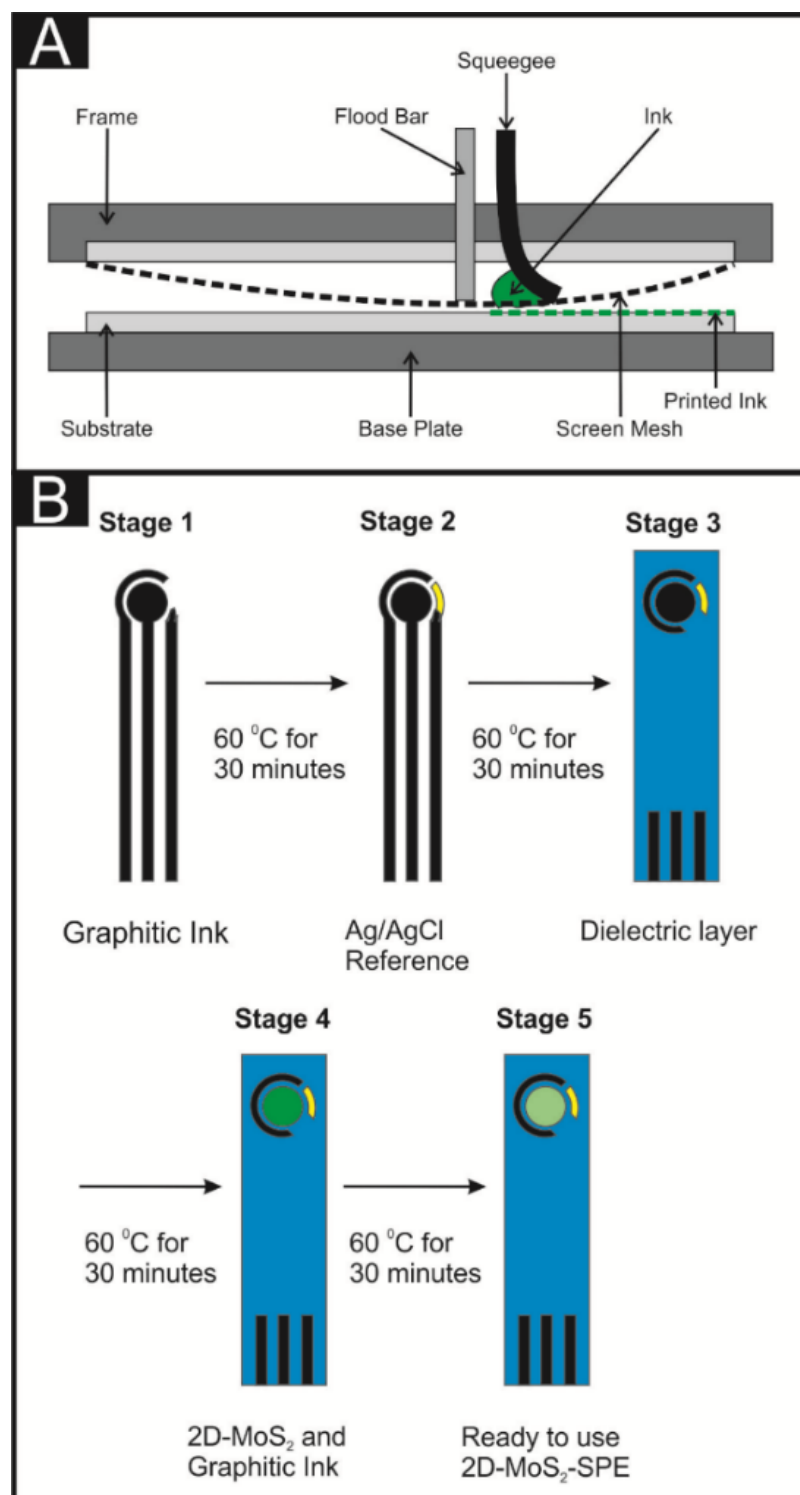


**Figure 2.17.** Illustration of the screen-printing process (A) employed in this paper and (B) the individual stages necessary in order to fabricate the mass producible 2D-MoS<sub>2</sub>-SPEs.

The 2D-MoS<sub>2</sub>-SPEs have a working area of 0.0707 cm<sup>2</sup>, however it is possible to scale this process to produce SPEs of any size. For the purpose of this work, electrochemical experiments were performed using the working electrode of the SPEs only, and the external reference and counter electrodes were utilised as detailed earlier, to allow a direct comparison between all the utilised electrodes. Note that the interaction between the graphite ink and the 2D-MoS<sub>2</sub>/2D-MoSe<sub>2</sub> is solely that of physical blending, as XPS of the surface of a 20% 2D-MoS<sub>2</sub>-SPE and 10% 2D-MoSe<sub>2</sub>-SPE demonstrates the same spectra as the 2D-MoS<sub>2</sub> powder described above (see Figure 2.18 and Figure 2.19).

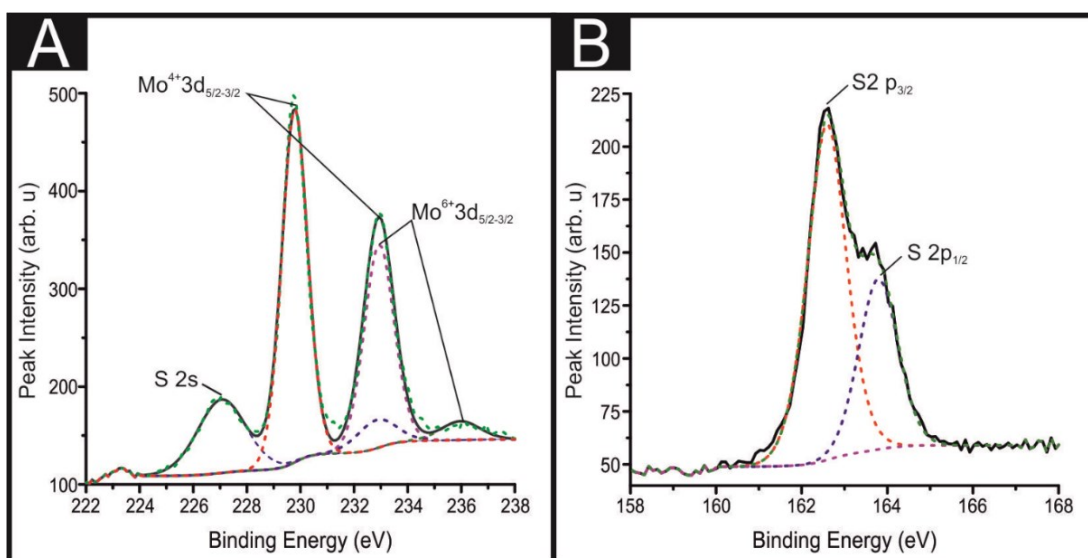


**Figure 2.18.** Characterisation of a 20% 2D-MoS<sub>2</sub>-SPE<sub>400nm</sub> via XPS analysis; High-resolution XPS spectra of Mo 3d and S 2p regions of MoS<sub>2</sub> (A and B respectively).

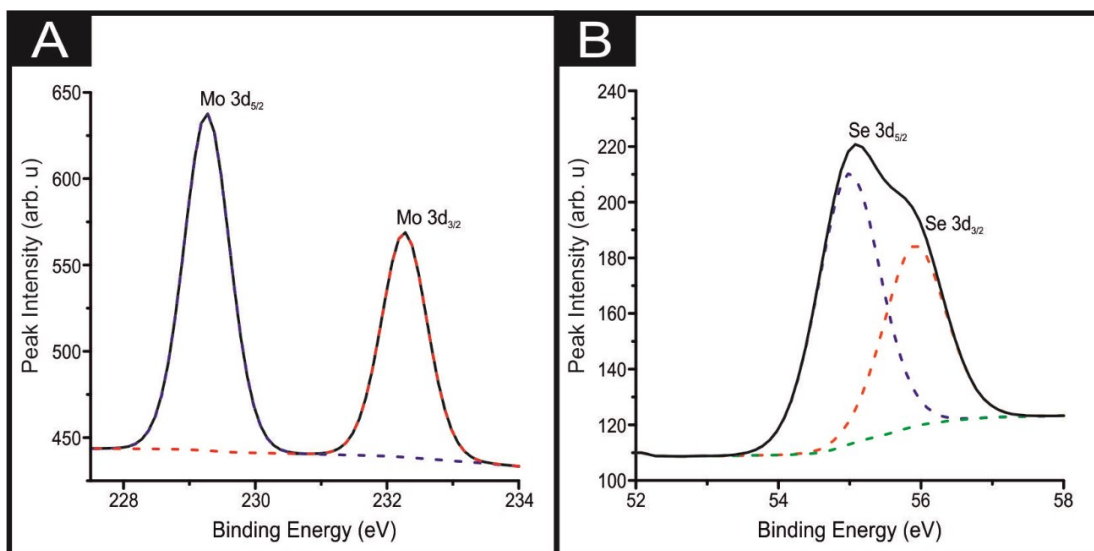


**Figure 2.19.** High-resolution XPS spectra of Mo 3d and Se 3d regions of a 10% MoSe<sub>2</sub>-SPE (A and B respectively).

## 2.6. Summation

---

This chapter reports a physiochemical characterisation, including Raman Spectroscopy, SEM, TEM, XPS and XRD, of the 2D-MoS<sub>2</sub> and 2D-MoSe<sub>2</sub> flakes utilised throughout this thesis. In summation both the 2D-MoS<sub>2</sub> and 2D-MoSe<sub>2</sub> can be considered high quality/pure nanosheets. This means, that the results obtained herein can be confidently attributed to the nanosheet being explored and that there is little chance of a contaminate convoluting the output signals. This Chapter also describes the methodology by which the electrodes are modified with the 2D nanomaterials, be that drop-casting or incorporation into SPEs.

# Chapter 3.

## Determining the Effect of Surfactant Upon the Electrochemical Activity of 2D-MoS<sub>2</sub>

Chapter 3 compares the HER electrochemical activity of commercially sourced 2D-MoS<sub>2</sub> (made without a surfactant) and 2D-MoS<sub>2</sub> made in house using a commonly employed surfactant (Sodium Cholate).

### 3.1. Introduction

---

Studies such as Ji *et al.*<sup>40</sup> have shown that 2D-MoS<sub>2</sub> can be used as an effective electrocatalyst towards the HER. In this case a loading of 48  $\mu\text{g cm}^{-2}$  of 2D-MoS<sub>2</sub> nanosheets onto a glassy carbon (GC) electrode resulted in a low HER overpotential and high current density of  $-120$  mV and  $1.26$  mA  $\text{cm}^{-2}$  ( $\eta = 150$  mV), respectively. An important question that arises from the utilisation of 2D-materials is how to fabricate them in order to explore their true electrochemical behaviour without the signal output being convoluted. This chapter therefore explores whether or not it was beneficial to commercially source or fabricate the 2D-MoS<sub>2</sub> in house.

There are numerous methodologies implemented within the literature for the production of 2D-MoS<sub>2</sub> nanosheets; liquid,<sup>115</sup> mechanical,<sup>116</sup> electrochemical (in this case of Bi<sub>2</sub>Se<sub>3</sub> and Bi<sub>2</sub>Te<sub>3</sub>)<sup>117</sup> and shear<sup>91</sup> exfoliation, to name just a few. It has also been shown by the work of Li *et al.*<sup>118</sup> that it is possible to fabricate monolayer dichalcogenides by chemical vapour deposition. A common occurrence within these 2D-MoS<sub>2</sub> production techniques, particularly liquid exfoliation, is the incorporation of a surfactant in order to stabilise the 2D materials, prevent re-aggregation and provide large quantities within surfactant-water solutions with relatively defect free flakes with nanometer lateral sizes.<sup>119</sup> For example Howe *et al.*<sup>120</sup> employed a range of bile salts, including: sodium cholate (SC), sodium deoxycholate and sodium

taurodeoxycholate in order to stabilise the 2D-MoS<sub>2</sub> dispersion during liquid exfoliation.

Numerous studies within the literature have employed a surfactant to stabilise various 2D-MoS<sub>2</sub> nanomaterials, which have subsequently been explored towards the HER; see Table 3.1. for a thorough overview. It has been previously noted in an exemplary study by Ambrosi *et al.*<sup>121</sup>, that it is possible to improve the electrochemical HER activity of 2D-MoS<sub>2</sub> *via* the addition of organolithium compounds in the exfoliation process. It is also worth noting that the solvent used in the exfoliation process can have a significant effect upon the 2D-MoS<sub>2</sub> activity, with a variation in the HER overpotential from 0.57 to 0.72 V when varying dispersion medias were used (acetonitrile, N,N-dimethylformamide, ethanol, methanol and water).<sup>122</sup> The work of Guo *et al*<sup>123</sup> has reported the hydrothermal synthesis of 2D-MoS<sub>2</sub> nanosheets using the surfactant cetyltrimethyl ammonium bromide (CTAB), which was explored towards the HER in acidic media, demonstrating a superior response of the CTAB-MoS<sub>2</sub> over that of surfactant free 2D-MoS<sub>2</sub>. This was attributed to the incorporation of CTAB into MoS<sub>2</sub> structures, inducing better electrical conductivity and exposing additional catalytically-active sites.<sup>123</sup> This likely occurs due to the CTAB preventing the 2D-MoS<sub>2</sub> aggregating back into multi-layer/bulk MoS<sub>2</sub>. However, what is evident in this work, and those reported within Table 3.1., is the question as to whether the observed electrochemical response of 2D-MoS<sub>2</sub> fabricated with a surfactant is solely due to the 2D-MoS<sub>2</sub> or whether the surfactant is contributing, be that detrimental or advantageous, to observed / apparent catalytic properties of the 2D-MoS<sub>2</sub>. It is of note that within the work of Guo *et al*,<sup>123</sup> as well as the other studies reported in Table 3.1., control experiments, that is, just a surfactant modified electrode/surface explored towards the HER, are lacking.

In order to explore the effect of a commonly employed surfactant on the HER activity of 2D-MoS<sub>2</sub>, the following chapter will compare and contrast the electrocatalytic activity of 2D-MoS<sub>2</sub> produced using a surfactant, sodium cholate (2D-MoS<sub>2</sub>-SC), and pristine 2D-MoS<sub>2</sub> (2D-MoS<sub>2</sub> produced without a surfactant) towards the HER.

**Table 3.1.** Comparison of literature reporting surfactant fabricated MoS<sub>2</sub> based catalysts that have been explored towards the HER.

Electrocatalyst	Surfactant	Supporting Electrode	Electrolyte	HER onset (–V)	Tafel Value (mV dec <sup>-1</sup> )	Reference
MoS <sub>2</sub> nanospheres	PVP	GC	0.5 M H <sub>2</sub> SO <sub>4</sub>	0.11 (vs. RHE)	72	124
MoS <sub>2</sub> nanosheets	CTAB	GC	0.5 M H <sub>2</sub> SO <sub>4</sub>	0.09 (vs. RHE)	55	123
MoS <sub>2</sub> -SWNT	SDS	GC	0.5 M H <sub>2</sub> SO <sub>4</sub>	0.20 (vs. RHE)	60	67
MNTs@rGO	octylamine	GC	0.5 M H <sub>2</sub> SO <sub>4</sub>	0.18 (vs. RHE)	69	125
2D-MoS <sub>2</sub> -SC	SC	SPEs	0.5 M H <sub>2</sub> SO <sub>4</sub>	0.61 (vs. SCE)	141	<i>This work</i>
2D-MoS <sub>2</sub>	none	SPEs	0.5 M H <sub>2</sub> SO <sub>4</sub>	0.42 (vs. SCE)	94	<i>This work</i>

**Key:** PVP: poly(vinylpyrrolidone); GC:glassy carbon; RHE: relative hydrogen electrode; CTAB: cetyltrimethyl ammonium bromide; SWNT: single walled nanotubes; SDS: sodium dodecylsulfate; MNT: MoS<sub>2</sub> nanotubes; rGO: reduced graphene oxide; SC: sodium cholate; SPEs: screen-printed electrodes.

## 3.2. Results and Discussion

### 3.2.1. Characterisation

---

Chapter 2 details how the 2D-MoS<sub>2</sub> nanosheets were fabricated (see Section 2.2.2.1) from bulk MoS<sub>2</sub> *via* a surfactant mediated liquid phase exfoliation process using the surfactant sodium cholate (SC). This 2D material is denoted as 2D-MoS<sub>2</sub>-SC. Independent physicochemical characterisation (see Characterisation Section (2.2.2.1) of the Chapter 2) revealed that the 2D-MoS<sub>2</sub>-SC comprises of nanosheets with average lateral widths and number of layers of *ca.* 120 nm and 2, respectively. TEM images of these 2D-MoS<sub>2</sub>-SC nanosheets can be seen in Figure 2.01(B). Additionally shown in Figure 2.01(A) are surfactant free 2D-MoS<sub>2</sub> nanosheets which have average lateral widths and number of layers *ca.* 62 nm and 3, respectively. XPS, XRD, Raman and extinction spectroscopy (observable in Chapter 2, Figure 2.02) further indicate that the 2D-MoS<sub>2</sub>-SC and 2D-MoS<sub>2</sub> comprise of high quality/purity nanosheets.

### 3.2.2. Electrocatalytic Activity of 2D-MoS<sub>2</sub> and 2D-MoS<sub>2</sub>-SC

---

The 2D-MoS<sub>2</sub> and 2D-MoS<sub>2</sub>-SC were immobilised upon screen-printed electrodes (SPE) and explored towards the HER in 0.5 M H<sub>2</sub>SO<sub>4</sub>, as is common, within the literature.<sup>75</sup> Figure 3.01.(A) shows typical linear sweep voltammograms (LSV) obtained for a bare/unmodified SPE; SPE modified with *ca.* 2.8 mg cm<sup>-2</sup> of SC; SPE modified with *ca.* 1725 ng cm<sup>-2</sup> of 2D-MoS<sub>2</sub>; SPE modified with *ca.* 1725 ng cm<sup>-2</sup> of 2D-MoS<sub>2</sub>-SC and a Pt electrode. The bare/unmodified SPE exhibits an HER onset of -880 mV (*vs.* SCE) and a current density of 1.37 mA cm<sup>-2</sup> at a potential of -1.5 V. The bare SPE exhibits significantly less electrocatalytic activity towards the HER than Pt, which has a HER onset of *ca.* -0.25 V. The observed HER overpotential for Pt is,

as expected, due to it being a metal that has a very small binding energy for  $H^+$ .<sup>11</sup> Note that the HER onset is analysed as the potential at which the observed current deviates from the background current by  $25 \mu A cm^{-2}$ , as is common within the literature.<sup>75</sup> It is clear from inspection of Figure 3.01.(A) that, upon electrically wiring  $1725 ng cm^{-2}$  of 2D-MoS<sub>2</sub>-SC, the HER onset potential becomes less electronegative, shifting by 249 mV to  $-0.61 V$  (vs. SCE), compared to a bare/unmodified SPE. There is also a corresponding increase in the achievable current to  $2.61 mA cm^{-2}$ . As expected the 2D-MoS<sub>2</sub>-SC has a significant benefit to the HER activity displayed by an SPE when it is modified upon its surface, which arises due to the low binding energy towards  $H^+$  at the edge sites of the 2D-MoS<sub>2</sub>-SC nanosheets.

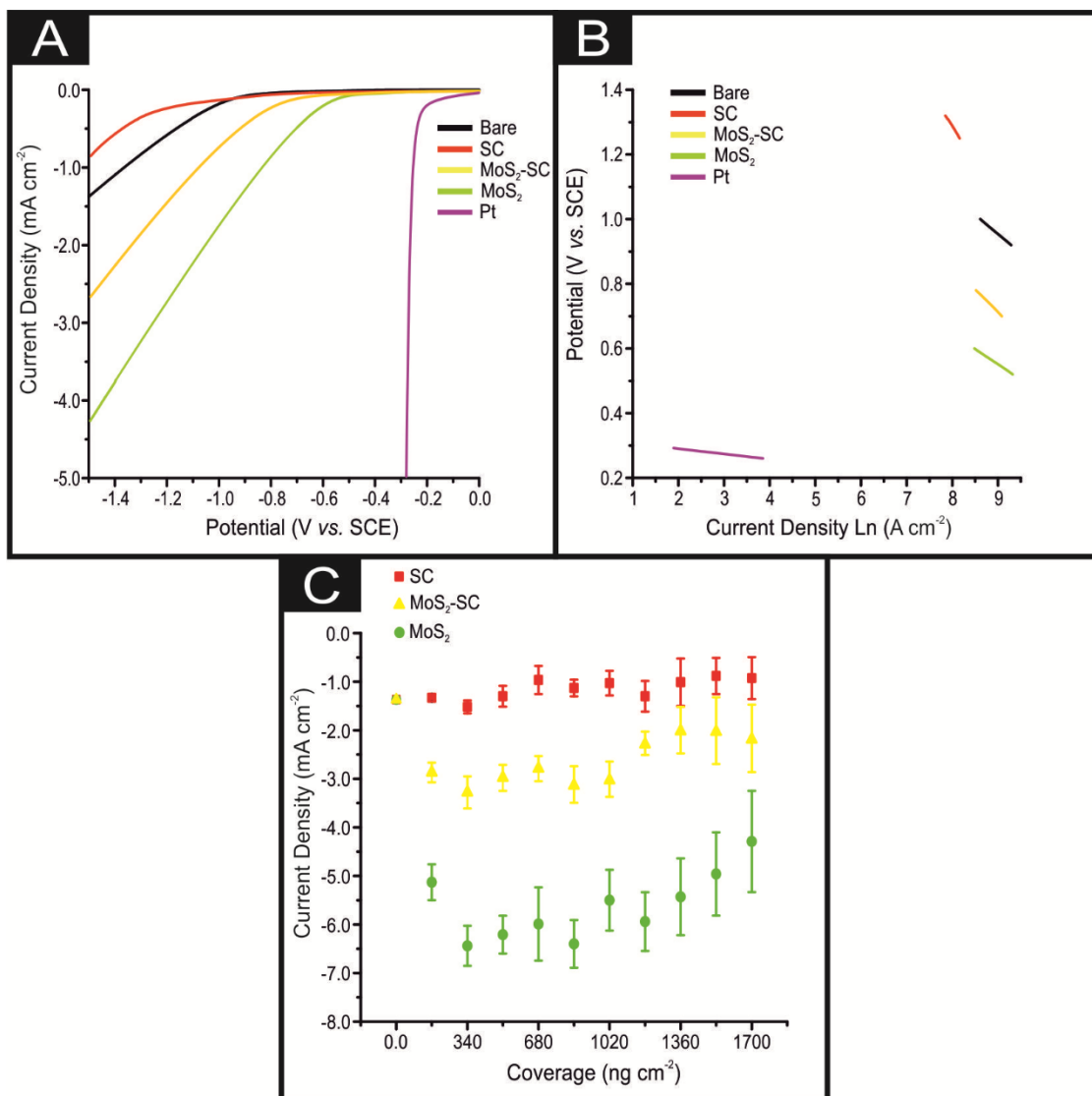


**Figure 3.01.** A) Typical LSV of bare/unmodified SPE, SPE modified with ca. 2.8 mg cm<sup>-2</sup> of SC, SPE modified with ca. 1725 ng cm<sup>-2</sup> of 2D-MoS<sub>2</sub>, SPE modified with ca. 1725 ng cm<sup>-2</sup> of 2D-MoS<sub>2</sub>-SC and a Pt electrode showing the onset of the HER. Scan rate; 0.25mVs<sup>-1</sup> (vs. SCE). Solution composition: 0.5 M H<sub>2</sub>SO<sub>4</sub>. (B) Tafel analysis; potential vs. Ln of current density for Faradaic section of the LSV presented in (A). (C) The current densities observed at -1.5 V for SPEs modified with 172, 345, 518, 690, 863, 1035, 1207, 1380, 1553 and 1726 ng cm<sup>-2</sup> of 2D-MoS<sub>2</sub> (green circles) and 2D-MoS<sub>2</sub>-SC (yellow triangles) as well as SPEs modified with ca. 282, 565, 848, 1131, 1414, 1697, 1980, 2263, 2545, 2828 mg cm<sup>-2</sup> of SC (red squares) (average standard deviation of 3 replicates). Scan rate; 0.25mVs<sup>-1</sup> (vs. SCE). Solution composition: 0.5 M H<sub>2</sub>SO<sub>4</sub>.

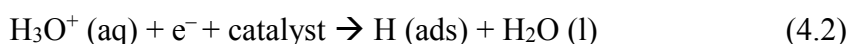
At first sight, one would believe that the 2D-MoS<sub>2</sub>-SC is electrocatalytic towards the HER, as judged by its improvement over that of a bare SPE. However, if one used instead 2D-MoS<sub>2</sub>, the observed result is a much greater HER activity than that of 2D-MoS<sub>2</sub>-SC, with a HER onset and achievable current of  $-0.48$  V (*vs.* SCE) and  $4.29$  mA cm<sup>-2</sup>, respectively. While the 2D-MoS<sub>2</sub> is less electrocatalytic towards the HER than Pt, it is the most beneficial electrocatalyst.

Insights from the current literature, for example Guo *et al*<sup>123</sup> have reported that CTAB-MoS<sub>2</sub> exhibited a superior response towards the HER over that of surfactant free MoS<sub>2</sub>, which was attributed to the incorporation of CTAB into MoS<sub>2</sub> increasing the electrical conductivity and exposure of additional catalytically-active sites.<sup>123</sup> However, in this case the opposite was observed. In order to understand this further, SC ( $2.8$  mg cm<sup>-2</sup>, the equivalent amount of SC present in a solution containing  $1725$  ng cm<sup>-2</sup> of 2D-MoS<sub>2</sub>-SC) was explored, and as shown within Figure 3.01., the HER onset potential is observed to become more electronegative compared to all the nanomaterials and electrodes studied, with the HER onset observed at  $-1.17$  V (*vs.* SCE). There is also a reduction in the achievable current to  $-0.88$  mA cm<sup>-2</sup>. It is clear that SC, *per se*, has a *detrimental* effect towards the HER.

### **3.2.3. Tafel Analysis in Order to Determine the Rate Limiting HER Step**

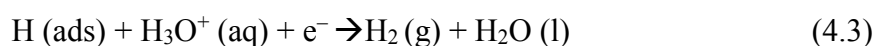
Pristine 2D-MoS<sub>2</sub> exhibits an improved HER over the 2D-MoS<sub>2</sub>-SC which is likely due to the presence of the SC blocking/shielding the active edge sites found on the MoS<sub>2</sub> nanosheets resulting in less H<sup>+</sup> being able to freely bind. As the 2D-MoS<sub>2</sub> demonstrates a greater proficiency at catalysing the HER it may be inferred that the underlying electrochemical reaction mechanism may be different than that of the 2D-

MoS<sub>2</sub>-SC, SC and bare SPE. A common approach within the literature at determining the particular HER mechanism taking place is *via* Tafel analysis on the Faradaic regions of the LSV's in Figure 3.01.(A).<sup>74</sup> The Tafel slopes are displayed in Figure 3.01.(B). A common approach in the literature is to employ Tafel analysis allowing the most likely electrochemical process to be theorised. Literature has suggested three possible steps in the reaction, each of which is capable of being the rate-determining step of the HER; this analysis is dependent on the corresponding Tafel slope. The initial H<sup>+</sup> adsorption step being the Volmer reaction, leading to the following equation:<sup>18-20</sup>



$$\frac{2.303RT}{\alpha F} \approx 120\text{mV}$$

The Volmer step can then be followed by one of two possible steps; either the Heyrovsky step:<sup>18-20</sup>



$$\frac{2.303RT}{(1+2)F} \approx 40\text{mV}$$

or the Tafel step:<sup>18-20</sup>



$$\frac{2.303RT}{2F} \approx 30\text{mV}$$

where the transfer coefficient, ( $\alpha$ ), is 0.5,  $F$  is the Faraday constant,  $R$  is the universal gas constant and  $T$  is the temperature at which the electrochemical experiment was performed. The values from the Tafel analysis (presented below each equation) are an indication of the reaction mechanism

The Tafel values obtained for the bare SPE, SPE modified with  $1725 \text{ ng cm}^{-2}$  of 2D-MoS<sub>2</sub>,  $1725 \text{ ng cm}^{-2}$  of 2D-MoS<sub>2</sub>-SC and  $14.14 \text{ } \mu\text{g cm}^{-2}$  of SC were found to correspond to 118, 94, 141 and 224 mV dec<sup>-1</sup>, respectively. Whilst, the Tafel values for the SC and 2D-MoS<sub>2</sub>-Sc are too large to be accurately explained by Tafel analysis, the obtained values for the Bare SPE and the modified SPEs suggests poor HER activity with the initial step of H<sup>+</sup> adsorption (Volmer) being the rate limiting step, with a small surface coverage of adsorbed hydrogen.

In order to ascertain the intrinsic catalytic activity being displayed by the 2D-MoS<sub>2</sub> and 2D-MoS<sub>2</sub>-SC on a per active site basis literature commonly employs a turn over frequency (ToF) calculation. The ToF was deduced *via* the methodology presented in the Chapter 4 along with Appendix Figure A.1.1. The resultant ToF values for were 0.191 and  $0.314 \frac{\text{H}_2/\text{s}}{\text{Surface Site}}$ , respectively. These values support the inference that 2D-MoS<sub>2</sub> is a more beneficial electrocatalyst than 2D-MoS<sub>2</sub>-SC. This could be a result of the SC partially blocking/shielding the electronegative S atoms located at the active edge sites of the 2D-MoS<sub>2</sub> nanosheets, leading to less H<sup>+</sup> adsorption. There are several assumptions that must be made in order for the TOF to be a valid comparison. Firstly due to the intrinsic differences between the underlying carbon based electrodes (i.e. EPPG and BDD) the TOF values are only valid where comparing modifications upon a single electrode type and not between electrodes.

There also has to be an assumption that the double layer capacitance values used within the TOF values determination is dominated by the active edge sites of the MoS<sub>2</sub> sheet. This assumption has a strong theoretical support as a study by Gerishcher *et al.*<sup>126</sup> showed that for a semi-conductor the overall capacitance is considered to be the space charge capacitance inside the solid, as the active components dominate response. Transferring this to MoS<sub>2</sub> it would be the active edge Mo and S sites where the Helmholtz double capacitance layer is located.

#### **3.2.4. Electrochemical HER: Critical Coverage of 2D-MoS<sub>2</sub> Modification**

---

Next, whether the greater electrocatalytic activity displayed by the 2D-MoS<sub>2</sub> over the 2D-MoS<sub>2</sub>-SC is observed across a range of different coverages/masses of modification was investigated. The electrochemical response was monitored as a function of coverage: 172, 345, 518, 690, 863, 1035, 1207, 1380, 1553 and 1726 ng cm<sup>-2</sup> of 2D-MoS<sub>2</sub> and 2D-MoS<sub>2</sub>-SC, as well as SPEs modified with *ca.* 282, 565, 848, 1131, 1414, 1697, 1980, 2263, 2545, 2828 mg cm<sup>-2</sup> of SC (the equivalent amount of SC present in a solution containing 2D-MoS<sub>2</sub>-SC). These results are displayed within Figure 3.01.(C) and show that the 2D-MoS<sub>2</sub> has a greater achievable current across the full range of coverages than the 2D-MoS<sub>2</sub>-SC. The SC displays no catalytic activity at any coverage, in fact, it results in a decrease in the achievable current. It is evident through inspection of Figure 3.01.(C) that a trend of increased current density (corresponding to increased MoS<sub>2</sub> nanosheet coverage (ng cm<sup>-2</sup>)) is subsequently followed by a decrease in current density and/or plateauing effect. This is apparent upon modification of both sets of SPEs modified with 2D-MoS<sub>2</sub> and 2D-MoS<sub>2</sub>-SC. A previous study by Rowley-Neale *et al.*<sup>74</sup> observed a similar trend and employed the

term “critical coverage” for the mass of modification where HER activity is no longer correlated to increased 2D-MoS<sub>2</sub> nanosheet deposition. Rowley-Neale and co-workers suggest that a critical coverage of modification arises due to instability of the 2D-MoS<sub>2</sub> nanosheets causing delamination from the platforms surface and/or an optimal ratio of active edge sites to inert basal planes being achieved, after which subsequent mass additions cause shielding of the edge sites and a detrimental decrease in this ratio. The results of the above study strongly support the aforementioned inference that SC has a detrimental effect upon the ability of 2D-MoS<sub>2</sub> nanosheets to catalyse the HER when used as a surfactant in the nanosheet production.

Comparing the results presented herein to the current literature, as overviewed in Table 3.1, it is found that control experiments, that is, just exploring the response of the surfactant towards the HER is seldom performed. For example Zhang *et al.*<sup>124</sup> compared 3D MoS<sub>2</sub>-poly(vinylpyrrolidone) nanospheres against surfactant free 2D-MoS<sub>2</sub> nanosheets, but did not implement any control measurements but despite comparing different materials (3D-MoS<sub>2</sub> vs. 2D-MoS<sub>2</sub>). In the case of the 2D-MoS<sub>2</sub>-cetyltrimethyl ammonium bromide (CTAB) reported by Guo *et al.*<sup>123</sup>, whilst similar materials are compared, the control experiment of just the CTAB is critically missing. It is likely in both these cases that the surfactant contributes towards the HER activity, itself and potentially produces a favourable orientation to expose active edge sites, albeit they utilise a different surfactant. However one cannot judge or determine the true origin of the response of the MoS<sub>2</sub> material towards the HER without the proper controls.

The above study, by highlighting the detrimental effect that SC has upon the signal output (HER activity) of 2D-MoS<sub>2</sub> nanosheets, emphasizes the necessity of future studies to perform thorough control experiments in order to ascertain the effect

(if any) that a surfactant is having upon the signal/electrochemical output of a particular 2D material.

### 3.3. Summation

---

This Chapter has demonstrated that the surfactant used in the liquid exfoliation of 2D-MoS<sub>2</sub> detrimentally affects its electrochemical activity towards the HER; 2D-MoS<sub>2</sub> outperforms 2D-MoS<sub>2</sub>-SC with the critical difference being the presence of SC with control experiments elegantly confirming SC is detrimental. Furthermore, a coverage study revealed that the catalytic effect of the 2D-MoS<sub>2</sub> nanosheets increased proportionally with mass deposited until a ‘critical coverage’ (mass) was achieved, after which the response was observed to plateau/decline. The likely cause of this effect is inferred herein and has clear implications (in this case) when employing other 2D nanosheet materials within the literature. This study is unique in that it has investigated the effect of a surfactant upon the HER activity of 2D-MoS<sub>2</sub> nanosheets and indicates that future research involving surfactant exfoliated 2D-MoS<sub>2</sub>, and indeed other nanomaterials, should consider the electrochemical behaviour of the surfactant utilised. In order to explore the true electrochemical activity of 2D-MoS<sub>2</sub> this thesis will utilise a commercially sourced pristine 2D-MoS<sub>2</sub> throughout the following chapters.

# Chapter 4.

## 2D-MoS<sub>2</sub> Nanosheets Explored Towards the Hydrogen Evolution Reaction

Chapter 4 utilises the drop-casting technique to modify four commonly employed carbon based electrodes (BDD, EPPG, GC and SPEs) with a range of 2D-MoS<sub>2</sub> masses then explore their electrochemical activity towards the HER.

### 4.1. Introduction

---

In other studies in which 2D-MoS<sub>2</sub> is utilised towards the HER, (see Table 4.1) glassy carbon (GC) has been exclusively used as a supporting electrode material, with few attempts to use alternative carbon based supports; this is clearly evident from inspection of Table 4.1.<sup>28, 40, 67, 127, 128</sup> For instance, Voiry, et al.<sup>67</sup> reported a low HER onset potential of *ca.* 100 mV for the HER using typical 2D-MoS<sub>2</sub> nanosheets deposited on a GC electrode. Yu, et al.<sup>129</sup> demonstrated a layer dependent electrocatalysis using MoS<sub>2</sub> (grown *via* chemical vapour disposition (CVD)) deposited on GC, which is correlated with electron hopping in the vertical direction of the 2D-MoS<sub>2</sub> layers. Other work utilising modified GC electrodes has demonstrated that edge exposed 2D-MoS<sub>2</sub> nanosheets are efficient HER catalysts and that bulk 2D-MoS<sub>2</sub> has low activity.<sup>69, 130</sup> This work indicates that an MoS<sub>2</sub> structure with a greater proportion of MoS<sub>2</sub> edge sites-to-basal planes will predictably give rise to improved HER kinetics, with an optimal material having a small geometric basal plane contribution (which is reportedly less active to the HER).<sup>69</sup> It has been shown that electrocatalytic activity towards the HER correlates linearly with the number of 2D-MoS<sub>2</sub> edge sites.<sup>21</sup>

**Table 4.1.** Comparison of current literature reporting the use of MoS<sub>2</sub> as a catalyst explored towards the HER.

Catalyst	Electrode / supporting material	Loading ( $\mu\text{g cm}^{-2}$ )	Electrolyte	HER onset (-mV)	Tafel ( $\text{mV dec}^{-1}$ )	Reference
MoS <sub>2</sub>	Silver	–	0.5 M H <sub>2</sub> SO <sub>4</sub>	~ -0.15	55-60	<a href="#">131</a>
MoS <sub>2</sub>	CP	4	0.5 M H <sub>2</sub> SO <sub>4</sub>	-200	120	<a href="#">132</a>
Narrow sheet MoS <sub>2</sub>	GC	280	0.5 M H <sub>2</sub> SO <sub>4</sub>	-103	49	<a href="#">128</a>
MoS <sub>2</sub> / CoSe <sub>2</sub>	GC	~280	0.5 M H <sub>2</sub> SO <sub>4</sub>	- 11	36	<a href="#">133</a>
MoS <sub>2</sub> / MCN	GC	190	0.5 M H <sub>2</sub> SO <sub>4</sub>	-100	41	<a href="#">134</a>
MoS <sub>2</sub> /RGO	GC	285	0.5 M H <sub>2</sub> SO <sub>4</sub>	-100	41	<a href="#">34</a>
MoS <sub>x</sub>	GC	9	1 M H <sub>2</sub> SO <sub>4</sub>	–	40	<a href="#">20</a>
MoS <sub>3</sub>	GC	32	1 M H <sub>2</sub> SO <sub>4</sub>	~ -100	54	<a href="#">135</a>
Fe- MoS <sub>2</sub>	GC	30.4	1 M H <sub>2</sub> SO <sub>4</sub>	–	39	<a href="#">136</a>
MoS <sub>2</sub> nanosheets	GC	48	0.5 M H <sub>2</sub> SO <sub>4</sub>	~ -150 to -200	70	<a href="#">38</a>
2D-MoS <sub>2</sub>	GC	280	0.5 M H <sub>2</sub> SO <sub>4</sub>	-93	42	<a href="#">137</a>
MoS <sub>2</sub>	GC	~8.5	0.5 M H <sub>2</sub> SO <sub>4</sub>	–	86	<a href="#">138</a>
MoS <sub>2</sub> film	GC	–	0.5 M H <sub>2</sub> SO <sub>4</sub>	–	ca 140	<a href="#">129</a>

Defect rich MoS <sub>2</sub> nanosheets	GC	285	0.5 M H <sub>2</sub> SO <sub>4</sub>	-120	50	<a href="#">139</a>
MoS <sub>2</sub> nanosheets	GC	–	0.5 M H <sub>2</sub> SO <sub>4</sub>	~ -100	ca 40	<a href="#">67</a>
Amorphous MoS <sub>x</sub> films	GC	–	1 M H <sub>2</sub> SO <sub>4</sub>	–	40	<a href="#">35</a>
MoS <sub>2</sub> NAS	GC	–	0.5 M H <sub>2</sub> SO <sub>4</sub>	-54	100	<a href="#">33</a>
Annealed MoS <sub>2</sub> /Ag	Ag/PET	6	0.5 M H <sub>2</sub> SO <sub>4</sub>	–	154	<a href="#">39</a>
MoS <sub>2</sub> /Ag Strain 0% *	Ag/PET	6	0.5 M H <sub>2</sub> SO <sub>4</sub>	–	145	<a href="#">39</a>
MoS <sub>2</sub> /Ag Strain 0.005% *	Ag/PET	6	0.5 M H <sub>2</sub> SO <sub>4</sub>	–	141	<a href="#">39</a>
MoS <sub>2</sub> /Ag strain 0.01% *	Ag/PET	6	0.5 M H <sub>2</sub> SO <sub>4</sub>	–	138	<a href="#">39</a>
MoS <sub>2</sub> /Ag strain 0.02% *	Ag/PET	6	0.5 M H <sub>2</sub> SO <sub>4</sub>	–	135	<a href="#">39</a>
MoS <sub>2</sub> /Ag	Ag/PET	2	0.5 M H <sub>2</sub> SO <sub>4</sub>	–	152	<a href="#">39</a>
MoS <sub>2</sub> /Ag strain 0.01% *	Ag/PET	2	0.5 M H <sub>2</sub> SO <sub>4</sub>	–	142	<a href="#">39</a>
MoS <sub>2</sub> /Ag	Ag/PET	6	0.5 M H <sub>2</sub> SO <sub>4</sub>	–	142	<a href="#">39</a>
MoS <sub>2</sub> /Ag strain 0.01% *	Ag/PET	6	0.5 M H <sub>2</sub> SO <sub>4</sub>	–	138	<a href="#">39</a>
MoS <sub>2</sub> /Ag	Ag/PET	12	0.5 M H <sub>2</sub> SO <sub>4</sub>	–	143	<a href="#">39</a>
MoS <sub>2</sub> /Ag strain 0.01% *	Ag/PET	12	0.5 M H <sub>2</sub> SO <sub>4</sub>	–	140	<a href="#">39</a>
MoS <sub>2</sub> nanoparticles	Graphite	–	–	-100 to -200	–	<a href="#">11</a>
Ni-Mo nanopowder	Ti	1	2 M KOH	-70	–	<a href="#">140</a>
Ni-Mo nanopowder	Ti	3	0.5 M H <sub>2</sub> SO <sub>4</sub>	-80	–	<a href="#">140</a>
Ni-Mo nanopowder	Ti	13.4	2 M KOH	-100	–	<a href="#">140</a>
Amorphous MoS <sub>x</sub>	GC	(10 <sup>17</sup> sites cm <sup>-2</sup> )	0.5 M H <sub>2</sub> SO <sub>4</sub>	-200	60	<a href="#">130</a>
2D-MoS <sub>2</sub> nanosheets	GC	1.019	0.5 M H <sub>2</sub> SO <sub>4</sub>	~ -480	40	This work

2D-MoS <sub>2</sub> nanosheets	EPPG	1.267	0.5 M H <sub>2</sub> SO <sub>4</sub>	~ -450	74	This work
2D-MoS <sub>2</sub> nanosheets	BDD	1.267	0.5 M H <sub>2</sub> SO <sub>4</sub>	~ -450	90.9	This work
2D-MoS <sub>2</sub> nanosheets	SPE	1.267	0.5 M H <sub>2</sub> SO <sub>4</sub>	~ -440	92	This work

**Key;** –: Value unknown; **GC:** glassy carbon; **CP:** carbon paper; **MCN:** mesoporous carbon nanospheres; **RGO:** reduced graphene oxide; **∗:** Optimised Loading; **NAS:** nano-assembled structures; **PET:** polyethylene terephthalate; **EPPG:** edge plane pyrolytic graphite; **BDD:** boron doped diamond; **SPE:** screen-printed graphite electrode; **\***: mechanical bent tensile-strain-induced two dimensional MoS<sub>2</sub> nanosheets

The above studies are novel in their approaches towards HER. However, they are lacking significantly from not altering the underlying electrode material and in doing so neglecting the ability to de-convolute the true electrochemical performance of 2D-MoS<sub>2</sub> nanosheets. It is also important to realise that for commercial application that a cheap electrode support will be required in the application of electrocatalysts utilised in the HER. Graphite screen-printed electrodes (SPEs) meet this criteria due, their advantages over other carbon based electrodes, which include scales of economy resulting in ultra-low cost of production, competitive electron transfer performance/properties, versatility, and the ability to tailor and mass-produce such electrodes.<sup>109</sup> The performance of 2D-MoS<sub>2</sub> can only be truly understood *via* immobilisation using a range of support materials with varying electrode kinetics (electrochemical activities). (*Note that commercially sourced 2D-MoS<sub>2</sub> is utilised in this chapter. the electrochemical output signal of 2D-MoS<sub>2</sub> can become convoluted when it is produced via a surfactant method as described in Chapter 3*). Secondly, it is usual practise within the literature to modify electrodes with only one mass (coverage) of MoS<sub>2</sub>, which again makes it difficult to extrapolate a true understanding of 2D-MoS<sub>2</sub> nanosheets electrochemical behaviour; again this critical parameter is explored in this Chapter.

## 4.2. Results and Discussion

### 4.2.1. Electrochemical Activity of 2D-MoS<sub>2</sub>

The electrochemical response of the 2D-MoS<sub>2</sub> nanosheets (1266.7 ng cm<sup>-2</sup>) immobilised upon SPEs were studied using cyclic voltammetry (CV). Figure. 4.01. shows a typically observed CV where two oxidation peaks at + 0.65 and + 1.0 V are clearly visible in the first cycle followed by several minor reduction peaks in the – 0.5 to – 1.5 V range.

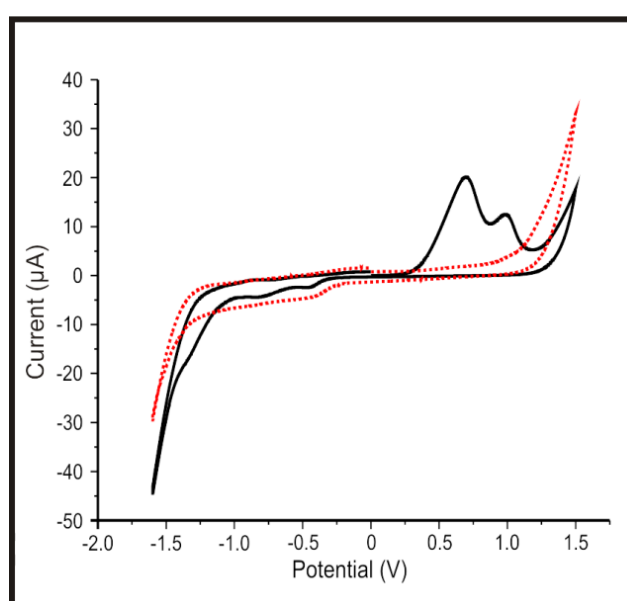
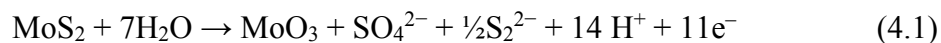


**Figure. 4.01.** Typical CV response of 2D-MoS<sub>2</sub> nanosheets immobilised upon a SPE in pH 7 phosphate buffer solution (PBS). First scan: solid black line. Second scan (representative of subsequent scans): red dotted line. Scan rate: 5 mVs<sup>-1</sup> (vs. SCE).

A pH 7 phosphate buffer was utilised as it allowed for a chemical stable environment in which the intrinsic redox reactions of 2D-MoS<sub>2</sub> could be studied without the possible convolution in signal out (CV) that an altering pH might cause. The initiation of the HER is evident in the cathodic response, with an onset potential of *ca.* –1.1 V. In terms of the anodic response, the two prominent oxidation peaks are due to irreversible reactions, probably the oxidation of Mo<sup>4+</sup> to Mo<sup>6+</sup> at edge and basal sites. Such oxidations are not observable in subsequent scans, which is expected to be

due to the MoO<sub>3</sub> dissolving into solution or being reduced to Mo<sup>3+</sup>, at which point it dissolves, explaining the origin of the observed reduction peak. This is represented in the equation below.<sup>132</sup>



It may also be possible that the Mo within the 2D-MoS<sub>2</sub> nanosheets has two dominant valence states, both of which are oxidised, resulting in the presence of the double peak. This inference is supported by the independent XPS analysis (see Experimental, Figures 2.06. and 2.07.), which indicated the presence of Mo in three different valence states for the 2D-MoS<sub>2</sub> nanosheet sample analysed. The double oxidation peak observed in Figure 4.01. is of interest and further study is required to determine its exact cause. The observed voltammetry (see Figure 4.01.) is in good agreement with Bonde, *et al.*<sup>132</sup> who explored nano-MoS<sub>2</sub>, deposited onto toray carbon paper in 0.5 M H<sub>2</sub>SO<sub>4</sub>, towards the HER. If the potential window is kept below the range where reported oxidation peaks occur, the HER activity of nano-MoS<sub>2</sub> remains stable.<sup>141</sup> The reduction peaks can also be accounted for by the reduction of S<sub>2</sub><sup>2-</sup> to H<sub>2</sub>S.<sup>132</sup> The double oxidation peak has previously been mischaracterised as a single oxidation peak due to the peaks merging occurring as a result of performing cyclic voltammetry at too high a scan rate.<sup>142</sup> This is important to note as the double peak convolutes the understanding of the electrochemical process occurring.

#### 4.2.2. Benchmarking the HER Activity of the Electrodes Utilised

Next, attention was turned to benchmarking the electrochemical system for the HER using commonly available electrodes in 0.5 M H<sub>2</sub>SO<sub>4</sub>, which is a widespread practice within the literature.<sup>21, 132, 138</sup> As is evident in Figure. 4.02.(A), the four unmodified carbon based electrodes are all significantly inferior to a Pt electrode, with respect to the potential required for HER onset and the current density reached.

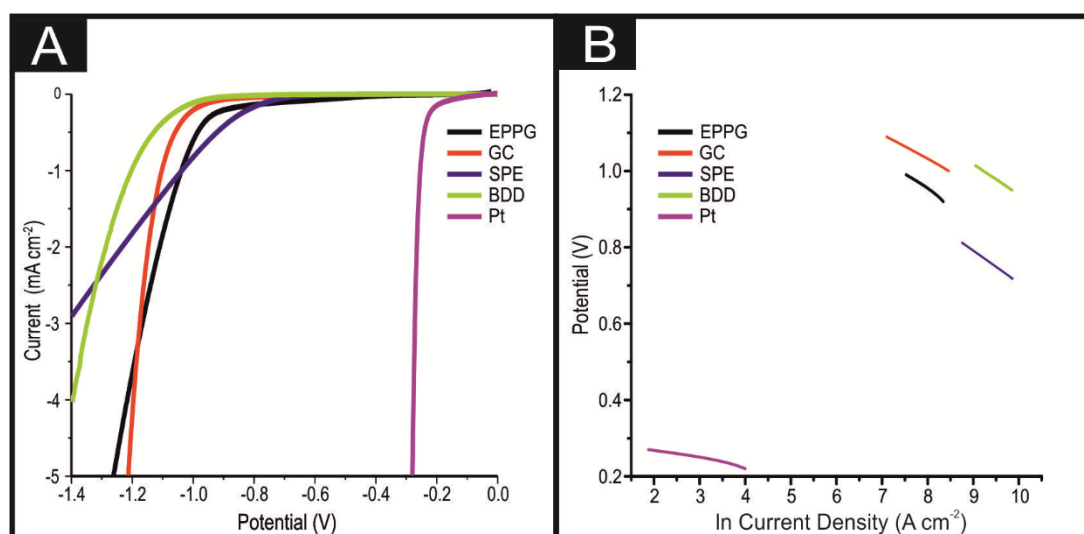


**Figure. 4.02.** (A) LSV of unmodified EPPG, GC, SPE, BDD and Pt electrodes showing the onset of the HER. In all cases, scan rate: 25 mVs<sup>-1</sup> (vs. SCE). Solution composition: 0.5 M H<sub>2</sub>SO<sub>4</sub>. (B) Tafel analysis; potential vs. natural log (ln) of current density for Faradaic section of the LSV presented in (A).

Note that the onset of HER is analysed as the potential at which the observed current initially begins to deviate from the background current by 25  $\mu\text{A cm}^{-2}$ . This is to be expected with Pt being a pure metal, which has a very small binding energy for H<sup>+</sup>.<sup>11</sup> It is evident that the onset potential for the HER occurs at *ca.* -1.05, -0.78, -0.76, -0.73, and -0.25 V at the GC, EPPG, BDD, SPE, and Pt electrodes, respectively. The SPEs exhibit the lowest onset potential for the HER when compared to all of the carbon-based electrodes utilised herein. The bare GC electrode exhibited the largest HER onset potential, indicating that it is not a beneficial electrode for the HER.

It is worth noting that the current density obtained at each of the unmodified electrodes towards the HER and how this progressively alters during the course of the measurement. Although it is apparent that a higher potential is required to initiate the HER at the GC electrode (by *ca.*  $-0.3$  V in contrast to the alternative carbon based electrodes), the current density recorded at this electrode appears to surpass that of the alternative materials.

. Tafel analysis was performed on the Faradaic sections of the LSV plots which can be observed in Figure. 4.02.(A). Tafel analysis was performed on the data presented in Figure. 4.02.(A) where the corresponding analysis is presented in Figure. 4.02. (B), which yielded Tafel values of *ca.* 89.2, 64.4, 94.4 and 81.2  $\text{mV dec}^{-1}$  for the unmodified EPPG, GC, SPE and BDD electrodes respectively. Using the above values for the unmodified electrodes, interpretation of the Tafel slopes reveals that the adsorption Volmer step is likely rate limiting for the SPE and EPPG electrodes. The discharge Heyrovsky step is predicted to be the rate limiting step at the GC electrode.<sup>18-20</sup> In the case of BDD, Tafel analysis does not allow a definitive mechanism to be estimated.

#### 4.2.4. Electrochemical Activity of 2D-MoS<sub>2</sub> Towards the HER at an Assigned Mass of Electrode Coverage

---

This work next explores the use of 2D-MoS<sub>2</sub> nanosheet modified carbon based electrodes towards the HER. As detailed in the introduction, the aim of this paper is to tackle the current issue of finding a cheap, more abundant, electrocatalyst alternative to Pt for the HER.<sup>11, 18</sup> This chapter investigates the potential current state

of the art (2D-MoS<sub>2</sub> nanosheets) and compare this to the benchmarking experiments with the aim of revealing valuable insights. First, the range of carbon based electrodes utilised above (namely GC, BDD, EPPG and SPEs) are modified with different percentage mass coverages of the 2D-MoS<sub>2</sub> nanosheets. Note that using various underlying support materials is seldom seen in the current literature and thus it is important that such control experiments are explored and reported for the first time within this thesis manuscript.

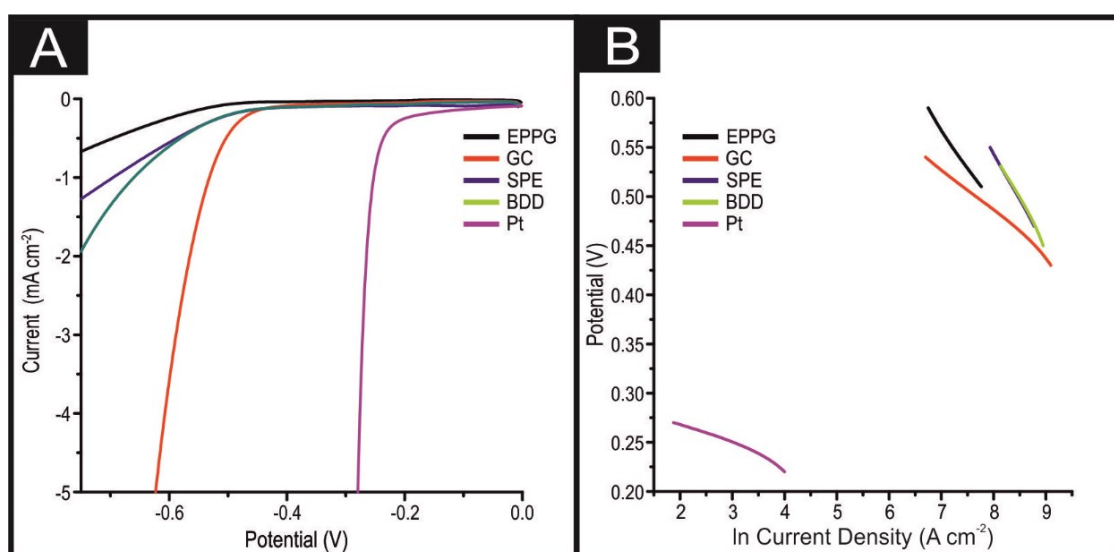


**Figure. 4.03.** (A) LSV of 1267 ng cm<sup>-2</sup> modified EPPG, GC, SPE, BDD electrodes and an unmodified Pt electrode showing the onset of the HER. In all cases, scan rate: 25 mVs<sup>-1</sup> (vs. SCE). Solution composition: 0.5 M H<sub>2</sub>SO<sub>4</sub>. (B) Tafel analysis; potential vs. natural log (ln) of current density for Faradaic section of the LSV presented in (A).

Inspection of Figure. 4.03.(A) reveals that using a 1267 ng cm<sup>-2</sup> modification of 2D-MoS<sub>2</sub> nanosheets results in a lowering of the potential required for onset of the HER and is accompanied by an increase in the observed current density, signifying an improved electrochemical response at each of the underlying electrode substrates utilised. Specifically, the HER onset potential was lowered to *ca.* -0.45, -0.48, -0.44 and -0.45 V for EPPG, GC, SPE, and BDD electrodes, respectively. Clearly, these

newly obtained values are significantly closer to the reported value using a Pt electrode (*ca.*  $-0.25$  V) than the initial values reported above at the unmodified carbon based electrodes. This implies that the 2D-MoS<sub>2</sub> nanosheets are effective electrocatalysts for the HER.

Tafel analysis was performed on the modified LSV profiles. Tafel slope values of *ca.* 74.7, 41.4, 90.0, and 90.9 mV dec<sup>-1</sup> were estimated at the EPPG, GC, SPE and BDD electrodes respectively (shown in Figure. 4.03(B)). Comparison of the Tafel values suggests that modification of the support electrodes with 2D-MoS<sub>2</sub> nanosheets does not cause a significant alteration in the mechanism or indeed the Faradic current density of the HER.<sup>69</sup> This however, is not the case when utilising the GC electrode, which exhibited a reasonable increase in current density resulting in the ‘discharge Heyrovsky’ step more probably becoming the rate limiting step. This implies that modification with the 2D-MoS<sub>2</sub> nanosheets allows for increased and sufficient H<sup>+</sup> adsorption, thus in turn catalysing the HER process.

In terms of analysing the current densities obtained, deposition of the 2D-MoS<sub>2</sub> nanosheets at a coverage of 1266.7 ng cm<sup>-2</sup> induces higher exchange current densities when compared to the unmodified alternative. It is probably that this results from the early onset of the HER (*i.e.* the decreased over-potential) and is not directly due to an overall increased reaction rate at the modified SPE and BDD electrodes, given that comparison is based on analysis at specific potentials. For the GC and EPPG electrodes there was an increase in the current density, which is due not only to the earlier HER onset potential, but also an increased current density slope. This is likely a result of the structure of MoS<sub>2</sub> on these electrodes having a high number of exposed active edge sites allowing for a greater amount of H<sup>+</sup> adsorption.

#### 4.2.5. Coverage of the Electrodes at Varying Masses of 2D-MoS<sub>2</sub>

The experimental data discussed above considers the use of 1267 ng cm<sup>-2</sup> (2D-MoS<sub>2</sub> nanosheet) modified electrodes. This work next considers explores the effects of different mass coverages of 2D-MoS<sub>2</sub> nanosheets on a given electrode.

In order to ascertain the level of 2D-MoS<sub>2</sub> coverage and relate this to the observed voltammetry, this work first investigates the respective Raman properties of the modified electrodes. Figure. 4.04. depicts the effect that larger deposition quantities of 2D-MoS<sub>2</sub> onto a SPE has upon the recorded Raman spectroscopy, where the evolution of the two characteristic peaks is evident and is discussed in more detail below.

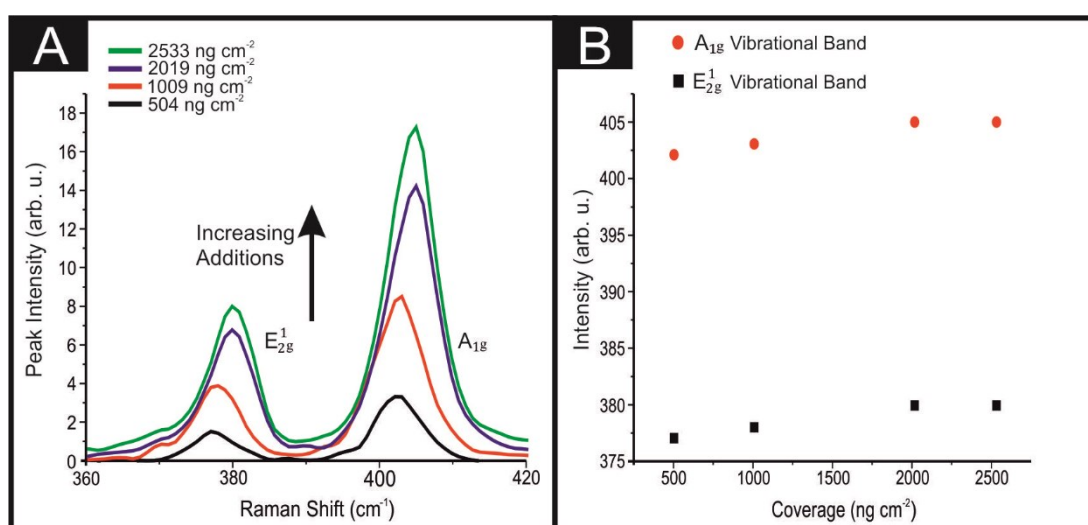


**Figure. 4.04.** (A) Raman Spectra peak intensity and position for 504 (black), 1009 (red), 2019 (blue) and 2533 (green) ng cm<sup>-2</sup> 2D-MoS<sub>2</sub> nanosheet modifications on SPEs. (B) Depicts 2D-MoS<sub>2</sub> nanosheet coverage plotted against Raman peak intensity for E<sub>2g</sub><sup>1</sup> (black) and A<sub>1g</sub> (red) vibrational bands, showing a constant peak distance of 24.7 cm<sup>-1</sup> at all coverages.

This work firstly analyses the effect of coverage on the electrode surface using Raman mapping and a SPE as the underlying support material (as a representative model). Through comparison of the underlying graphite peak area at ca. 1550 cm<sup>-1</sup>

against the area of the 2D-MoS<sub>2</sub> Raman peaks at *ca.* 380 and 405 cm<sup>-1</sup>, the surface area coverage of the electrode was investigated. It is evident that increasing the mass deposition of 2D-MoS<sub>2</sub> on the SPE surface results in an increased intensity in the respective assigned Raman peaks (see Figure. 4.05). Raman maps are presented in Figure. 4.06 which concur with the previous inference and show that with increased mass deposition a thicker (largely uniform) layered coverage is achieved across the entire electrode surface.

Through analysis of the respective Raman maps depicted in Figures 4.05., it is likely that the deposition of  $504 \text{ ng cm}^{-2}$  2D-MoS<sub>2</sub> nanosheets results in the complete coverage of the underlying SPE support material (which has a surface area of  $0.0707 \text{ cm}^2$ ). With each additional modification this layer of deposited MoS<sub>2</sub> will thicken (see Figure 4.05).

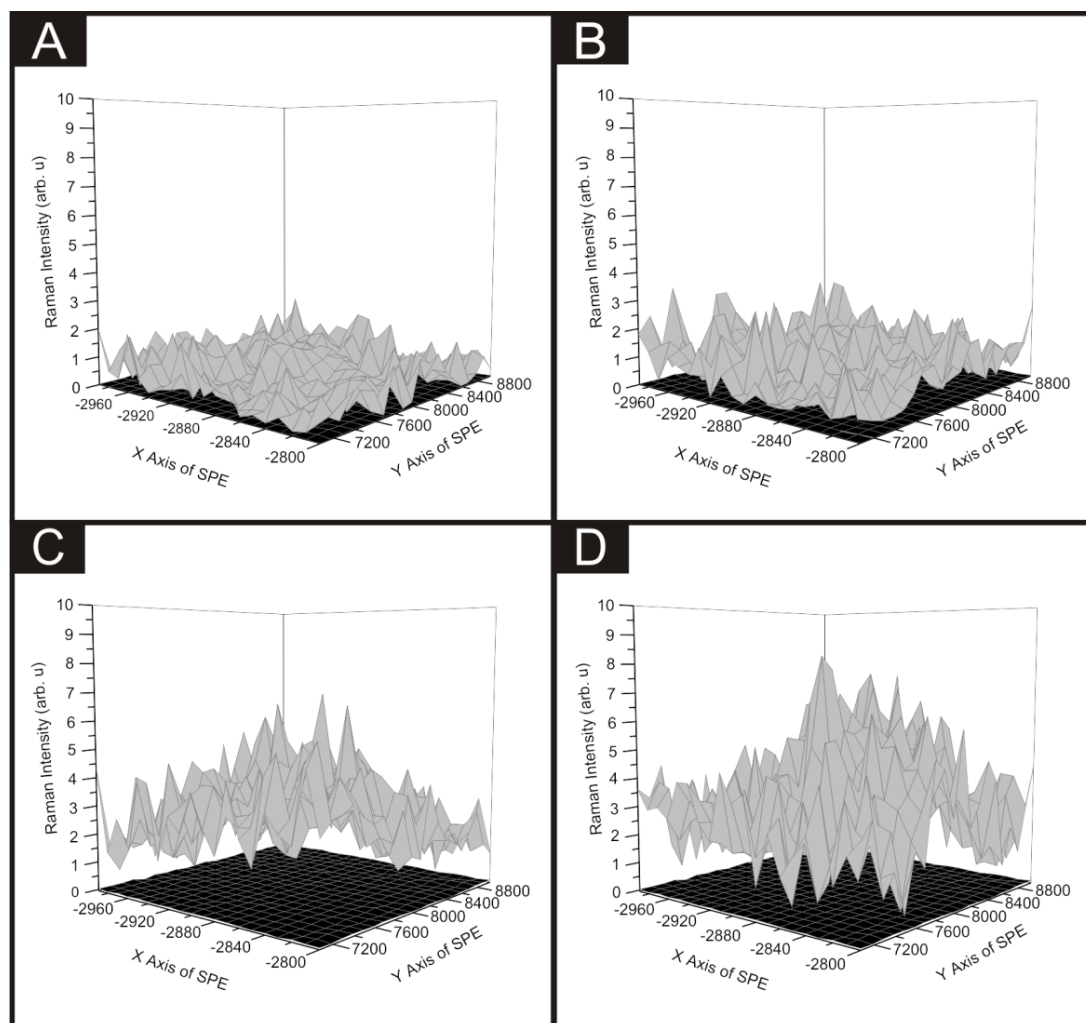


**Figure. 4.05.** Raman maps of SPE surface, each point showing the intensity ratio between the sum of the characteristic MoS<sub>2</sub> peak areas ( $380$  and  $405 \text{ cm}^{-1}$ ) against the area of the underlying graphite peak ( $1550 \text{ cm}^{-1}$ ). Using varying surface coverages of the 2D-MoS<sub>2</sub> nanosheets;  $504$  (A),  $1009$  (B),  $2019$  (C) and  $2533$  (D)  $\text{ng cm}^{-2}$ . The grey maps are the modified electrodes and the black map in each represents an unmodified electrode surface.

It is possible to determine the stacking number by comparison of  $E_{2g}^1$  and  $A_{1g}$  vibrational bands (VB) as the observed Raman spectrum evolves with the number of layers present. The  $E_{2g}^1$  VB results (at *ca.* 382  $\text{cm}^{-2}$ ) due to the opposite vibration of two S atoms in respect to a Mo atom, whereas the  $A_{1g}$  peak (at *ca.* 407  $\text{cm}^{-2}$ ) represents the S atoms vibrating in opposite directions and out of plane.<sup>89, 90</sup> Literature suggests that as  $\text{MoS}_2$  moves from single layer to bulk, the  $E_{2g}^1$  VB downshifts from 384 to 382  $\text{cm}^{-2}$ , whilst  $A_{1g}$  VB shifts upwards from 403 to 408  $\text{cm}^{-1}$ , where a separation of *ca.* 19  $\text{cm}^{-1}$  between the VBs is indicative of single layer  $\text{MoS}_2$  and a value of *ca.* 25  $\text{cm}^{-1}$  represents the bulk material.<sup>90 33, 64</sup> This observed increase in the Raman shift of the  $E_{2g}^1$  VB with greater mass additions from *ca.* 377 to 380  $\text{cm}^{-1}$ , (see Figure. 4.04.(A)). However the response observed herein may result from the specific morphology and stacking structures of the 2D- $\text{MoS}_2$  on the underlying support material given that previous studies have reported a similar shift relating to the  $E_{2g}^1$  band and attributed this to uniaxial strain or heterostructure stacking.<sup>143</sup> Interestingly, analysis of the  $A_{1g}$  peak corresponds to the predicted theorem for a transition from single-layer to multi-layer 2D- $\text{MoS}_2$  nanosheets with an increasing Raman shift from *ca.* 402 to 405  $\text{cm}^{-1}$ .<sup>64, 89</sup>

Furthermore, when considering the separation of the two VBs (given that this value is also indicative of the number of  $\text{MoS}_2$  layers present), the shift in the difference of the VB positions between  $A_{1g}$  and  $E_{2g}^1$  gives a consistent value of 24.7  $\text{cm}^{-1}$  with increasing coverages, indicating that +4 layers (*i.e.* bulk)  $\text{MoS}_2$  is present at all four mass coverages utilised herein (see Figure. 4.04(B)). Consideration of the above factors in conjunction with the independent lateral grain size calculations (UV-VIS) indicates that the structural model of the 2D- $\text{MoS}_2$  nanosheets utilised herein is likely that of re-assembly, with the few-layer nanosheets forming bulk  $\text{MoS}_2$  upon

deposition onto the electrode surface. Further work on whether the morphology of a SPEs surface causes uniaxial strain and/or heterostructure stacking of the 2D-MoS<sub>2</sub> nanosheets would be of great interest. Note that confirmatory tests were performed in which the aliquots deposited above were immobilised onto an alternative silicon wafer support in order to overcome potential issues with the underlying surface. Such control experiments (data not shown) exhibited the same separation values as identified above (*ca.* 25.1 cm<sup>-1</sup>) between the two VBs and thus confirms that the 2D-MoS<sub>2</sub> nanosheets likely form bulk MoS<sub>2</sub> once deposited/immobilised onto a support surface. It can be predicted that further additions of the material results in the formation of thicker or rougher ‘bulk’ layers.

#### 4.2.6. Electrochemical Activity of 2D-MoS<sub>2</sub> towards the HER at Varying Masses of Electrode Coverage

---

Returning to the analysis of the HER, the effects of different mass deposition on the different electrode surfaces was next explored. Using a fixed potential (−0.75 V) at which each electrode exhibits an observable current, the current densities relating to the HER were recorded. It is evident through inspection of Figure. 4.06. that a trend of increased current density (corresponding to increased 2D-MoS<sub>2</sub> nanosheet coverage (ng cm<sup>-2</sup>)) is subsequently followed by a decrease in current density and/or plateauing effect.

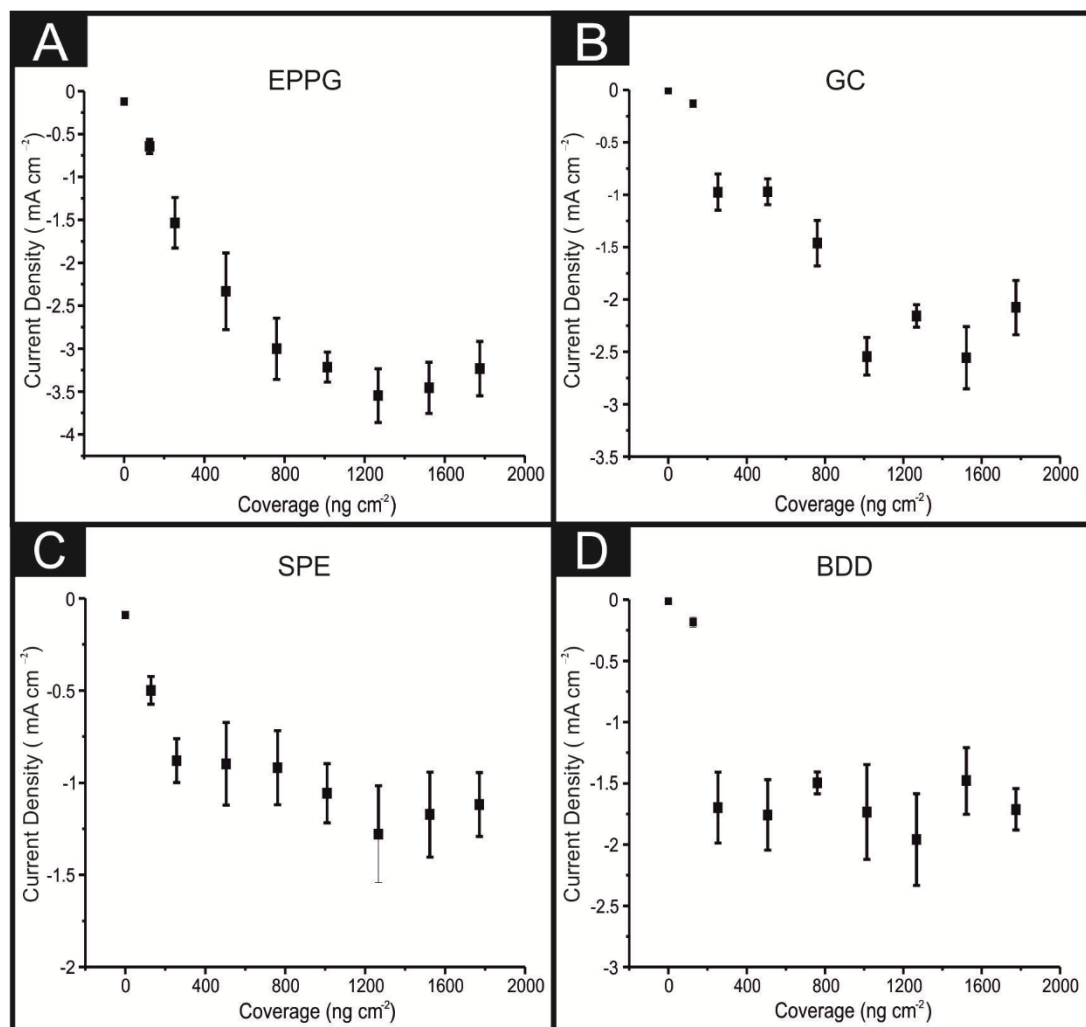


**Figure 4.06.** Current density values taken at  $-0.75$  V from LSV from 0, 128.6, 252, 504, 762, 1009, 1267, 1524 and 1771 ng cm<sup>-2</sup> 2D-MoS<sub>2</sub> nanosheets immobilised upon: (A) EPPG, (B) GC, (C) SPE (D) BDD. Each graph showing the plateauing effect of current density when a critical coverage of the 2D-MoS<sub>2</sub> nanosheets is deposited onto the electrodes surface. Error bars are the average and standard deviation of 3 replicates.

This effect is apparent upon modification of each of the four underlying electrode materials studied with the material of interest. Over the modification range tested, the maximum/optimal current density was found to correlate to a 2D-MoS<sub>2</sub> nanosheet coverage of *ca.* 1014.4, 1266.7, 1266.7, 1266.7 ng cm<sup>-2</sup> for the GC, EPPG,

SPE and BDD electrodes, respectively. Tafel analysis on these optimal mass modifications reveals values of *ca.* 40, 74, 92 and 90.9 mV dec<sup>-1</sup>. GC and BDD, when modified with the 2D-MoS<sub>2</sub> nanosheets, demonstrate a fast discharge mechanism, with H<sup>+</sup> adsorption no longer the rate-limiting step.<sup>5</sup> Through analysis of the values reported above it is clear that, of the four electrodes modified, electrodes with slower kinetics (such as the GC and BDD) exhibit a favourable electrocatalytic effect when modified with 2D-MoS<sub>2</sub> nanosheets towards the HER. Contrary to this, the EPPG, which possesses faster underlying rate kinetics, exhibited only a slight change towards an altered reaction mechanism and further in the case of the SPE there was no observable change.

#### 4.2.7.1. Assessment of the Intrinsic Electrochemical Activity of 2D-MoS<sub>2</sub> Nanosheets

---

An array of approaches are employed to study the intrinsic catalytic activity of 2D-MoS<sub>2</sub> nanosheets within the literature. In order to deduce how the observable catalytic activity alters with changes in the mass of 2D-MoS<sub>2</sub> nanosheet modification, this work employs two commonly used techniques below: the assessment of catalytic turn over frequency (ToF) and the number of active sites present on the surface of the electrode.<sup>95, 130</sup>

#### 4.2.7.2. Roughness Factor Calculation

---

In order to use the turn over frequency (ToF) formula described by Benck, *et al.*<sup>130</sup> there is a prerequisite step, whereby roughness factors of the modified SPE surfaces have to be calculated; see Figure 4.07. This is commonly done *via* analysis of the electrode surfaces by white light profilometry (WLP), or a double layer capacitance

technique described later. WLP topography for SPE's modified with (A) 252, (B) 1009 and (C) 2019  $\text{ng cm}^{-2}$  of 2D-MoS<sub>2</sub> nanosheets can be observed in Figure 4.07.

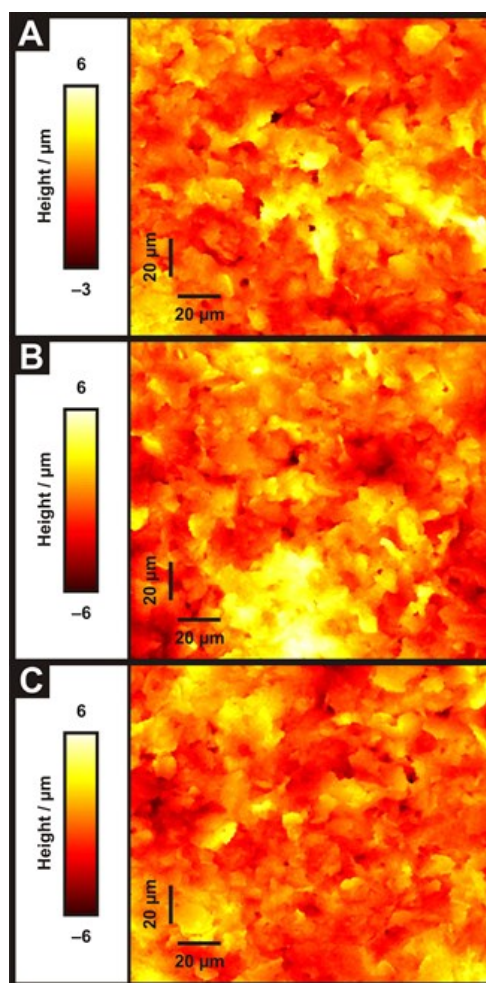


**Figure 4.07.** White light profilometry surface topography maps of SPE's modified with (A) 252, (B) 1009 and (C) 2019  $\text{ng cm}^{-2}$  of 2D-MoS<sub>2</sub> nanosheets. It is evident that the surface roughness remains relatively constant with the increasing 2D-MoS<sub>2</sub> nanosheet modification.

These were calculated using a ZeGage 3D Optical Surface Profiler, produced by Zygo. The surface topography of the 2D-MoS<sub>2</sub> nanosheets was measured once deposited onto the SPEs, and these measurements were subsequently used to provide a value for the roughness factor ( $R_F$ ) used in this work. The surface profile maps shown in Figure 4.08 were analysed using a Matlab script based on the following equation:

$$R_F = \frac{\sum_{k=0}^{M-2} \sum_{i=0}^{N-2} A_{kl}}{(M-1)(N-1)\delta x \delta y} \quad (4.5)$$

where  $M$  and  $N$  are the total number of points in the  $x$  and  $y$  directions, respectively,  $x$  and  $y$  are the distances between the points in the  $x$  and  $y$  directions, and where:

$$A_{kl} = \frac{1}{4} \left( \sqrt{\delta y^2 + (z(x_k, y_i) - z(x_k, y_{i+1}))^2} + \sqrt{\delta y^2 + (z(x_{k+1}, y_i) - z(x_{k+1}, y_{i+1}))^2} \right) + \left( \sqrt{\delta x^2 + (z(x_k, y_i) - z(x_{k+1}, y_i))^2} + \sqrt{\delta y^2 + (z(x_k, y_{i+1}) - z(x_{k+1}, y_{i+1}))^2} \right) \quad (4.6)$$

(Equations 4.5 and 4.6 were deduced by David A. G. Sawtell, Faculty of Science and Engineering, School of Science and the Environment, Division of Chemistry and Environmental Science, Manchester Metropolitan University, Chester Street, Manchester M1 5GD, UK), with  $z$  being the height above the surface at a coordinate  $(x, y)$ . Although similar to the surface area ratio ( $S_{dr}$ ) typically used for surface topology measurements,<sup>144</sup> the equation has been modified to provide the ratio of interfacial area to the area of the projected horizontal plane, rather than the increment of the interfacial surface area to the projected horizontal plane. This modification has been made as the roughness factor is described as the ratio of the catalyst active surface area to the substrate geometric surface area.<sup>130</sup> The roughness factors were consistently found to occur in the range 1.918 to 1.934, even for the three SPEs modified with 252, 1009 and 2019 ng cm<sup>-2</sup> of 2D-MoS<sub>2</sub> nanosheets, respectively. This shows that the WLP probes only the outside/upper layer of the exposed 2D nanosheets and is insensitive to the surface coverage/mass of material immobilised and does not provide us with the *electrochemically active area*. Consequentially this approach will limit the interpretation of the ToF.

As an alternative to WLP, a method proposed by Shin *et al.*<sup>95</sup> for the determination of the double layer capacitance can be used to calculate the active

surface area of the 2D-MoS<sub>2</sub> nanosheet modified SPE electrode. Using an unmodified SPE and SPEs modified with 252, 1009 and 2019 ng cm<sup>-2</sup> 2D-MoS<sub>2</sub> nanosheets, cyclic voltammetry was performed using a potential range of 0.01 to 0.11 V, which is in the non-Faradaic window, at each of the following scan rates 20, 40, 60, 80, 100 mVs<sup>-1</sup>. The potential range used is presumed to have no Faradaic processes occurring, therefore cathodic and anodic current densities are associated with charging of the electrical double layer (see Figure 4.08.).

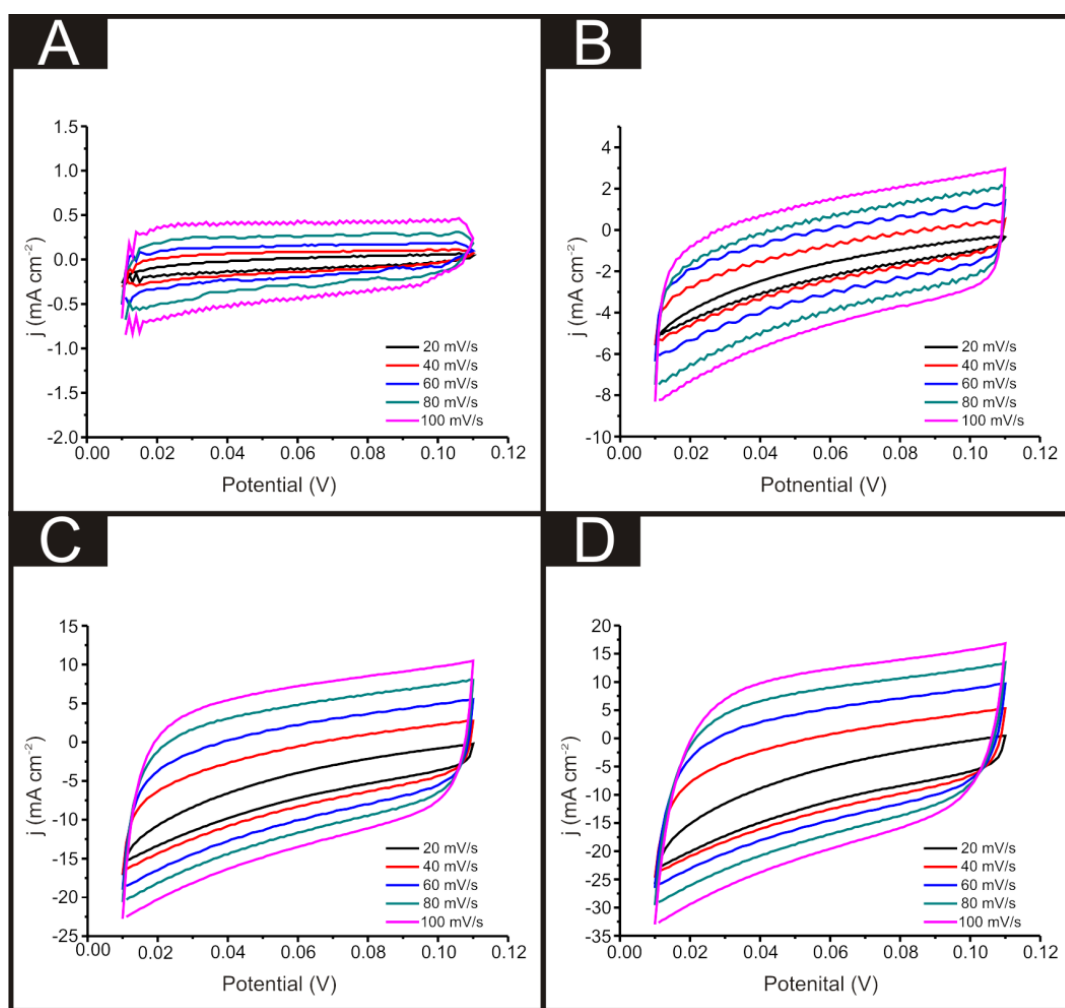


**Figure 4.08.** CVs recorded in 0.5 M H<sub>2</sub>SO<sub>4</sub> solution for SPE's with varying amounts of 2D-MoS<sub>2</sub> nanosheet modification; (A) 0, (B) 252, (C) 1009, (D) 2019 ng cm<sup>-2</sup>.

Figure. 4.09. shows the difference between the anodic and cathodic current at 0.06 V *versus* the corresponding scan rate. The slope of each set of points in Figure 4.09. being proportional to a doubling of the double layer capacitance. The double layer capacitance values determined are 8.7, 68, 218, 322  $\mu\text{F cm}^{-2}$  for SPEs modified with 0, 252, 1009 and 2019  $\text{ng cm}^{-2}$  2D-MoS<sub>2</sub> nanosheets, respectively. The 7.8 $\times$  increase in double layer capacitance from unmodified to 252  $\text{ng cm}^{-2}$  2D-MoS<sub>2</sub> nanosheet modification reveals that, post modification, there is a significant adherence of 2D-MoS<sub>2</sub> nanosheets upon the SPE electrode surface. There is a further 3.2 $\times$  and 4.7 $\times$  increase in the capacitance value from that of 252 to 1009 and 2019  $\text{ng cm}^{-2}$  2D-MoS<sub>2</sub> nanosheets modifications, respectively. It is inferred that this is associated with a thickening of the 2D-MoS<sub>2</sub> nanosheets deposited. The disparity between the increase in capacitance and the increase in  $\text{ng cm}^{-2}$  2D-MoS<sub>2</sub> nanosheets is of interest and further study on the matter is required.

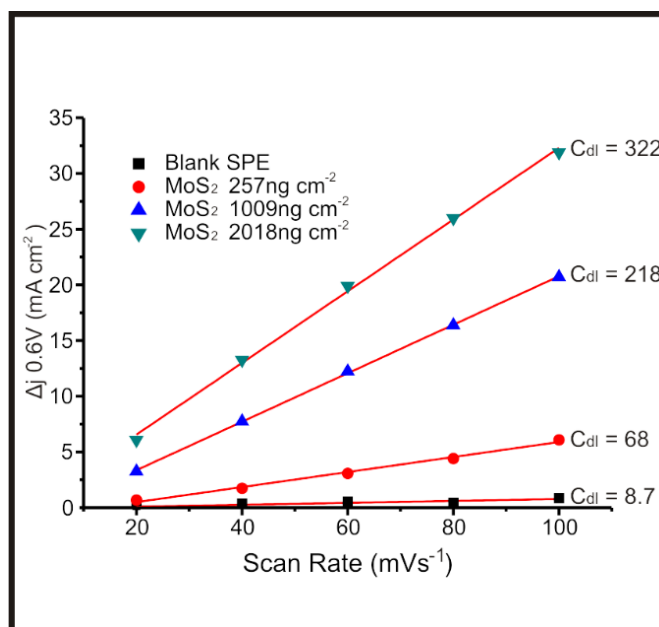


**Figure. 4.09.** The difference in anodic and cathodic current density taken at +0.06 V *versus* scan rate ( $\text{mVs}^{-1}$  vs. SCE). The slope of the linear regression indicates the value of double layer capacitance ( $C_{dl}$ ).

### 4.2.7.3. Turn over Frequency Calculation

---

In order to evaluate how the intrinsic catalytic activity of the 2D-MoS<sub>2</sub> nanosheets alters with varying modification on a ‘per active site’ basis, the ToF was deduced using a method reported previously by Benck, *et al.*<sup>130</sup> Their derivation is repeated here for clarity using values associated with the 252 ng cm<sup>-2</sup> modified SPE.<sup>130, 145</sup> In this calculation it is assumed that the surface of the 2D-MoS<sub>2</sub> nanosheets is atomically flat (although the true modification will have a finite roughness).<sup>130</sup> Taking the sulfur to sulfur bond distance to be 3.15 Å which corresponds to an area of 4.296 Å<sup>2</sup>/S atom<sup>130, 146</sup> which can be used to calculate the surface area occupied by each MoS<sub>2</sub>:

$$4.296 \frac{\text{Å}^2}{\text{S atom}} * \frac{2 \text{ S atom}}{1 \text{ MoS}_2} = 8.593 \frac{\text{Å}^2}{\text{MoS}_2} \quad (4.7)$$

Using the derived area for a MoS<sub>2</sub> molecule (corresponding to the number of surface sites for a flat standard) it is possible to determine the number of MoS<sub>2</sub> molecules per cm<sup>2</sup> geometric area:

$$\frac{1 \text{ MoS}_2}{8.593 \text{ Å}^2} * \frac{10^{16} \text{ Å}^2}{0.0707 \text{ cm}^2} = 1.646 * 10^{16} \frac{\text{MoS}_2}{\text{cm}^2} \quad (4.8)$$

The number of electrochemically accessible surface sites can be determined from the following:

$$\frac{\# \text{ Surface Sites (Catalyst)}}{\text{cm}^2 \text{ geometric area}} = \frac{\# \text{ Surface Sites (Flat Standard)}}{\text{cm}^2 \text{ geometric area}} * R_F \quad (4.9)$$

It is also essential to accurately determine the roughness factor ( $R_F$ ) for each modified electrode surface, which was performed using white light profilometry (WLP) (See Figure. 4.08.), as is common within the literature.

The described WLP technique yielded  $R_F$  values which represent the entire surface area of the electrode, rather than the electroactive area (see later). In the case

of the 252 ng cm<sup>-2</sup> modified SPE, the number of surface sites per cm<sup>2</sup> corresponds to 3.16 × 10<sup>16</sup> surface sites per cm<sup>2</sup>. The following allows the ToF on a per-site basis to be determined:

$$TOF \text{ per site} = \frac{\# \text{ Total Hydrogen Turn Overs / cm}^2 \text{ geometric area}}{\# \text{ Surface Sites (Catalyst) / cm}^2 \text{ geometric area}} \quad (4.10)$$

Taking the value of current density (mA cm<sup>-2</sup>) at the potential of -0.75 V (at a 100 mVs<sup>-1</sup> scan rate) and using the  $R_F$  calculated via WLP, per-site the ToF can be deduced from the following:

$$\left( j \frac{\text{mA}}{\text{cm}^2} \right) \left( \frac{1 \text{ A}}{1000 \text{ mA}} \right) \left( \frac{1 \text{ C/s}}{1 \text{ A}} \right) \left( \frac{1 \text{ mol } e^-}{96,485.3 \text{ C}} \right) \left( \frac{1 \text{ mol } H_2}{2 \text{ mol } e^-} \right) \left( \frac{6.02214 \times 10^{23}}{1 \text{ mol } H_2} \right) = 2.59 * 10^{15} \frac{H_2/s}{\text{cm}^2} \text{ per } \frac{\text{mA}}{\text{cm}^2} \quad (4.11)$$

Using Equation 4.12 and value derived from Equation 4.11, it is possible to determine a value for the ToF:

$$\left( 2.59 * 10^{15} \frac{H_2/s}{\text{cm}^2} \right) \left( \frac{\text{mA}}{\text{cm}^2} \right) \left( \frac{1 \text{ cm}^2}{3.16 * 10^{16} \text{ surface sites}} \right) = 0.81 \frac{H_2/s}{\text{surface sites}} \quad (4.12)$$

At the chosen potential (-0.75 V) the current densities were found to correspond to 0.83, 1.16 and 1.17 mA cm<sup>-2</sup> for SPEs (SPEs used as representative example of the carbon based electrodes utilised) modified with 252, 1009 and 2019 ng cm<sup>-2</sup> of 2D-MoS<sub>2</sub> nanosheets. The  $R_F$  values calculated *via* the WLP method (which provides the topography of the uppermost surface) were found to correspond to 1.918, 1.934 and 1.924, respectively. Using these values the ToF values deduced from the above equations were found to correspond to 0.81, 1.14 and 1.15  $\frac{H_2/S}{\text{Surface Site}}$ . The stability of the WLP  $R_F$  values across the range of modifications results in relatively little variation of the ToF values obtained. Benck, *et al.*<sup>130</sup> suggest that the upper and lower possible ToF could be one order of magnitude greater or less than the given value. If the chosen

potential is altered to  $-1.5$  V, the current densities at this potential are found to be 4.25, 4.43 and 4.33 mA cm<sup>-2</sup> for the 252, 1009 and 2019 ng cm<sup>-2</sup> 2D-MoS<sub>2</sub> nanosheets modified SPEs, respectively. Using the same technique and the WLP  $R_F$  values above, however replacing the current densities at  $-0.75$  V for those at  $-1.5$  V, the ToF values are 0.59, 0.61 and 0.6  $\frac{H_2/S}{\text{Surface Site}}$  for the 252, 1009 and 2019 ng cm<sup>-2</sup> 2D-MoS<sub>2</sub> nanosheets modified SPEs, respectively. Clearly, alerting the potential at which the current densities are recorded has a significant affect upon the ToF recorded.

As mentioned earlier in order to deduce  $R_F$  values which are representative of the *true* electroactive area of an electrode, a double layer capacitance technique can be employed (see roughness factor calculation above). Note that the double layer capacitance technique is preferential to the WLP technique as it describes the true electroactive surface area of the electrode including accessible pores and the thickness of multiple layers deposited, whereas WLP is limited in that it bases its calculated value only on a scan of the topography of the uppermost surface in question; simply, the WLP only probes the outermost layer and cannot determine a relatively thick layer from a thin layer. The double layer capacitance technique for determining  $R_F$  is reported above.

Taking the current density values corresponding to a  $-0.75$  V potential and replacing the WLP  $R_F$  values for 1.0, 3.3 and 4.8, which are the  $R_F$  values calculated *via* double layer capacitance for SPEs modified with 252, 1009 and 2019 ng cm<sup>-2</sup> of 2D-MoS<sub>2</sub> nanosheets, the ToF was found to correspond to 1.58, 0.6 and 0.46  $\frac{H_2/S}{\text{Surface Site}}$ . The values estimated for the ToF herein are in rough agreement with the range of ToF values Xie, *et al.*<sup>139</sup> states should be expected for various types of MoS<sub>2</sub> structures. It is evident that, as a result of increasing the mass of 2D-MoS<sub>2</sub> nanosheets

deposited onto an SPE, there is a resulting decrease in the ToF ( $\frac{H_2/s}{\text{Surface Site}}$ ). This is possibly the result of larger masses of 2D-MoS<sub>2</sub> nanosheets, once deposited, forming a MoS<sub>2</sub> structure whereby there is increased shielding of active edge sites by inactive basal planes.<sup>69, 130</sup> Again, if the current densities are altered to those corresponding to a – 1.5 V potential, whilst using the same technique and double layer capacitance  $R_F$  values, above, the ToF values deduced are 1.14, 0.37 and 0.24  $\frac{H_2/s}{\text{Surface Site}}$  for the 252, 1009 and 2019 ng cm<sup>-2</sup> 2D-MoS<sub>2</sub> nanosheets modified SPEs, respectively. Of note is the significant affect that altering the potential at which the current densities are measured has upon the determined ToF values. This ability to manipulate the ToF value deduced makes it essential to create an industry standard for what potentials should be used when dealing with ToF calculations. This would allow for more ready comparison between different studies involving ToF.

As previously stated, the double layer capacitance technique provides a true electrocatalytic surface area of the given electrode, whereas the WLP technique provides a scan of topography of the uppermost surface. It can therefore be assumed that the  $R_F$  values deduced *via* double layer capacitance offer more accurate ToF values.

#### 4.2.7.4. Number of Electrocatalytic Active Sites

---

Determining the number of active sites present on the surface of an electrode offers valuable insight into its catalytic properties. Shin and co-workers<sup>95</sup> have shown that it is possible to derive the number of 2D-MoS<sub>2</sub> nanosheet active sites ( $N$ ) present on the surface of the catalyst using the following equation:

$$N = R_F(N_A d / M_f)^{2/3} \quad (4.13)$$

where  $N_A$  is Avogadro's number,  $d$  is the film density (*ca.*  $2.35 \times 10^{-4} \text{ g cm}^{-3}$ , which was derived *via* the use of WLP to observe the step height, in this case  $21.9 \text{ }\mu\text{m}$ , between the bare electrode surface and a mass of  $514 \text{ ng cm}^{-2}$  2D-MoS<sub>2</sub> nanosheets deposited),  $M_f$  is the molecular weight of MoS<sub>2</sub>, and  $R_F$  is the roughness factor, which in this case is defined as the ratio of the real surface area to the geometric area. The geometric area (and the electrochemically active area) of the electrode surface can vary significantly due to the surface roughness and porosity of the sample. In this case, the  $R_F$  was derived using double layer capacitance as it is linearly proportional to catalytic surface area (see roughness factor calculation above).<sup>147</sup> The double layer capacitance values determined (*via* cyclic voltammetry, see Figure. 2.08) are 8.7, 68, 218, 322  $\mu\text{F cm}^{-2}$  for SPEs modified with 0, 252, 1009 and 2019  $\text{ng cm}^{-2}$  2D-MoS<sub>2</sub> nanosheets, respectively. As a benchmark, the double layer capacitance value for amorphous MoS<sub>2</sub> is reported to be  $66.7 \mu\text{F cm}^{-2}$ .<sup>129</sup>  $R_F$  values for SPEs modified with 252, 1009 and 2019  $\text{ng cm}^{-2}$  of 2D-MoS<sub>2</sub> nanosheets were estimated to be *ca.* 1.02, 3.26 and 4.83, respectively. The  $R_F$  values derived using double layer capacitance show an increment with greater masses of 2D-MoS<sub>2</sub> nanosheet modification.  $R_F$  values for BDD, EPPG, GC and SPE post modification are presented in Table 4.2.

**Table 4.2.** The determined roughness factor ( $R_F$ ) values and the number of active sites (per  $\text{cm}^2$ ) for BDD, EPPG, GC and SPE all of which had been modified with 0, 252, 1009, 2019  $\text{ng cm}^{-2}$  2D-MoS<sub>2</sub> nanosheets. Values determined using double layer capacitance obtained via cyclic voltammetry between the potential range of 0.01V and 0.1V.

Electrode	MoS <sub>2</sub> Modification ( $\text{ng cm}^{-2}$ )	Roughness Factor	Number of active sites
<b>BDD</b>	2019	2.2	$2.01 \times 10^{12}$
	1009	1.5	$1.38 \times 10^{11}$
	252	0.3	$3.03 \times 10^{11}$
<b>EPPG</b>	2019	7.7	$7.05 \times 10^{12}$
	1009	5.5	$5.05 \times 10^{12}$
	252	4.2	$3.84 \times 10^{12}$
<b>GC</b>	2019	2.6	$2.35 \times 10^{12}$
	1009	2.1	$1.95 \times 10^{12}$
	252	1.0	$8.95 \times 10^{11}$
<b>SPE</b>	2019	4.8	$4.43 \times 10^{12}$
	1009	3.3	$3.00 \times 10^{12}$
	252	1.0	$9.36 \times 10^{11}$

The number of active sites per  $\text{cm}^2$  are summarised in Table 4.2. where there is a (positive) linear correlation between number of active sites and mass of 2D-MoS<sub>2</sub> deposited. It can therefore be asserted that there is a physicochemical change within the structure of the 2D-MoS<sub>2</sub> present upon the surface of the electrode, which leads to the exposure of less active sites per additional  $\text{ng cm}^{-2}$  modification after a certain ‘critical coverage’ (this is also evident through inspection of Figure 4.06.), or no further increase in the number of the active sites accessible to the solution. It is clear that the number of active sites (and related HER performance) increase (improve) with the addition of larger quantities of 2D-MoS<sub>2</sub> onto the underlying electrode surface up to the point where the specified critical coverage is achieved.

#### 4.2.7.5. Critical coverage of 2D-MoS<sub>2</sub> Modification

---

It is evident that the increased mass deposition of 2D-MoS<sub>2</sub> nanosheets on a given electrode surface results in an improvement in the current passed, in addition to a lowered HER onset potential (improved electrochemical response). As is apparent from the above discussion (and inspection of Figure 4.06.), this increase in the catalytic performance of a given modified electrode material (which corresponds to the addition of 2D-MoS<sub>2</sub> nanosheets) reaches a plateau after which further additions of the target material do not result in an improved electrochemical performance. This ‘critical coverage’ of modification is likely due to the structure of the 2D-MoS<sub>2</sub> nanosheets altering to that of a bulk formation (see earlier), thereby exposing fewer edge sites, and thus inhibiting the beneficial electrochemical properties of single-, few-, quasi- MoS<sub>2</sub> nanosheets. Alternatively, this plateau could signify the mass (a critical coverage of *ca.* 1009 ng cm<sup>-2</sup> of the 2D-MoS<sub>2</sub> nanosheets) at which the structure of MoS<sub>2</sub> can no longer structurally support itself upon the electrode surface (becoming unstable), diminishing and detaching from the surface of the electrode, eliminating the catalytic advantages of further additions (such that in some cases the catalytic response begins to deteriorate). Similar observations have been reported for the case of graphene.<sup>148-151</sup> This could arise due to the disconnection of 2D-MoS<sub>2</sub> nanosheet layers during the course of the experiment (*i.e.* instability of the modified layer on the electrode surface due to the large quantity/mass present), which is brought about once such a ‘critical coverage’ is achieved.

The intra-repeatability of the modified and unmodified SPEs was tested ( $N = 3$ ). The % Relative Standard Deviation (% RSD) in the onset potential of the HER was found to be *ca.* 0.8, 1.4, 1.5, and 4.6 % for the 0 (unmodified), 252, 1009 and 2019 ng cm<sup>-2</sup> modified SPEs, respectively. It is clear that the % RSD increases with

greater modifications of the 2D-MoS<sub>2</sub>, probably a result of the factors stated above and potentially resulting in reduced catalytic effects. Furthermore, the % RSD in the current densities observed were found to be *ca.* 12.4, 13.5, 10.5, and 15.5 % at the 0 (unmodified), 252, 1009 and 1771 ng cm<sup>-2</sup> modified SPEs respectively. The high RSD values in this case are indicative of the structural instability of the deposited 2D-MoS<sub>2</sub> nanosheet film on the underlying electrode surface, which likely leads to delamination and thus high levels of variation within the effective surface area and currents passed. From the above inferences, this work suggests that the structural model of 2D-MoS<sub>2</sub> nanosheets is that of re-assembly, such that upon modification with increasing amounts of 2D-MoS<sub>2</sub> nanosheets, bulk layers of MoS<sub>2</sub> materialise upon the surface of the support electrodes.<sup>148, 150</sup>

Electrochemical impedance spectroscopy (EIS) was used to determine the impedance of the electrode system as coverage of 2D-MoS<sub>2</sub> nanosheets was increased, see Figure 4.10.<sup>70</sup> For a description of this technique see Chapter 2 page 49. It was observed that the charge transfer resistance ( $\Omega$ ) for all electrodes decreased after modification with 252 ng cm<sup>-2</sup> 2D-MoS<sub>2</sub> nanosheets and further decreased after modification with 1009.5 ng cm<sup>-2</sup>. Again a plateauing was observed in the response with increased coverage (for example after modification with 2019 ng cm<sup>-2</sup>). The  $\Omega$  values of the unmodified SPE ( $3.51 \times 10^5 \Omega$ ) reduced to  $1.69 \times 10^5 \Omega$  after 252 ng cm<sup>-2</sup> and then to  $3.27 \times 10^3 \Omega$  upon a 1009 ng cm<sup>-2</sup> 2D-MoS<sub>2</sub> nanosheet modification, after which the response plateaued, having an impedance value of  $3.21 \times 10^3 \Omega$  by modification with 2019 ng cm<sup>-2</sup>. The intrinsic error values for the aforementioned results were recorded as  $1.78 \times 10^{-4}$ ,  $1.73 \times 10^{-3}$ ,  $1.2 \times 10^{-2}$ , and  $1.21 \times 10^{-2} \Omega$  respectively, note these are errors within the potentiostats recording not relative standard deviation values.

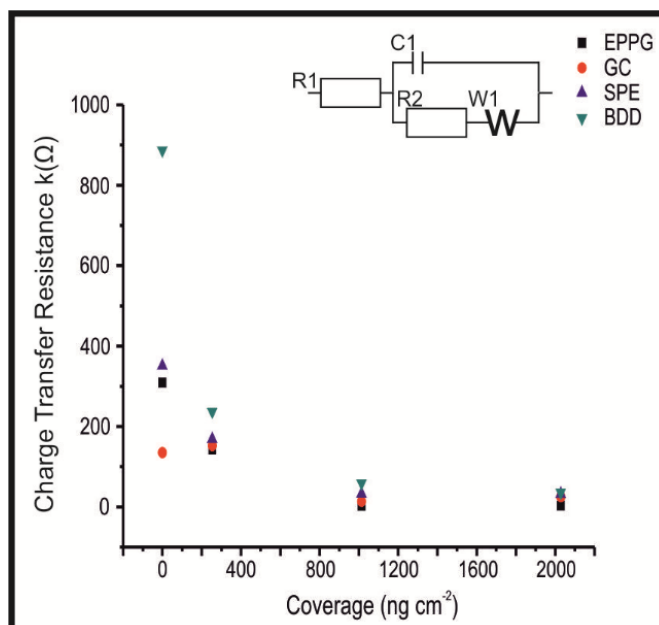


**Figure 4.10** An EIS study showing charge transfer resistance (ohm) values for EPPG, GC, SPE and BDD against 2D-MoS<sub>2</sub> nanosheet coverages of 0, 252, 1009 and 2019 ng cm<sup>-2</sup>. Increasing coverage leading to a decrease in EIS followed by a plateau. The EIS study was carried out in 0.5 M H<sub>2</sub>SO<sub>4</sub>, the frequency was from 0.1–100,000 Hz, and an amplitude of 10 mV (vs. SCE). Inset: circuit utilised within experiments.

This EIS supports the above inferences and indicates that the 2D-MoS<sub>2</sub> is an effective electrocatalyst with respect to the HER when deposited on a carbon electrode surface.

Finally, it is essential to assess the electrochemical stability of 2D-MoS<sub>2</sub> nanosheets as a catalyst for the HER and ORR when drop coated onto an electrode surface (following on from the reported % RSD values noted above). This is a practical consideration for real applications where durability and longevity are necessary.<sup>6, 34, 95</sup> SPEs were used as a representative example for the four carbon based electrodes used within this study. A 1000 cycle voltammetry scan from 0 to -0.8 V at 25 mVs<sup>-1</sup> was performed on SPEs modified with 252, 1009, 2019 ng cm<sup>-2</sup> of 2D-MoS<sub>2</sub> nanosheets. A decrease in the catalytic activity of each electrode was observed (see Figure. 4.11.).

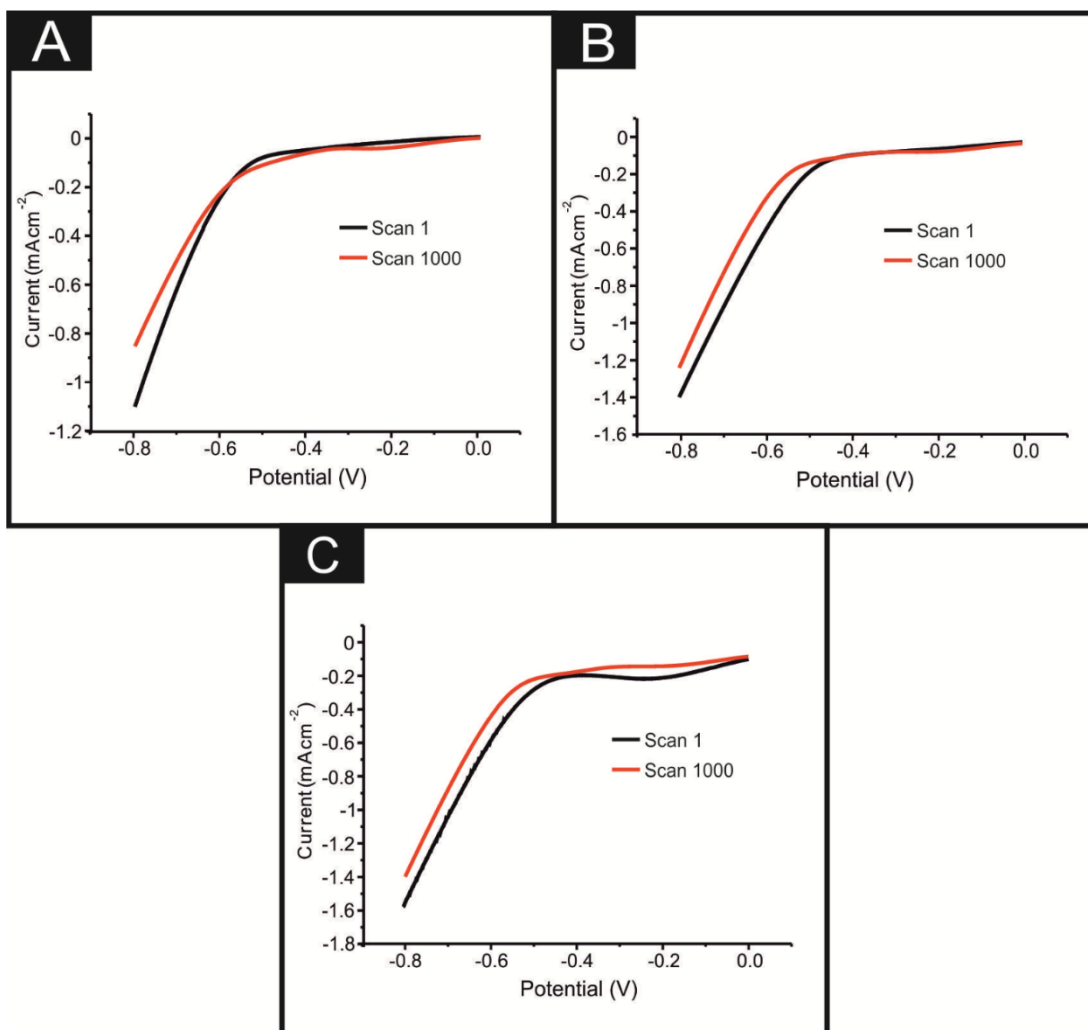


**Figure 4.11.** Stability studies using SPEs modified with (A) 252, (B) 1009 and (C) 2019  $\text{ng cm}^{-2}$  2D-MoS<sub>2</sub> nanosheets. Cyclic Voltammetry was performed between the potential range of 0 to  $-0.8$  V, repeated for 1000 cycles, these figures show the initial (black line) and 1000<sup>th</sup> (red line) scans.

At 0.6 V the decrease from the initial scan current was 6.8%, 32.3%, 26.9% for the SPEs modified with 252, 1009 and 2019  $\text{ng cm}^{-2}$ , respectively. The observed activity loss is significant especially for the 1009 and 2019  $\text{ng cm}^{-2}$  modified electrodes. According to Shin, *et al.*<sup>95</sup> high stability of amorphous MoS<sub>2</sub> is rarely reported with the decrease in activity being associated with either: surface absorptives, which may poison the active sites of the 2D-MoS<sub>2</sub> nanosheets;<sup>130</sup> or the delamination of the 2D-MoS<sub>2</sub> nanosheets from the substrate.<sup>130</sup> However, it is likely a combination of these

two effects, with the delamination of 2D-MoS<sub>2</sub> nanosheets becoming more prevalent at higher modifications. This inference is supported by the EIS observations detailed earlier. Another consideration in terms of industrial application is cost of the four carbon based electrodes studied, the GC offered the greatest current density and most noted HER onset potential decrease upon modification with 2D-MoS<sub>2</sub> nanosheets. GC's production cost makes its application as a catalyst on an industrial scale economically unfeasible. The SPE offers an attractive alternative to using GC in real-world industrial applications. After modification with 2D-MoS<sub>2</sub> nanosheets, the HER onset potential is lowered to a value equivalent of GC's. One issue could potentially be that the modified SPE exhibits a lower current density compared to that of GC. However, due to the nature of SPE's production they can be produced with a wide degree of tailorability, varying in shape, surface area and carbon composition. As such, SPEs, can be produced with a larger surface area than that of GC, thereby increasing the currents possible and ultimately the amount of hydrogen produced. This combined with the ultra-low cost of fabricating SPEs makes them an exceptionally cost effective and easily producible supporting electrode material for HER. There is potential to incorporate 2D-MoS<sub>2</sub> nanosheets into the carbon based inks used to produce SPEs, thereby eliminating the time consuming modification step. Further research aimed at identifying and resolving the reason for the poor catalytic stability is essential if 2D-MoS<sub>2</sub> nanosheet modified SPEs have a future industrial application.

### 4.3. Summation

---

This Chapter explored the catalytic performance of 2D-MoS<sub>2</sub> nanosheets towards the HER. In order to overcome issues prevalent within the literature, and to allow for the ascertainment of the true electrochemical performance of commercially sourced pristine 2D-MoS<sub>2</sub>. It was then utilised to modified a range of carbon based underlying support electrodes, namely GC, BDD, EPPG and SPEs; this approach is usually neglected within the literature. Application of the 2D-MoS<sub>2</sub> modified electrodes revealed a catalytic performance towards the HER, with lower onset potentials and higher current densities observed when utilising the target material. The supporting electrode was found to be of key importance, influencing the improvements observed in the electrochemical performance. This indicates that 2D-MoS<sub>2</sub> nanosheet modified electrodes can potentially serve as a viable, low cost and more abundant replacement to current Pt based electro-catalysts.

This work is distinct from the literature given that it also correlated the electrochemical responses with supplementary Raman mapping of the electrode surface (and other complementary physicochemical characterisation), whilst exploring the effect of 2D-MoS<sub>2</sub> coverage. Coverage studies revealed that the catalytic effect of the 2D-MoS<sub>2</sub> nanosheets increased (as indicated by ToF and ‘number of active sites’ calculations) until a ‘critical coverage’ (mass) was achieved, after which the response was observed to plateau. The likely cause of this effect is inferred herein and has clear implications (in this case) for other research fields.

The chapter provided insights into the observable electrochemistry and HER mechanism prevalent at 2D-MoS<sub>2</sub> nanosheet modified electrodes, which has clear potential to be beneficially applied/utilised as an electrocatalyst if the diligent control

measures reported herein are sufficiently applied. Given this the following chapter will explore the electrocatalytic effect of 2D-MoS<sub>2</sub> on the ORR.

# Chapter 5.

## 2D-MoS<sub>2</sub> Nanosheets Explored Towards the Oxygen Reduction Reaction

Chapter 5 utilises the drop-casting technique to modify four commonly employed carbon based electrodes (BDD, EPPG, GC and SPEs) with a range of 2D-MoS<sub>2</sub> masses then explores their electrochemical activity towards the ORR.

### 5.1. Introduction

---

Chapter 4 demonstrated that 2D-MoS<sub>2</sub> is an effective electrocatalyst towards the HER, this Chapter now explores its use as an electrocatalyst towards the ORR. Previous studies in this field have shown that 2D-MoS<sub>2</sub> displays some electrocatalytic effective towards the ORR, for example Huang *et al.*<sup>66</sup> utilised MoS<sub>2</sub> ultra-thin nanosheets drop cast onto a rotating disk glassy carbon electrode and observed a 7.8 fold increase in current density and a *ca.* 170 mV positive shift in ORR onset, exhibiting a strong 4 electron mechanism selectivity for the ORR mechanism in alkaline media.

Current literature reports are thoroughly overviewed in Table 5.1 and are sophisticated in their approaches towards the ORR. However, they are limited, since they follow typical conventions found within the literature when MoS<sub>2</sub> materials are explored as electrocatalysts towards the ORR; those being: (1) the use of glassy carbon (GC) almost exclusively as a supporting electrode material, with few or no attempts made to use / explore alternative carbon based supports. *Note that the performance of 2D-MoS<sub>2</sub> can only be truly understood via immobilisation using a range of supporting materials with varied electrode kinetics (electrochemical activities);* (2) within the literature, electrodes are modified with only one mass (coverage) of a given MoS<sub>2</sub> based material, which again makes it difficult to extrapolate

a true understanding of the electrochemical behaviour of 2D-MoS<sub>2</sub>; (3) the use of only KOH as an electrolyte, which makes the results relevant for alkaline fuel cells. However they are not applicable to PEM fuel cells which typically utilise an acidic electrolyte.<sup>152</sup> These three conventions, commonly practised in the field, neglect the ability to deconvolute the *true* electrochemical performance of 2D-MoS<sub>2</sub> materials whilst also making their findings non-applicable to real world applications in PEM fuel cells.

The work of this chapter breaks from academic convention (see points 1-3 above) by performing diligent control experiments, analogous to those performed in Chapter 4, which have been overlooked within the current academic literature, namely: exploring different supporting electrode substrates used to electrically wire 2D-MoS<sub>2</sub> and different immobilised masses upon the ORR, reaction all of which, is for the first time, performed in an acidic electrolyte. The use of acidic conditions mimic those found within a typical PEM fuel cell, providing a greater validity to real world PEM fuel cell applications.<sup>153</sup>

**Table 5.1.** Comparison of current literature reporting the use of 2D-MoS<sub>2</sub> and related catalytic materials explored towards the ORR.

Catalyst	Electrode / supporting material	Loading ( $\mu\text{g cm}^{-2}$ )	Deposition Technique	Cycling Stability (CS)	Potential of CS	CS Performance	Electrolyte	ORR onset (V)	Reference
Flower Like MoS <sub>2</sub>	GC	–	Drop-casting	2000 cycles	–	a	0.1 M KOH	– 0.14 (vs. Ag/AgCl)	<sup>152</sup>
CO(OH) <sub>2</sub> –MoS <sub>2</sub> /rGO	GC	510	Hydrothermal	5000 cycles	+ 1.00 to 0.00 (V vs. RHE)	a	0.1 M KOH	+ 0.86 (vs. RHE)	<sup>154</sup>
MoS <sub>2</sub> -rGO	GC	ca. 1529 <sup>*</sup>	Drop-casting	500 cycles	0.00 to – 0.25 (V vs. RHE)	b	0.1 M KOH	+ 0.80 (vs. RHE)	<sup>155</sup>
O–MoS <sub>2</sub> -87	GC	283	Drop-casting	10,000 sec	+ 0.80 (V vs. RHE)	a	0.1 M KOH	+ 0.94 (vs. RHE)	<sup>66</sup>
AuNP/MoS <sub>2</sub> films	GC	50	Drop-casting	20,000 sec	– 0.25 (V vs. SCE)	a	0.1 M KOH	– 0.10 (vs. SCE)	<sup>156</sup>
MoS <sub>2</sub> /NG	GC	–	Drop-casting	–	–	–	0.1 M KOH	– 0.12 (vs. SCE)	<sup>61</sup>
30% MoS <sub>2</sub> /CoSe <sub>2</sub>	RDE	–	–	50,000 sec	+ 0.30 (V vs. RHE)	a	0.5 M H <sub>2</sub> SO <sub>4</sub>	0.74 V (vs. RHE)	<sup>62</sup>
MoS <sub>2</sub> /Pd	GC	10	Drop-casting	4000 cycles	0.00 to – 0.54 (V vs. RHE)	a	0.1 M KOH	ca. – 0.10 (vs. SCE)	<sup>157</sup>
(Pt) <sub>7</sub> /2H-MoS <sub>2</sub> <sup>*</sup>	–	–	–	–	–	–	–	Over potential of 0.33 V	<sup>158</sup>
MoS <sub>2</sub>	GC	71	Drop-casting	–	–	–	0.1 M KOH	+ 0.78 (vs. RHE)	<sup>159</sup>
2D-MoS <sub>2</sub>	SPE	1009 <sup>*</sup>	Drop-Casted	1000 cycles	0.00 to – 1.4 (V vs. SCE)	b	0.1 M H <sub>2</sub> SO <sub>4</sub>	+ 0.10 (vs. SCE)	<sup>75</sup>
2D-MoS <sub>2</sub>	SPE	20% <sup>▲</sup>	Screen-Printed	1000 cycles	0.00 to – 1.4 (V vs. SCE)	b	0.1 M H <sub>2</sub> SO <sub>4</sub>	+ 0.16 (vs. SCE)	This Work

**Key:** –: Value unknown, rGO: reduced graphene oxide, <sup>\*</sup>; homogeneous solution containing 0.3 mg of catalyst per 10  $\mu\text{l}$ , NP: nanoparticle, O–MoS<sub>2</sub>-87; O–MoS<sub>2</sub> which had 87  $\mu\text{l}$  of aqueous hydrogen peroxide used in its synthesis, GC; glassy carbon, SPE; screen printed electrode, RHE; reversible hydrogen electrode, SCE; saturated calomel electrode, NG;

nitrogen doped graphene, \*; percentage optimal mass of 2D-MoS<sub>2</sub> (range tested: 252 to 2533 ng cm<sup>-2</sup>), RDE; rotating disk electrode, †; investigated using density functional theory, ▲; percentage mass of 2D-MoS<sub>2</sub> to mass of conductive carbon ink ratio. <sup>a</sup>; degradation in the achievable current density over the duration reported, <sup>b</sup>; increase in the achievable current density over the duration reported.

## 5.2. Results and Discussion

### 5.2.1. Benchmarking the ORR Activity of the Electrodes Utilised

---

Chapter 4 focused on using 2D-MoS<sub>2</sub> as an electrocatalyst for the HER and showed 2D-MoS<sub>2</sub> to be electroactive when immobilised on carbon based electrode substrates.<sup>74</sup> It was therefore essential to benchmark the electrochemical activity of the 2D-MoS<sub>2</sub> when deposited using BDD, EPPG, GC and SPEs and explored in degassed 0.1M H<sub>2</sub>SO<sub>4</sub>. This was to ensure that no electroactivity was observed in the region of a linear sweep voltammogram (LSV) where the ORR is expected to occur, as this would convolute the interpretation of the ORR, the results of which can be observed in Figure 5.01.

Figure 5.01(A) shows LSVs BDD, EPPG, GC, Pt and SPEs in a 0.1 M H<sub>2</sub>SO<sub>4</sub> solution which was oxygenated for 1 hour, giving a 0.9 mM concentration of oxygen.<sup>54, 55</sup> Through inspection of these figures, a clear peak is observed for the ORR. An onset potential of  $-0.22$ ,  $-0.30$  and  $-0.39$ , and an oxygen reduction peak maxima at *ca.*  $-0.51$ ,  $-0.85$  and  $-1.00$  V is observed for EPPG, GC and SPE, respectively. All of which are significantly more electronegative than that of the Pt's ORR peak and onset potential of  $+0.46$  and  $+0.13$  V, respectively. The lack of an observable oxygen reduction peak for the BDD electrode (whilst using an acidic electrolyte) corresponds with previous literature.<sup>54</sup> Yano *et al.*<sup>160</sup> suggest that for ORR to be initiated at a BDD electrode it must first undergo a pre-treatment step at  $+1.4$  V vs. (Ag/AgCl).<sup>54</sup>

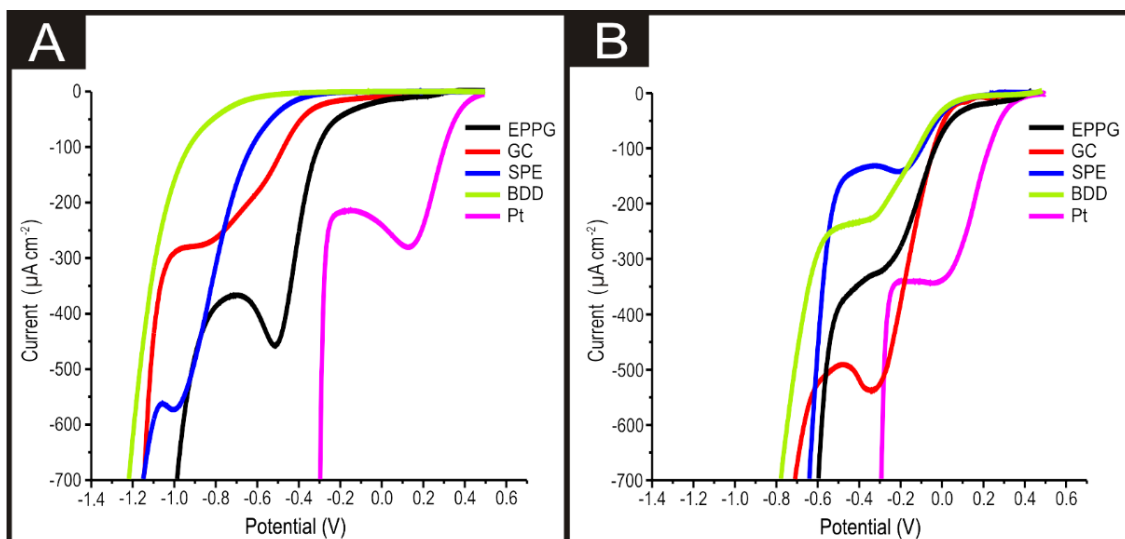


**Figure 5.01.** (A) LSVs of bare/unmodified EPPG, GC, SPE, BDD and Pt electrodes showing signals corresponding to the ORR. (B) LSVs recorded using  $1524 \text{ ng cm}^{-2}$  2D-MoS<sub>2</sub> modified EPPG, GC, SPE, BDD and Pt electrodes showing the position of ORR peaks. In all cases; scan rate:  $25 \text{ mVs}^{-1}$  (vs. SCE) and a solution composition of  $0.1 \text{ M H}_2\text{SO}_4$  which is oxygen saturated.

This pre-treatment step serves to oxidise the  $\text{sp}^2$  hybridised carbon species, the suspected location for the  $\text{sp}^2$  species being the grain boundaries of the  $\text{sp}^3$  diamond structure.<sup>19</sup> The oxidised  $\text{sp}^2$  species subsequently mediate the ORR.

### 5.2.2. Electrochemical Activity of 2D-MoS<sub>2</sub> towards the ORR at an Assigned Mass of Electrode Coverage

Figure 5.01.(B) shows LSV's of BDD, EPPG, GC, SPE and Pt (all of which had been modified with  $1524 \text{ ng cm}^2$  of 2D-MoS<sub>2</sub>). Inspection of this figure reveals that there is a significant positive shift in the ORR onset to *ca.*  $+ 0.1 \text{ V}$  for all of the carbon electrodes utilised. There is a corresponding decrease in the observed oxygen reduction peak potentials by *ca.*  $0.25$ ,  $0.39$  and  $0.82 \text{ V}$  for EPPG, GC and SPEs, respectively compared to their bare/unmodified counterparts. For the case of the BDD, this is now able to reduce oxygen at  $-0.29 \text{ V}$ , which is comparable with the three other

carbon based electrodes utilised. The SPEs exhibit the least electronegative oxygen reduction peak potential of  $-0.16$  V. Clearly, the immobilisation of 2D-MoS<sub>2</sub> onto the chosen carbon based electrodes significantly reduces the overpotential for the ORR to occur, when compared against the bare/unmodified electrodes. Thus, there has been a reduction in the reactions activation energy to a potential that is closer to the value obtained at the unmodified Pt electrode (*ca.* + 0.46 V). The above data implies that 2D-MoS<sub>2</sub> is an effective electrocatalyst for the ORR when modified upon the surface of various carbon based electrodes.

### 5.2.3. Electrochemical Activity of 2D-MoS<sub>2</sub> towards the ORR at Varying Masses of Electrode Coverage

---

Previous work utilising 2D-MoS<sub>2</sub> as an electrocatalyst for the HER revealed that there is an optimal immobilised mass, where the structure of said material has the highest ratio of active edge planes to comparatively inert basal planes.<sup>74</sup> This work therefore investigated the effect of altering the immobilised mass of 2D-MoS<sub>2</sub> onto the carbon based electrodes upon the ORR. Figure 5.02. shows the peak positions of the ORR (black circles) using LSV ( $25 \text{ mVs}^{-1}$  vs. SCE) in 0.1 M H<sub>2</sub>SO<sub>4</sub> for BDD, EPPG, GC and SPEs following modification with 0, 252, 504, 762, 1009, 1267, 1524, 1771, 2009, 2261 and 2533 ng cm<sup>-2</sup> of 2D-MoS<sub>2</sub>.

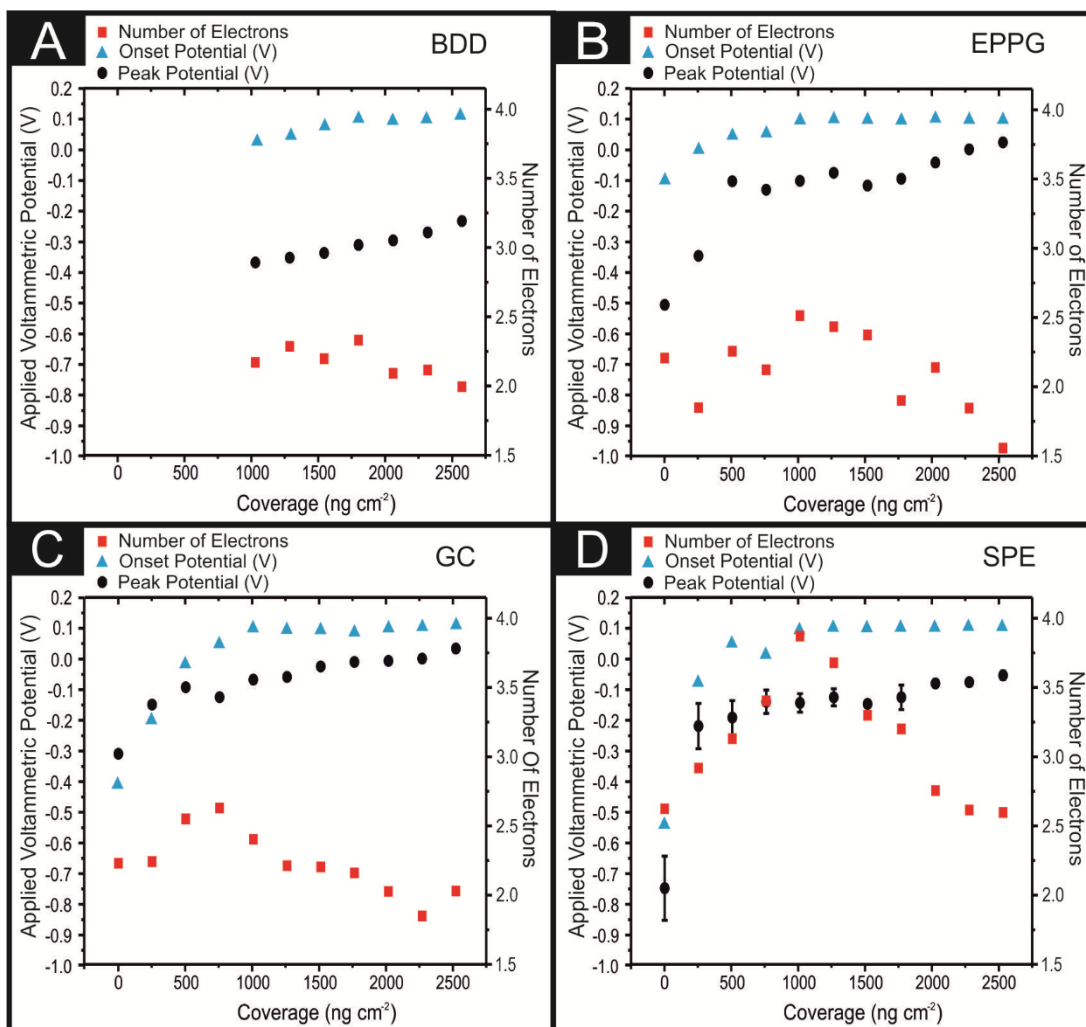


**Figure 5.02.** ORR peak positions (black circles, left Y axis) taken from LSV, the ORR onset potential (blue triangles, left Y axis) and the number of electrons involved in the reaction mechanism (red squares, right Y axis) for 0, 252, 504, 762, 1009, 1267, 1524, 1771, 2018, 2261 and 2533 ng cm<sup>-2</sup> of 2D-MoS<sub>2</sub> deposited onto the following electrodes: (A) BDD, (B) EPPG, (C) GC and (D) SPE. Error bars are the standard deviation of 3 replicates. In all cases; scan rate: 25 mVs<sup>-1</sup> (vs. SCE) and a solution composition of 0.1 M H<sub>2</sub>SO<sub>4</sub> which is oxygen saturated.

It is evident from inspection of Figure 5.02. that there is a trend of a decreasing ORR reduction peak position associated with an increase in the mass of 2D-MoS<sub>2</sub> immobilised onto each of the electrode surfaces utilised. The EPPGs, GCs and SPEs modified with 256 and 504 ng cm<sup>-2</sup> of 2D-MoS<sub>2</sub> experienced a dramatic decrease in

the ORR peak potential from *ca.*  $-0.46$ ,  $-0.59$  and  $-0.85$  V for the bare/unmodified to *ca.*  $-0.23$ ,  $-0.25$  and  $-0.32$  V for the modified (with  $504 \text{ ng cm}^{-2}$  2D-MoS<sub>2</sub>) electrodes, respectively. Subsequent increases in the mass of 2D-MoS<sub>2</sub> immobilisation resulted in minor reductions of the ORR peak position which was incrementally reduced to  $-0.16$ ,  $-0.15$  and  $-0.2$  V by  $2533 \text{ ng cm}^{-2}$  of 2D-MoS<sub>2</sub> for the EPPG, GC and SPE, respectively. Interestingly, no ORR peak was observable for modifications less than  $1009 \text{ ng cm}^{-2}$  on the BDD electrode, whilst BDD modified with  $1009 \text{ ng cm}^{-2}$  of 2D-MoS<sub>2</sub> had a ORR peak potential of *ca.*  $-0.37$  V. As with the other carbon based electrodes, the ORR peak potential was incrementally reduced to  $-0.23$  V by  $2533 \text{ ng cm}^{-2}$  of 2D-MoS<sub>2</sub> modification on BDD.

With respect to the ORR onset, Figure 5.02. (blue triangles) implies that for the bare/unmodified electrodes, the SPE has the most electronegative ORR onset potential at  $-0.54$  V, closely followed by GC at  $-0.4$  V. EPPG has the least negative, thus the most favourable ORR onset potential at  $-0.1$  V, whilst (as mentioned previously) the ORR does not occur at a bare/unmodified BDD. EPPG, GC and SPE electrodes all have a positive shift in their ORR potential with increased mass deposition of 2D-MoS<sub>2</sub> until at  $1009 \text{ ng cm}^{-2}$ , where the ORR onset potential is  $+0.1$  V in all cases; after this mass of modification the onset potential plateaus until the final mass of modification of  $2533 \text{ ng cm}^{-2}$ . This demonstrates that after 2D-MoS<sub>2</sub> has been immobilised onto a carbon based electrode, the kinetics of the supporting electrode itself has little effect upon the ORR onset potential, particularly after complete coverage of the surface at  $1009 \text{ ng cm}^{-2}$ . This work suggests that the ORR onset potential is solely determined *via* the mass of 2D-MoS<sub>2</sub> deposited until complete coverage, thus the response of  $+0.1$  V, which is likely that solely of 2D-MoS<sub>2</sub>.

It is apparent from the above discussion (and inspection of Figure 5.02.) the observed increase in the catalytic performance of a given modified electrode material (which corresponds to the addition of 2D-MoS<sub>2</sub>) begins to plateau, after which further additions of the target material result in increasingly smaller improvements to the electrochemical performance. This ‘critical coverage’ of modification is plausibly due to either achieving complete coverage of the given underlying electrode material, or that the structure of the 2D-MoS<sub>2</sub> is that of reassembly, whereby few layer MoS<sub>2</sub> alters to a bulk morphology. Forming bulk MoS<sub>2</sub> would result in the exposure of less edge planes in proportion to basal planes and consequently mitigate the beneficial electrochemical properties of single-, few-, quasi- 2D-MoS<sub>2</sub> nanosheets. Alternatively, this plateau could signify the mass (a critical coverage of *ca.* 504 ng cm<sup>-2</sup> of 2D-MoS<sub>2</sub> for the ORR peak potential and 1009 ng cm<sup>-2</sup> for the ORR onset potential)<sup>74</sup> at which the structure of MoS<sub>2</sub> can no longer structurally support itself upon the electrode surface (becoming unstable due to the quantity/mass present) and delaminates. Thereby, eliminating the catalytic benefits of additional 2D-MoS<sub>2</sub> immobilisation which does not adhere to the electrodes surface throughout the course of the experiment. Similar observations have been reported for the case of graphene.<sup>148-151</sup> It is also supported by the observation of a critical coverage of 2D-MoS<sub>2</sub> towards the HER, in Chapter 4. This is not the case here however as there is not an observable reduction in the performance of the modified electrodes. Trying to visually assess the extent of 2D-MoS<sub>2</sub> coverage on the surface of an SPE and any subsequent possible SEM analysis was found to be inconclusive as the 2D-MoS<sub>2</sub> proved to be indistinguishable from the SPE surface.

The intra-repeatability of the modified and bare/unmodified SPEs was tested ( $N = 3$ ) and can be observed in Figure 5.02. (D). The % Relative Standard Deviation

(% RSD) in the ORR peak position was found to diminish with a greater mass of 2D-MoS<sub>2</sub> immobilised onto the SPE's surface. The % RSD decrease with greater modifications of 2D-MoS<sub>2</sub> confirms that the observed plateauing is evidently not due to the delamination of the 2D-MoS<sub>2</sub> from the electrodes surface as this would predictably result in increasing % RSDs with increased mass of modification. The observed plateauing effect is therefore probably a result of the 2D-MoS<sub>2</sub> reassembling to a stable bulk structure and as a consequence of this exposing fewer reactive edge planes.

The coverage effect reported above is interesting and strongly correlates with the optimal coverage phenomena described in Chapter 4, as such this study will next consider whether the responses observed are strictly due to the electronic properties of the 2D-MoS<sub>2</sub> (and are solely diffusional in nature), or if thin-layer effects are present and complicating the interpretation. Scan rate studies were performed on the full range of 2D-MoS<sub>2</sub> modified electrodes, where the voltammetric peak height ( $I_p$ ) was monitored as a function of scan rate ( $\nu$ ), with a plot of peak height *versus* square-root of the scan rate revealing clear linear trends and resultantly indicating diffusional processes. Furthermore, as is expected for the case of the semi-infinite diffusion model as governed by the Randles–Ševčík equation,<sup>3, 161</sup> analysis of  $\log I_p$  *versus*  $\log \nu$  revealed gradients of no greater than *ca.* 0.52 (see Table A.1 within the Appendix for detailed values), indicating the absence of thin-layer effects (such that the electrolyte is not trapped within the mesh/framework of the modified electrode) and representing a response that is purely diffusional in each case.<sup>150, 151</sup> Using the equation  $\delta = \sqrt{6D \frac{\Delta E}{\nu}}$  it was possible to determine the thickness of the diffusion layer present for each of the modified electrodes, taking  $\Delta E$  as the half width potential for a CV using the redox

probe 1 mM  $[\text{Ru}(\text{NH}_3)_6]^{3+/2+}$  in 0.1 M KCl (scan rate of 25  $\text{mVs}^{-1}$ ). Where  $D$  is the diffusional coefficient,  $\Delta E$  is the potential width and  $v$  is scan rate.<sup>162</sup> The results of which can be seen in Table A.1 of the Appendix. With a layer roughness on the electrodes surfaces approaching 2 microns it is clear that the observed diffusion layer geometries are significantly larger than that of the electrodes surface layer roughness's, signifying the diffusion layer overlaps the electrodes morphology.

The “critical coverage” of 2D-MoS<sub>2</sub> describes the mass of 2D-MoS<sub>2</sub> immobilisation on a carbon based electrode's surface where optimal catalytic activity is observed and after which the catalytic benefits plateau or diminish with additional masses of 2D-MoS<sub>2</sub> immobilisation. The findings presented herein are strongly supported by the results of a Chapter 4, which observed a similar correlation between the mass of 2D-MoS<sub>2</sub> immobilised onto a carbon electrode substrate and its catalytic activity, in this case towards the HER. In this study the critical coverage was observed to be *ca.* 1267  $\text{ng cm}^{-2}$  on SPEs, at which point the HER onset was lowered by 0.29 V.<sup>74</sup> The combination of the results presented herein and those of the aforementioned HER study confirms that the electrocatalytic activity of 2D-MoS<sub>2</sub> is mass and therefore structure dependent. Future studies reported in literature involving 2D-MoS<sub>2</sub> should endeavour to vary the mass of 2D-MoS<sub>2</sub> utilised in order to deconvolute its optimum electrocatalytic activity. It also proves that 2D-MoS<sub>2</sub> is a promising catalyst that could be utilised to increase the efficiency and energy output of hydrogen fuel cells, thereby making them a more viable alternative to FF combustion as a method of energy generation.

#### 5.2.4. Tafel Analysis and Assessment of the ORR mechanism

It is evident from above that immobilisation of 2D-MoS<sub>2</sub> onto a carbon based electrode substrate reduces the ORR onset and peak potential. Next, consideration was given to the question of whether 2D-MoS<sub>2</sub> once, immobilised onto the carbon based electrodes demonstrated preferential selectivity for the ORR to occur *via* the desirable 4 electron pathway (producing H<sub>2</sub>O) or the 2 electron pathway (producing H<sub>2</sub>O<sub>2</sub>, which is detrimental to PEM fuel cells).<sup>51</sup> Tafel analysis is a common approach employed within the literature to deduce the number of electrons involved in the ORR electrochemical mechanism.<sup>163</sup>

Initially, a plot of  $\ln(I)$  vs.  $E_p$  (V) was considered for each of the four carbon based electrodes (see Appendix Table A.1. and Figure 5.03.) and for each mass of 2D-MoS<sub>2</sub> modification. This was performed *via* analysis of the voltammograms depicting the ORR (which were utilised to produce Figure 5.02.) and using the following equation:<sup>163</sup>  $\frac{\delta \ln I}{\delta E} = \frac{(\alpha n')F}{RT}$ . The slope of the  $\ln(I)$  vs.  $E_p$  (V) plot, mentioned above, corresponds to  $\delta \ln I / \delta E_p$ , where  $\alpha$  is the electron transfer coefficient,  $F$  is the Faraday constant,  $n'$  is the number of electrons transferred in the rate determining step,  $R$  is the gas constant and  $T$  is the solution temperature in Kelvin. Literature has previously suggested that the rate determining step involving the transfer of the first electron is electrochemically irreversible resulting in  $n'$  being 1.<sup>164</sup>

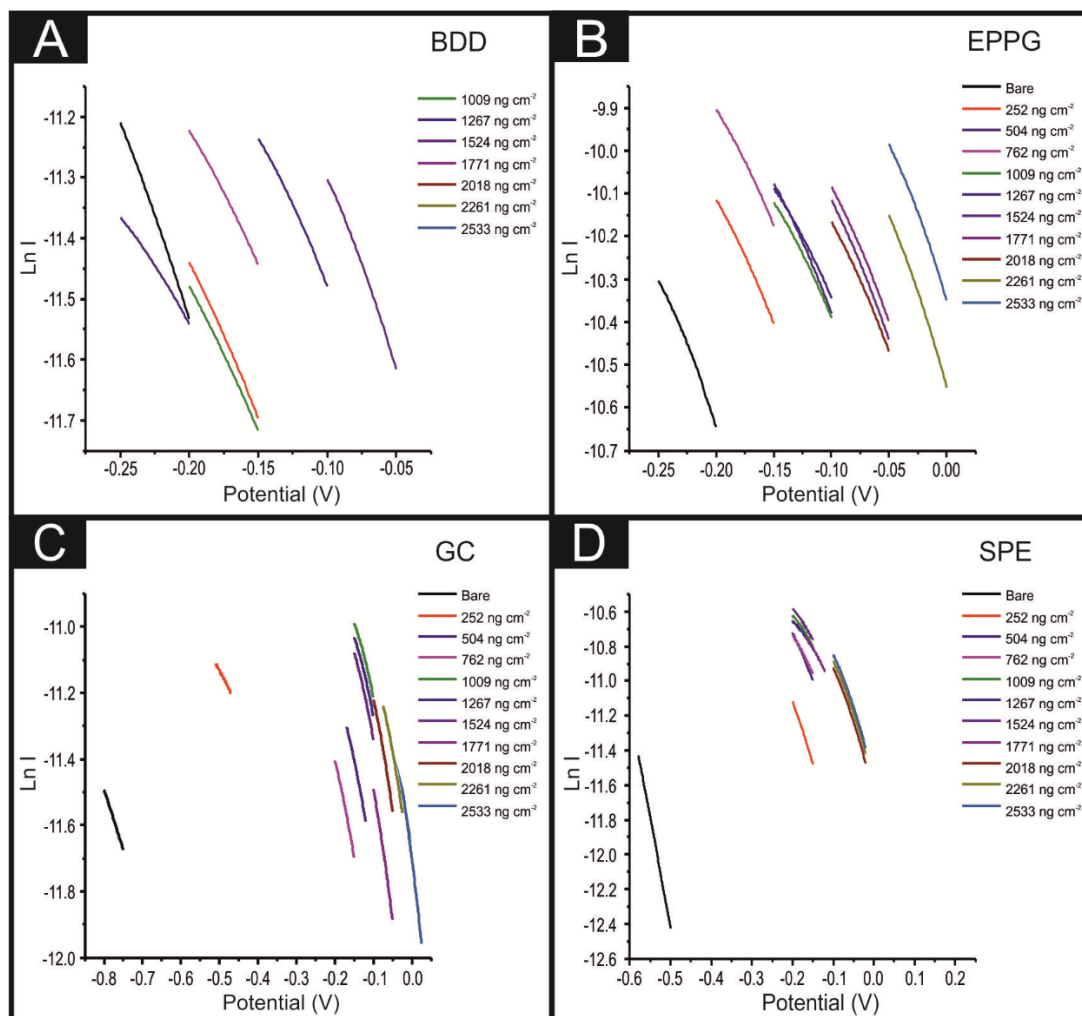


**Figure 5.03.** Tafel slopes corresponding to the Faradaic region of the LSVs for (A) BDD, (B) EPPG, (C) GC and (D) SPE all of which have been modified with 0, 252, 504, 762, 1009, 1267, 1524, 1771, 2018, 2261 and 2533  $\text{ng cm}^{-2}$  of 2D-MoS<sub>2</sub>

Taking the above into consideration  $an'$  values for all of the modified electrodes were deduced. Using these values, the number of electrons involved in the ORR reaction mechanism,  $n$ , was deduced using the  $an'$  calculated from the Tafel equation (see above) and the Randles-Ševčík equation for an irreversible electrochemical process, seen below:<sup>70</sup>

$$I_{P, Irrev} = \pm 0.496(an')^{1/2} nFAC(FDv/RT)^{1/2} \quad (5.1)$$

where  $C$  is concentration,<sup>165</sup> which is assumed for the oxygen saturated solution (0.9 mM), a literature diffusion coefficient value of  $2.0 \times 10^{-5} \text{ cm}^2 \text{ s}^{-1}$ <sup>54, 166</sup> is assumed,<sup>20, 58</sup>

and  $A$  is the area of the electrode. Figure 5.02. shows the number of electrons ( $n$ ) involved in the reaction mechanism for the carbon based electrodes for 0, 252, 504, 762, 1009, 1267, 1524, 1771, 2018, 2261 and 2533  $\text{ng cm}^{-2}$  of 2D-MoS<sub>2</sub> immobilisation. EPPG and GC have similar trends involving 2.23 and 2.21 electrons, respectively, for  $n$  involved in their ORR mechanism on a bare/unmodified electrode, followed by a slight increase to a maximum value of 2.63 at 762  $\text{ng cm}^{-2}$  for EPPG and 2.51 at 1009  $\text{ng cm}^{-2}$  for GC. A gradual decrease is then observed with greater masses of immobilisation until EPPG has a 2 electron process at 2533  $\text{ng cm}^{-2}$  and GC has a 1.56 electron process at 2533  $\text{ng cm}^{-2}$ . BDD remains relatively stable in the ORR reaction mechanism between 2 to 2.5  $n$  involved for a range of modifications between 1009 to 2533  $\text{ng cm}^{-2}$ . There appears to be a slight decrease with greater masses of 2D-MoS<sub>2</sub> immobilisation, however, it is of little significance. The results above show that for bare/unmodified and 2D-MoS<sub>2</sub> wired BDD, EPPG and GC the  $n$  involved never exceeds  $n = 3$  which suggest that H<sub>2</sub>O<sub>2</sub> is the major product of the reaction occurring, rather than the desired H<sub>2</sub>O. It can, therefore, be assumed that whilst 2D-MoS<sub>2</sub> lowers the ORR onset and peak potential for BDD, EPPG and GC electrodes, it has a minor effect upon the reaction mechanism taking place.

Note, of the carbon based electrodes utilised within this study, GC had the lowest number of electrons involved in its ORR reaction mechanism. This raises the question of why it is the commonly used electrode within the literature, as it is clearly the least effective at enabling the desirable 4 electron ORR mechanism. Future studies should use a range of bare/unmodified carbon based electrodes, which exhibit different heterogeneous electron transfer (HET) kinetics resulting in unique interactions between the supporting carbon based electrode and any deposited material, breaking

from the convention of solely using GC; this will help establish the true electrocatalytic activity of a given material.

SPEs show the highest initial  $n$  involved in the ORR reaction mechanism at 2.67 for a bare/unmodified electrode (this corresponds to the literature).<sup>164</sup> From 256 to 1009 ng cm<sup>-2</sup> of 2D-MoS<sub>2</sub> immobilised on a SPE's surface, there is an increase in the  $n$  involved in the ORR reaction mechanism to 3.96. Greater than 1009 ng cm<sup>-2</sup> masses of 2D-MoS<sub>2</sub> modification result in a decrease in the  $n$  involved until  $n$  is 2.64 at 2533 ng cm<sup>-2</sup>. Unlike BDD, EPPG and GC electrodes, it is clear that 2D-MoS<sub>2</sub>, once deposited onto a SPE, not only results in a significant decrease in the ORR onset and peak position, but also in a beneficial change in the ORR reaction mechanism from *ca.* 2 to a 4 electron process, indicating that the major product of the ORR is the desired H<sub>2</sub>O and not the detrimental H<sub>2</sub>O<sub>2</sub>. The reason for 2D-MoS<sub>2</sub> altering the  $n$  involved for SPE and not for BDD, EPPG and GC is due to the SPEs having “rougher” surfaces, resulting in the 2D-MoS<sub>2</sub> once deposited exhibiting structural/electronic orientations not capable on the “smoother” surfaces of BDD, EPPG and GC.<sup>164</sup> A comparison was made between the surface topography of BDD, EPPG, GC and SPE using white light profilometry (a ZeGage 3D Optical Surface Profiler, produced by Zygo, was utilised for this). The surface of a SPE was observed to be significantly rougher (with a root mean squared value of the heights over the whole surface (SQ) of 1904.9 nm), than that of BDD, EPPG and GC which had values of 7.5, 26.1 and 15.9 nm respectively (See Figure 5.04.).

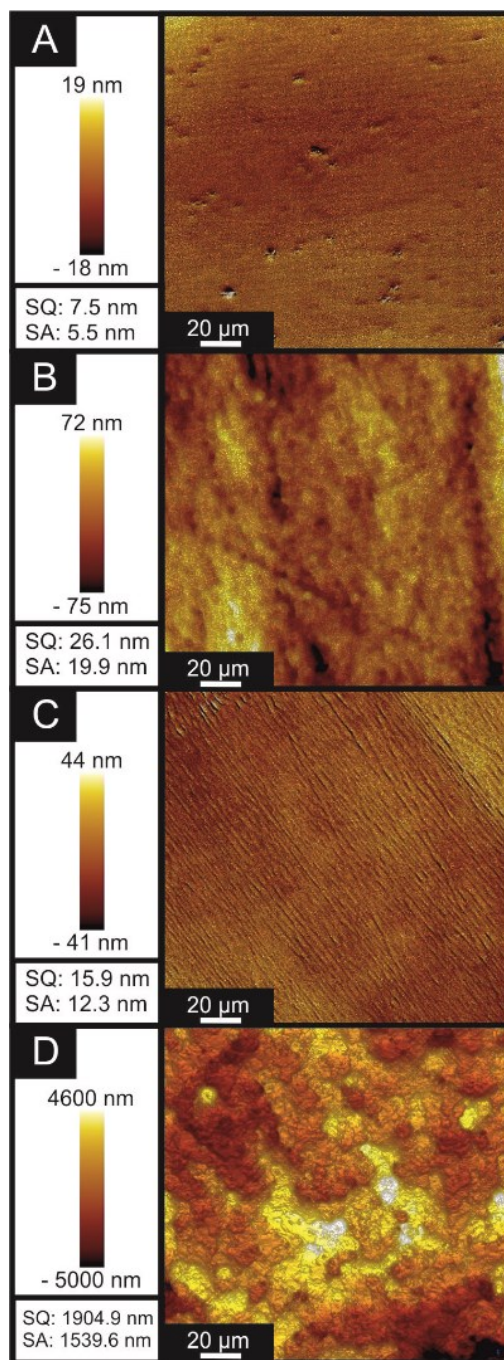


**Figure 5.04.** White light profilometry surface topography maps of bare/unmodified (A) BDD, (B) EPPG, (C) GC and (D) SPE. It is evident that the surface roughness of an SPE is far greater than that of the other carbon based electrodes. SQ being the Root mean squared value of the heights over the whole surface, SA being is the arithmetic average values of absolute height values over the whole surface.

Next, it was necessary to determine whether the SPEs greater roughness resulted in a greater exposure of 2D-MoS<sub>2</sub>. This was determined *via* an evaluation of

the roughness factors ( $R_F$ ), for BDD, EPPG, GC and SPE modified with 0, 256, 1009 and 2018  $\text{ng cm}^{-2}$  of 2D-MoS<sub>2</sub>. In order to deduce  $R_F$  values which are representative of the *true* electrochemical area of an electrode, a double layer capacitance technique can be employed (the methodology of which can be seen in Roughness Factor Calculations Section of Chapter 4). Appendix Table A.2. clearly shows that SPEs have significantly larger  $R_F$  values at every mass of 2D-MoS<sub>2</sub> modification, for example at 2018  $\text{ng cm}^{-2}$  2D-MoS<sub>2</sub> the  $R_F$  for SPE is 37 whereas the  $R_F$  value for BDD, EPPG and GC is 13.5, 2 and 6.4, respectively.

Given topographic roughness and the  $R_F$  values determined above, it is suggested that the correlation between an underlying substrate's roughness and the ability of immobilised 2D-MoS<sub>2</sub> to electrocatalyse the ORR *via* a 4 electron process, is a result of the structural/electronic orientations which occur for 2D-MoS<sub>2</sub> when it is immobilised on a rough surface. This is further supported by Figure 5.05. and 5.06. Figure 5.05. which shows SEM images of; (A) the surface of a typical SPE and (B) the surface of an SPE which has been polished. Figure 5.05.(B) can visually be seen to be smoother than that of Figure 5.05.(A).<sup>164, 167</sup>

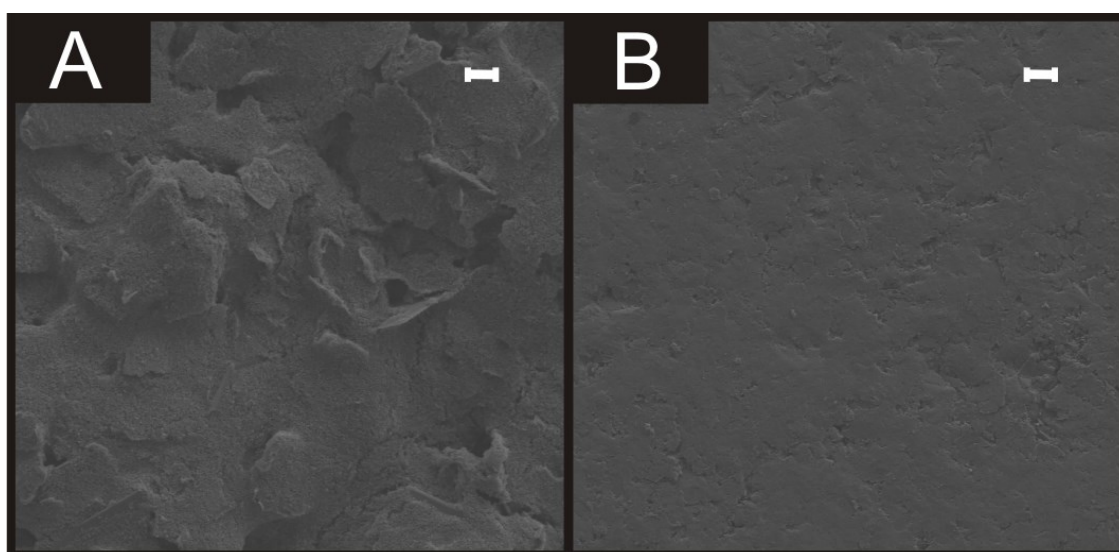


**Figure 5.05.** SEM images of a typical SPE (A) and of a SPE which has been polished (B). Scale bar: 10 $\mu\text{m}$ .

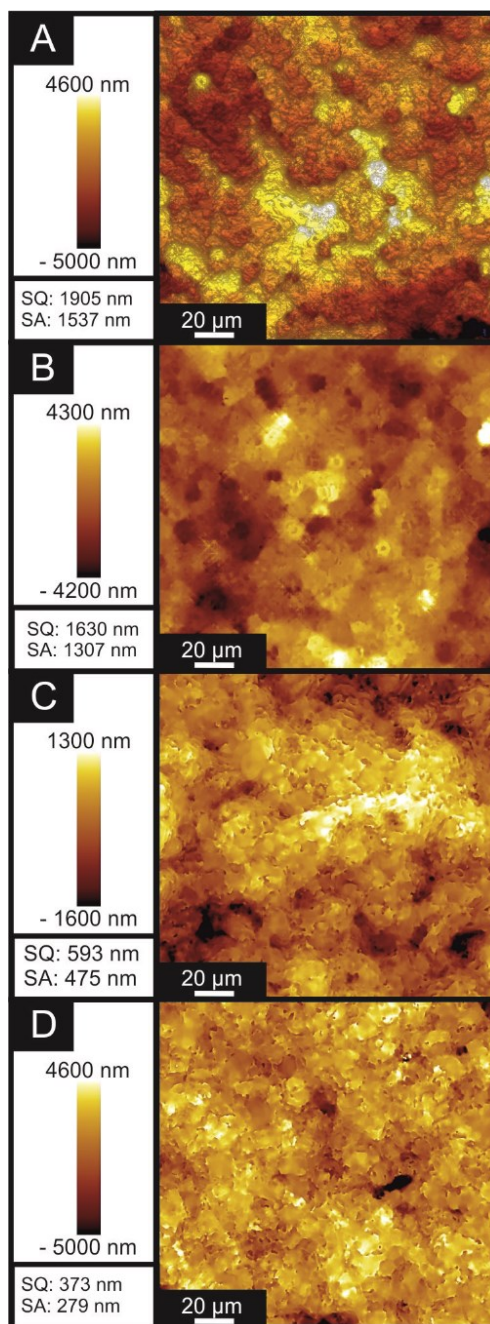


**Figure 5.06.** White light profilometry surface topography maps of (A) a bare/unmodified and unpolished SPE, (B) an unpolished SPE modified with  $1009 \text{ ng cm}^{-2}$  of 2D-MoS<sub>2</sub>, (C) a bare/unmodified and polished SPE and (D) a polished SPE modified with  $1009 \text{ ng cm}^{-2}$  of 2D-MoS<sub>2</sub>. It is evident that the surface roughness of a unpolished SPE is far greater than that of a polished SPE. SQ being the Root mean squared value of the heights over the whole surface, SA being is the arithmetic average values of absolute height values over the whole surface.

Figure 5.06. shows that a SPE, following being polished, has a significantly smaller SQ value of 593 nm compared to that of 1905 nm for an unpolished SPE. Figure 5.06. (B) and (D) show that the surface of an SPE becomes smoother post 1009 ng cm<sup>-2</sup> of 2D-MoS<sub>2</sub> immobilisation. When 1009 ng cm<sup>-2</sup> of 2D-MoS<sub>2</sub> is deposited upon the polished SPE's surface, the  $R_F$  value obtained is 13.5 (see Appendix Table 10.2) and allowed the ORR to occur *via* a 3.4 electron pathway, both of which are significantly less than that of the unpolished (rougher) alternative. It is inferred that the increased catalytic behaviours observed for a rougher surface electrode are due to the unique structural/electronic orientations, which are formed once 2D-MoS<sub>2</sub> is immobilised onto an SPE. This results in an exposure of larger numbers of active edge plane sites/edge plane-like defects than their BDD, EPPG and GC counterparts, and thereby, offering a greater catalytic prospective. Future studies should consider which supporting material they employ as the results observed above show that this has a significant effect upon the deposited material's structure and electron transfer kinetics.

Whilst other studies have managed to produce a 4 electron pathway using alkaline conditions, (such as Suresh *et al.*<sup>152</sup>), given that all previous studies utilising MoS<sub>2</sub> materials towards the ORR are shown in Table 5.1., this report is the first to observe the ORR occur *via* the 4 electron pathway (thus producing H<sub>2</sub>O rather than H<sub>2</sub>O<sub>2</sub>) in acidic conditions using an 2D-MoS<sub>2</sub> based electrocatalytic material on a carbon based substrate (SPEs). Clearly, these results are of significant importance as it is acidic conditions found within a PEM fuel cell, thusly making the results of this study highly applicable to real world industry.

This work clearly indicates that there is an optimal/critical coverage, which is determined to be *ca.* 1009 ng cm<sup>-2</sup> for SPEs, whereby there is the largest average  $n$  (4) involved in the ORR reaction mechanism, as well as a significant improvement in the

ORR onset and peak potential. Subsequent studies within the literature which use 2D-MoS<sub>2</sub> should consider using a range of differing loadings/modifications in order to deconvolute the true/optimal electrocatalytic performance of a given electrocatalyst.

### 5.3. Summation

---

The work reported in this chapter sought to break from the conventions found within the literature when 2D-MoS<sub>2</sub> materials are explored towards the ORR, of solely using GC as a supporting electrode, using only one mass of the electrocatalytic material to modify the supporting electrode and using KOH as the electrolyte. In these ways, it is analogous to the work reported in the previous chapter towards the HER.

The study implemented a range of diligent control experiments. Rather than solely using GC as a supporting electrode this study employed BDD, EPPG, GC and SPE's. The ORR onset was reduced to *ca.* + 0.1 V for EPPG, GC and SPEs at a 2D-MoS<sub>2</sub> loading of 1524 ng cm<sup>-2</sup> modification, which is far closer to Pt at + 0.46 V compared to the bare/unmodified EPPG, GC and SPE counterparts. BDD was observed to have an ORR onset potential of - 0.03 V at 2D-MoS<sub>2</sub> 1524 ng cm<sup>-2</sup> modification. Using a range of 2D-MoS<sub>2</sub> modification masses rather than one set mass allowed us to observe that a critical coverage of 2D-MoS<sub>2</sub> had been achieved (in this case *ca.* 1009 ng cm<sup>2</sup>). At this critical coverage, there is optimal catalytic activity, after which the catalytic benefits plateau with additional masses of 2D-MoS<sub>2</sub> immobilisation. This is as a result of the structure of 2D-MoS<sub>2</sub> at the critical coverage exposing the largest ratio of electroactive edge planes, after which the structure is that of bulk MoS<sub>2</sub>. 0.1 M H<sub>2</sub>SO<sub>4</sub> was utilised as an electrolyte for all the experiments described herein, unlike previous studies, which used KOH. Performing the experiments in an acidic electrolyte resembles the conditions in which PEM fuel cells operate, making the observations presented herein highly applicable to industry.

SPEs were the only carbon based electrode found to allow the ORR to occur *via* the desirable 4 electron pathway (producing H<sub>2</sub>O rather than H<sub>2</sub>O<sub>2</sub>) at 2D-MoS<sub>2</sub>

(*ca.* 1009 ng cm<sup>2</sup>). This is likely as a result of the structurally rougher SPE surfaces allowing for unique 2D-MoS<sub>2</sub> structural/electronic orientations, where larger numbers of active edge planes are exposed, which are not possible on the “smoother” BDD, EPPG and GC electrodes. Whilst other reports have managed to produce a 4 electron process this study appears to be the first to observe the ORR to occur *via* a 4 electron process in acidic conditions using a 2D-MoS<sub>2</sub> based electrocatalyst material on a carbon based substrate. There is no reason why the findings of this study would not be applicable to other 2D materials, which opens up new avenues of research where the surface roughness of a supporting electrode could be altered allowing 2D materials to exhibit unique and unreported structural/electronic orientations and electrochemical behaviours.

This chapter strays from the literature conventions and in doing so deconvolutes the true electrochemical behaviour of 2D-MoS<sub>2</sub> and revealed SPEs as a valid alternative to GC for research purposes and for Pt in real world fuel cell applications. SPEs are significantly cheaper, adaptable and mass producible when compared to Pt and other carbon based electrodes examined herein, whilst upon modification with an optimal mass of 2D-MoS<sub>2</sub>, exhibit preferential electrocatalytic activity towards the ORR.

## Chapter 6.

# 2D-MoS<sub>2</sub> Incorporated Screen-Printed Electrodes explored towards the Hydrogen Evolution and Oxygen Reduction Reactions

Chapter 6 firstly describes a facile technique by which 2D-MoS<sub>2</sub> can be incorporated into a graphitic ink (on a percentage mass basis) that then can be utilised to produce SPEs (2D-MoS<sub>2</sub>-SPE). These 2D-MoS<sub>2</sub>-SPEs are then electrochemically explored towards the HER and ORR.

### 6.1. Introduction

---

Chapters 4 and 5 demonstrate that 2D-MoS<sub>2</sub> is an effective electrocatalyst towards the HER and ORR. The following chapter explores how 2D-MoS<sub>2</sub> can be incorporated into a screen-printed electrode in order to produce intrinsically electrocatalytic electrodes, with particular attention being focused on their application towards the ORR. Table 6.1. represents a thorough overview of the literature reporting MoS<sub>2</sub> based electrode materials explored towards the ORR. From inspection of this table the repeated use of the drop-casting technique as a method of modifying the supporting electrode, typically glassy carbon. The drop-casting technique is defined as the process of dispersing an electrocatalytic material into a suitable media/solvent, from which aliquots are then taken and pipetted onto the chosen electrode surface. This solvent evaporates, leaving behind the electrocatalytic material immobilised upon the electrode surface, which allows “electrical wiring” of the electrocatalytic material. Whilst being a convenient technique to test the electrocatalytic properties of a material, it has several disadvantages, those being; poor cycling stability, low levels of reproducibility, lack of scalability for industrial applications and uniform coverage of the material deposited. The latter is especially a problem when using 2D materials, which have altering heterogeneous electrode transfer (HET) kinetics between their

nanosheet, intermediate and bulk forms.<sup>114</sup> A prevalent challenge in this field has been to find an alternative method of modifying a supporting electrode that does not display the disadvantages associated with drop-casting. Additionally, there is an issue of how one can translate the identified electrocatalytic material from the laboratory into industry, namely as electrodes in PEMFCs, for example.

In an attempt to overcome the critical issues identified above, this chapter reports the design, fabrication and evaluation of inks that incorporate 2D-MoS<sub>2</sub>, which are able to be screen-printed producing 2D-MoS<sub>2</sub> screen-printed electrodes (2D-MoS<sub>2</sub>-SPE). These inks and 2D-MoS<sub>2</sub>-SPEs are shown to be electrocatalytic towards the ORR. The 2D-MoS<sub>2</sub>-SPEs have the advantage of tailability, where different amounts and lateral sizes of the 2D material can be incorporated, which change the electrochemical performance and critically have scales of economy, due to their ability to be mass produced, and critically provide a route to the mass production of electrocatalytic surfaces that have potential to be utilised in fuel cells. Figure 2.17.(C) (see Chapter 2, page 87) shows the exact SPE design utilised herein. Future studies could seek to incorporate any of the plethora of 2D nanomaterials into inks in order to produce SPEs designed to meet a niche electrochemical applications.

## 6.2. Results and Discussion

### 6.2.1. Fabrication and Characterisation of the MoS<sub>2</sub>-SPEs

---

The 2D-MoS<sub>2</sub> screen-printed electrodes were fabricated, as described in the Experimental Section 2.5.1. using the *ca.* 400 nm, 2 μm and 6 μm flake size 2D-MoS<sub>2</sub> powders. For a full physicochemical analysis, including TEM, SEM, XPS and XRD, see Experimental Section 2.2.4. Initially the SPEs produced *via* incorporation with *ca.* 400 nm flake size 2D-MoS<sub>2</sub> (2D-MoS<sub>2</sub>-SPE<sub>400nm</sub>) are utilised as a representative example for the 2D-MoS<sub>2</sub>-SPE. Later in this chapter the effect of flake size upon the 2D-MoS<sub>2</sub>-SPEs catalytic ability will be explored.

### 6.2.2. Electrocatalytic Activity of the 2D-MoS<sub>2</sub>-SPEs towards the HER

---

Chapters 3 and 4 have shown that 2D-MoS<sub>2</sub> is electrocatalytic towards the HER,<sup>74</sup> it was therefore essential to benchmark the 2D-MoS<sub>2</sub>-SPE<sub>400nm</sub> in 0.5 M H<sub>2</sub>SO<sub>4</sub>. This was to assess its capacity of being used as an effective electrocatalyst towards the HER.

Figure 6.01.(A) shows linear sweep voltammetry (LSV) for a SPE as well as for 5, 10, 20 and 40% 2D-MoS<sub>2</sub>-SPE<sub>400nm</sub> in 0.5 M H<sub>2</sub>SO<sub>4</sub>, which had been thoroughly degassed using pure nitrogen. This was performed in order to explore their ability to catalyse the HER as is common within the literature.<sup>75</sup> The SPE exhibited a HER onset of -880 mV and a current density of 0.095 mA cm<sup>-2</sup> at a potential of -0.75 V. As expected, this is far more electronegative than the HER onset of Pt (*ca.* -0.25 V). The observed small electronegative HER onset potential for Pt is due to it being a pure metal that has a very small binding energy for H<sup>+</sup>.<sup>11</sup> Note that the HER onset is

analysed as the potential at which the observed current deviates from the background current by  $25 \mu\text{A cm}^{-2}$ .

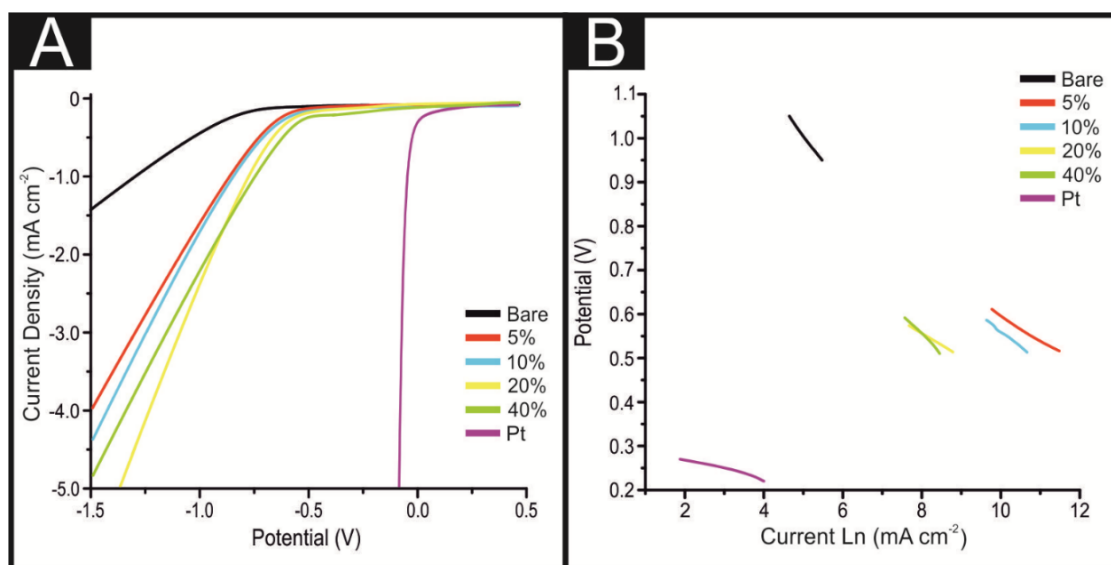


**Figure 6.01.** LSVs of (bare) SPEs, 5%, 10%, 20% and 40% 2D-MoS<sub>2</sub>-SPE<sub>400nm</sub> showing the onset of the HER. Scan rate:  $25 \text{ mVs}^{-1}$  (vs. SCE). Solution composition:  $0.5 \text{ M H}_2\text{SO}_4$ .

It is clearly observable that all the 2D-MoS<sub>2</sub>-SPE<sub>400nm</sub> have a HER onset potential which is less electronegative than a SPE and closer to the optimal of Pt. There is a gradual decrease in the electronegativity of the HER onset from  $-0.56$  to  $-0.50$  V as the percentage mass of 2D-MoS<sub>2</sub> is increased from 5 to 40%. There is also a significant increase in the recorded current density with the 5, 10, 20 and 40% 2D-MoS<sub>2</sub>-SPE<sub>400nm</sub> exhibiting current densities at  $-0.75$  V of  $-0.314$ ,  $-0.499$ ,  $-0.795$  and  $-1.016 \text{ mA cm}^{-2}$ , respectively, indicating a far greater production of the desired H<sub>2</sub> (gas), compared to the SPE. The decrease in the electronegativity of the HER overpotential and the increase in observed current density indicates that the 2D-MoS<sub>2</sub> incorporated ink is an effective electrocatalyst towards the HER.

### 6.2.2.1. Tafel Analysis in Order to Determine the Rate Limiting HER Step Exhibited by the 2D-MoS<sub>2</sub>-SPE<sub>S400nm</sub>

---

In order to ascertain the HER reaction mechanism, this study implemented the commonly used Tafel analysis in the same manner as the previous chapters.<sup>74, 168, 169</sup> Tafel analysis was performed on the Faradaic sections of the LSVs for a bare SPE, 5, 10, 20 and 40 % 2D-MoS<sub>2</sub>-SPE<sub>S400nm</sub>, shown in Figure 6.01.(A), with the resultant Tafel slopes being exhibited in Figure 6.01.(B). The Tafel slope values obtained for the SPE, 5, 10, 20 and 40% 2D-MoS<sub>2</sub>-SPE<sub>S400nm</sub> correspond to 120, 89, 85, 74 and 87 mV dec<sup>-1</sup>. Interpretation of these values suggests that the rate limiting step of the HER reaction mechanism on these electrodes is the “adsorption Volmer” step. It is clear that there is an optimal percentage mass ratio of 2D-MoS<sub>2</sub> at *ca.* 20% where the greatest amount of HER activity is observed. At this optimal ratio it is likely that the structural model of the 2D-MoS<sub>2</sub>-ink has proportionally the greatest number of exposed electrocatalytic edge planes to relatively inert basal planes of 2D-MoS<sub>2</sub>. Thus, resulting in the least electronegative HER onsets and the highest achievable current densities. Once the percentage mass of 2D-MoS<sub>2</sub> within the ink has exceeded the optimal ratio there is a severe reduction in the observed current density, as observed *e.g.* for the 40% 2D-MoS<sub>2</sub>-SPE<sub>S400nm</sub>. This reduction in the achievable current density is possibly a result of the structure of 2D-MoS<sub>2</sub> at percentages greater than 20% recombining into bulk forms within the SPE ink and resulting in a smaller number of exposed planes for H<sup>+</sup> binding.

### 6.2.2.2. HER Turn Over Frequency of the 2D-MoS<sub>2</sub>-SPE<sub>S400nm</sub>

---

In order to assess the intrinsic catalytic activity being displayed by the 2D-MoS<sub>2</sub> upon the surface of the 2D-MoS<sub>2</sub>-SPE<sub>400nm</sub> on a “per active site basis”, the turn over frequency (ToF) was deduced (the methodology by which the ToF values were deduced is presented in Chapter 4, Section 4.2.5.2. with the double layer capacitance values being determined from Appendix Figures A.2 and A.3). Resultant ToF values for the 5, 10, 20 and 40% 2D-MoS<sub>2</sub>-SPEs were found to correspond to 0.596, 0.342, 0.293 and 0.125  $\frac{H_2/s}{Surface\ Site}$ , respectively. It is evident that, with an increased percentage of 2D-MoS<sub>2</sub> there is a decrease in the ToF value obtained. This could be a result of larger ratios of 2D-MoS<sub>2</sub> to conductive carbon ink leading to competition for available H<sup>+</sup> between the active edge-plane sites present on the surface. It could also be as a result of the larger masses of 2D-MoS<sub>2</sub> forming a structure where there is increased shielding of the electronegative S atoms located at the active edge planes by the relatively inactive basal planes

### 6.2.3.1. Electrocatalytic Activity of the 2D-MoS<sub>2</sub>-SPE<sub>S400nm</sub> towards the ORR

---

Figure 6.02.(A) shows typical linear sweep voltammograms (LSV) obtained using a SPE, 5%, 10%, 20%, 40% 2D-MoS<sub>2</sub>-SPE<sub>400nm</sub> and, for comparative purposes, a Pt electrode in oxygenated 0.1 M H<sub>2</sub>SO<sub>4</sub>.<sup>75</sup>

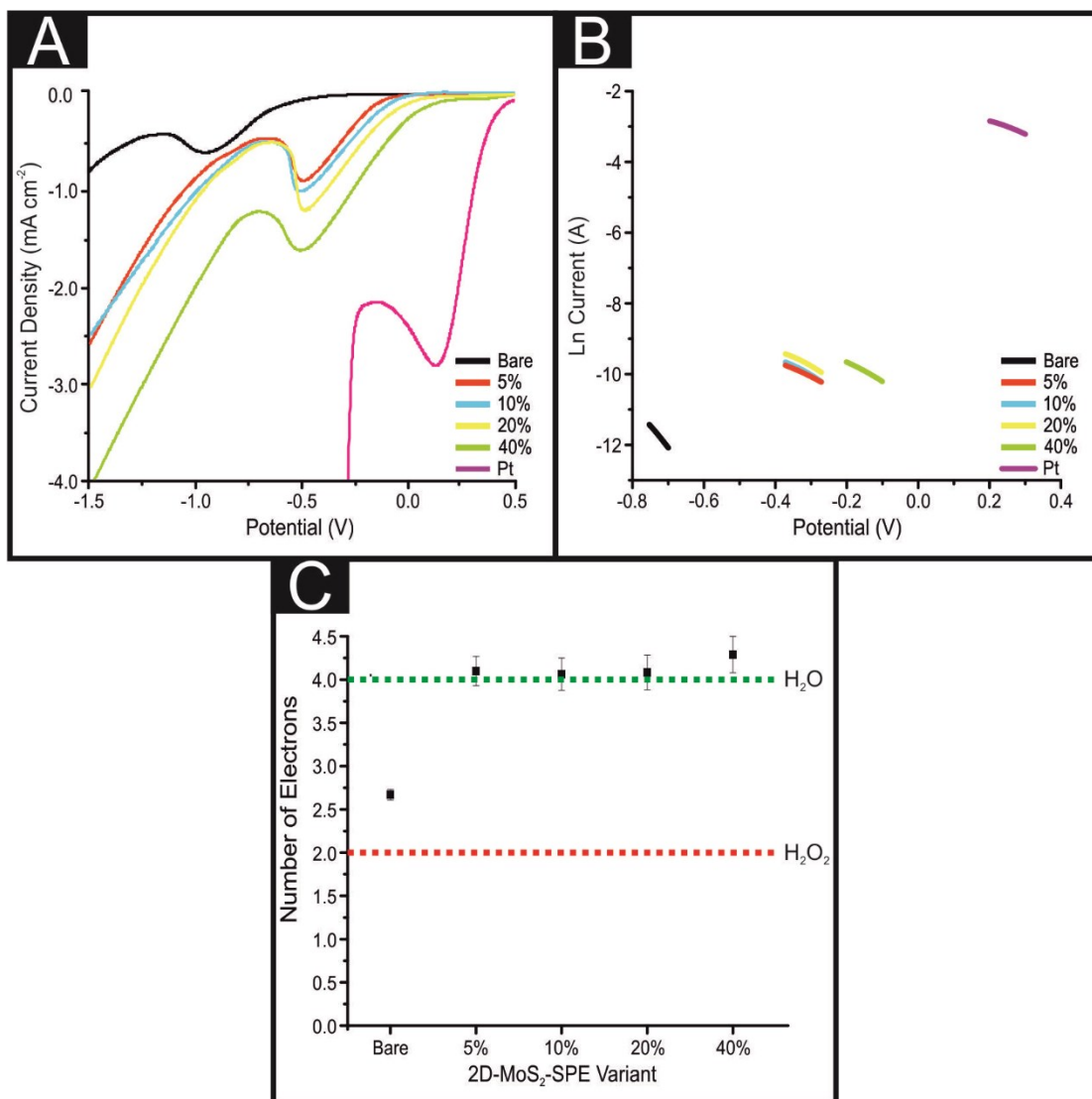


**Figure 6.02.** (A) LSVs of SPE and 5%, 10%, 20% and 40% 2D-MoS<sub>2</sub>-SPE<sub>s400nm</sub> showing the onset and peak potential for the ORR. Scan rate: 25 mVs<sup>-1</sup> (vs. SCE). Solution composition: 0.1 M H<sub>2</sub>SO<sub>4</sub>. (B) Tafel analysis; ln of current density vs potential for Faradaic section of the LSV presented in (A). (C) The number of electrons involved in the ORR mechanism for a (bare) SPE and 5%, 10%, 20% and 40% 2D-MoS<sub>2</sub>-SPE<sub>s400nm</sub> (average standard deviation of 3 replicates). The green and red dotted lines show the number of electrons required for the ORR process to proceed via the desirable mechanism to produce H<sub>2</sub>O ( $n = 4$ ) or the undesirable mechanism to H<sub>2</sub>O<sub>2</sub> ( $n = 2$ ) respectively.

Upon inspection of this figure, it is clear that the (bare) SPE has the most electronegative ORR onset potential and smallest peak current of *ca.* -0.53 V and -635  $\mu\text{A cm}^{-2}$ , respectively. The Pt electrode displays the optimal ORR onset potential

and largest peak current of + 0.46 V and 2.92 mA cm<sup>-2</sup>, respectively. The 2D-MoS<sub>2</sub>-SPE<sub>400nm</sub> display a significantly less electronegative onset potential, as well as an increase in the peak ORR current compared to the SPE, however they also have a more electronegative and smaller peak current compared to that of the Pt electrode. It is clearly observable that, as the percentage mass incorporation of 2D-MoS<sub>2</sub> into 2D-MoS<sub>2</sub>-SPE<sub>400nm</sub> increased, there is a decrease in the electronegativity and increase in current density, with the ORR onset and peak potential going from *ca.* -0.19 to + 0.16 V and *ca.* -0.89 to -1.62 mA cm<sup>-2</sup> for a 5 % to a 40 % incorporation of 2D-MoS<sub>2</sub> into 2D-MoS<sub>2</sub>-SPE<sub>400nm</sub>, respectively. This effect is likely attributed to the 40 % 2D-MoS<sub>2</sub>-SPE<sub>400nm</sub> having the largest mass of 2D-MoS<sub>2</sub> present, which results in it having the largest number of active edge sites accessible upon the electrodes surface; it is evident that as the mass incorporation of 2D-MoS<sub>2</sub> increases the ORR onset becomes less electronegative and the peak potential increases. This is different to the HER where the 40% incorporation resulted in a less beneficial response than the 20% 2D-MoS<sub>2</sub>-SPE<sub>400nm</sub>.

In order to ensure that the responses observed are strictly due to the electronic properties of the 2D-MoS<sub>2</sub> (and are solely diffusional in nature), or if thin-layer effects are present and complicating the interpretation, scan rate studies were performed on the full range of herein utilised 2D-MoS<sub>2</sub> modified electrodes. The voltammetric peak height ( $I_p^{\text{Irrev}}$ ) was monitored as a function of voltammetric scan rate ( $v$ ), with a plot of peak height versus square-root of the scan rate revealing clear linear trends and resultantly indicating diffusional processes. Furthermore, as is expected for the case of the semi-infinite diffusion model as governed by the Randles–Ševčík. Analysis of  $\log I_p^{\text{Irrev}}$  versus  $\log v$  revealed gradients of no greater than *ca.* 0.52 (see Table 6.1. for detailed values), indicating the absence of thin-layer effects.

**Table 6.1.** Determined values for the Tafel Slope Gradient and  $\log I / \log v$  for a (bare) SPE, 5, 10, 20 and 40% 2D-MoS<sub>2</sub>-SPE<sub>400nm</sub>.

Electrode	Slope Gradient ( $\delta \ln I / \delta E_p$ )	$\log I / \log v$
SPE	12.23	0.44
5% 2D-MoS <sub>2</sub> -SPE <sub>400nm</sub>	5.47	0.43
10% 2D-MoS <sub>2</sub> -SPE <sub>400nm</sub>	5.19	0.38
20% 2D-MoS <sub>2</sub> -SPE <sub>400nm</sub>	4.7	0.37
40% 2D-MoS <sub>2</sub> -SPE <sub>400nm</sub>	3.7	0.35

This means that the surface structure of the electrodes does not consist of furrows in which the electrolyte can become trapped within the mesh/framework of the modified electrode. Thus the electrochemical response observed is purely diffusional for all the 2D-MoS<sub>2</sub>-SPE<sub>400nm</sub>.

### 6.2.3.2. Tafel Analysis and Assessment of the ORR Mechanism for the 2D-MoS<sub>2</sub>-SPE<sub>400 nm</sub>

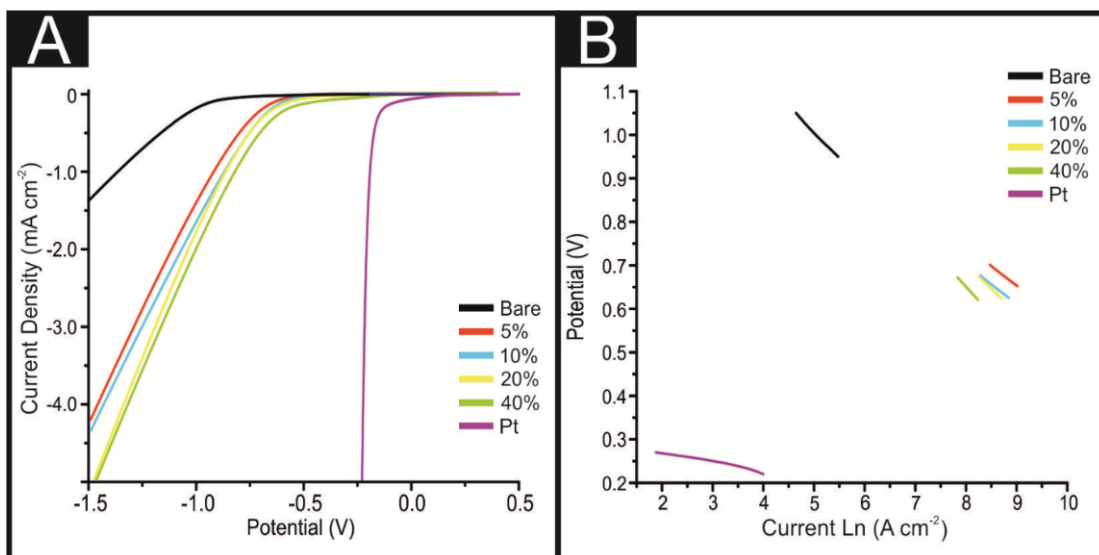
Next, consideration was given to the question of whether the 2D-MoS<sub>2</sub>-SPE<sub>400nm</sub> demonstrated preferential selectivity for the ORR to occur *via* the desirable 4 electron pathway (producing H<sub>2</sub>O) or the 2 electron pathway (producing H<sub>2</sub>O<sub>2</sub>, which is detrimental to PEM fuel cells; as described in Section 1.1.2.).<sup>51</sup> As there is not a rotating disk electrode methodology for determining the number of electrons involved in the ORR that is compatible with the screen-printed electrodes developed in this work, Tafel analysis was utilised, in the same manner as Chapter 5 (see Figure 6.02.(B) and Table 6.1).. This allowed the number of electrons involved in the ORR electrochemical mechanism to be determined.<sup>163</sup>

Figure 6.02.(C) shows the number of electrons ( $n$ ) involved in the reaction mechanism for the SPE and all the 2D-MoS<sub>2</sub>-SPE<sub>400nm</sub> variants. The results above show that for SPEs,  $n = 2.67$  which suggest that H<sub>2</sub>O<sub>2</sub> is the major product of the reaction occurring rather than the desired H<sub>2</sub>O, as is suggested independently within the literature.<sup>170</sup> On the other hand, the 5, 10, 20 and 40 % 2D-MoS<sub>2</sub>-SPE<sub>400nm</sub> exhibit an average ( $N = 3$ )  $n$  of *ca.* 4.10, 4.06, 4.08 and 4.29, indicating that the major product of the ORR is the *desired* H<sub>2</sub>O and not the detrimental H<sub>2</sub>O<sub>2</sub>. Whilst other studies have managed to produce a 4 electron pathway, such as Suresh *et al.*<sup>152</sup> in alkaline conditions and Chapter 4 in acidic conditions, both of which utilised the drop-casting technique and show a decrease in the achievable current over the course of a cycling stability test. It is believed that this study is the first to produce a screen-printable electrocatalytic 2D-MoS<sub>2</sub> incorporated electrode that are observed to exhibit an ORR reaction mechanism that occurs *via* the desirable 4-electron pathway producing H<sub>2</sub>O.

#### 6.2.4. Exploring the Effect of Altering the MoS<sub>2</sub> Flake Size upon the HER Activity of the 2D-MoS<sub>2</sub>-SPEs

---

A further important consideration was the effect of MoS<sub>2</sub> particle size upon the 2D-MoS<sub>2</sub>-SPEs ability to catalyse the HER. This study therefore fabricated 2D-MoS<sub>2</sub>-SPE<sub>S2μm</sub> and 2D-MoS<sub>2</sub>-SPE<sub>S6μm</sub> variants in order to explore their ability to catalyse the ORR, the results of which are shown in Figure 6.03. and 6.04.



**Figure 6.03.** LSVs of (bare) SPEs, 5%, 10%, 20% and 40% 2D-MoS<sub>2</sub>-SPE<sub>2μm</sub> showing the onset of the HER. Scan rate: 25 mVs<sup>-1</sup> (vs. SCE). Solution composition: 0.5 M H<sub>2</sub>SO<sub>4</sub>

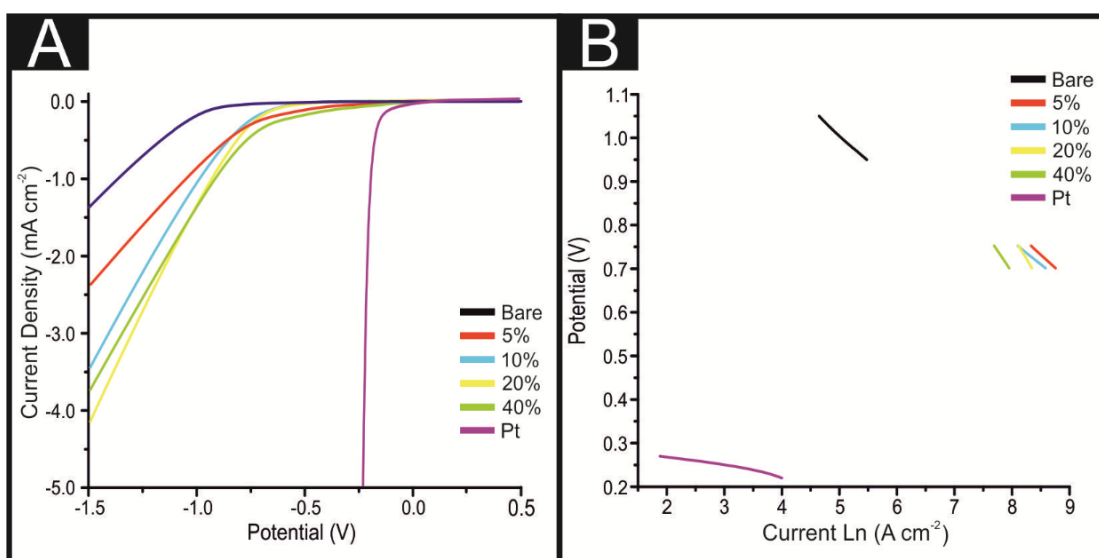


**Figure 6.04.** LSVs of (bare) SPEs, 5%, 10%, 20% and 40% 2D-MoS<sub>2</sub>-SPE<sub>6μm</sub> showing the onset of the HER. Scan rate: 25 mVs<sup>-1</sup> (vs. SCE). Solution composition: 0.5 M H<sub>2</sub>SO<sub>4</sub>

It is clear from inspection of Figures 6.03 and 6.04 that the optimal 40% 2D-MoS<sub>2</sub>-SPE<sub>2μm</sub> had a less electronegative onset potential at ca. -0.6 V than any of the

2D-MoS<sub>2</sub>-SPE<sub>S6μm</sub>. These onset potentials are significantly more electronegative than those displayed by the 2D-MoS<sub>2</sub>-SPE<sub>S400nm</sub> (see Figure 6.01.) In regards to the achievable current densities (at -0.75V) and Tafel slopes the 40% 2D-MoS<sub>2</sub>-SPE<sub>S2μm</sub> and 2D-MoS<sub>2</sub>-SPE<sub>S6μm</sub> displayed values of -0.7 mA cm<sup>-2</sup> and 120 mV dec<sup>-1</sup>, and -0.64 mA cm<sup>-2</sup> and 200 mV dec<sup>-1</sup> respectively. When compared with the values for a 40% 2D-MoS<sub>2</sub>-SPE<sub>S400nm</sub> it is clearly deducible that implementing a smaller particle size of MoS<sub>2</sub> to produce 2D-MoS<sub>2</sub>-SPEs results in more beneficial HER activity. The observed change in HER performance is a clear result of the differing morphologies of the 2D-MoS<sub>2</sub> used in the fabrication of the SPEs where it appears that the smaller flake sizes have a greater proportion of active edge sites (exposed sulphur sites for H<sup>+</sup> binding) than that of an equivalent mass of a larger flake size. With none of the 2D-MoS<sub>2</sub>-SPEs observed to have a Tafel value smaller *ca.* 90 mV dec<sup>-1</sup> it can be inferred that the rate limiting step in all cases is the adsorption Volmer step. This implies that 2D-MoS<sub>2</sub>-SPEs, whilst preferential to carbon based electrodes, are significantly less catalytic than pristine 2D-MoS<sub>2</sub> drop-cast onto an electrode (i.e. GC) as presented in Chapter 3.

### 6.2.5. Exploring the Effect of Altering the MoS<sub>2</sub> flake size upon the ORR Activity of the 2D-MoS<sub>2</sub>-SPEs

---

A further important consideration was the effect of MoS<sub>2</sub> particle size upon the 2D-MoS<sub>2</sub>-SPEs ability to catalyse the ORR. This study therefore utilised the 2D-MoS<sub>2</sub>-SPE<sub>S2μm</sub> and 2D-MoS<sub>2</sub>-SPE<sub>S6μm</sub> variants in order to explore their ability to catalyse the ORR, the results of which are shown in Figures 6.05. and 6.06.

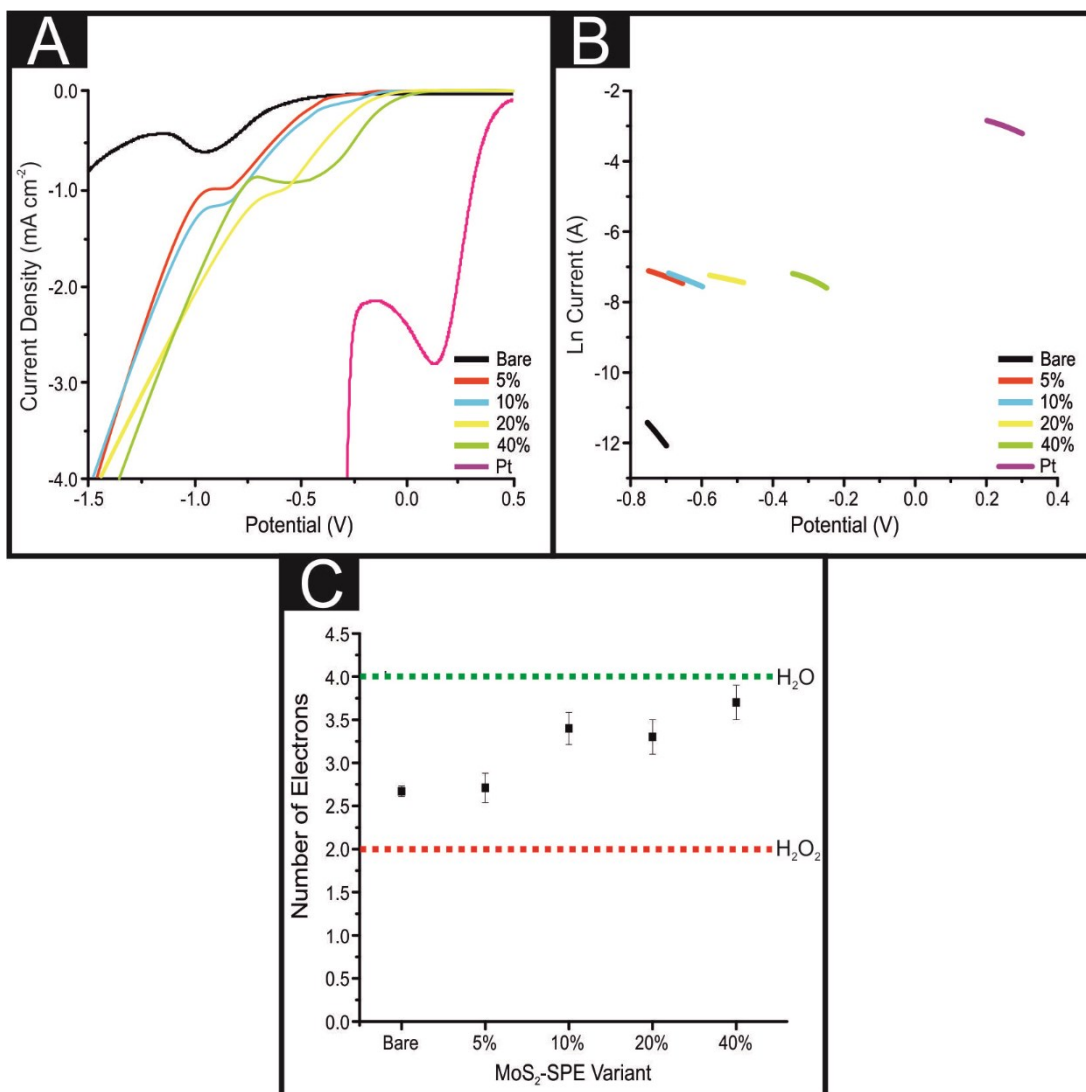


**Figure 6.05.** (A) LSVs of (bare) SPE, 5%, 10%, 20% and 40% 2D-MoS<sub>2</sub>-SPEs<sub>2μm</sub> showing the onset and peak potential for the ORR. Scan rate: 25 mVs<sup>-1</sup> (vs. SCE). Solution composition: 0.1 M H<sub>2</sub>SO<sub>4</sub>. (B) Tafel analysis; ln of current density vs potential for Faradaic section of the LSV presented in (A). (C) The number of electrons involved in the ORR mechanism for a (bare) SPE, 5%, 10%, 20% and 40% 2D-MoS<sub>2</sub>-SPEs<sub>2μm</sub> (average of 3 results plus standard deviation). The green and red dotted lines show the number of electrons required for the ORR process to proceed via the desirable mechanism to produce H<sub>2</sub>O ( $n = 4$ ) or the undesirable mechanism to H<sub>2</sub>O<sub>2</sub> ( $n = 2$ ) respectively.

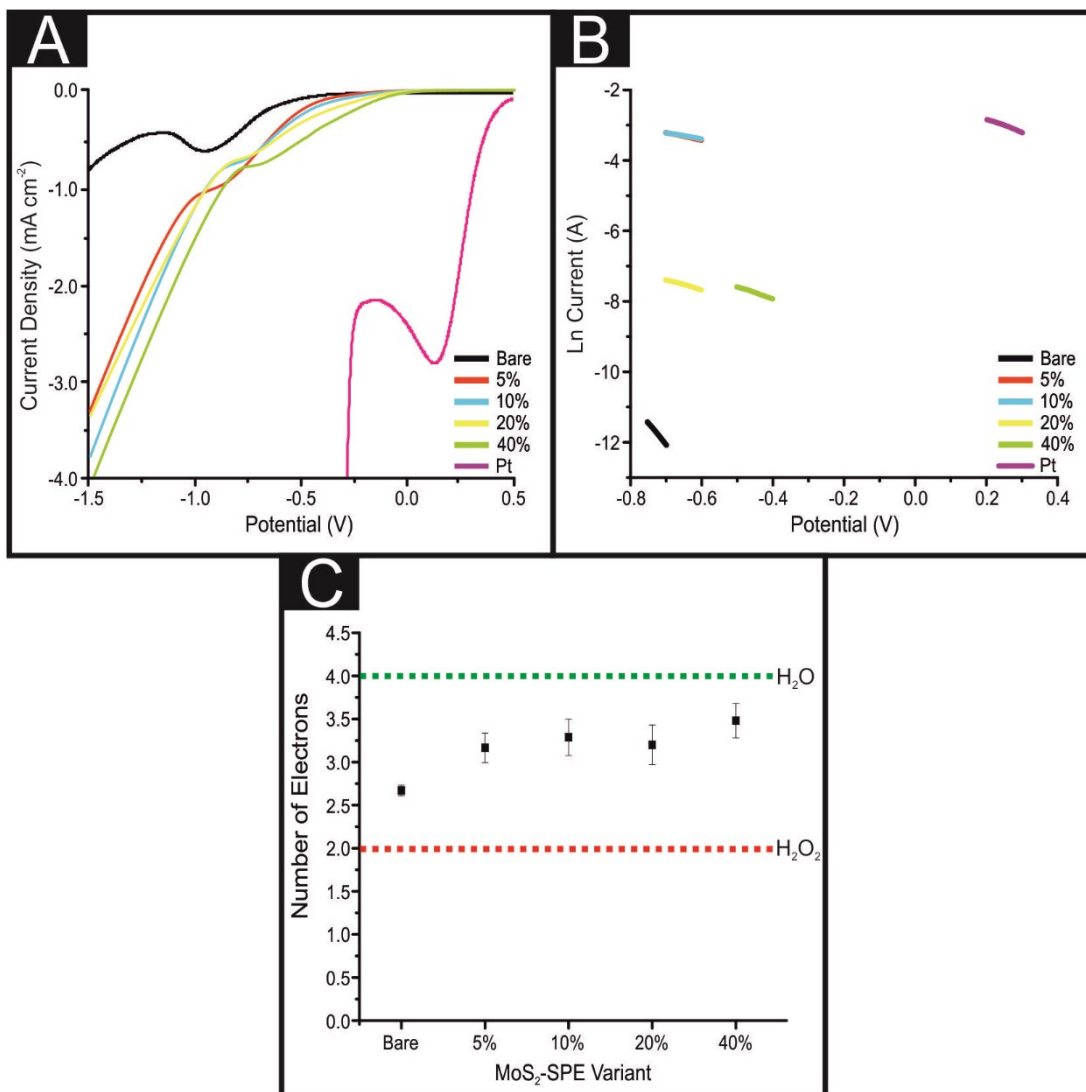


**Figure 6.06.** (A) LSVs of (bare) SPE, 5%, 10%, 20% and 40% 2D-MoS<sub>2</sub>-SPE<sub>S6μm</sub> showing the onset and peak potential for the ORR. Scan rate: 25 mVs<sup>-1</sup> (vs. SCE). Solution composition: 0.1 M H<sub>2</sub>SO<sub>4</sub>. (B) Tafel analysis; ln of current density vs potential for Faradaic section of the LSV presented in (A). (C) The number of electrons involved in the ORR mechanism as a function of electrode composition: (bare) SPE, 5%, 10%, 20% and 40% 2D-MoS<sub>2</sub>-SPE<sub>S6μm</sub> (average of 3 results plus standard deviation). The green and red dotted lines show the number of electrons required for the ORR process to proceed *via* the desirable mechanism to produce H<sub>2</sub>O ( $n = 4$ ) or the undesirable mechanism to H<sub>2</sub>O<sub>2</sub> ( $n = 2$ ) respectively.

2D-MoS<sub>2</sub>-SPE<sub>S2μm</sub> displayed an ORR onset potential for its optimal mass modification (40%) of *ca.* -0.07 V (see Figure 6.05.(A)), which is less electronegative than the ORR onset displayed by the 40% 2D-MoS<sub>2</sub>-SPE<sub>S6μm</sub> (see Figure 6.06.(A)). The ORR onset potentials for the 2D-MoS<sub>2</sub>-SPE<sub>S2μm</sub> and 2D-MoS<sub>2</sub>-SPE<sub>S6μm</sub> were both more electronegative than that displayed by the 2D-MoS<sub>2</sub>-SPE<sub>S400m</sub>. In regards to the number of electrons involved in the ORR reaction mechanism, neither the 2D-MoS<sub>2</sub>-SPE<sub>S2μm</sub> nor the 2D-MoS<sub>2</sub>-SPE<sub>S6μm</sub> allowed for the desirable 4 electron pathway at any percentage mass of incorporation (See Figure 6.05.(C) and Figure 6.06.(C)). It is clearly deducible that implementing a smaller particle size of MoS<sub>2</sub> to produce 2D-MoS<sub>2</sub>-SPEs results in more beneficial ORR activity. As is the case for the HER (explored above) it is likely that the smaller flakes have a proportion of active edge sites (exposed molybdenum sites for oxygen binding) than that of an equivalent mass of a larger flake size.

Electrochemical impedance spectroscopy (EIS) was next used to determine the impedance of the electrode system as the percentage of 2D-MoS<sub>2</sub> increased within the 2D-MoS<sub>2</sub>-SPE<sub>S400nm</sub> ink. Figure 6.07. indicates that the charge transfer resistance ( $\Omega$ ) for all of the 2D-MoS<sub>2</sub>-SPE<sub>S400nm</sub> decreased in comparison to the SPE, which had a  $\Omega$  value of  $6.7 \times 10^3 \Omega$ . Upon a 5% incorporation of 2D-MoS<sub>2</sub> there was a proportionally large  $\Omega$  value decreased to  $3.5 \times 10^3 \Omega$  after which there was a gradual decrease to  $2.2 \times 10^3 \Omega$  by the 40% 2D-MoS<sub>2</sub>-SPE<sub>S400nm</sub>. Error values, corresponding to the expected error in the circuit modelling for the aforementioned results, were recorded as  $6.9 \times 10^{-1}$ ,  $4.9 \times 10^{-1}$ ,  $4.8 \times 10^{-1}$ ,  $5.6 \times 10^{-1}$  and  $3.3 \times 10^{-1} \Omega$  for the SPE, 5, 10, 20 and 40% 2D-MoS<sub>2</sub>-SPE<sub>S400nm</sub>, respectively.

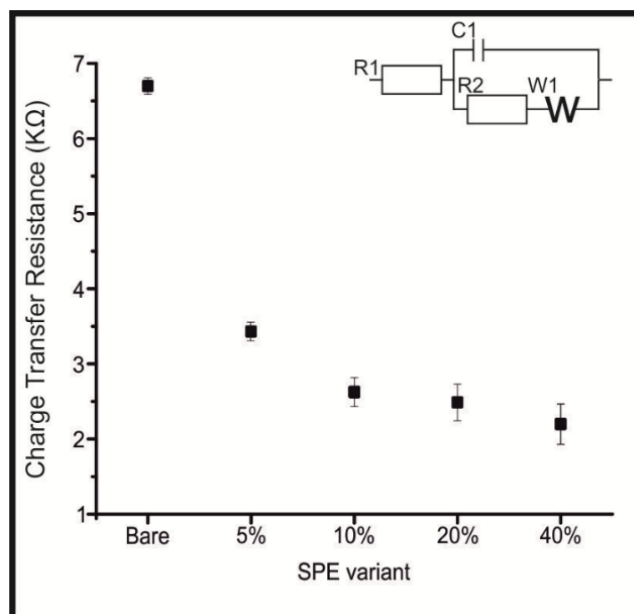


**Figure 6.07.** An EIS study showing charge transfer resistance (ohm) values for the (bare) SPE, 5, 10, 20 and 40% 2D-MoS<sub>2</sub>-SPE<sub>S400nm</sub> (average of 3 results plus standard deviation). The EIS study was carried out in a solution of 1 mM potassium ferrocyanide (II) / 1 M KCl, the frequency was from 0.1–100,000 Hz using an amplitude of 10 mV (vs. SCE). Inset: circuit utilised within experiments. Error values stated within the manuscript.

From the data presented above it is possible to determine that at large (micron) particle sizes and at low percentage incorporation of 2D-MoS<sub>2</sub> into the 2D-MoS<sub>2</sub>-SPE<sub>S400nm</sub> there is a relatively low number of electrochemical pathways. Upon increasing the percentage of 2D-MoS<sub>2</sub> to graphitic ink utilised to produce the 2D-MoS<sub>2</sub>-SPE<sub>S400nm</sub> there is a decrease in the charge transfer resistance, which results in an improvement in the electrochemical response where the ORR process begins to predominately favour the desirable 4 electrochemical produce (H<sub>2</sub>O product).

### 6.2.6. The Cycling Stability and 2D-MoS<sub>2</sub> Coverage of the 2D-MoS<sub>2</sub>-SPEs

---

It was essential for this study to ascertain whether the printing technique implemented herein resulted in a complete and uniform coverage of 2D-MoS<sub>2</sub> onto a SPE's surface. This study therefore employed a Raman mapping technique, encompassing the entire surface of a SPE or 2D-MoS<sub>2</sub>-SPE<sub>400nm</sub>. At each of the points within the Raman grid, a comparison was made between the observed intensity of the peak at 380 cm<sup>-1</sup> (characteristic of 2D-MoS<sub>2</sub>) and the underlying graphite peak at 1580 cm<sup>-1</sup>, thus allowing one to observe the coverage effect of the 2D-MoS<sub>2</sub>.

Figure 6.08. shows that increasing the percentage mass of 2D-MoS<sub>2</sub> within the graphitic ink, used to produce the 2D-MoS<sub>2</sub>-SPE<sub>400nm</sub> surface results in an increased intensity of the 380 cm<sup>-1</sup> Raman peak, signifying that there is a positive correlation between the percentage of 2D-MoS<sub>2</sub> within the separate inks and the 2D-MoS<sub>2</sub> present on the electrodes surface. The visible red (the Raman map of a SPE) coverage in Figure 6.08.(A) signifies that the incorporation of 5% 2D-MoS<sub>2</sub> into the graphitic ink is not a sufficient mass to result in a complete surface coverage. At 10% 2D-MoS<sub>2</sub> incorporation within the ink, there are no visible red points. This study, therefore, proposes that this is the mass at which complete coverage of the electrode surface by 2D-MoS<sub>2</sub> is achieved. Note that due to similarity between the 2D-MoS<sub>2</sub> nanosheets and the graphite/ binder present on the surface of a SPE any attempt to visually distinguish the presence of 2D-MoS<sub>2</sub> on the 2D-MoS<sub>2</sub>-SPE<sub>400nm</sub> surface was unsuccessful, as can be seen in Figure 6.09.

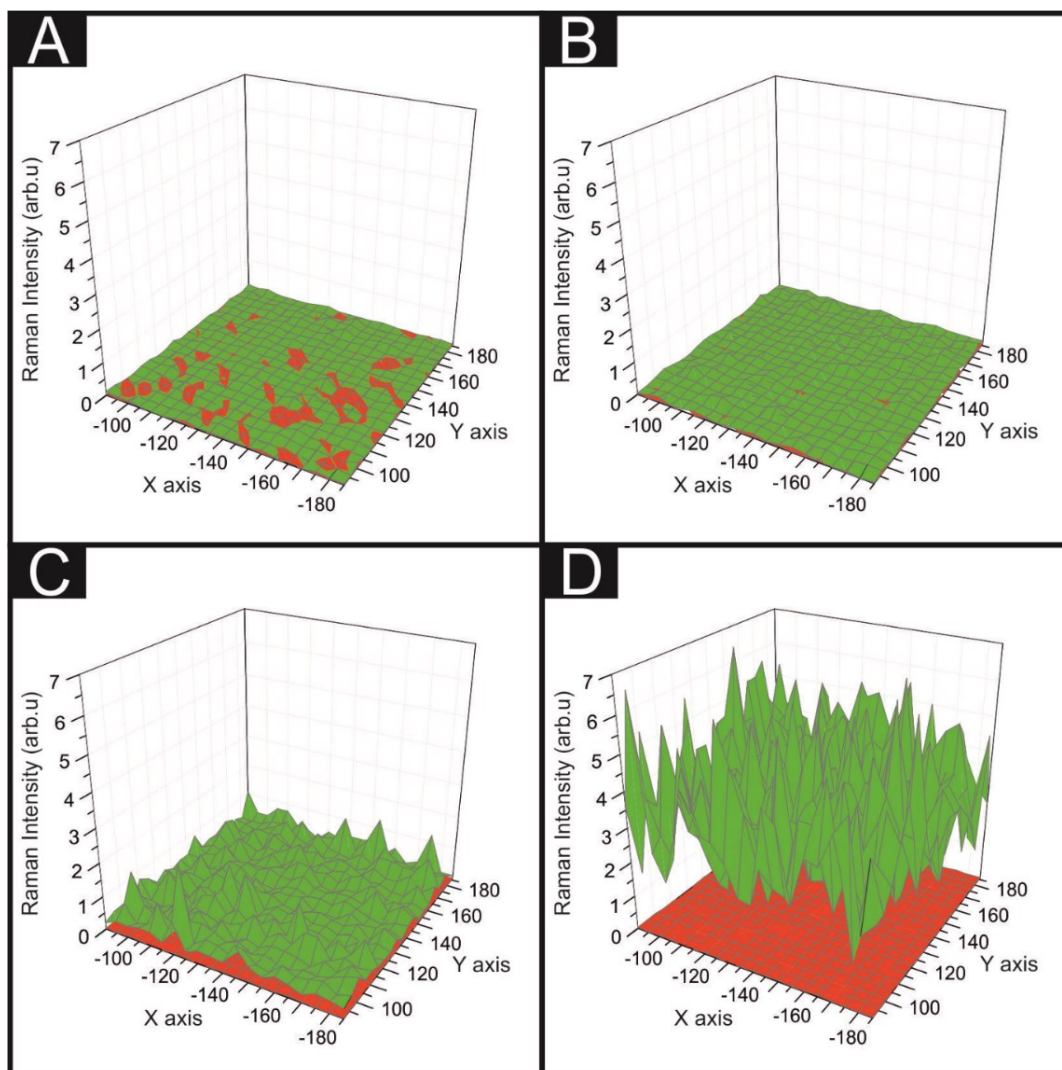


**Figure 6.08.** Raman maps of (A) 5% 2D-MoS<sub>2</sub>-SPE<sub>400nm</sub>, (B) 10% 2D-MoS<sub>2</sub>-SPE<sub>400nm</sub>, (C) 20% 2D-MoS<sub>2</sub>-SPE<sub>400nm</sub> and (D) 40% 2D-MoS<sub>2</sub>-SPE<sub>400nm</sub>. Each point shows the intensity ratio between the sum of the characteristic MoS<sub>2</sub> peak areas (380 cm<sup>-1</sup>) against the area of the underlying graphite peak (1580 cm<sup>-1</sup>). The green map is the 2D-MoS<sub>2</sub>-SPE and the underlying red in each map represents an unmodified electrode surface.

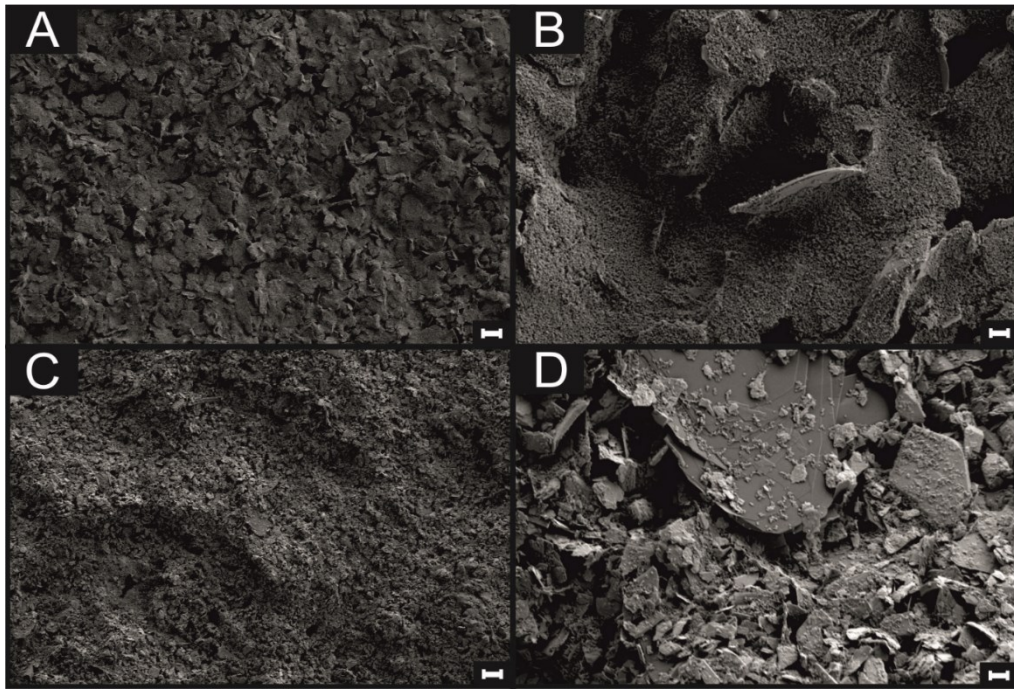


**Figure 6.09.** SEM images of a (bare) SPE surface (A and B) and a 40% 2D-MoS<sub>2</sub>-SPE<sub>400nm</sub> (C and D). SEM magnifications were  $\times 1000$  with a scale bar of  $10\ \mu\text{m}$  and  $\times 10,000$  with a scale bar of  $1\ \mu\text{m}$ , respectively for the progressive images (A to B and C to D).

In order to ascertain the cycling stability of the 2D-MoS<sub>2</sub>-SPEs, 1000 repeat scans were carried out on a 20% 2D-MoS<sub>2</sub>-SPE<sub>S400nm</sub>, which acted as a representative example for all of the 2D-MoS<sub>2</sub>-SPEs. This is a vital consideration, especially for industrially applications where stability and longevity are essential characteristics of an electrode material. Unlike the drop-casting methodology utilising a screen-printing technique has direct transferability to industry as electrocatalytic and PEMFC electrodes are made by screen-printing. Note the development of incorporated SPEs is an advanced form of electrode modification and intrinsically does not allow for a comparison against the drop-casted electrodes described in earlier chapters. A comparison of this manner would however be irrelevant in all regards apart from electrode stability, which we have herein investigated. It is evident upon inspection of Figure 6.10.(A) that the 20% 2D-MoS<sub>2</sub>-SPE<sub>400nm</sub> displays remarkable stability in

respect to its achievable current, as it goes from 41.24 to 41.34  $\mu\text{A}$  for the 1<sup>st</sup> to 1000<sup>th</sup> scan (based upon the current at  $-0.75\text{ V}$  and a cyclic voltammetry (CV) potential range of 0 to  $-1.4\text{ V}$ ).

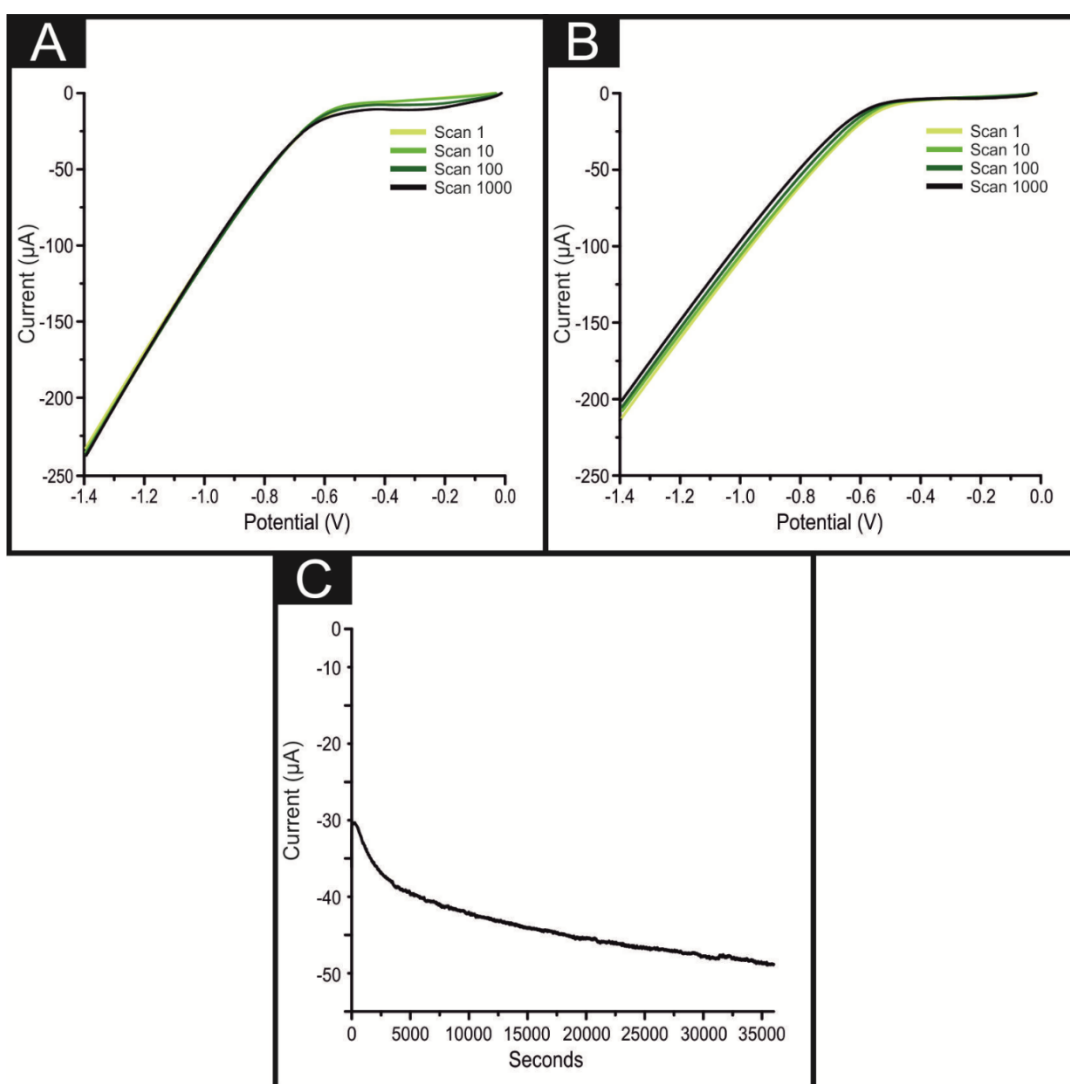


**Figure 6.10.** Cyclic stability examination of (A) 20% 2D-MoS<sub>2</sub>-SPE<sub>400nm</sub> and (B) a SPE with 250 ng cm<sup>-2</sup> of 2D-MoS<sub>2</sub> drop-cast onto its surface. Performed via cycling voltammetry (scan rate: 100 mVs<sup>-1</sup> (vs. SCE), using a carbon counter electrode) between the potential range of 0 to  $-1.4\text{ V}$ , repeated for 1000 cycles. These figures show the initial (yellow line), 10<sup>th</sup> (green line) scans, 100<sup>th</sup> (dark green) and 1000<sup>th</sup>

*scan (black line). (C) The current observed using chronoamperometry with the potential held at  $-0.75\text{ V}$  (vs. SCE) for 36,000 seconds using a 20% 2D-MoS<sub>2</sub>-SPE<sub>400nm</sub> recorded in 0.5 M H<sub>2</sub>SO<sub>4</sub>.*

Note, a carbon based electrode was used as a counter electrode rather than the typical Pt electrode for the duration of this cycling stability. This was to prevent any contamination of the working electrode by in-situ deposition from the Pt counter electrode *via* the mechanism described by Gottlieb *et al.*<sup>171</sup> which would serve to convolute the observed results. Returning to Figure 6.10., there is a redox peak visible at *ca.*  $-0.3\text{ V}$  on the 1000<sup>th</sup> scan which is not visible on the 1<sup>st</sup>, 10<sup>th</sup> and 100<sup>th</sup> scans. This can be attributed to the ORR occurring as oxygen is likely to have permeated the 0.1 M H<sub>2</sub>SO<sub>4</sub> electrolyte over the course of the cycling stability experiment.<sup>75</sup> In order to further explore the stability of the 20% 2D-MoS<sub>2</sub>-SPE<sub>400nm</sub> chronoamperometry was performed at  $-0.75\text{ V}$  for 36,000 seconds as reported within Figure 6.10.(C). The achieved maximum current increased in magnitude from  $-30\text{ }\mu\text{A}$  at 0 seconds to  $-37.4\text{ }\mu\text{A}$  at 2,500 seconds, after which there was a more gradual increase in the current to  $-48.9\text{ }\mu\text{A}$  at 36,000 seconds. Table 6.2. shows the elemental compositions, deduced *via* XPS, of a 20% 2D-MoS<sub>2</sub>-SPE<sub>400nm</sub> *pre-* and *post-* 1000 repeat scans described above. It is clear that no contaminants are present which may have contributed to the prolonged current stability exhibited by the 2D-MoS<sub>2</sub>-SPE<sub>400nm</sub>, such as Pt.

**Table 6.2.** Compositional analysis of XPS spectra for a SPE, 20% 2D-MoS<sub>2</sub>-SPE<sub>400nm</sub> pre- and post- 1000 repeat scan in 0.5 M H<sub>2</sub>SO<sub>4</sub>. Scan rate: 100 mVs<sup>-1</sup> (vs. SCE). Results shown in atom percentage concentration, excluding H which is not detected by this technique.

Electrode	Element	Atom % Concentration
SPE	C 1s	13.46
	O 1s	8.43
	Cl 2p	56.86
2D-MoS <sub>2</sub> -SPE <sub>400nm</sub> pre-1000 scans	C 1s	67.37
	O 1s	11.3
	Cl 2p	6.24
	Mo 3d	4.72
	S 2p	9.63
	Si 2p	0.74
2D-MoS <sub>2</sub> -SPE <sub>400nm</sub> post-1000 scans	C 1s	76.94
	O 1s	7.65
	Cl 2p	8.13
	Mo 3d	1.81
	S 2p	3.67
	Si 2p	1.8

The cycling stability tests infer that the 2D-MoS<sub>2</sub>-SPEs display remarkable stability observed is due to the intrinsic properties of the 2D-MoS<sub>2</sub>-SPE that arise due to the anchoring of 2D-MoS<sub>2</sub> within the bespoke formulated ink. The elemental composition of a 2D-MoS<sub>2</sub>-SPE<sub>400nm</sub> pre- and post- 1000 repeat scan shows significant variation in its elemental concentrations, further study to determine the cause of this would be of interest. It was essential to compare the cycling stability of drop-casting the 2D-MoS<sub>2</sub> onto the surface of a SPE in order to ascertain whether incorporating the 2D-MoS<sub>2</sub> into

the bulk SPE ink offers an advantage in this respect. Figure 6.10.(B) shows the observed CVs of a SPE that had *ca.* 252 ng cm<sup>-2</sup> of 2D-MoS<sub>2</sub> drop-cast onto its surface and then subsequently underwent a cycling stability test under identical conditions as implemented above. Upon inspection of this figure that the HER onset potential became slightly more electronegative over the course of 1000 repeat scans, with the 1<sup>st</sup> scan having a HER onset of *ca.* -480 mV (*vs.* SCE) compared to -520 mV (*vs.* SCE) for the 1000<sup>th</sup> scan. There is also a 21.9 % reduction evident in the observed current (from -49.2 μA at the 1<sup>st</sup> scan to -38.4 μA at the 1000<sup>th</sup> scan, based upon the current at -0.75 V and a CV potential range of 0 to -1.4 V). This reduction of the achievable current is likely due to the delamination of the 2D-MoS<sub>2</sub> from the electrode surface over the course of 1000 scans. Given the results of the cycling stability studies, it can be interfered that by incorporating the 2D-MoS<sub>2</sub> into the bulk SPE ink (rather than drop-casting the 2D-MoS<sub>2</sub>) results in a greater stability of the achievable current.

The intra-repeatability of the 2D-MoS<sub>2</sub>-SPE<sub>S400nm</sub> was also tested (*N* = 3). The percentage relative standard deviation (% RSD) for the observed ORR onset potential and number of electrons involved in the ORR pathway were found to correspond to 2.30, 4.14, 4.57, 4.66 and 4.89 % and 2.13, 4.75, 5.48, 5.74 and 5.82 % for the SPE, 5, 10, 20 and 40% 2D-MoS<sub>2</sub>-SPE<sub>S400nm</sub>, respectively. There is clearly a trend of increasing %RSD corresponding to an increase in the percentage of 2D-MoS<sub>2</sub> within the 2D-MoS<sub>2</sub>-SPE<sub>S400nm</sub>. This study postulates that this is due to a greater percentage of 2D-MoS<sub>2</sub> present leading to a larger number of variations within the orientation of the modified 2D-MoS<sub>2</sub> structure, whereby there will be a different ratio of active edge planes to comparatively inert-basal-planes. The small %RSD values observed for the ORR current density give rise to the high/favourable reproducibility of the screen-printing technique utilised herein to produce the 2D-MoS<sub>2</sub>-SPE<sub>S400nm</sub>. In order to

emphasize the advantages in terms of reproducibility displayed by the 2D-MoS<sub>2</sub>-SPE<sub>S400nm</sub> over drop-casting the 2D-MoS<sub>2</sub>, the RSD value corresponding to the ORR onset potential for SPEs modified with *ca.* 252 ng cm<sup>-2</sup> of 2D-MoS<sub>2</sub> *via* drop-casting were explored. This was observed to be 17.52 %, respectively, which is significantly larger than any of the RSD values (see above) displayed by a 2D-MoS<sub>2</sub>-SPE<sub>S400nm</sub>.

Clearly the 2D-MoS<sub>2</sub>-SPEs have numerous advantages over traditional carbon based electrodes, such as their reproducibility, tailorability and vast economy of scales, whilst also being highly electrocatalytic towards the ORR and HER.

### 6.3. Summation

---

This chapter has reported the production, characterisation and implementation of 2D-MoS<sub>2</sub> electrocatalytic inks that are herein utilised to produce screen-printed electrodes/surfaces (2D-MoS<sub>2</sub>-SPE). Through tailoring the lateral width of the MoS<sub>2</sub> flakes utilised in the 2D-MoS<sub>2</sub>-SPEs production from an average size of *ca.* 400 nm to 2 and 6 μm, it was possible to optimise the 2D-MoS<sub>2</sub>-SPEs electrocatalytic activity towards the ORR and HER. There is a clear trend of increased ORR activity associated with the incorporation of a smaller MoS<sub>2</sub> flake size. This study prescribes this observation to be due to a higher ratio of electrocatalytic Mo and S sites, found at the actives edges of the flake, available relative to the inert basal planes.

Utilising a mass ratio of 40% (400 nm) 2D-MoS<sub>2</sub> to 60% carbon ink to produce optimised 2D-MoS<sub>2</sub>-SPE<sub>S400nm</sub>, results in a ORR onset potential, peak current and average *n* value of + 0.16 V, -1.62 mA cm<sup>-2</sup> and 4.29, respectively. Whilst, also displaying a HER onset potential, current density at -0.75V and Tafel values of -0.50 V, 1.016 mA cm<sup>-2</sup> and 87 mV dec<sup>-1</sup>. These values clearly show that the 40% 2D-

MoS<sub>2</sub>-SPE<sub>400nm</sub> is significantly more electrocatalytic towards the ORR and HER than a typical graphite based SPE. Most promising of all is the observation that at any of the optimised 5, 10, 20 and 40% 2D-MoS<sub>2</sub>-SPE<sub>S400nm</sub> the ORR reaction mechanism was occurring *via* the desirable 4 electron pathway (H<sub>2</sub>O product), rather than the 2 electron pathway (H<sub>2</sub>O<sub>2</sub> product). The 2D-MoS<sub>2</sub>-SPE<sub>400nm</sub> were also shown to be electrochemically stable in regards to their signal output (current), with an optimised 20% 2D-MoS<sub>2</sub>-SPEs displaying an increase of 0.21 %  $\mu$ A in their achievable current being observed over the course of 1000 repeat scans.

The technique by which the 2D-MoS<sub>2</sub> was incorporated into inks and the subsequently fabrication of 2D-MoS<sub>2</sub>-SPE<sub>S400nm</sub> can be readily extended as a template for industrial and research applications seeking to produce cheap, stable and reproducible electrodes/surfaces that would display the unique and interesting electrochemical properties associated with a plethora of 2D nanomaterials that could be incorporated into an ink.

# Chapter 7.

## 2D-MoSe<sub>2</sub> Incorporated Screen-Printed Electrodes Explored towards the Hydrogen Evolution Reaction

Chapter 7 utilises the technique for incorporating 2D-nanomaterials into SPEs in order to fabricate 2D-MoSe<sub>2</sub> incorporated SPEs (2D-MoSe<sub>2</sub>-SPE). These 2D-MoSe<sub>2</sub>-SPEs are then electrochemically explored towards the HER.

### 7.1. Introduction

---

Chapter 6 shows that it is possible to produce electrocatalytic inks, *via* the incorporation of 2D nanomaterials (2D-MoS<sub>2</sub>), which then can be utilised to fabricate 2D-MoS<sub>2</sub>-SPEs that are highly catalytic towards the ORR and moderately electrocatalytic towards HER. This chapter explores the use of 2D-MoSe<sub>2</sub> as a possible preferential HER electrocatalyst that could be incorporated into SPEs.

Modification of carbon based electrodes with electrocatalytic 2D-materials, such as transition metal dichalcogenides (TMD), the most thoroughly researched being 2D-MoS<sub>2</sub>,<sup>74</sup> has become a common approach towards tackling the problem of hydrogen production outlined above.<sup>33, 40, 60, 74, 172</sup> 2D-MoSe<sub>2</sub> has been shown to be an effective electrocatalyst for the HER, however, literature is comparatively sparse compared to 2D-MoS<sub>2</sub>, with Table 7.1. representing a thorough overview of all the studies currently available. 2D-MoSe<sub>2</sub> is a typical TMD semiconducting material, having a structure which is analogous to 2D-MoS<sub>2</sub>, comprising a single layer of Mo sandwiched between two layers of Se atoms (with strong coordinate bonds).<sup>173</sup> 2D-MoSe<sub>2</sub> monolayers are held together *via* weak van der waals forces.<sup>174</sup> Theoretical studies suggest that it is the active edge planes of TMD nanosheets that exhibit the catalytic activity towards the HER, possessing

exchange current densities close to that of the Pt-group metals, whilst the basal planes are relatively inert.<sup>101</sup> Note that terminated edge planes and defect sites of the 2D-MoSe<sub>2</sub> will comprise both Mo and Se atoms, each having distinct electrochemical properties. In this case, it is the dangling bonds of the electronegatively charged Se atoms, located at the edge sites, which have an affinity for binding electropositive H<sup>+</sup> atoms within the electrolyte that arises from having a density functional theory calculated binding energy towards H<sup>+</sup> of -0.05 eV,<sup>175</sup> Thus, these are considered to be the sites responsible for the 2D-electrochemical activity towards the HER.<sup>176</sup> Whilst the studies reported in Table 7.1. are diligent in their approach to exploring MoSe<sub>2</sub> based catalysts towards the HER, there is again a noticeable convention of solely utilising GC electrodes as a supporting electrode material with which to electrically “wire” the catalytic material, with limited attempts to utilise alternative supporting electrodes. Similar to Pt, GC is relatively expensive and thus limits its applicability within electrolyzers and fuel cells.

In an attempt to produce a desirable alternative to the GC and Pt electrodes currently utilised within electrolyzers, this study aims to produce a facile and highly reproducible technique for the creation of highly electrocatalytic SPE variants by doping readily available carbon ink recipes with varying percentage (mass) contributions of 2D-MoSe<sub>2</sub>. It is expected that the fabricated electrodes will exhibit high reproducibility, excellent cycling stability and demonstrate low overpotentials towards the HER. Several studies within the literature have previously used the term “ink”,<sup>155, 177</sup> when describing the slurry containing their particular electrocatalyst, however according to the available literature, this study is the first to produce, characterise and implement a true screen-printable 2D-MoSe<sub>2</sub> incorporated electrocatalytic ink.

**Table 7.1.** Comparison of current literature reporting the use of MoSe<sub>2</sub> and related catalytic materials explored towards the HER.

Catalyst	Supporting Electrode	Loading	Deposition Technique	Cycling Stability (CS) Duration	Potential Range of CS	CS performance	Electrolyte	HER onset (V)	Tafel (mV dec <sup>-1</sup> )	Reference
MoSe <sub>2</sub> /GN	GC	–	PECVD on a graphite disc.	6000 secs	Continuous at – 0.15 (V vs. RHE)	Ca. 88% retention	0.5 M H <sub>2</sub> SO <sub>4</sub>	– 0.05 (V vs. RHE)	61	101
MoSe <sub>2</sub> /rGO	GC	0.16 mg cm <sup>-2</sup>	Drop-casting	7200 secs	+ 0.10 to – 0.35 (V vs. RHE)	b	0.5 M H <sub>2</sub> SO <sub>4</sub>	– 0.05 (V vs. RHE)	69	178
MoSe <sub>2</sub> nanofilm	Carbon NW and NF	–	RSP	15,000 cycles	+ 0.10 to – 0.28 (V vs. RHE)	c	0.5 M H <sub>2</sub> SO <sub>4</sub>	– 0.11 (V vs. RHE)	60	103
Vertically aligned MoSe <sub>2</sub>	GC	0.0135 µg cm <sup>-2</sup>	Grown on GC	1000 cycles	0.00 to – 0.45 (V vs. SCE)	b	0.5 M H <sub>2</sub> SO <sub>4</sub>	– 0.20 (V vs. RHE)	105-120	138
MoS <sub>2(1-x)Se<sub>2x</sub></sub> nanoflakes	GC	ca. 0.28 mg cm <sup>-2</sup>	Drop-casting	8000 cycles	0.00 to – 0.44 (V vs. SCE)	b	0.5 M H <sub>2</sub> SO <sub>4</sub>	– 0.35 to – 0.38 (V vs. SCE)	45	179
MoSe <sub>2</sub> nanosheets	GC	–	Drop-casting	2000 cycles	+ 0.10 to – 0.30 (V vs. RHE)	b	0.5 M H <sub>2</sub> SO <sub>4</sub>	– 0.08 (V vs. RHE)	80	84
MoSe <sub>2</sub> /CoSe <sub>2</sub> composite (1:1 ratio)	GC	0.29 mg cm <sup>-2</sup>	Drop-casting	1000 cycles	+ 0.10 and – 0.50 V (vs. RHE)	b	0.5 M H <sub>2</sub> SO <sub>4</sub>	– 0.11 (V vs. RHE)	73	180
MoSe <sub>2</sub> -NiSe	GC	0.29 mg cm <sup>-2</sup>	Drop-casting	1000 cycles	+ 0.20 and – 0.30 V (vs. RHE)	b	0.5 M H <sub>2</sub> SO <sub>4</sub>	– 0.15 (V vs. RHE)	56	177
MoSe <sub>2</sub> nanosheets	Carbon cloth	–	EPD	1000 cycles	+ 0.10 and – 0.35 V (vs. RHE)	b	0.5 M H <sub>2</sub> SO <sub>4</sub>	– 0.22 (V vs. RHE)	76	181
2D-MoSe <sub>2</sub> ink	SPE	5% *	Screen-Printed	33,600 secs / 1000 cycles	0.00 to – 1.40 (V vs. SCE)	c	0.5 M H <sub>2</sub> SO <sub>4</sub>	– 0.44 (V vs. SCE)	49	This Work
2D-MoSe <sub>2</sub> ink	SPE	10% *	Screen-Printed	33,600 secs / 1000 cycles	0.00 to – 1.40 (V vs. SCE)	c	0.5 M H <sub>2</sub> SO <sub>4</sub>	– 0.45 (V vs. SCE)	47	This Work
2D-MoSe <sub>2</sub> ink	SPE	20% *	Screen-Printed	33,600 secs / 1000 cycles	0.00 to – 1.40 (V vs. SCE)	c	0.5 M H <sub>2</sub> SO <sub>4</sub>	– 0.43 (V vs. SCE)	63	This Work

2D-MoSe <sub>2</sub> ink	SPE	40% *	Screen-Printed	33,600 secs / 1000 cycles	0.00 to -1.40 (V vs. SCE)	c	0.5 M H <sub>2</sub> SO <sub>4</sub>	-0.43 (V vs. SCE)	230	This Work
--------------------------	-----	-------	----------------	---------------------------	---------------------------	---	--------------------------------------	-------------------	-----	-----------

---

**Key:** -: Value unknown, GN: graphene nanosheets, GC: glassy carbon, PECVD: Plasma-enhanced chemical vapor deposition, <sup>a</sup>; the achievable current density is stable over the duration reported, RHE; reversible hydrogen electrode, <sup>b</sup>; degradation in the achievable current density over the duration reported, SCE; saturated calomel electrode, rGO: reduced graphene oxide, NW: nanowires, NF: nanofibers, EPD: electrophoresis deposition, \*: mass of 2D-MoSe<sub>2</sub> to mass of conductive carbon ink ratio, SPE; screen-printed electrode, <sup>c</sup>; increase in the achievable current density over the duration reported

## 7.2. Results and Discussion

### 7.2.1. Fabrication and Characterisation of the 2D-MoSe<sub>2</sub>-SPEs

---

Chapter 4 has shown that SPEs can be used as a preferential alternative to GC electrodes as a supporting material towards the HER.<sup>74</sup> The typical method of modifying a supporting electrode with a desired electrocatalyst is the drop-casting technique (see Table 7.1), which has several disadvantages (as outlined above). In order to overcome these disadvantages, this study has created novel conductive inks *via* the incorporation of 5, 10, 20 and 40% 2D-MoSe<sub>2</sub> into to carbon ink on a % mass ratio (*i.e.*  $M_P$  to  $M_I \times 100$ ) in the same manner as the 2D-MoS<sub>2</sub>-SPEs described in Chapter 6. Subsequently this study utilises these novel inks to create 2D-MoSe<sub>2</sub> containing screen-printed electrodes (2D-MoSe<sub>2</sub>-SPE) *via* the screen-printing technique described in the Experimental Section, which were explored towards the HER and their electrocatalytic performance for future implementation was examined.

#### 7.2.2.1. Electrocatalytic Activity of the 2D-MoSe<sub>2</sub>-SPEs towards the HER

---

It was first essential to benchmark the electrochemical behaviour of a bare/unmodified SPE towards the HER in 0.5 M H<sub>2</sub>SO<sub>4</sub> as is common within the literature.<sup>75</sup> Figure 7.01.(A) shows linear sweep voltammetry (LSV) for a bare/unmodified SPE as well as for 5, 10, 20 and 40% 2D-MoSe<sub>2</sub>-SPEs.

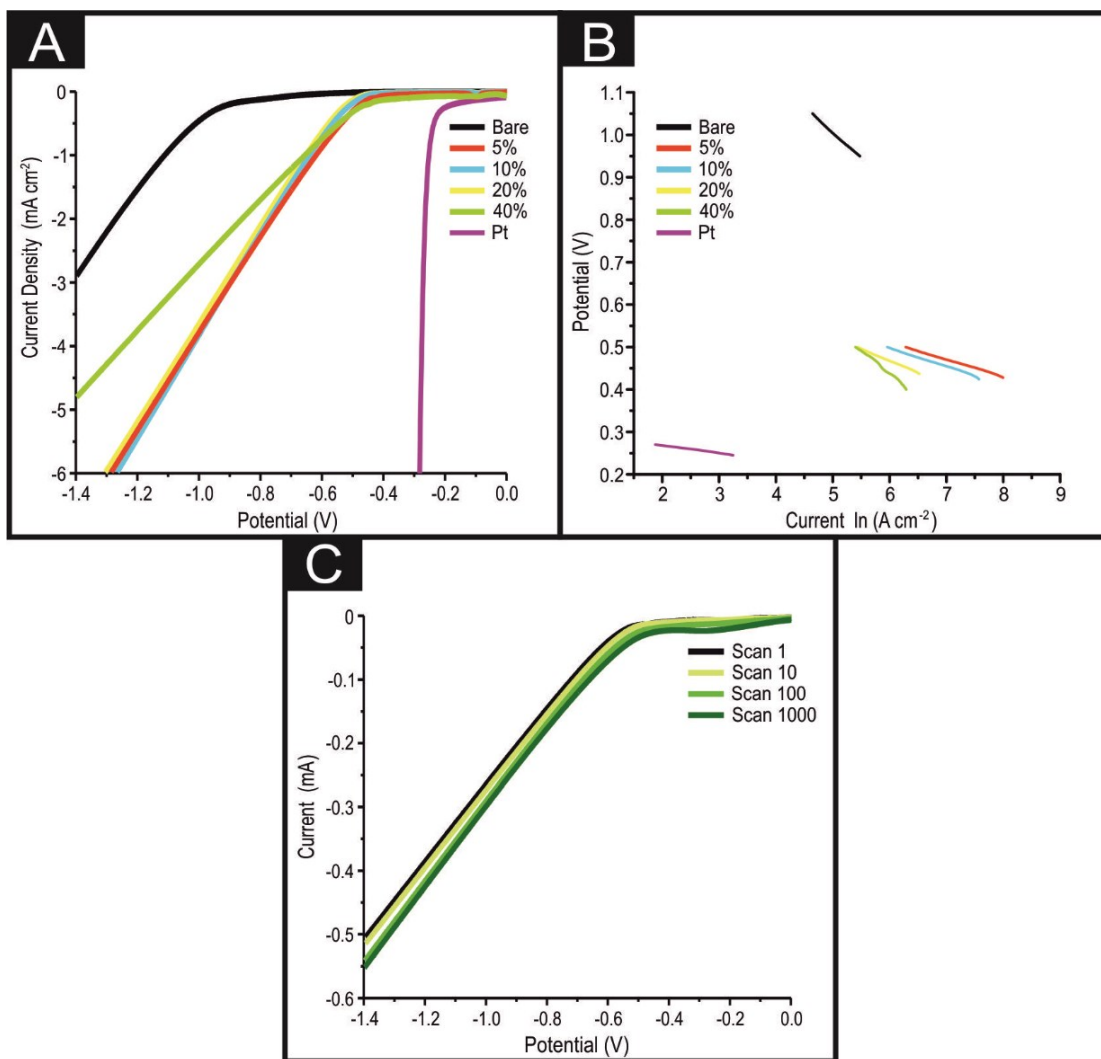


**Figure 7.01.** (A) LSV of bare/unmodified SPE, 5%, 10%, 20% and 40% 2D-MoSe<sub>2</sub>-SPEs showing the onset of the HER. Scan rate: 25 mVs<sup>-1</sup> (vs. SCE). Solution composition: 0.5 M H<sub>2</sub>SO<sub>4</sub>. (B) Tafel analysis; potential vs. ln of current density for Faradaic section of the LSV presented in (A). (C) Cyclic stability examination of a 10% 2D-MoSe<sub>2</sub>-SPE via LSV (scan rate: 100 mVs<sup>-1</sup> (vs. SCE)) was performed between the potential range of 0 to -1.4 V, repeated for 1000 cycles, these figures show the initial (black), 10<sup>th</sup> (yellow) scans, 100<sup>th</sup> (light green) and 1000<sup>th</sup> scan (dark green).

The bare/unmodified SPE exhibited a HER onset of -880 mV and a current density of 0.095 mA cm<sup>-2</sup> at a potential of -0.75 V. As expected this is far more electronegative than the HER onset of Pt (ca. -0.25 V).

It is clearly observable that all the 2D-MoSe<sub>2</sub>-SPEs have a HER onset potential which occurs at *ca.* -430 mV (see Figure 7.01.(A)). This value is significantly less electronegative than that of a bare/unmodified SPE and closer to the optimal of Pt. There is also a substantial increase in the recorded current density with the 5, 10, 20 and 40% 2D-MoSe<sub>2</sub>-SPEs exhibiting a current density at -0.75 V of 1.7, 1.8, 1.9 and 1.5 mA cm<sup>-2</sup> respectively, indicating a far greater production of the desired H<sub>2</sub> (gas) compared to the bare/unmodified SPE. The decrease in the electronegativity of the HER overpotential and the increase in observed current density indicates that the 2D-MoSe<sub>2</sub> incorporated ink is an effective electrocatalyst towards the HER. Whilst the 40% 2D-MoSe<sub>2</sub>-SPE has a comparable HER onset to the other 2D-MoSe<sub>2</sub>-SPEs, it appears to produce H<sub>2</sub> (gas) at a slower rate, represented by the smaller current density at -0.75 V.

#### 7.2.2.2. Tafel Analysis in order to Determine the Rate Limiting HER step Exhibited by the 2D-MoSe<sub>2</sub>-SPEs

---

As the 2D-MoSe<sub>2</sub>-SPEs demonstrate a greater proficiency at catalysing the HER it can be inferred that the electrochemical reaction mechanism occurring must be altering to account for this. In the same manner as the previous chapters, Tafel analysis was utilised in order to determine the exact reaction mechanism.<sup>74</sup>

Tafel analysis was performed on the Faradaic sections of the LSVs shown in Figure 7.01.(A) with the resultant Tafel slopes being exhibited in Figure 7.01.(B). The Tafel slope values obtained for the bare/unmodified SPE, 5, 10, 20 and 40% 2D-MoSe<sub>2</sub>-SPEs correspond to 120, 49, 47, 63 and 230 mV dec<sup>-1</sup>. Interpretation of these values suggests that the rate limiting step of the HER reaction mechanism on the SPE

is, once again, the “adsorption Volmer” step, whereas it is plausibly the “discharge Heyrosky step” for the 5, 10 and 20% 2D-MoSe<sub>2</sub>-SPEs. This change in the HER mechanism is indicative of a reduction in the free energy barrier of the discharge step, resulting in an improvement of the observed HER activity.<sup>103</sup> The 40% 2D-MoSe<sub>2</sub>-SPE Tafel slope value is too large to be accurately described by the Tafel analysis, however the size of the value implies very poor HER activity with the initial step of H<sup>+</sup> adsorption being the rate limiting step, with a small surface coverage of adsorbed hydrogen.

It is clear from the above analysis that there is an optimal ratio of 2D-MoSe<sub>2</sub> to carbon ink. In this case the optimal ratio is between 10% and 20%. At this optimal ratio it is probable that the structural model of the 2D-MoSe<sub>2</sub>-ink has proportionally the greatest number of exposed electrocatalytic edge planes to relatively inert basal planes of 2D-MoSe<sub>2</sub>. Thus, resulting in the least electronegative HER onsets and the highest achievable current densities. Once the percentage mass of 2D-MoSe<sub>2</sub> within the ink has exceeded the optimal ratio there is a severe reduction in the observed current density, as observed for the 40% 2D-MoSe<sub>2</sub>-SPE. This reduction in the achievable current density is possibly a result of the structure of 2D-MoSe<sub>2</sub> at percentages greater than 20% recombining into bulk forms within the SPE ink and results in an increase in the charge transfer resistance and smaller number of exposed edge plane for H<sup>+</sup> binding. Interestingly this is the same trend exhibited by the 2D-MoS<sub>2</sub>-SPE<sub>S400nm</sub> towards the HER, this strongly suggests that 20% is optimal concentration for of a 2D nanomaterial to be incorporated into an SPE, if that SPE is to be utilised towards the HER.

### 7.2.2.3. HER Turn over Frequency of the 2D-MoSe<sub>2</sub>-SPEs

---

In order to assess the intrinsic catalytic activity being displayed by the 2D-MoSe<sub>2</sub> upon the surface of the 2D-MoSe<sub>2</sub>-SPE on a “per active site basis”, the turn over frequency (ToF) was deduced in a similar manner to the ToF calculation presented for the 2D-MoS<sub>2</sub> in Chapter 4, however with subtle differences, it is therefore, once again, described below. The 2D-MoSe<sub>2</sub> alters with varying percentage of ink modification on a ‘per active site’ basis, the ToF was deduced using a modified method reported previously.<sup>74, 130</sup> In this calculation it is assumed that the surface of the 2D-MoSe<sub>2</sub> nanosheets are atomically flat (although the true modification will have a finite roughness).<sup>130</sup> Taking the selenium to selenium bond distance to be 2.735 Å which corresponds to an area of 4.12 Å<sup>2</sup>/Se atom, which can be used to calculate the surface area occupied by each MoSe<sub>2</sub>:

$$4.12 \frac{\text{Å}^2}{\text{Se atom}} * \frac{2 \text{ Se atom}}{1 \text{ MoSe}_2} = 8.24 \frac{\text{Å}^2}{\text{MoSe}_2} \quad (7.1)$$

Using the derived area for a MoSe<sub>2</sub> molecule (corresponding to the number of surface sites for a flat standard), it is possible to determine the number of MoSe<sub>2</sub> molecules per cm<sup>2</sup> geometric area:

$$\frac{1 \text{ MoSe}_2}{8.24 \text{ Å}^2} * \frac{10^{16} \text{ Å}^2}{0.0707 \text{ cm}^2} = 1.717 * 10^{16} \frac{\text{MoSe}_2}{\text{cm}^2} \quad (7.2)$$

The number of electrochemically accessible surface sites can be determined from the following:

$$\frac{\# \text{ Surface Sites (Catalyst)}}{\text{cm}^2 \text{ geometric area}} = \frac{\# \text{ Surface Sites (Flat Standard)}}{\text{cm}^2 \text{ geometric area}} * R_F \quad (7.3)$$

It is also essential to accurately determine the roughness factor ( $R_F$ ) for each of the 2D-MoSe<sub>2</sub>-SPE's as is common within the literature (the  $R_F$  value was deduced using

the double layer capacitance method described in Chapter 4 along with Appendix Figures A.4 and A.5). The following allows the ToF on a per-site basis to be determined:

$$TOF \text{ per site} = \frac{\# \text{ Total Hydrogen Turn Overs} / \text{cm}^2 \text{ geometric area}}{\# \text{ Surface Sites (Catalyst)} / \text{cm}^2 \text{ geometric area}} \quad (7.4)$$

Taking the value of current density ( $\text{mA cm}^{-2}$ ) at the potential of  $-0.75 \text{ V}$  (at a  $25 \text{ mVs}^{-1}$  scan rate) and using the  $R_F$  calculated, per-site the ToF can be deduced from the following:

$$\left( j \frac{\text{mA}}{\text{cm}^2} \right) \left( \frac{1 \text{ A}}{1000 \text{ mA}} \right) \left( \frac{1 \text{ C/s}}{1 \text{ A}} \right) \left( \frac{1 \text{ mol } e^-}{96,485.3 \text{ C}} \right) \left( \frac{1 \text{ mol } H_2}{2 \text{ mol } e^-} \right) \left( \frac{6.02214 \times 10^{23}}{1 \text{ mol } H_2} \right) = 5.358 * 10^{15} \frac{H_2/Se}{\text{cm}^2} \text{ per } \frac{\text{mA}}{\text{cm}^2} \quad (7.5)$$

Using equation 7.6 and a value derived from formula 7.5, it is possible to determine a value for the ToF:

$$\left( 5.358 * 10^{15} \frac{H_2/Se}{\text{cm}^2} \right) \left( \frac{10 \frac{\text{mA}}{\text{cm}^2}}{\frac{\text{mA}}{\text{cm}^2}} \right) \left( \frac{1 \text{ cm}^2}{3.604 * 10^{16} \text{ surface sites}} \right) = 1.48 \frac{H_2/Se}{\text{surface sites}} \quad (7.6)$$

At the chosen potential ( $-0.75 \text{ V}$ ), the current densities were found to correspond to  $-1.52$ ,  $-1.72$ ,  $-1.67$  and  $-1.01 \text{ mA cm}^{-2}$  for the 5, 10, 20 and 40% 2D-MoSe<sub>2</sub>-SPE's. Using these values the ToF values deduced from the above equations were found to correspond to 2.76, 1.48, 0.92 and  $0.36 \frac{H_2/Se}{\text{Surface Site}}$ .

It is evident that with an increased percentage of 2D-MoSe<sub>2</sub>, there is a decrease in the ToF value obtained. This could be a result of larger ratios of 2D-MoSe<sub>2</sub> to conductive carbon ink leading to competition for available H<sup>+</sup> between the active edge plane sites present on the surface. It could also be as a result of the larger masses of 2D-MoSe<sub>2</sub> forming a structure where there is increased shielding of the

electronegative Se atoms located at the active edge planes by the relatively inactive basal planes.<sup>173</sup>

### 7.2.3. The Cycling Stability and 2D-MoSe<sub>2</sub> Coverage of the 2D-MoSe<sub>2</sub>-SPEs

---

Once again it was necessary to ascertain whether the printing technique implemented herein resulted in a complete and uniform coverage of 2D-MoSe<sub>2</sub> onto a SPE's surface. Therefore, the Raman mapping technique described in earlier chapters was employed on a SPE and 2D-MoSe<sub>2</sub>-SPEs. At each of the points within the Raman grid a comparison was made between the observed intensity of the peak at 240 cm<sup>-1</sup> (characteristic of 2D-MoSe<sub>2</sub>) and the underlying graphite peak at 1580 cm<sup>-1</sup>, thus allowing one to observe the coverage effect of the 2D-MoSe<sub>2</sub>. It is evident upon inspection of Figure 7.02. that increasing the percentage mass of 2D-MoSe<sub>2</sub> within the graphitic ink, used to produce the 2D-MoSe<sub>2</sub>-SPEs surface, results in an increased intensity of the 240 cm<sup>-1</sup> Raman peak.

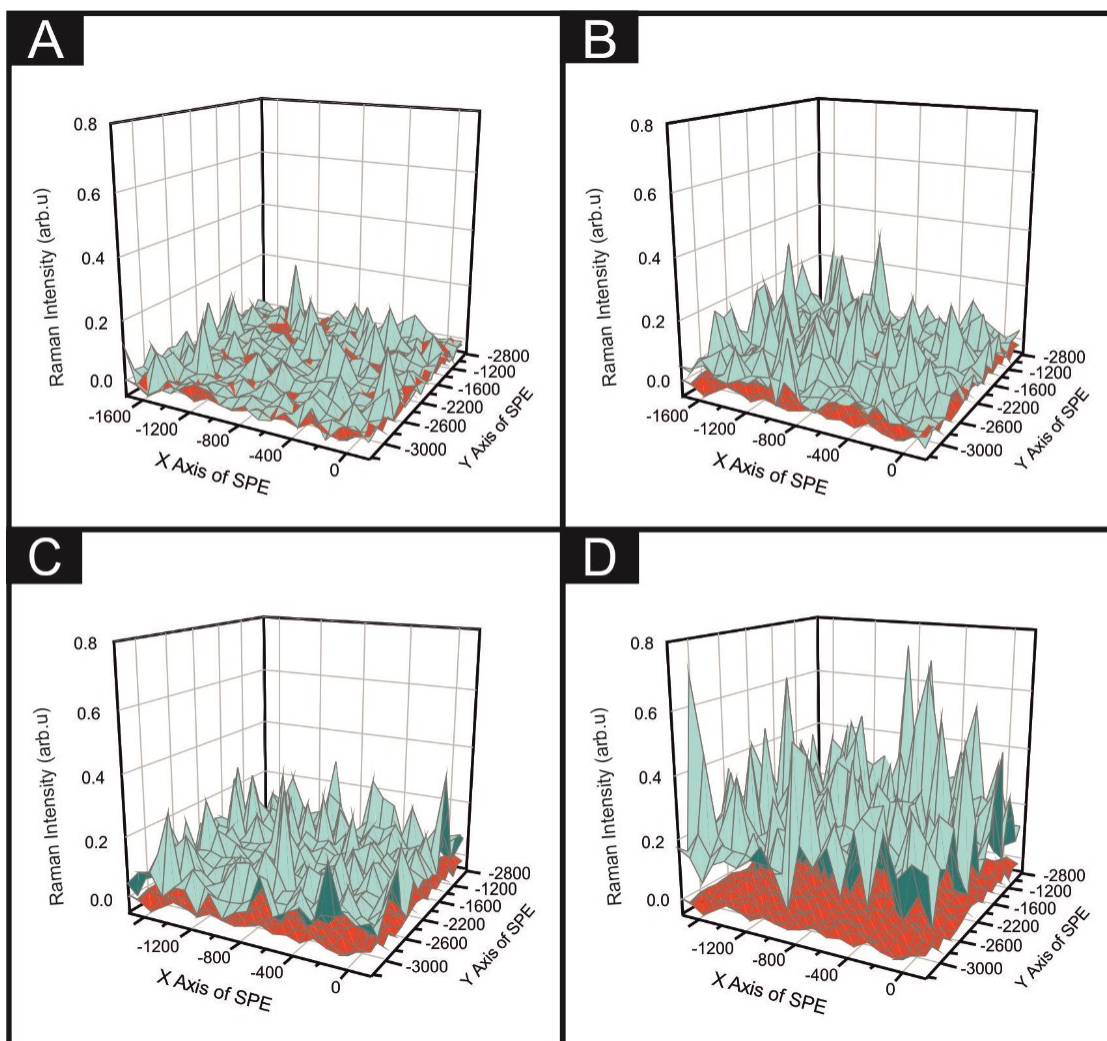


**Figure 7.02.** Raman maps showing the surface of (A) 5% 2D-MoSe<sub>2</sub>-SPE, (B) 10% 2D-MoSe<sub>2</sub>-SPE, (C) 20% 2D-MoSe<sub>2</sub>-SPE and (D) 40% 2D-MoSe<sub>2</sub>-SPE. Each point shows the intensity ratio between the sum of the characteristic MoSe<sub>2</sub> peak areas (240 cm<sup>-1</sup>) against the area of the underlying graphite peak (1580 cm<sup>-1</sup>). The green maps are the 2D-MoSe<sub>2</sub>-SPE and the underlying red in each map represents an unmodified electrode surface.

These results signify that there is a positive correlation between the percentage of 2D-MoSe<sub>2</sub> within the separate inks and the 2D-MoSe<sub>2</sub> on the surface of the electrode. The visible red (the Raman map of a bare/unmodified SPE) coverage in Figure 7.02.(A) signifies that the incorporation of 5% 2D-MoSe<sub>2</sub> into the graphitic ink is not a sufficient mass to result in a complete coverage of the underlying SPE's surface. At 10% 2D-MoSe<sub>2</sub> incorporation within the ink, the number of points in which

the underlying red is visible has greatly diminished. This study therefore suggest that the 10% 2D-MoSe<sub>2</sub>-SPE has complete and uniform coverage upon the electrodes surface. Note that trying to visually assess 2D-MoSe<sub>2</sub> on the surface of an SPE *via* SEM analysis was found to be inconclusive given that the 2D-MoSe<sub>2</sub> proved to be indistinguishable from the underlying SPE surface, as evident in Figure 7.03.

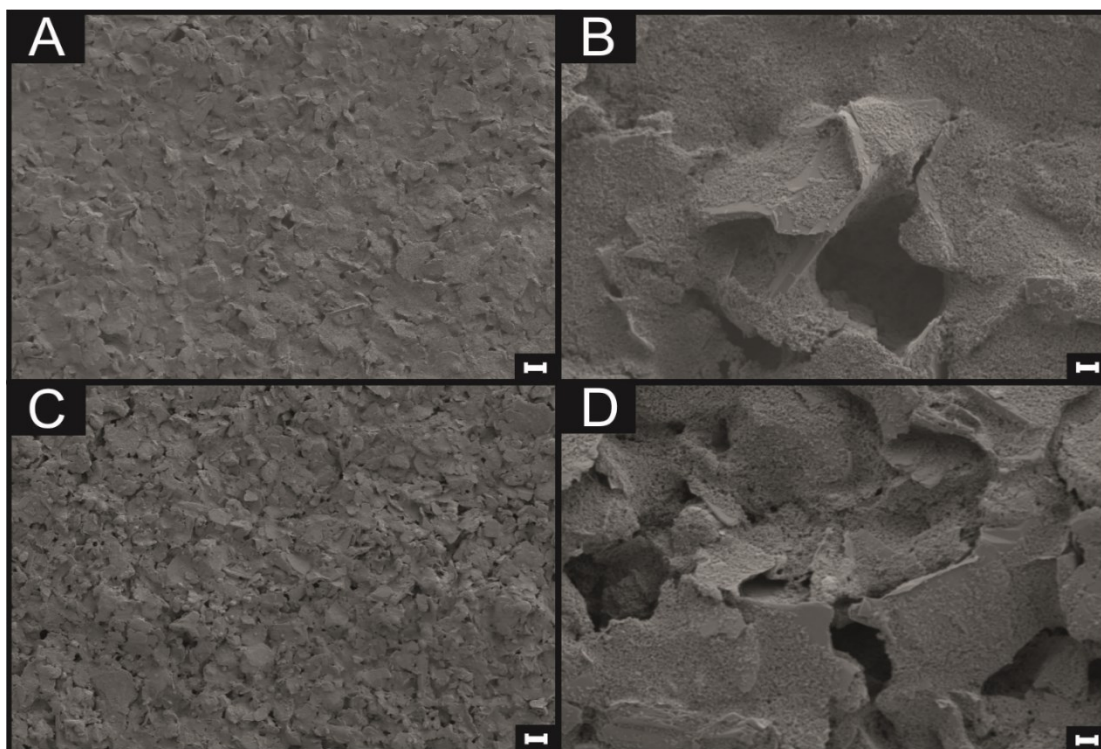


**Figure 7.03.** SEM images of a bare/unmodified SPE surface (A and B) and a 10% 2D-MoSe<sub>2</sub>-SPE (C and D). SEM magnifications were  $\times 1k$  (scale bar, 10  $\mu m$ ) and  $\times 10k$  (scale bar, 1  $\mu m$ ) respectively for the progressive images (A to B and C to D).

The intra-repeatability of the 2D-MoSe<sub>2</sub>-SPEs were evaluated ( $N = 3$ ). The percentage relative standard deviation (% RSD) for the observed HER onset potential and current density values at  $-0.75$  V were found to correspond to 0.74, 1.41, 1.82 and 1.95 % and 5.30, 3.64, 4.68 and 3.91 % for the 5, 10, 20 and 40% 2D-MoSe<sub>2</sub>-SPEs, respectively. With respect to the observed HER onset, there is clearly a trend of increasing %RSD corresponding to an increase in the percentage of 2D-MoSe<sub>2</sub> within the 2D-MoSe<sub>2</sub>-SPEs. It is postulated that this is due to a greater percentage of 2D-

MoSe<sub>2</sub> present leading to a larger number of variations within the orientation of the modified 2D-MoSe<sub>2</sub> structure, whereby there will be a different ratio of active edge planes to comparatively inert basal planes.<sup>101</sup> The small %RSD values observed for the HER onset and current density give rise to the high/favourable reproducibility of the screen-printing technique utilised herein to produce the 2D-MoSe<sub>2</sub>-SPEs. In order to emphasize the advantages in terms of reproducibility displayed by the 2D-MoSe<sub>2</sub>-SPEs over drop-casting the 2D-MoSe<sub>2</sub>, the RSD values are explored that correspond to the current density values at -0.75 V for bare SPEs with 400 ng cm<sup>-2</sup> of 2D-MoSe<sub>2</sub>. This was observed to be 11.43 %, which is significantly larger than any of the RSD values (see above) displayed by a 2D-MoSe<sub>2</sub>-SPE.

Electrochemical impedance spectroscopy (EIS) was used to determine the impedance of the electrode system as the percentage of 2D-MoSe<sub>2</sub> increased within the SPE ink. Figure 7.04. indicates that the charge transfer resistance ( $\Omega$ ) for all of the 2D-MoSe<sub>2</sub>-SPEs decreased in comparison to the bare/unmodified SPE, which had a  $\Omega$  value of  $6.7 \times 10^3 \Omega$ . The  $\Omega$  value decreased from  $4.1 \times 10^3$  to  $2.3 \times 10^3 \Omega$  with a change in the percentage 2D-MoSe<sub>2</sub> ink composition from 5% to 10% 2D-MoSe<sub>2</sub>-SPEs, respectively. A subsequent further increase was observed corresponding with the 20% and 40% inks to 3.0 and 4.3  $\Omega$  respectively. The 40% 2D-MoSe<sub>2</sub>-SPE having the highest  $\Omega$  value of all the 2D-MoSe<sub>2</sub>-SPEs examined herein which again is attributed to the MoSe<sub>2</sub> forming bulk structures resulting in resistance changes. Error values for the aforementioned results were recorded as  $6.9 \times 10^{-1}$ ,  $4.4 \times 10^{-1}$ ,  $5.9 \times 10^{-1}$ ,  $3.4 \times 10^{-1}$  and  $7.7 \times 10^{-1} \Omega$  for the SPE, 5, 10, 20 and 40% 2D-MoSe<sub>2</sub>-SPEs, respectively. The EIS data presented above supports the prior inference that 2D-MoSe<sub>2</sub>-SPEs are effective electrocatalysts for the HER and that the optimal mass of ink modification is *ca.* 10%.

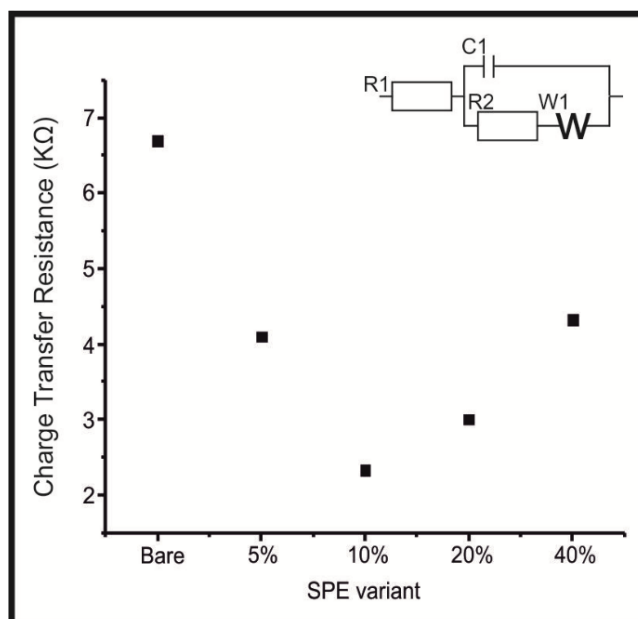


**Figure 7.04.** An EIS study showing charge transfer resistance (ohm) values for the bare/unmodified, 5, 10, 20 and 40% 2D-MoSe<sub>2</sub>-SPE. The EIS study was carried out in 1 mM potassium ferrocyanide (II) in 1 M KCl, the frequency was from 0.1–100,000 Hz using an amplitude of 10 mV (vs. SCE). Inset: circuit utilised within experiments.

Next, it was essential to assess the electrocatalytic stability of 2D-MoSe<sub>2</sub>-SPEs towards the HER. This is a vital consideration in the utilisation of this technology for industrial applications where concerns over stability and longevity are at the forefront. Using a 10% 2D-MoSe<sub>2</sub>-SPE as a representative example for all of the 2D-MoSe<sub>2</sub>-SPEs, it is evident upon inspection of Figure 7.01.(C) that the 10% 2D-MoSe<sub>2</sub>-SPE retains its HER onset of *ca.* –430 mV. This electrode exhibits a 31.6% increase in the current from –103.1 to –148.6 μA at the 1<sup>st</sup> to the 1000<sup>th</sup> repeat scan (based upon the current at –0.75 V and a cyclic voltammetry (CV) potential range of 0 to –1.4 V). The observed increase in current density could be a result of several contributing factors, such as the prolonged exposure of the 2D-MoSe<sub>2</sub>-SPE to the acidic electrolyte, partially corroding polymers found within the carbon ink and thus leading to the exposure of a greater number of 2D-MoSe<sub>2</sub> active edge planes. Another possible

explanation is the chemical alteration of the electrodes surface leading to more favourable HER activity. Table 7.2. shows the elemental compositions, deduced *via* XPS, of a 10% 2D-MoSe<sub>2</sub>-SPE pre and post the 1000 repeat scans described above.

**Table 7.2.** *Compositional analysis of XPS spectra for a 10% 2D-MoSe<sub>2</sub>-SPE pre and post 1000 repeat scan in 0.5 M H<sub>2</sub>SO<sub>4</sub>. Scan rate utilised 100 mV s<sup>-1</sup> (vs. SCE). Results shown in atom percentage concentration, excluding H which is not detected by this technique.*

Electrode	Element	Atom % Composition
10% 2D-MoSe <sub>2</sub> -SPE <i>pre</i> - 1000 repeat scans	C	84.51
	Cl	10.45
	O	4.35
	Se	0.43
	Mo	0.25
10% 2D-MoSe <sub>2</sub> -SPE <i>post</i> - 1000 repeat scans whilst utilising a platinum counter	Na	1.75
	O	16.65
	N	0.89
	C	72.48
	Cl	5.76
	Se	0.19
	Si	1.03
	P	0.51
	Al	0.64
	Mo	0.06
Pt	0.04	
10% 2D-MoSe <sub>2</sub> -SPE <i>post</i> - 1000 repeat scans whilst utilising a carbon counter	Na	0.09
	O	24.9
	N	1.45
	C	66.59
	Cl	4.51
	Se	1.01
	Si	0.55
Mo	0.23	
	Al	0.67

There is a trace amount of Pt (0.04%) on the post 1000 scan 2D-MoSe<sub>2</sub>-SPE that is not present on the pre-scan 2D-MoSe<sub>2</sub>-SPE, this may have contributed to the increased current. Figure 7.05. shows that the increase in achievable current cannot solely be

prescribed to Pt contamination, as there is also an increase of 34.7 % in achievable current when a carbon counter is utilised during the cycling stability test.

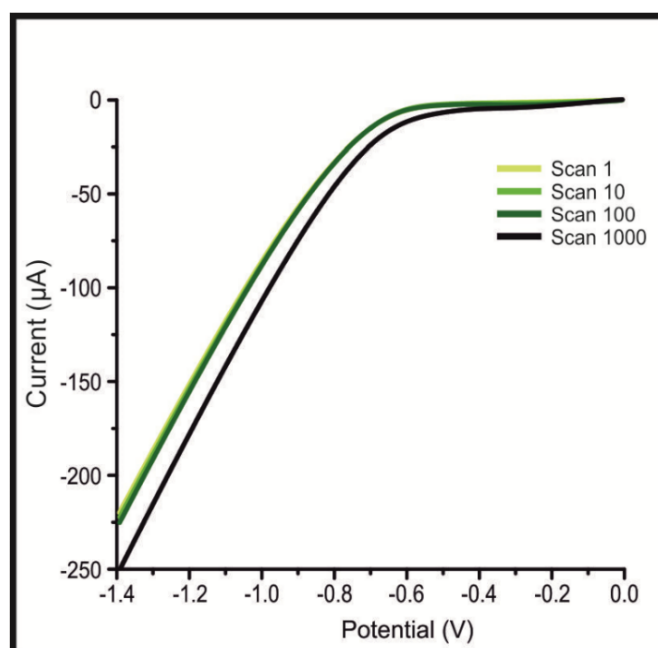


**Figure 7.05.** Cyclic stability examination of a 10% 2D-MoSe<sub>2</sub>-SPE LSV performed between the potential range of 0 to -1.4 V using a carbon counter electrode, repeated for 1000 cycles. The figures shows the initial (yellow line), 10<sup>th</sup> (green line) scans, 100<sup>th</sup> (dark green) and 1000<sup>th</sup> scan (black line). Scan rate: 100 mVs<sup>-1</sup> (vs. SCE).

The Pt contamination arose *via in-situ* deposition from the Pt counter electrode *via* the mechanism described by Gottlieb *et al.*<sup>171</sup> This is supported by Table 7.2., which shows the lack of any Pt in the elemental analysis of a 2D-MoSe<sub>2</sub>-SPE surface which underwent a 1000 scan cycling stability study whilst utilising a carbon counter, rather than a Pt counter. Further work to ascertain the exact reason of the observed increase in current density would be of interest and is planned for future studies. A small reduction peak at -0.3 V is observed on the 1000<sup>th</sup> scan, which is not present in the 1<sup>st</sup>, 10<sup>th</sup> and 100<sup>th</sup> scan. This observation can be attributed to the oxygen reduction reaction occurring as oxygen is likely to have permeated the 0.5 M H<sub>2</sub>SO<sub>4</sub> electrolyte over the course of the cycling stability experiment.<sup>75</sup> In order to further explore the

stability of the 10% 2D-MoSe<sub>2</sub>-SPE, chronoamperometry was employed at  $-0.75$  V for 36,000 seconds as reported within Figure 7.06.

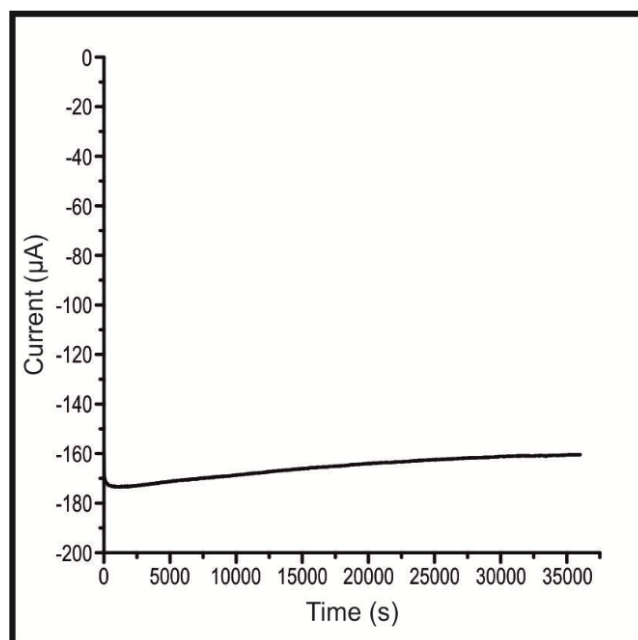


**Figure 7.06.** The current observed using chronoamperometry with the potential held at  $-0.75$  V (vs. SCE) for 36,000 seconds using a 10% 2D-MoSe<sub>2</sub>-SPE recorded in 0.5 M H<sub>2</sub>SO<sub>4</sub>.

The achieved maximum current was  $-174$   $\mu$ A at 1,214 seconds after which there was a gradual decrease in the magnitude of the current to  $-160$   $\mu$ A at 36,000 seconds. It was essential to assess whether the observed stability of the 10% 2D-MoSe<sub>2</sub> was due to the incorporation of the 2D-MoSe<sub>2</sub> into the bulk SPE ink and that drop-casting the 2D-MoSe<sub>2</sub> would not lead to a similar stability being observed. Figure 7.07. shows the observed CVs of a SPE that had 400 mg cm<sup>-2</sup> of 2D-MoSe<sub>2</sub> drop-cast onto its surface and then subsequently underwent a cycling stability test under identical conditions as implemented above.

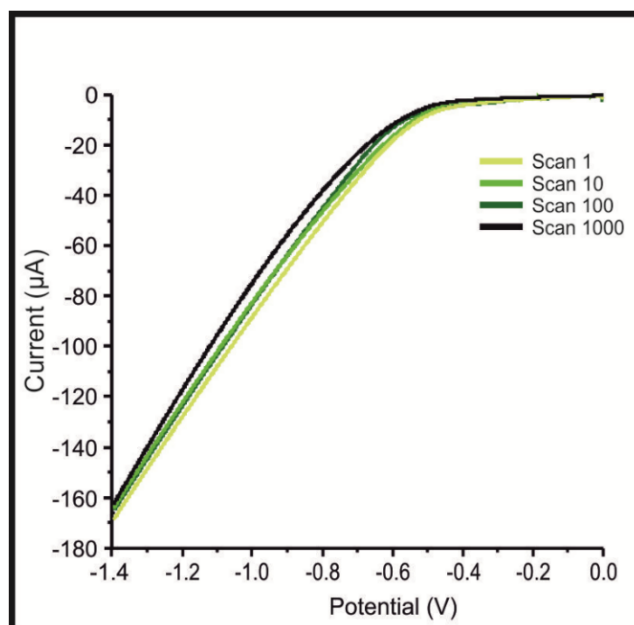


**Figure 7.07.** Cyclic stability examination of a 2D-MoSe<sub>2</sub>-SPE<sub>400nm</sub> modified, via the drop-casting technique using LSVs. The potential range of 0 to -1.4 V was utilised and repeated for 1000 cycles. The figures show the initial (yellow line), 10<sup>th</sup> (green line) scans, 100<sup>th</sup> (dark green) and 1000<sup>th</sup> scan (black line). Scan rate: 100 mVs<sup>-1</sup> (vs. SCE).

It is clear upon inspection of this figure that the HER onset potential remained stable at ca. -480 mV (vs. SCE) across the duration of the 1000 scans, however there is a 27.4% reduction evident in the observed current (from -41.9 µA at the 1<sup>st</sup> scan to -30.3 µA at the 1000<sup>th</sup> scan, based upon the current at -0.75 V and a CV potential range of 0 to -1.4 V). This reduction in the magnitude of the achievable current is likely due to the delamination of the 2D-MoSe<sub>2</sub> from the electrode's surface over the course of 1000 scans. Given the results of the cycling stability studies, it can be interfered that by incorporating the 2D-MoSe<sub>2</sub> into the bulk SPE ink (rather than drop-casting the 2D-MoSe<sub>2</sub>) results in a greater stability of the achievable current. Of note within the literature is the inconsistent approach of testing the electrochemical stability of a potential electrocatalyst towards the HER. Each separate study alters the potential range, duration (time) and number of cycles implemented. This point is particularly

evident upon inspection of Table 7.1. Future studies should endeavour to produce and adhere to a universal literature standard methodology that not only would vigorously test the cycling stability of an electrocatalyst, but also allow for easy comparisons to be established between distinct studies.

SPEs have several advantages over traditional carbon based electrodes, such as their reproducibility, tailorability and vast economy of scales. They have however historically lacked in comparable and competitive HER activity. The results presented herein demonstrate that this problem can be addressed *via* the utilisation of 2D-MoSe<sub>2</sub>-SPEs exhibit low HER overpotentials and large current densities, with the distinct advantage of having the desired electrocatalyst incorporated into their ink/structure resulting in excellent cycling stability. Whilst the 2D-MoSe<sub>2</sub>-SPEs have a more electronegative HER onset potential compared to Pt based electrodes, their low production cost and short manufacturing time make them desirable alternatives for situations where the efficiency of Pt based electrodes is not an adequate trade-off for their high cost. It would be of interest in future studies to alter the size (as Chapter 6 does with 2D-MoS<sub>2</sub>), morphology and surface composition of the 2D-MoSe<sub>2</sub> utilised to produce the 2D-MoSe<sub>2</sub>-inks and explore their activity towards the HER.

### 7.3. Summation

---

This chapter reports, for the first time, the production of a 2D-MoSe<sub>2</sub> electrocatalytic ink which can be utilised to produce screen-printed electrodes / surfaces that exhibit low HER onset, high reproducibility and excellent cycling stability. The use of screen-printing allows a mass scalable approach to produce 2D-MoSe<sub>2</sub> electrocatalytic surfaces. Incorporating the known electrocatalyst 2D-MoSe<sub>2</sub> into the screen-printed ink at an optimal ratio of 10% 2D-MoSe<sub>2</sub> mass (90% carbon ink) results in a HER onset, Tafel value and a turn over frequency of *ca.* -460 mV (*vs.* SCE), 47 mV dec<sup>-1</sup> and  $1.48 \frac{H_2/S}{\text{Surface Site}}$  respectively. These values show that the 10% 2D-MoSe<sub>2</sub>-SPE is significantly more electrocatalytic towards the HER in comparison to a bare/unmodified SPE or 2D-MoS<sub>2</sub>-SPE<sub>400nm</sub> that have a HER onset and Tafel value of -880 mV (*vs.* SCE), 120 mV dec<sup>-1</sup> and -500 mV (*vs.* SCE) and mV dec<sup>-1</sup>, respectively. The fabricated 2D-MoSe<sub>2</sub>-SPEs exceed, in terms of the HER activity, any previous studies that have utilised SPE's towards the HER.

As was the case for the 2D-MoS<sub>2</sub>-SPEs of Chapter 6, the 2D-MoSe<sub>2</sub>-SPEs are shown to have a uniform and stable coverage of 2D-MoSe<sub>2</sub> *via* Raman mapping. The 2D-MoSe<sub>2</sub>-SPEs display no degradation in the observed HER onset over the course of 1000 repeat scans, with, in fact, a 31.6% increase in the achievable current density over this period. This remarkable stability, which arises from the incorporation/anchoring of the 2D-MoSe<sub>2</sub> into the SPE ink, exceeds the stability observed when 400 mg cm<sup>-2</sup> of 2D-MoSe<sub>2</sub> was drop-casted onto a SPE (which, displayed a 27.4% decrease over the same experimental duration). This study has provided insights into the electrochemistry occurring and the HER mechanism prevalent at the novel 2D-MoSe<sub>2</sub>-SPEs, showing that they have clear potential to be

utilised as beneficial alternatives to GC and Pt in future research and industrial applications. Even more so than the optimised 2D-MoS<sub>2</sub>-SPEs<sub>400nm</sub> of Chapter 6, as the 2D-MoSe<sub>2</sub>-SPEs displayed less electronegative HER onset potentials and larger achievable current densities. Few studies have such a direct transferability to their desired field, whilst also opening a vast number of avenues for future research that seeks to utilise 2D-nanomaterials in order to produce cheap, stable and tailorable electrocatalytic electrodes for use in electrolyzers and PEMFCs.

## Conclusion.

---

This thesis has reported a number of significant contributions to the field of electrochemistry, in particular, the study of 2D-nanomaterials towards the electrocatalysis of the hydrogen evolution (HER) and oxygen reduction reactions (ORR).

The first of these contributions arises in Chapter 3 when it is shown that the electrocatalytic activity of 2D-MoS<sub>2</sub> nanosheets can be negatively impacted by the use of a surfactant (sodium cholate) in their fabrication. Future studies seeking to utilise 2D-MoS<sub>2</sub> should be mindful of these results and carefully choose their fabrication techniques, as well as perform essential benchmarking experiments, to ensure that the signal outs (in terms of onset potentials and current densities) they observe are not convoluted, be that negativity or positively, by a surfactant.

Chapters 4 and 5 highlight three significant shortcomings within the existing literature surrounding 2D-MoS<sub>2</sub> research towards the HER and ORR, these being; the almost exclusive use of glassy carbon (GC) as a supporting electrode, the application of a single mass of catalytic material upon said electrode, and nearly sole use of KOH as the electrolyte for ORR experiments. Chapter 4 and 5 therefore add to the scientific literature by using a range of 2D-MoS<sub>2</sub> masses to modify several commonly employed carbon based underlying support electrodes (that had varying heterogeneous electron transfer kinetics), namely GC, boron doped diamond (BDD), edge plane pyrolytic graphite (EPPG) and screen-printed electrodes (SPE). The supporting electrode was found to be a key contributor to the observed HER and ORR performance of the 2D-MoS<sub>2</sub>. The coverage study revealed a critical coverage where optimal catalytic activity is observed, and after which the catalytic benefits plateau with additional modification.

By straying from the norms of literature on these two points this study helps deconvolute the true electrochemical behaviour of 2D-MoS<sub>2</sub> and highlight SPEs ability to act as cheap, mass producible and effective alternatives to other more expensive carbon based electrodes. The use of an acidic electrolyte when exploring the ORR allowed for this study to be the first, within the literature, to show a desirable 4 electron ORR pathway when using 2D-MoS<sub>2</sub> as an electrocatalyst within an acidic media. Additionally using an acidic electrolyte enable the results of this study to be directly transferable to use in industrial PEM fuel cells that are typically acidic.

The last, and arguable the most noteworthy outcome of this thesis is the development of a facile technique for the production of 2D-material incorporated inks that can be utilised to fabricate tailored SPEs, which show unique electrochemical characteristics. With Chapter 6 showing how an optimised 2D-MoS<sub>2</sub>-SPE<sub>400nm</sub> can significantly reduce the ORR onset and allow the reaction mechanism to occur by the 4 electron pathway. Whilst, Chapter 7 demonstrates that a 2D-MoSe<sub>2</sub>-SPE exhibits highly beneficial electrochemical activity towards the HER, with a small overpotential and high achievable current density. In both cases, the 2D-material incorporated SPEs exhibited remarkable stability with no degradation in their achievable current or onset potentials over the course of 1000 repeat scans. As stated in the conclusion of Chapters 6 and 7, the production of such inks and the resultant SPEs mitigate the need to *post hoc* modify electrodes *via* the drop-casting technique and thereby avoid the low reproducibility and poor stability inherent to drop-casting.

This thesis has met the aims and objectives initially proposed (see page 9). It has made a significant contribution to the potential implementation of a hydrogen base energy economy by introducing optimised 2D-MoS<sub>2</sub> and 2D-MoSe<sub>2</sub> as cheap and earth abundant alternatives to Pt for the HER (within an PEM electrolyser) and ORR

(within a PEM fuel cell), respectively. With the subsequent development of electrocatalytic inks acting as a conduit by which the findings of this study can be transferred into industrial applications.

## Future work.

---

Proceeding from the findings of this thesis, which focused on finding cost effective alternatives for the cathodic reactions within electrolyers (HER) and proton exchange membrane fuel cells (PEMFC) (ORR), it would be interest to investigate 2D-nanomaterials towards the oxygen evolution (OER) and hydrogen oxidation reactions (HOR) which are anodic reactions within the respective technologies. If cheaper and more abundant alternatives to noble metal catalysts could be found for the OER and HOR, the four essential reactions associated for electrolyers and PEMFCs would be made considerable cheaper for industrial applications. This in turn would significantly increase the economic incentive for a hydrogen based energy economy.

The screen-printing technique, outlined in Chapters 6 and 7, for the production of 2D-MoS<sub>2</sub> and 2D-MoSe<sub>2</sub> incorporate SPEs is easily up scalable. This scalability could be explored with “full scale” electrodes being produced for electrolyers and PEMFCs. These then could be tested against the industry standards in regards to their efficiency and cost competitiveness.

## Appendix.

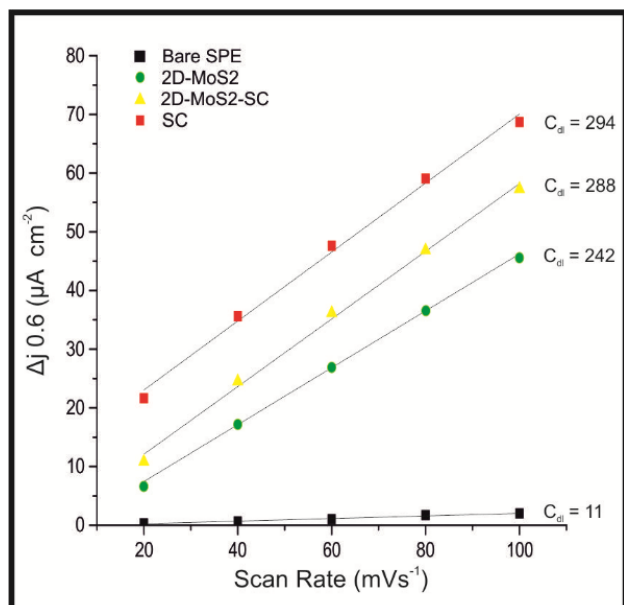


**Figure A.1.** The difference in anodic and cathodic current density (potential range 0.01 to 0.11 V) taken at +0.06 V *versus* scan rate ( $\text{mV s}^{-1}$  vs. SCE) for a bare/unmodified SPE, SPE modified with *ca.*  $2.8 \text{ mg cm}^{-2}$  of SC, SPE modified with *ca.*  $1725 \text{ ng cm}^{-2}$  of 2D-MoS<sub>2</sub> and a SPE modified with *ca.*  $1725 \text{ ng cm}^{-2}$  of 2D-MoS<sub>2</sub>-SC. The slope of the linear regression indicates the value of double layer capacitance ( $C_{dl}$ :  $\mu\text{F cm}^{-2}$ ). Solution composition: 0.5 M H<sub>2</sub>SO<sub>4</sub>.

**Table A.1.** Determined values for the Tafel slopes,  $\log V/\log I$  and the size of the diffusional zone/thickness for BDD, EPPG, GC and SPE which had been modified with 0, 252, 504, 762, 1009, 1267, 1524, 1771, 2018, 2261 and 2533  $\text{ng cm}^{-2}$  of 2D- $\text{MoS}_2$ .

Electrode	Modification ( $\text{ng cm}^{-2}$ )	Tafel Slope	$\log V/\log I$	Diffusion Zone/thickness at 25 $\text{mVs}^{-1}$ (cm)
<b>BDD</b>	Bare	NA	0.433	$1.86 \times 10^{-4}$
	252	NA	0.431	$1.89 \times 10^{-4}$
	504	NA	0.446	$1.85 \times 10^{-4}$
	762	NA	0.456	$1.89 \times 10^{-4}$
	1009	6.501	0.467	$1.85 \times 10^{-4}$
	1267	5.12	0.458	$1.98 \times 10^{-4}$
	1524	3.522	0.457	$1.96 \times 10^{-4}$
	1771	4.412	0.474	$1.89 \times 10^{-4}$
	2018	4.764	0.471	$1.98 \times 10^{-4}$
	2261	4.875	0.476	$1.95 \times 10^{-4}$
	2533	6.218	0.477	$2.01 \times 10^{-4}$
<b>EPPG</b>	Bare	6.836	0.471	$1.57 \times 10^{-4}$
	252	5.795	0.467	$1.76 \times 10^{-4}$
	504	6.066	0.499	$1.69 \times 10^{-4}$
	762	5.424	0.491	$1.55 \times 10^{-4}$
	1009	4.226	0.504	$1.45 \times 10^{-4}$
	1267	5.102	0.504	$1.50 \times 10^{-4}$
	1524	6.505	0.507	$1.46 \times 10^{-4}$

	1771	6.295	0.492	$1.67 \times 10^{-4}$
	2018	6.043	0.511	$1.64 \times 10^{-4}$
	2261	7.988	0.516	$1.65 \times 10^{-4}$
	2533	7.275	0.497	$1.67 \times 10^{-4}$
<hr/>				
<b>GC</b>	Bare	3.652	0.46	$1.57 \times 10^{-4}$
	252	8.52	0.457	$1.55 \times 10^{-4}$
	504	5.777	0.481	$1.74 \times 10^{-4}$
	762	5.878	0.462	$1.83 \times 10^{-4}$
	1009	4.506	0.493	$1.73 \times 10^{-4}$
	1267	4.78	0.482	$1.75 \times 10^{-4}$
	1524	5.264	0.496	$1.82 \times 10^{-4}$
	1771	7.969	0.484	$1.58 \times 10^{-4}$
	2018	6.793	0.477	$1.59 \times 10^{-4}$
	2261	6.466	0.487	$1.50 \times 10^{-4}$
	2533	9.338	0.502	$1.79 \times 10^{-4}$
<hr/>				
<b>SPE</b>	Bare	12.225	0.437	$1.64 \times 10^{-4}$
	252	7.042	0.445	$1.74 \times 10^{-4}$
	504	5.52	0.421	$1.89 \times 10^{-4}$
	762	4.4	0.465	$1.81 \times 10^{-4}$
	1009	3.57	0.438	$1.93 \times 10^{-4}$
	1267	3.189	0.445	$1.94 \times 10^{-4}$
	1524	3.603	0.434	$2.16 \times 10^{-4}$
	1771	4.12	0.441	$2.12 \times 10^{-4}$

2018	6.233	0.466	$2.21 \times 10^{-4}$
2261	6.041	0.441	$2.17 \times 10^{-4}$
2533	6.048	0.478	$2.16 \times 10^{-4}$

---

**Table A.2.** The determined roughness factor  $R_F$  values for BDD, EPPG, GC and SPE which had been modified with 0, 252, 1009, 2019  $\text{ng cm}^{-2}$  2D-MoS<sub>2</sub>. Values determined using double layer capacitance obtained via cyclic voltammetry between the potential range of 0.01V and 0.1V.

Electrode	MoS <sub>2</sub> Modification ( $\text{ng cm}^{-2}$ )	Roughness Factor ( $R_F$ )
<b>GC</b>	2019	6.4
	1009	5.8
	252	2.6
	0	1.0
<b>SPE</b>	2019	37.0
	1009	25.0
	Polished 1009	13.5
	252	7.8
	0	1.0
<b>EPPG</b>	2019	2.0
	1009	1.4
	252	1.2
	0	1.0
<b>BDD</b>	2019	13.5
	1009	9.0
	252	2.14
	0	1.0

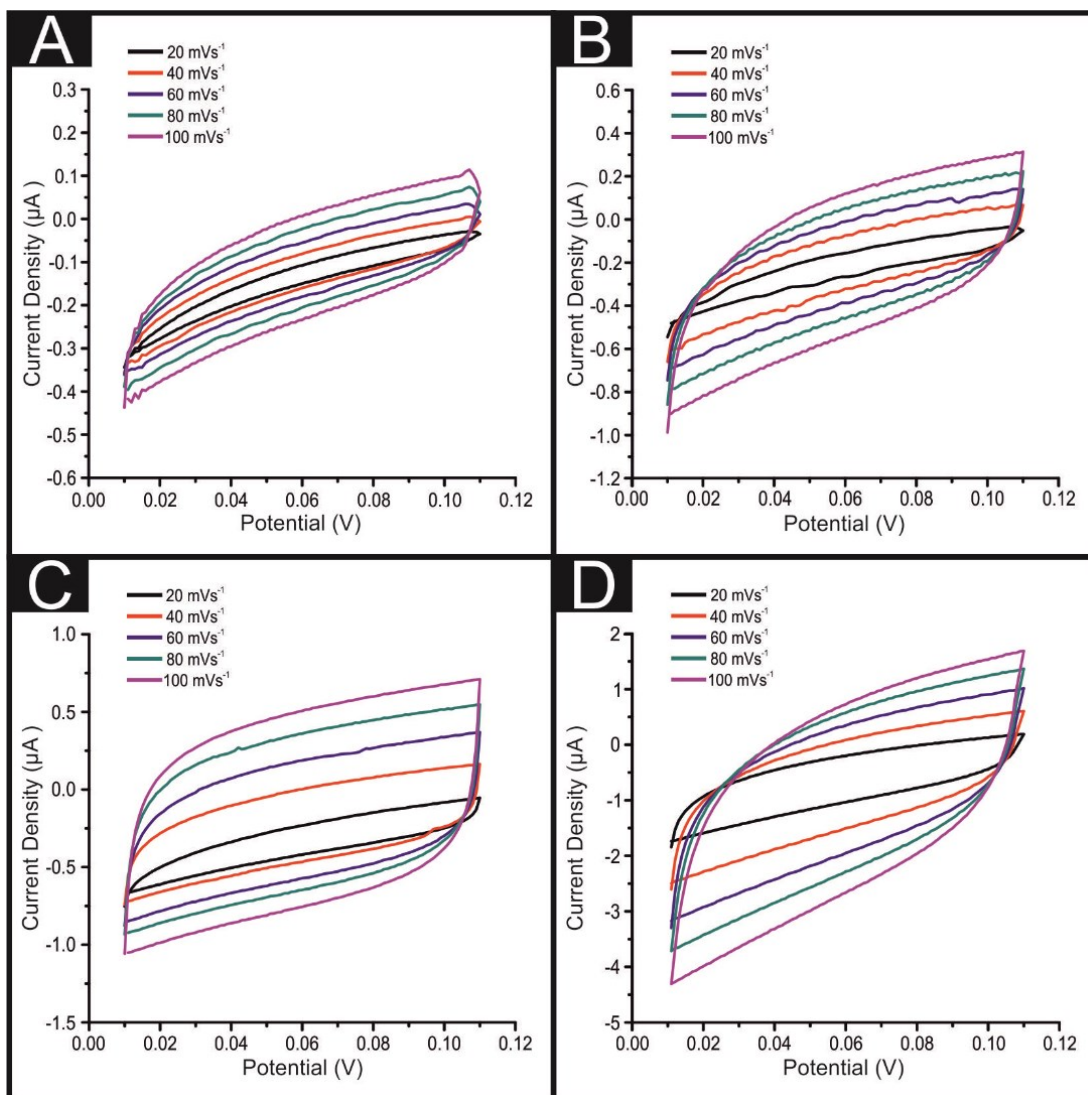


**Figure A.2.** Typical CVs recorded for (A) 5, (B) 10, (C) 20 and (D) 40 % 2D-MoS<sub>2</sub>-SPEs<sub>400nm</sub> between 0.01 to 0.11 V (non-Faradaic region), at various scan rates (vs. SCE) of 20, 40, 60, 80 and 100 mVs<sup>-1</sup>. Solution composition: 0.5 M H<sub>2</sub>SO<sub>4</sub>.

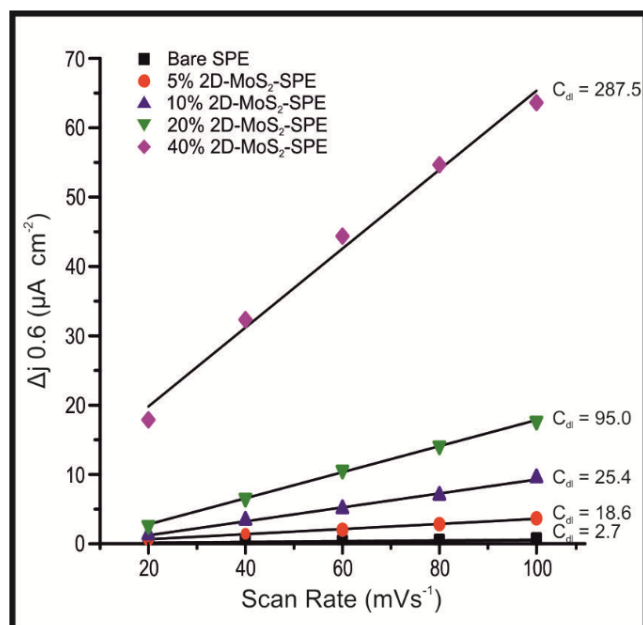


**Figure A.3.** The difference in the anodic and cathodic current density of a (bare) SPE, 5, 10, 20 and 40 % 2D-MoS<sub>2</sub>-SPEs<sub>400nm</sub> taken at +0.06 V from Figure A.2. versus scan rate (mVs<sup>-1</sup> vs. SCE). The slope of the linear regression is the value of double layer capacitance,  $C_{dl}$ : ( $\mu F\ cm^{-2}$ ). Solution composition: 0.5 M H<sub>2</sub>SO<sub>4</sub>.

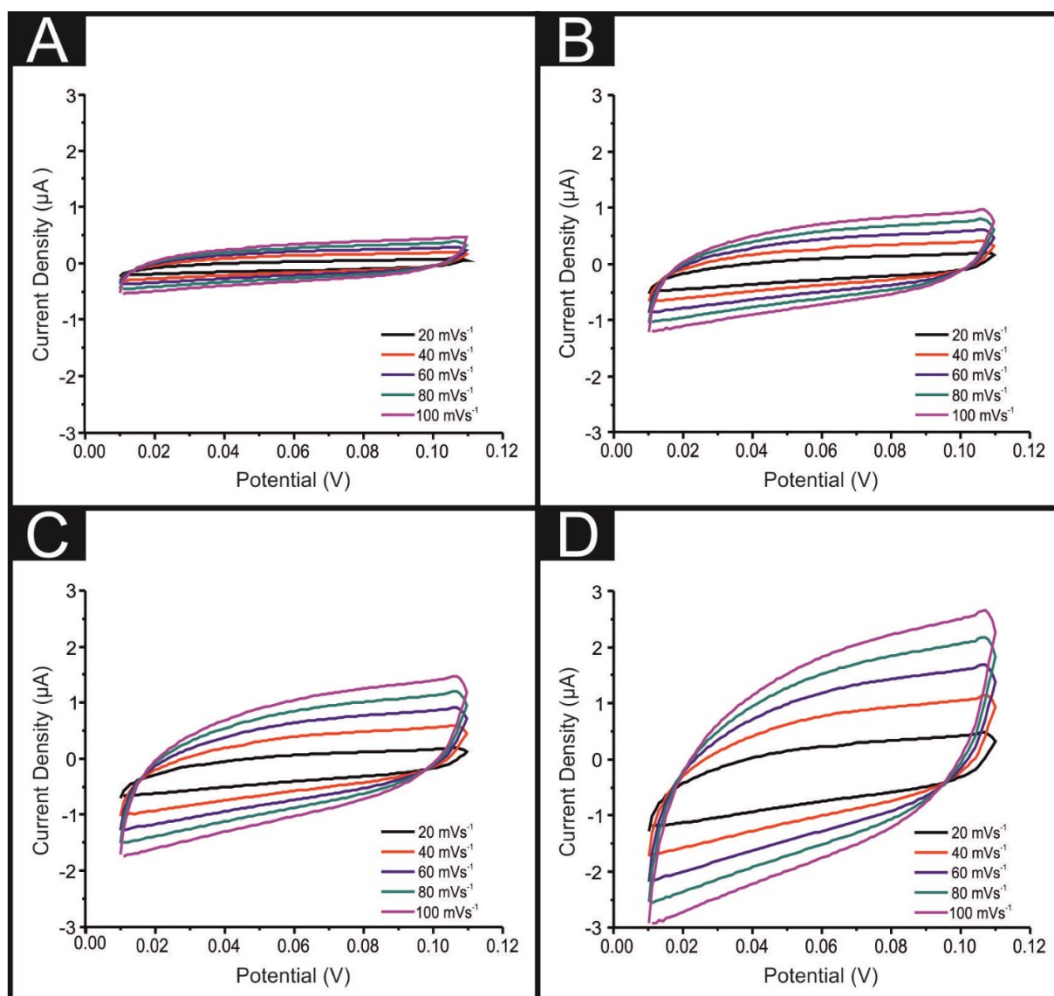


**Figure A.4.** Typical cyclic voltammograms recorded in a solution of 0.5 M H<sub>2</sub>SO<sub>4</sub> using 5, 10, 20 and 40% 2D-MoSe<sub>2</sub>-SPEs. Scan rate: 100 mVs<sup>-1</sup> (vs. SCE). Solution composition: 0.5 M H<sub>2</sub>SO<sub>4</sub>.

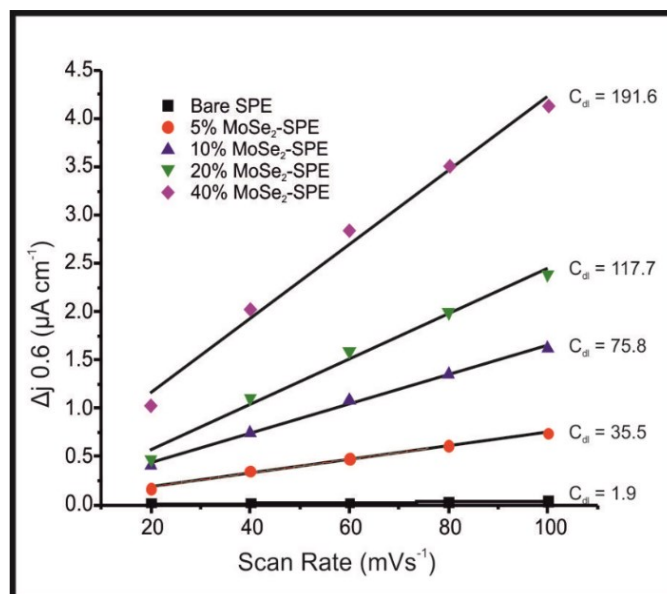


**Figure A.5.** The difference in the anodic and cathodic current density of a (bare) SPE, 5, 10, 20 and 40 % 2D-MoS<sub>2</sub>-SPEs<sub>400nm</sub> taken at +0.06 V from Figure A.4. versus scan rate (100 mVs<sup>-1</sup> vs. SCE). The slope of the linear regression is the value of double layer capacitance,  $C_{dl}$ : ( $\mu F\ cm^{-2}$ ). Solution composition: 0.5 M H<sub>2</sub>SO<sub>4</sub>.

## References.

---

1. G. Instruments, <https://www.gamry.com/application-notes/instrumentation/potentiostat-fundamentals/>, Accessed 04/05/2017.
2. C. G. Zoski, *Handbook of Electrochemistry*, Elsevier, Oxford, 2007.
3. R. G. Compton and C. E. Banks, *Understanding Voltammetry*, Imperial College Press, London, 2 edn., 2011.
4. A. J. Bard and L. R. Faulkner, *Electrochemical Methods: Fundamentals and Applications*, John Wiley and Sons, INC, New York, USA 2001.
5. Y. Z. Yufei Zhao, Zhiyu Yang, Yiming Yan and Kening Sun, *Sci. Technol. Adv. Mater* 2013, 14.
6. T. Wang, L. Liu, Z. Zhu, P. Papakonstantinou, J. Hu, H. Liu and M. Li, *Energy Environ. Sci.*, 2013, 6, 625-633.
7. A. J. López-Menéndez, R. Pérez and B. Moreno, *J. Environ. Manage.*, 2014, 145, 368-373.
8. T. D. M. G. Schultz, G. P. Brasseur, W. Zittel, *Science* 2003, 302, 624-627.
9. T. Hua, R. Ahluwalia, L. Eudy, G. Singer, B. Jermer, N. Asselin-Miller, S. Wessel, T. Patterson and J. Marcinkoski, *J. Power Sources*, 2014, 269, 975-993.
10. J. Andrews and B. Shabani, *WIREs Energy Environ*, 2014, 3, 474-489.
11. B. Hinnemann, P. G. Moses, J. Bonde, K. P. Jørgensen, J. H. Nielsen, S. Horch, I. Chorkendorff and J. K. Nørskov, *J. Am. Chem. Soc.*, 2005, 127, 5308-5309.
12. V. Mehta and J. C. Cooper, *J. Power Sources*, 2003, 114, 32-53.
13. J. Wu, X. Z. Yuan, J. J. Martin, H. Wang, J. Zhang, J. Shen, S. Wu and W. Merida, *J. Power Sources*, 2008, 184, 104-119.
14. F. A. d. Bruijn, V. A. T. Dam and G. J. M. Janssen, *Fuel Cells*, 2008, 8, 3-22.
15. S. K. Kamarudin, W. R. W. Daud, A. Md.Som, M. S. M. S. Takriff and A. W. Mohammad, *J. Power Sources*, 2006, 157, 641-649.
16. P. C. K. Vesborg, B. Seger and I. Chorkendorff, *J. Phys. Chem. Lett.*, 2015, 6, 951-957.
17. C. A. Martinson, G. v. Schoor, K. R. Uren and D. Bessarabov, *Int. J. Hydrogen Energy*, 2014, 39, 20865-20878.
18. N. M. Marković and P. N. Ross Jr, *Surf. Sci. Rep.*, 2002, 45, 117-229.
19. N. M. Marković, B. N. Grgur and P. N. Ross, *J. Phys. Chem. B*, 1997, 101, 5405-5413.
20. A. B. Laursen, S. Kegnaes, S. Dahl and I. Chorkendorff, *Energy Environ. Sci.*, 2012, 5, 5577-5591.

21. T. F. Jaramillo, K. P. Jørgensen, J. Bonde, J. H. Nielsen, S. Horch and I. Chorkendorff, *Science*, 2007, 317, 100-102.
22. B. X. Ya Yan , Zhichuan Xu , and Xin Wang *ACS Catal.*, 2014, 693–1705.
23. K. Ravindra, L. Bencs and R. Van Grieken, *Sci. Total Environ.*, 2004, 318, 1-43.
24. R. L. McCreery, *Chem. Rev.*, 2008, 108, 2646-2687.
25. D. A. C. Brownson and C. E. Banks, *Electrochem. Commun.*, 2011, 13, 111-113.
26. M. Lu, K. E. Toghil and R. G. Compton, *Electroanalysis*, 2011, 23, 1089-1094.
27. M. Musameh, J. Wang, A. Merkoci and Y. Lin, *Electrochem. Commun.*, 2002, 4, 743-746.
28. A. Koca, *Int. J. Hydrogen Energy In*, 2009, 34, 2107-2112.
29. Y. Shen, J. Liu, J. Jiang, B. Liu and S. Dong, *J. Phys. Chem. B*, 2003, 107, 9744-9748.
30. J. Yin, J. B. Jia and L. D. Zhu, *In*, 2008, 33, 7444-7447.
31. Y. Zheng, Y. Jiao, Y. Zhu, L. H. Li, Y. Han, Y. Chen, A. Du, M. Jaroniec and S. Z. Qiao, *Nat Commun*, 2014, 5.
32. Z. Chen, D. Cummins, B. N. Reinecke, E. Clark, M. K. Sunkara and T. F. Jaramillo, *Nano Lett.*, 2011, 11, 4168-4175.
33. D. Y. Chung, S.-K. Park, Y.-H. Chung, S.-H. Yu, D.-H. Lim, N. Jung, H. C. Ham, H.-Y. Park, Y. Piao, S. J. Yoo and Y.-E. Sung, *Nanoscale*, 2014, 6, 2131–2136.
34. Y. Li, H. Wang, L. Xie, Y. Liang, G. Hong and H. Dai, *J. Am. Chem. Soc.* , 2011, 133, 7296-7299.
35. D. Merki, S. Fierro, H. Vrubel and X. Hu, *Chem. Sci*, 2011, 2, 1262-1267.
36. L. F. Pan, Y. H. Li, S. Yang, P. F. Liu, M. Q. Yu and H. G. Yang, *Electrochem. Commun.*, 2014, 50, 13135-13137.
37. Y. H. Chang, C. T. Lin, T. Y. Chen, C. L. Hsu, Y. H. Lee, W. J. Zhang, K. H. Wei and L. J. Li, *Adv. Mater.*, 2013, 25, 756-760.
38. P. C. Joensen, E. D. Alberding, N. Frindt, R. F., *J. Phys. C: Solid State Phys.*, 1987, 20, 4043-4053.
39. J. H. Lee, W. S. Jang, S. W. Han and H. K. Baik, *Langmuir*, 2014, 30, 9866-9873.
40. S. Ji, Z. Yang, C. Zhang, Z. Liu, W. W. Tjiu, I. Y. Phang, Z. Zhang, J. Pan and T. Liu, *Electrochim. Acta*, 2013, 109, 269-275.
41. RadisavljevicB, RadenovicA, BrivioJ, GiacomettiV and Kisa, *Nat Nano*, 2011, 6, 147-150.
42. S. Tongay, J. Zhou, C. Ataca, K. Lo, T. S. Matthews, J. Li, J. C. Grossman and J. Wu, *Nano Lett.*, 2012, 12, 5576-5580.
43. M.-L. Tsai, S.-H. Su, J.-K. Chang, D.-S. Tsai, C.-H. Chen, C.-I. Wu, L.-J. Li, L.-J. Chen and J.-H. He, *ACS Nano*, 2014, 8, 8317-8322.

44. T. J. Schmidt, U. A. Paulus, H. A. Gasteiger and R. J. Behm, *J. Electroanal. Chem.*, 2001, 508, 41-47.
45. D. Banham, S. Ye, K. Pei, J. Ozaki, T. Kishimoto and Y. Imashiro, *J. Power Sources*, 2015, 285, 334-348.
46. M.-R. Gao, J.-X. Liang, Y.-R. Zheng, Y.-F. Xu, J. Jiang, Q. Gao, J. Li and S.-H. Yu, *Nat Commun*, 2015, 6, 5982.
47. A. A. Gewirth and M. S. Thorum, *Inorg. Chem.*, 2010, 49, 3557-3566.
48. Y. Liu, X. Yue, K. Li, J. Qiao, D. P. Wilkinson and J. Zhang, *Coord. Chem. Rev.*, 2016, 315, 153-177.
49. M.-R. Gao, Y.-F. Xu, J. Jiang, Y.-R. Zheng and S.-H. Yu, *J. Am. Chem. Soc.*, 2012, 134, 2930-2933.
50. M. Gara and R. C. Compton, *New J. Chem.*, 2011, 35, 2647-2652.
51. K. Uosaki, G. Elumalai, H. Noguchi, T. Masuda, A. Lyalin, A. Nakayama and T. Taketsugu, *J. Am. Chem. Soc.*, 2014, 136, 6542-6545.
52. F. Jaouen, E. Proietti, M. Lefevre, R. Chenitz, J-P.Dodelet, G. Wu, H. T. Chung, C. M. Johnston and P. Zelenay, *Energy Environ. Sci.*, 2011, 4, 114-130.
53. L. Gubler, S. M. Dockheer and W. H. Koppenol, *J. Electrochem. Soc.*, 2011, 158, B755-B769.
54. M. Gara and R. G. Compton, *New J. Chem.*, 2011, 35, 2647-2652.
55. E. P. Randviir and C. E. Banks, *Electroanalysis*, 2014, 26, 76-83.
56. K. K. Ravindra, L. L. Bencs and R. V. Grieken, *Sci. Total Environ.*, 2004, 318, 1-43.
57. M.-R. Gao, S. Liu, J. Jiang, C.-H. Cui, W.-T. Yao and S.-T. Yu, *A*, 2010, 20, 9355-9361.
58. E. P. Randviir, D. A. C. Brownson, M. Gomez-Mingot, D. K. Kampouris, J. Iniesta and C. E. Banks, *Nanoscale*, 2012, 4, 6470-6480.
59. M.-R. Gao, Y.-F. Xu, J. Jiang and S.-H. Yu, *Chem. Soc. Rev.*, 2013, 42, 2986-3017.
60. C. Ataca, M. Topsakal, E. Aktürk and S. Ciraci, *J. Phys. Chem. C*, 2011, 115, 16354-16361.
61. K. Zhao, W. Gu, L. Zhao, C. Zhang, W. Peng and Y. Xian, *Electrochim. Acta*, 2015, 169, 142-149.
62. B. Yu, H. Min, H. Wu, S. Wang, Y. Ding and G. Wang, *J. Mater. Sci.*, 2017, 52, 3188-3198.
63. N. A. Dhas and K. S. Suslick, *J. Am. Chem. Soc.*, 2005, 127, 2368-2369.
64. F. Cesano, S. Bertarione, A. Piovano, G. Agostini, M. M. Rahman, E. Groppo, F. Bonino, D. Scarano, C. Lamberti, S. Bordiga, L. Montanari, L. Bonoldi, R. Millini and A. Zecchina, *Catal. Sci. Technol.*, 2011, 1, 123-136.

65. G. Li, D. Zhang, Q. Qiao, Y. Yu, D. Peterson, A. Zafar, R. Kumar, S. Curtarolo, F. Hunte, S. Shannon, Y. Zhu, W. Yang and L. Cao, *J. Am. Chem. Soc.*, 2016, 138, 16632–16638.
66. H. Huang, X. Feng, C. Du, S. Wu and W. Song, *J. Mater. Chem. A*, 2015, 3, 16050-16056.
67. D. Voiry, M. Salehi, R. Silva, T. Fujita, M. Chen, T. Asefa, V. B. Shenoy, G. Eda and M. Chhowalla, *Nano Lett.*, 2013, 13, 6222-6227.
68. S. S. Chou, M. De, J. Kim, S. Byun, C. Dykstra, J. Yu, J. Huang and V. P. Dravid, *J. Am. Chem. Soc.*, 2013, 135, 4584-4587.
69. D. Wang, Z. Pan, Z. Wu, Z. Wang and Z. Liu, *J. Power Sources*, 2014, 264, 229-234.
70. D. A. C. Brownson and C. E. Banks, *The Handbook of Graphene Electrochemistry*, Springer, London, 1 edn., 2014.
71. V. V. Pavlishchuk and A. W. Addison, *Inorg. Chim. Acta*, 2000, 298, 97-102.
72. M. Carmo, D. L. Fritz, J. Mergel and D. Stolten, *Int. J. Hydrogen Energy*, 2013, 38, 4901-4934.
73. S. Litster and G. McLean, *J. Power Sources*, 2004, 130, 61-76.
74. S. J. Rowley-Neale, D. A. C. Brownson, G. C. Smith, D. A. G. Sawtell, P. J. Kelly and C. E. Banks, *Nanoscale*, 2015, 7, 18152-18168.
75. S. J. Rowley-Neale, D. A. C. Brownson, J. M. Fearn, G. C. Smith, X. Ji and C. E. Banks, *Nanoscale*, 2016, 8, 14767-14777.
76. T. J. Davies, C. E. Banks and R. G. Compton, *J. Solid State Electrochem.*, 2005, 9, 797-808.
77. N.-T. Suen, S.-F. Hung, Q. Quan, N. Zhang, Y.-J. Xu and H. M. Chen, *Chem. Soc. Rev.*, 2017, 46, 337-365.
78. X. Jiao, C. Batchelor-McAuley, E. Kätelhön, J. Ellison, K. Tschulik and R. G. Compton, *J. Phys. Chem. C*, 2015, 119, 9402-9410.
79. J. Kim and A. J. Bard, *Anal. Chem.*, 2016, 88, 1742-1747.
80. Sigma-Aldrich,  
<http://www.sigmaaldrich.com/catalog/product/aldrich/804169?lang=en&region=GB>,  
Accessed 05/12/2016.
81. Sigma-Aldrich,  
<http://www.sigmaaldrich.com/catalog/product/aldrich/234842?lang=en&region=GB>,  
Accessed 03/01/2017.
82. Sigma-Aldrich,  
<http://www.sigmaaldrich.com/catalog/product/aldrich/69860?lang=en&region=GB&gclid=Cj0KEQiAtK3DBRCBxt-Yxduq5p4BEiQAbFiaPRsU->

- [tFywfxAXj963r\\_sUoDCdqX4Jdjkp9EzmUix5kq8aAqYc8P8HAQ](http://tFywfxAXj963r_sUoDCdqX4Jdjkp9EzmUix5kq8aAqYc8P8HAQ), Accessed 03/01/2017.
83. Graphene Supermarket, <https://graphene-supermarket.com/MoS2-Pristine-Flakes-in-Solution.html>, Accessed 24/11/2016.
  84. Z. Lei, S. Xu and P. Wu, *Phys. Chem. Chem. Phys.*, 2016, 18, 70-74.
  85. Innovation in Surface Spectroscopy and Microscopy Systems, [http://www.specs.de/cms/front\\_content.php?idcat=209](http://www.specs.de/cms/front_content.php?idcat=209), Accessed 20/03/2016.
  86. M. P. Seah and S. J. Spencer, *J. Electron. Spectrosc. Relat. Phenom.*, 2006, 151, 178-181.
  87. J. H. Scofield, *J. Electron. Spectrosc. Relat. Phenom.*, 1976, 8, 129-137.
  88. CasaXPS, <http://www.casaxps.com/>, Accessed 2/02/2016.
  89. H. Li, Q. Zhang, C. C. R. Yap, B. K. Tay, T. H. T. Edwin, A. Olivier and D. Baillargeat, *Adv. Funct. Mater.*, 2012, 22, 1385-1390.
  90. C. Lee, H. Yan, L. E. Brus, T. F. Heinz, J. Hone and S. Ryu, *ACS Nano*, 2010, 4, 2695-2700.
  91. E. Varrla, C. Backes, K. R. Paton, A. Harvey, Z. Gholamvand, J. McCauley and J. N. Coleman, *Chem. Mater.*, 2015, 27, 1129-1139.
  92. C. Backes, R. J. Smith, N. McEvoy, N. C. Berner, D. McCloskey, H. C. Nerl, A. O'Neill, P. J. King, T. Higgins, D. Hanlon, N. Scheuschner, J. Maultzsch, L. Houben, G. S. Duesberg, J. F. Donegan, V. Nicolosi and J. N. Coleman, *Nat Commun*, 2014, 5.
  93. L. Yadgarov, C. L. Choi, A. Sedova, A. Cohen, R. Rosentsveig, O. Bar-Elli, D. Oron, H. Dai and R. Tenne, *ACS Nano*, 2014, 8, 3575-3583.
  94. J. A. Wilson and A. D. Yoffe, *A. D. Adv. Phys.*, 1969, 19, 193-335.
  95. S. Shin, Z. Jin, D. H. Kwon, R. Bose and Y.-S. Min, *Langmuir*, 2015, 31, 1196-1202.
  96. K. Liu, L. Zhang, T. Cao, C. Jin, D. Qiu, Q. Zhou, A. Zettl, P. Yang, S. G. Louie and F. Wang, *Nat. Commun.*, 2014, 5, 4966.
  97. L. Tao, H. Long, B. Zhou, S. F. Yu, S. P. Lau, Y. Chai, K. H. Fung, Y. H. Tsang, J. Yao and D. Xu, *Nanoscale*, 2014, 6, 9713-9719.
  98. K. Hu, X. Hu, Y. Xu, X. Sun and Y. Jiang, in *Tribology of Nanocomposites*, ed. P. J. Davim, Springer Berlin Heidelberg, Berlin, Heidelberg, 2013, DOI: 10.1007/978-3-642-33882-3\_3, pp. 41-60.
  99. Sigma-Aldrich, <http://www.sigmaaldrich.com/catalog/product/aldrich/778087?lang=en&region=GB>, Accessed 07/09/2016.
  100. D. Nam, J.-U. Lee and H. Cheong, *Sci. Rep.*, 2015, 5, 17113.

101. S. Mao, Z. Wen, S. Ci, X. Guo, K. Ostrikov and J. Chen, *Small*, 2015, 11, 414-419.
102. H. Tang, K. Dou, K. C-C, Q. Kuanga and S. Yang, *J. Mater. Chem. A*, 2014, 2, 360-364.
103. H. Wang, D. Kong, P. Johanes, J. J. Cha, G. Zheng, K. Yan, N. Liu and Y. Cui, *Nano Lett.*, 2013, 13, 3426-3433.
104. A. B. Laursen, A. S. Varela, F. Dionigi, H. Fanchiu, C. Miller, O. L. Trinhammer, J. Rossmeisl and S. Dahl, *J. Chem. Educ.*, 2012, 89, 1595-1599.
105. D. Marin, F. Medicuti and C. Teijeiro, *J. Chem. Educ.*, 1994, 71, A277.
106. E. P. Randviir, D. A. C. Brownson, J. P. Metters, R. O. Kadara and C. E. Banks, *PCCP*, 2014, 16, 4598-4611.
107. L. R. Cumba, J. P. Smith, D. A. C. Brownson, J. Iniesta, J. P. Metters, D. R. d. Carmo. and C. E. Banks, *Analyst*, 2015, 140, 1543-1550.
108. C. W. Foster, J. Pillay, J. P. Metters and C. E. Banks, *Sensors (Basel, Switzerland)*, 2014, 14, 21905-21922.
109. C. W. Foster, J. P. Metters and C. E. Banks, *Electroanalysis*, 2013, 25, 2275-2282.
110. J. P. Metters, M. Gomez-Mingot, J. Iniesta, R. O. Kadara and C. E. Banks, *Sens. Actuators, B*, 2013, 177, 1043-1052.
111. J. P. Smith, J. P. Metters, O. I. G. Khreit, O. B. Sutcliffe and C. E. Banks, *Anal. Chem.*, 2014, 86, 9985-9992.
112. O. Ramdani, J. P. Metters, L. C. S. Figueiredo-Filho, O. Fatibello-Filho and C. E. Banks, *Analyst*, 2013, 138, 1053-1059.
113. J. P. Smith, J. P. Metters, D. K. Kampouris, C. Lledo-Fernandez, O. B. Sutcliffe and C. E. Banks, *Analyst*, 2013, 138, 6185-6191.
114. C. W. Foster, R. O. Kadara and C. E. Banks, *Screen-Printing Electrochemical Architectures*, Springer International Publishing, Germany, 1 edn., 2016.
115. L. Niu, J. N. Coleman, H. Zhang, H. Shin, M. Chhowalla and Z. Zheng, *Small*, 2016, 12, 272-293.
116. H. Li, J. Wu, Z. Yin and H. Zhang, *Acc. Chem. Res.*, 2014, 47, 1067-1075.
117. A. Ambrosi, Z. Sofer, J. Luxa and M. Pumera, *ACS Nano*, 2016, 10, 11442-11448.
118. S. Li, S. Wang, D.-M. Tang, W. Zhao, H. Xu, L. Chu, Y. Bando, D. Golberg and G. Eda, *Appl. Mater. Today*, 2015, 1, 60-66.
119. R. J. Smith, P. J. King, M. Lotya, C. Wirtz, U. Khan, S. De, A. O'Neill, G. S. Duesberg, J. C. Grunlan, G. Moriarty, J. Chen, J. Wang, A. I. Minett, V. Nicolosi and J. N. Coleman, *Adv. Mater.*, 2011, 23, 3944-3948.
120. R. C. T. Howe, R. I. Woodward, G. Hu, Z. Yang, E. J. R. Kelleher and T. Hasan, *Phys. Status Solidi B*, 2016, 253, 911-917.
121. A. Ambrosi, Z. Sofer and M. Pumera, *Small*, 2015, 11, 605-612.

122. X. J. Chua and M. Pumera, *Phys. Chem. Chem. Phys.*, 2017, 19, 6610-6619.
123. Z. Guo, Q. Ma, Z. Xuan, F. Du and Y. Zhong, *RSC Adv.*, 2016, 6, 16730-16735.
124. S. Zhang, B. V. R. Chowdari, Z. Wen, J. Jin and J. Yang, *ACS Nano*, 2015, 9, 12464-12472.
125. L. Song, M. Zhao, X. Li, Z. Zhang and L. Qu, *RSC Adv.*, 2016, 6, 70740-70746.
126. H. Gerischer, R. McIntyre, D. Scherson and W. Storck, *J. Phys. Chem.*, 1987, 91, 1930-1935.
127. N. Tateishi, K. Yahikozawa, K. Nishimura and Y. Takasu, *Electrochim. Acta*, 1992, 37, 2427-2432.
128. M.-R. Gao, M. K. Y. Chan and Y. Sun, *Nat Commun*, 2015, 6.
129. Y. Yu, S.-Y. Huang, Y. Li, S. N. Steinmann, W. Yang and L. Cao, *Nano Lett.*, 2014, 14, 553-558.
130. J. D. Benck, Z. Chen, L. Y. Kuritzky, A. J. Forman and T. F. Jaramillo, *ACS Catal.*, 2012, 2, 1916-1923.
131. T. F. Jaramillo, K. P. Jørgensen, J. Bonde, J. H. Nielsen, S. Horch and I. Chorkendorff, *Science*, 2007, 317, 100-102.
132. J. Bonde, P. G. Moses, T. F. Jaramillo, J. K. Norskov and I. Chorkendorff, *Faraday Discuss.*, 2009, 140, 219-231.
133. M.-R. Gao, J.-Z. Liang, Y.-R. Zheng, Y.-F. Xu, J. Jiang, Q. Gao, J. Li and S.-H. Yu, *Nat Commun*, 2015, 6.
134. X. Bian, J. Zhu, L. Liao, M. D. Scanlon, P. Ge, C. Ji, H. H. Girault and B. Liu, *Electrochem. Commun.*, 2012, 22, 128-132.
135. H. Vrubel, D. Merki and X. Hu, *Energy Environ. Sci.*, 2012, 5, 6136-6144.
136. D. Merki, H. Vrubel, L. Rovelli, S. Fierro and X. Hu, *Chem. Sci.*, 2012, 3, 2515-2525.
137. H. Zhu, F. Lyu, M. Du, M. Zhang, Q. Wang, J. Yao and B. Guo, *ACS Appl. Mater. Interfaces*, 2014, 6, 22126-22137.
138. D. Kong, H. Wang, J. J. Cha, M. Pasta, K. J. Koski, J. Yao and Y. Cui, *Nano Lett.*, 2013, 13, 1341-1347.
139. J. Z. Xie, Hao. Li, Shuang. Wang, Ruoxing. Sun, Xu. Zhou, Min. Zhou, Jingfang. Lou, Xiong Wen. Xie, Yi, *Adv. Mater.*, 2013, 25, 5807-5813.
140. J. R. McKone, B. F. Sadtler, C. A. Werlang, N. S. Lewis and H. B. Gray, *ACS Catal.*, 2012, 3, 166-169.
141. S. Ding, D. Zhang, J. S. Chen and X. W. Lou, *Nanoscale*, 2012, 4, 95-98.
142. A. H. Loo, A. Bonanni, A. Ambrosi and M. Pumera, *Nanoscale*, 2014, 6, 11971-11975.

143. K. Zhang, S. Hu, Y. Zhang, T. Zhang, X. Zhou, Y. Sun, T.-X. Li, H. J. Fan, G. Shen, X. Chen and N. Dai, *ACS Nano*, 2015, 9, 2704-2710.
144. T. Patois, B. Lakard, S. Monney, X. Roizard and P. Fievet, *Synth. Met.*, 2011, 161, 2498-2505.
145. J. D. Benck, T. R. Hellstern, J. Kibsgaard, P. Chakthranont and T. F. Jaramillo, *ACS Catal.*, 2014, 4, 3957-3971.
146. S. Helveg, J. V. Lauritsen, E. Lægsgaard, I. Stensgaard, J. K. Nørskov, B. S. Clausen, H. Topsøe and F. Besenbacher, *Physical Review Letters*, 2000, 84, 951-954.
147. M. A. Lukowski, A. S. Daniel, F. Meng, A. Forticaux, L. Li and S. Jin, *J. Am. Chem. Soc.*, 2013, 135, 10274-10277.
148. D. A. C. Brownson, A. C. Lacombe, D. K. Kampouris and C. E. Banks, *Analyst*, 2012, 137, 420-423.
149. D. A. C. Brownson, L. C. S. Figueiredo-Filho, X. Ji, M. Gomez-Mingot, J. Iniesta, O. Fatibello-Filho, D. K. Kampouris and C. E. Banks, *J. Mater. Chem.A*, 2013, 1, 5962-5972.
150. D. A. C. Brownson, L. J. Munro, D. K. Kampouris and C. E. Banks, *RSC Adv.*, 2011, 1, 978-988.
151. D. A. C. Brownson, D. K. Kampouris and C. E. Banks., *Chem. Soc. Rev.*, 2012, 41, 6944-6976.
152. C. Suresh, S. Mutyala and J. Mathiyarasu, *Mater. Lett.*, 2016, 164, 417-420.
153. C. Médard, M. Lefèvre, J. P. Dodelet, F. Jaouen and G. Lindbergh, *Electrochim. Acta*, 2006, 51, 3202-3213.
154. R. Illathvalappil, S. M. Unni and S. Kurungot, *Nanoscale*, 2015, 7, 16729-16736.
155. J. Zhou, H. Xiao, B. Zhou, F. Huang, S. Zhou, W. Xiao and D. Wang, *Appl. Surf. Sci.*, 2015, 358, Part A, 152-158.
156. T. Wang, J. Zhuo, Y. Chen, K. Du, P. Papakonstantinou, Z. Zhu, Y. Shao and M. Li, *ChemCatChem*, 2014, 6, 1877-1881.
157. L.-X. Zuo, L.-P. Jiang and J.-J. Zhu, *Ultrason. Sonochem.*, 2017, 35, Part B, 681-688.
158. P. Bothra, M. Pandey and S. K. Pati, *Catal. Sci. Technol.*, 2016, 6, 6389-6395.
159. X. J. Chua, J. Luxa, A. Y. S. Eng, S. M. Tan, Z. Sofer and M. Pumera, *ACS Catal.*, 2016, 6, 5724-5734.
160. T. Yano, E. Popa, D. A. Tryk, K. Hashimoto and A. Fujishima, *J. Electrochem. Soc.*, 1999, 146, 1081-1087.
161. S. J. Rowley-Neale, D. A. C. Brownson and C. E. Banks, *Nanoscale*, 2016, 8, 15241-15251.

162. C. E. Banks and R. G. Compton, *Understanding voltammetry*, Imperial College Press, London, 2007.
163. U. A. Paulus, A. Wokaun, G. G. Scherer, T. J. Schmidt, V. Stamenkovic, V. Radmilovic, N. M. Markovic and P. N. Ross, *J. Phys. Chem. B*, 2002, 106, 4181-4191.
164. A. F. Khan, E. P. Randviir, D. A. C. Brownson, X. Ji, G. C. Smith and C. E. Banks, *Analyst*, 2016, In Press.
165. T. Kaskiala, *Miner. Eng.*, 2002, 15, 853-857.
166. P. Han and D. M. Bartels, *J. Phys. Chem.*, 1996, 100, 5597-5602.
167. L. R. Cumba, C. W. Foster, D. A. C. Brownson, J. P. Smith, J. Iniesta, B. Thakur, D. R. D. Carmo and C. E. Banks, *Analyst*, 2016, 141, 2791-2799.
168. A. B. Laursen, S. Kegnaes, S. Dahl and I. B. Chorkendorff, *Energy Environ. Sci.*, 2012, 5, 5577-5591.
169. N. M. Marković and P. N. R. Jr, *Surf. Sci. Rep.*, 2002, 45, 117-229.
170. A. F. Khan, E. P. Randviir, D. A. C. Brownson, X. Ji, G. C. Smith and C. E. Banks, *Electroanalysis*, 2016, 31, 1521-4109.
171. E. Gottlieb, M. Kopeć, M. Banerjee, J. Mohin, D. Yaron, K. Matyjaszewski and T. Kowalewski, *ACS Appl. Mater. Interfaces*, 2016, 8, 21531-21538.
172. Y. Li, H. Wang, L. Xie, Y. Liang, G. Hong and H. Dai, *J. Am. Chem. Soc.*, 2011, 133, 7296-7299.
173. H. Wang, X. Wang, L. Wang, J. Wang, D. Jiang, D. Li, Y. Zhang, H. Zhong and Y. Jiang, *J. Phys. Chem. C*, 2015, 119, 10197-10205.
174. J. Morales, J. Santos and J. L. Tirado, *Solid State Ionics*, 1996, 83, 57-64.
175. C. Tsai, K. Chan, F. Abild-Pedersen and J. K. Nørskov, *Phys. Chem. Chem. Phys.*, 2014, 16, 13156-13164.
176. C. Xu, S. Peng, C. Tan, H. Ang, H. Tan, H. Zhang and Q. Yan, *J. Mater. Chem. A*, 2014, 2, 5597-5601.
177. X. Zhou, Y. Liu, H. Ju, B. Pan, J. Zhu, T. Ding, C. Wang and Q. Yang, *Chemistry of Materials*, 2016, 28, 1838-1846.
178. H. Tang, K. Dou, C.-C. Kaun, Q. Kuanga and S. Yang, *J. Mater. Chem. A*, 2014, 2, 360-364.
179. Q. Gong, L. Cheng, C. Liu, M. Zhang, Q. Feng, H. Ye, M. Zeng, L. Xie, Z. Liu and Y. Li, *ACS Catal.*, 2015, 5, 2213-2219.
180. C. H. Mu, H. X. Qi, Y. Q. Song, Z. P. Liu, L. X. Ji, J. G. Deng, Y. B. Liao and F. Scarpa, *RSC Adv.*, 2016, 6, 23-30.
181. Y. D. Liu, L. Ren, Z. Zhang, X. Qi, H. X. Li and J. X. Zhong, *Sci. Rep.*, 2016, 6, 22516-22525.

## Publications Arising from this Thesis.

1. S. J. Rowley-Neale, D. A. C. Brownson, G. C. Smith, D. A. G. Sawtell, P. J. Kelly and C. E. Banks, *Nanoscale*, 2015, 7, 18152-18168.
2. S. J. Rowley-Neale, D. A. C. Brownson, J. M. Fearn, G. C. Smith, X. Ji and C. E. Banks, *Nanoscale*, 2016, 8, 14767-14777.
3. S. J. Rowley-Neale, D. A. C. Brownson, and C. E. Banks, *Nanoscale*, 2016, 8, 33, 15241-15251
4. S. J. Rowley-Neale, C. W. Foster, G. C. Smith, D. A. C. Brownson and C. E. Banks, *Sustainable Energy Fuels*, 2017, 1, 74-83. (*This paper was highlighted on the front cover of issue 1 of this journal, the front cover is viewable on the final page of this thesis*)
5. S. J. Rowley-Neale, G. C. Smith. and C. E. Banks, *ACS Appl. Mater. Interfaces*, 2017, DOI: 10.1021/acsami.7b05104.
6. IN PRESS. G. B. de-Mello, L. Smith, S. J. Rowley-Neale, J. Bruber, S.J. Hutton, C. E. Banks, *RSC Adv.*, 2017, TBA, TBA